



The University of Manchester

SCATTERING ICE CLOUDS

A THESIS

SUBMITTED TO THE UNIVERSITY OF MANCHESTER

FOR THE DEGREE OF

DOCTOR OF PHILOSOPHY (PHD)

IN THE FACULTY OF ENGINEERING AND PHYSICAL SCIENCES

2015

HELEN RHIAN SMITH

The School of Earth, Atmospheric and Environmental Sciences

Contents

Abstract	4
Declaration	5
Copyright	6
Acknowledgments	7
1 Introduction	8
1.1 Motivation	8
1.2 Thesis Outline	11
References	13
2 Scattering Theory	15
2.1 Electromagnetic Radiation	15
2.1.1 Polarisation	16
2.2 Stokes Parameters	17
2.3 Scattering by a single particle	18
2.3.1 The scattering phase matrix	18
2.3.2 Phase function and asymmetry parameter	20
2.3.3 Depolarisation	22
2.4 Resolving the Scattering Phase Matrix	23
2.4.1 Theoretical methods	23
2.4.2 Scattering Models	27
References	29
3 Literature Review	31
3.1 Ice crystal Habit	31
3.1.1 Ground based studies	31

3.1.2	In-situ studies	32
3.1.3	Laboratory studies	37
3.1.4	The Morphology Diagram	40
3.1.5	Deviation from pristine forms	41
3.2	Single Scattering by Ice Crystals	44
3.2.1	Theoretical Studies	44
3.2.2	Single Scattering Measurements	48
3.3	Application of Single Scattering Properties to Climate Prediction	53
3.3.1	General Circulation Models	53
3.3.2	Ice cloud Microphysical Parametrizations	53
3.3.3	Radiative Parametrizations	54
	References	57
4	Paper 1: ‘Laboratory Investigations into scattering properties of hollow ice particles’	70
4.1	Summary	70
4.2	Author contributions	70
5	Paper 2: Exact and near backscattering measurements of the linear depolarisation ratio of various crystal habits generated in a laboratory cloud chamber.	105
5.1	Summary	105
5.2	Author contributions	105
6	Paper 3: Using Laboratory and Field Observations to constrain a single habit shortwave optical parametrization for cirrus	141
6.1	Summary	141
6.2	Author contributions	141
7	Discussion	189
7.1	Principal Conclusions	189
7.2	Further Work	192
7.2.1	Particle modelling	192
7.2.2	Instrumentation	193
7.3	Final remarks	193
	References	194

Word count = 51,047

Scattering Ice Clouds

Helen Rhian Smith

A thesis submitted to the University of Manchester
for the degree of Doctor of Philosophy, 2015

The 2013 meeting of the Intergovernmental Panel on Climate Change concluded that the coupling of clouds to the Earth's climate is one of the biggest uncertainties faced in predicting climate change today. Cirrus clouds are of particular interest because the extensive variability in particle size, shape and complexity poses a number of challenges in the accurate modelling of optical properties. The dependence of the single-scattering properties on particle shape demand accurate representation of the crystal geometries in scattering models, geometries which can vary from simple hexagonal prisms to complex multi-branched aggregates.

This work, presented as a series of papers, uses laboratory studies to investigate the single scattering properties of ice crystals. Of particular focus here are columns with internal cavities. The first paper investigates the phase function, P_{11} and asymmetry parameter, g of varying crystal habits, whilst the second paper focuses on polarised scattering. One of the main findings is the difference in internal structure between hollow columns grown at warmer temperatures ($\approx -7^\circ\text{C}$) and those grown at colder temperatures ($\approx -30^\circ\text{C}$). Measurements were used to create new particle geometries for use in scattering models. The third paper makes use of findings from papers 1 & 2 to create an optical parametrization for cirrus, utilizing the new particle geometry.

Declaration

The University of Manchester
PhD Candidate Declaration

Candidate Name: Helen Rhian Smith

Faculty: Faculty of Engineering and Physical Sciences

Thesis Title: Scattering Ice Clouds

Declaration to be completed by the candidate:

I declare that no portion of this work referred to in this thesis has been submitted in support of an application for another degree or qualification of this or any other university or other institute of learning.

Signed:

Date: November 2015

Copyright

- i The author of this thesis (including any appendices and/or schedules to this thesis) owns any copyright in it (the "Copyright")¹ and s/he has given The University of Manchester the right to use such Copyright for any administrative, promotional, educational and/or teaching purposes.
- ii Copies of this thesis, either in full or in extracts, may be made only in accordance with the regulations of the John Rylands University Library of Manchester. Details of these regulations may be obtained from the Librarian. This page must form part of any such copies made.
- iii The ownership of any patents, designs, trade marks and any and all other intellectual property rights except for the Copyright (the "Intellectual Property Rights") and any reproductions of copyright works, for example graphs and tables ("Reproductions"), which may be described in this thesis, may not be owned by the author and may be owned by third parties. Such Intellectual Property Rights and Reproductions cannot and must not be made available for use without the prior written permission of the owner(s) of the relevant Intellectual Property Rights and/or Reproductions.
- iv Further information on the conditions under which disclosure, publication and exploitation of this thesis, the Copyright and any Intellectual Property Rights and/or Reproductions described in it may take place is available from the Head of School of Earth, Atmospheric and Environmental Sciences (or the Vice-President) and the Dean of the Faculty of Faculty of Engineering and Physical Sciences, for Faculty of Faculty of Engineering and Physical Sciences candidates.

¹This excludes material already printed in academic journals, for which the copyright belongs to said journal and publisher. Pages for which the author does not own the copyright are numbered differently from the rest of the thesis.

Acknowledgments

This work was funded by a Doctoral Training Grant (DTG) awarded by the Natural Environment Research Council (NERC), in conjunction with a CASE award from Met Office. The Manchester Ice Cloud Chamber (MICC) and equipment within it is part funded by the project ACID-PRUF grant number NE/I020121/1, which supports all experiments in the cloud chamber.

First and foremost, I would like to thank my supervisors: Ann Webb, Paul Connolly and Anthony Baran for their continued supervision and guidance throughout my PhD. I am incredibly grateful for your time over the years and your support has not only allowed me to complete my PhD, but also continue to a career in science. Many thanks must go to various colleagues who have contributed to this project, including my coauthors Evelyn Hesse, Andrew Smedley and Peter Hill and the laboratory technicians Barry Gale, Lee Paul and Carl Dixon. In addition to direct contributions, I would like to say thank you to a variety of friends, colleagues and acquaintances who I've been lucky enough to meet at conferences and workshops. Our stimulating discussions have given me new perspectives and your enthusiasm for your work has kept me inspired.

Finally I would like to thank the numerous people who helped in shaping my career before I started my PhD. I was lucky enough to have fantastic teachers who have taken an active interest in my professional development, from my A-level teachers to my undergraduate lecturers and supervisors. In particular I would like to thank my undergraduate supervisor Richard Pilkington for allowing me to design my own dissertation project that would eventually lead me into this field. Last but not least, I'd like to thank my family. My brother has always inspired me to try harder by proving himself a worthy academic rival. And Mum and Dad, thank you for raising me to be curious about the world. I could not have completed this without your continued moral, financial and technical support.

CHAPTER 1

Introduction

"How full of the creative genius is the air in which these are generated! I should hardly admire them more if real stars fell and lodged on my coat."

The journal of Henry David Thoreau, 1856

1.1 Motivation

Cirrus, or ice crystal clouds, are thin, wispy clouds, appearing high in the Earth's atmosphere. The constituent ice crystals can give rise to colourful optical phenomena, such as the ice halo and the sun dog (figure 1.1). Although somewhat ethereal in appearance, cirrus has gained recognition as a significant contributor to the regulation of the Earth's climate.



Figure 1.1: Left: Cirrus clouds over The University of Manchester, August 2013. Right: Ice halo and sun dogs over North Dakota, photograph courtesy of Ron Stenz, University of North Dakota.

There are several contributors to energy flows in the Earth's atmosphere, as shown in figure 1.2. At the top of the atmosphere, radiation from the sun is absorbed by atmospheric gases. X-ray and far infrared radiation is mostly absorbed in the thermosphere,

and below this, the short-wave ultraviolet radiation is absorbed by ozone. The remaining solar radiation can then be reflected or absorbed by clouds, water vapour, gases and aerosols before it reaches the Earth's surface. At the Earth's surface, the incoming solar radiation may be reflected or absorbed depending on the surface. Where the radiation is absorbed, it can be stored as latent or sensible heat, or re-emitted as terrestrial (long-wave) radiation. This terrestrial radiation radiates back to space, although a portion is absorbed and re-emitted by clouds and greenhouse gases. Clouds can therefore have two opposing contributions to the Earth's climate by both reflecting short-wave radiation back to space, and trapping long-wave radiation.

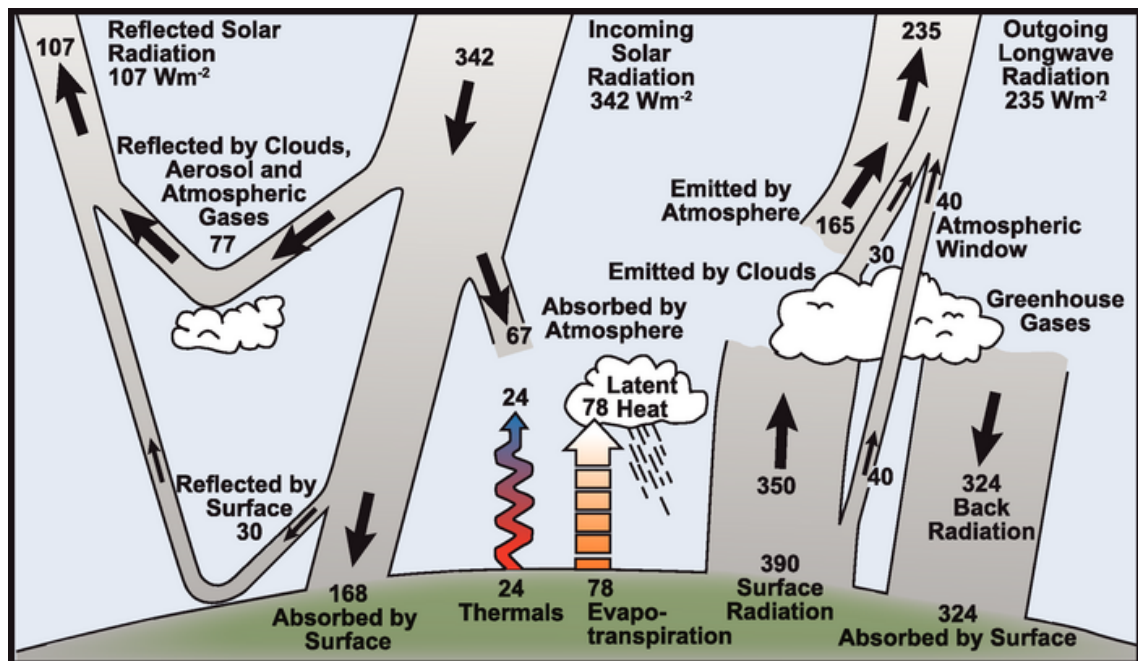


Figure 1.2: Radiative fluxes in the atmosphere. Figure courtesy of the IPCC [1].

The scattering properties of clouds are affected by a plethora of variables. The constituent particles can vary widely from spherical droplets to large, complex ice structures. The formation and subsequent distribution of cloud particle shape and size can be affected by interactions with atmospheric aerosol. The 2013 meeting of the Intergovernmental Panel on Climate Change has therefore highlighted the coupling of clouds with the Earth's climate as one of the major uncertainties in predicting climate change today, as illustrated in figure 1.3 [2].

Although all clouds are highlighted as a large source of uncertainty, cirrus clouds are of particular interest here. Whilst water clouds consist of quasi-spherical particles, cirrus clouds consist of innumerable crystal geometries which range in size over orders of magnitude. Differences in crystal shape have been demonstrated to cause significant differences in the single scattering properties of the ice crystal, and therefore the bulk optical properties of the cloud [3, 4, 5]. Changes in ice crystal size can also have a critical impact upon the bulk scattering properties of a cloud. One study showed that changing the ice particle size can lead to changes in the net radiative effect of up to 60 W m^{-2} [6], where

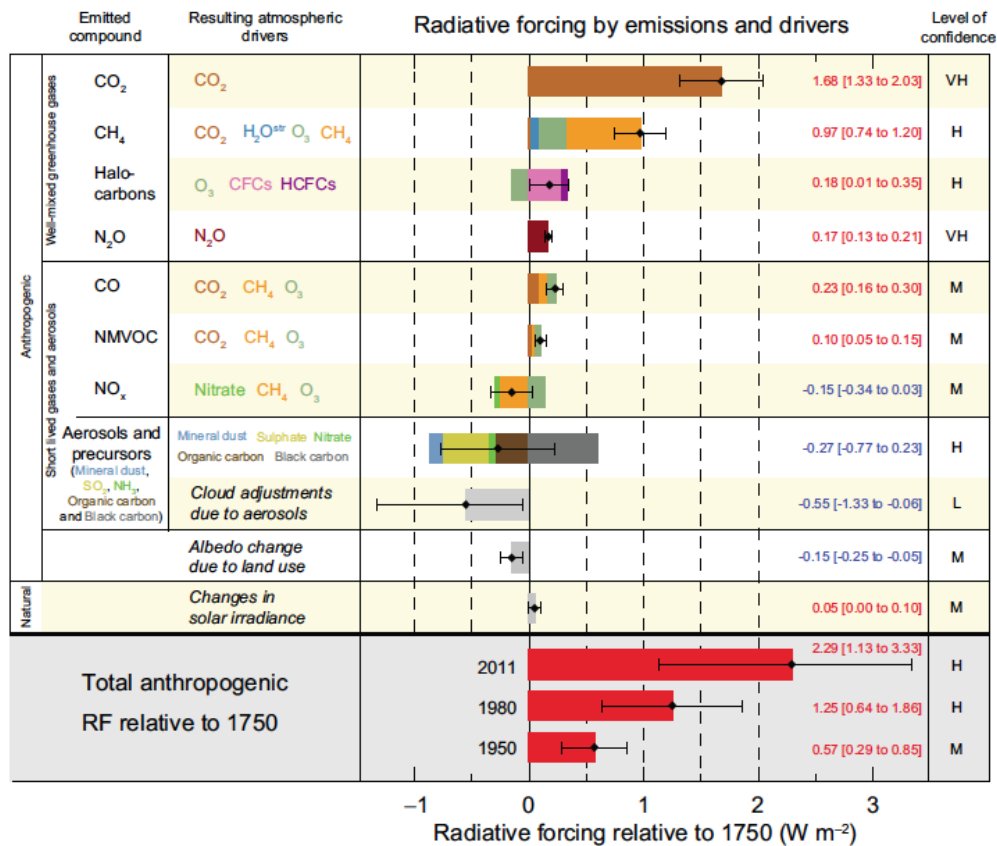


Figure 1.3: Radiative forcing contributions and uncertainties, figure reproduced courtesy of the IPCC (figure SPM.5, page 14 WG1AR5) [2].

the net radiative effect is defined as the sum of the short-wave and long-wave radiation effect. Furthermore, the variety in crystal size means that currently, no one scattering model can be used to treat the entire size distribution of particles in cirrus. Further to the range of crystal shapes, cirrus has an extensive global coverage of about 30%, with coverage reaching 60–70% in tropical regions [7], as shown in figure 1.4.

In addition to the importance in the Earth’s climate, scattering by nonspherical particles is a field with far reaching applications from atmospheric, biological and chemical sciences, to various industrial processes [8, 9, 10, 11]. As discussed, atmospheric ice can vary largely in size, shape and complexity, and therefore the problem of measuring or modelling scattering by ice crystals is particularly complex. As such, light scattering by ice crystals is an active area of research in the scattering community, and many scattering models have been created with the primary focus on ice crystals [12, 13, 14, 15, 16]. Therefore, the study of ice has led to various advances in the theoretical treatment of light scattering by nonspherical particles, and is a topic which continues to contribute to the wider research community.

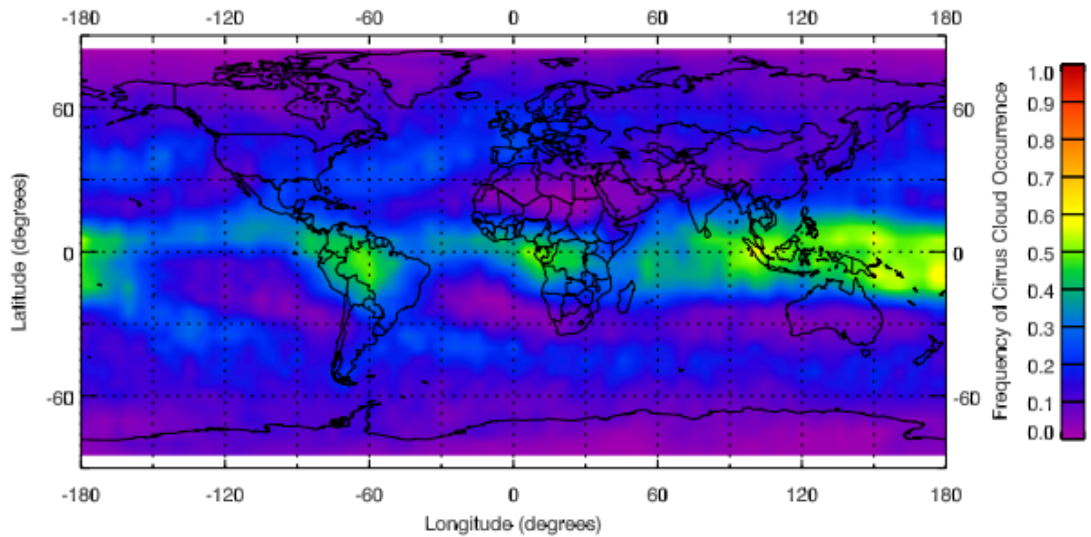


Figure 1.4: Global distributions of cirrus cloud from CloudSat Cloud-Aerosol Lidar and Infrared Path-finder Satellite Observations (CALIPSO) measurements. Image reproduced from Sassen et. al. 2008 [7]

1.2 Thesis Outline

As outlined above, cirrus clouds are a significant contributor to the Earth-Atmosphere radiation balance. Large uncertainties exist in correctly modelling radiative fluxes and radiances from ice cloud, from the measurement and modelling of ice particle geometries, to the accurate theoretical treatment of their single scattering properties. Although theoretical and in-situ studies are numerous, few laboratory studies have been conducted. Laboratory studies offer different capabilities compared with in-situ studies, such as the use of alternative apparatus and the ability to constrain environmental variables. Therefore, the main aim of this thesis was to quantify scattering properties of real ice crystals via laboratory experiments, and to develop/test models to put the measurements into context.

The theory section aims to summarize the basic scattering knowledge and establish the associated terminology used throughout the thesis. The literature review then covers relevant work in ice microphysics, ice optics and the application to global circulation models. The findings from the PhD are presented as three journal papers.

In the first paper, we recognize that current crystal model geometries are too simple and real measurements of realistically grown crystals are lacking. So an objective was to, for the first time, bring together scattering measurements from the Manchester Ice Cloud Chamber (MICC) and interpret the results with a scattering model. In this paper, phase functions (discussed in section 2.3.2) were measured for 5 ice crystal types (solid plates, hollow plates, solid columns and 2 types of hollow column). These measurements were used to construct particle geometries which were then tested in two light scattering codes.

In the second paper, we focus on the measurement and modelling of the linear depolarisation ratio (discussed in section 2.3.3). Linear depolarisation ratio is becoming

more important with the development of new in-situ and remote sensing techniques, and there are scant observational data available [17, 18]. Hence, an optical arrangement was developed to measure linear depolarisation in the cloud chamber environment, and measurements were compared to simulations from ray tracing.

In order to demonstrate the potential of laboratory measurements to improve models, paper 3 uses a new crystal geometry (which was developed in paper one and further tested in paper 2) applied to a climate model. In this investigation, a particle model which yields realistic values for asymmetry parameter (based on observations) is tested in a single habit parametrization for cirrus.

Brief summaries of each paper are given before each results chapter, and author contributions are stated. After the presentation of the results chapters, results are summarised and discussed in the conclusions section.

References

- [1] Intergovernmental Panel on Climate Change. *The Physical Science Basis: Contribution of Working Group I to the Fourth Assessment Report of the IPCC*. Cambridge University Press, Cambridge, 2007.
- [2] Intergovernmental Panel on Climate Change. *The Physical Science Basis: Contribution of Working Group I to the Fifth Assessment Report of the IPCC*. Cambridge University Press, Cambridge, 2013.
- [3] Macke, A. and Mishchenko, M. I. “Applicability of regular particle shapes in light scattering calculations for atmospheric ice particles”. In: *Applied Optics* 35 (1996), pp. 4291–4296.
- [4] Ulanowski, Z., Hesse, E., Kaye, P. H., and Baran, A. J. “Light scattering by complex ice-analogue crystals”. In: *Journal of Quantitative Spectroscopy and Radiative Transfer* 100.1–3 (2006), pp. 382–392. DOI: 10.1016/j.jqsrt.2005.11.052.
- [5] Yang, P. and Liou, K. N. “Geometric-optics-integral-equation method for light scattering by nonspherical ice crystals”. In: *Applied optics* 35.33 (1996), pp. 10–14.
- [6] Zhang, Y., Macke, A., and Albers, F. “Effect of crystal size spectrum and crystal shape on stratiform cirrus radiative forcing”. In: *Atmospheric Research* 52 (1999), pp. 59–75.
- [7] Sassen, K., Wang, Z., and Liu, D. “Global distribution of cirrus clouds from CloudSat Cloud-Aerosol Lidar and Infrared Pathfinder Satellite Observations (CALIPSO) measurements.” In: *Journal of Geophysical Research* 113 (D00A12 2008).
- [8] A. Wax. *Biomedical Applications of Light Scattering*. The McGraw-Hill Companies, Inc., 2010. ISBN: 9780071598804.
- [9] C. C. Gravatt. “The Applications of Light Scattering”. In: *Applied Spectroscopy* 25.5 (July 1971), pp. 509–516.
- [10] A. A. Kokhanovsky. *Light Scattering Reviews 5: Single Light Scattering and Radiative Transfer*. Springer Praxis Books / Environmental Sciences. Springer Berlin Heidelberg, 2010. ISBN: 9783642103360.
- [11] M. P. Diebold. *Application of Light Scattering to Coatings: A User’s Guide*. Springer International Publishing, 2014. ISBN: 9783319120157.
- [12] Macke, A., Mueller, J., and Raschke, E. “Single scattering properties of atmospheric ice crystals”. In: *Journal of Atmospheric Science* 53 (1996), pp. 2813–2825.

- [13] Hesse, E., McCall, D., Ulanowski, Z., Stopford, C., and Kaye, P. H. “Application of RTDF to particles with curved surfaces”. In: *Journal of Quantitative Spectroscopy and Radiative Transfer* 110 (2009), pp. 1599–1603.
- [14] Groth, S. P., Baran, A. J., Betcke, T., Havemann, S., and Smigaj, W. “The boundary element method for light scattering by ice crystals and its implementation in BEM++”. In: *Journal of Quantitative Spectroscopy and Radiative Transfer* 167 (2015), pp. 40–52. DOI: 10.1016/j.jqsrt.2015.08.001.
- [15] Konoshonkin, A. V., Kustova, N. V., and Borovoy, A. G. “Beam splitting algorithm for light scattering by atmospheric ice crystals. Part1. Theory.” In: *Atmospheric and Oceanic Optics* 28 (04 2015), pp. 324–330.
- [16] Yang, P. and Liou, K. N. “Geometric-optics-integral-equation method for light scattering by nonspherical ice crystals”. In: *Applied Optics* 35 (1996), pp. 6568–6584.
- [17] Baumgardner, D., Newton, R., Kramer, M., Meyer, J., Beyer, A., Wendisch, M., and Vochezer, P. “The cloud particle spectrometer with polarization detection (CPSPD): A next generation open-path cloud probe for distinguishing liquid cloud droplets from ice crystals”. In: *Atmospheric Research* 142 (2014), pp. 2–14. DOI: 10.1016/j.atmosres.2013.12.010.
- [18] Van Diedenhoven, B., Cairns, B., Fridlind, A. M., Ackerman, A. S., and Garrett, T. J. “Remote sensing of ice crystal asymmetry parameter using multi-directional polarization measurements - Part 2: Application to the Research Scanning Polarimeter”. In: *Atmospheric Chemistry and Physics* 13.6 (Mar. 2013), pp. 3185–3203. DOI: 10.5194/acp-13-3185-2013.

2.1 Electromagnetic Radiation

In order to discuss the scattering of an electromagnetic wave, we must first consider the basic properties of electromagnetic radiation. Electromagnetic radiation comprises two orthogonal components: an electric field, E , and a magnetic field, B . Consider a linearly polarised plane wave, the two fields are perpendicular to the direction of propagation as shown in figure 2.1.

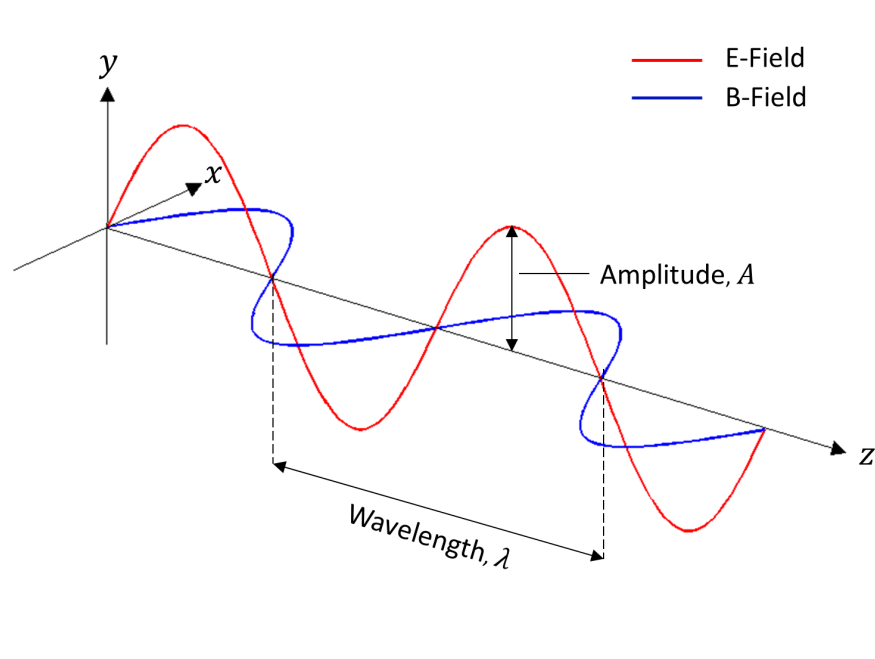


Figure 2.1: A plane electromagnetic wave propagating in the z direction. The electric, (E), and magnetic, (B) field components are depicted in red and blue respectively.

The wave shown in figure 2.1, can be described by the fundamental wave properties: amplitude, A , wavelength λ , cyclic frequency, ν , and speed c . However it is more common to use the angular frequency, ω , which is related to the cyclic frequency by $\omega = 2\pi\nu$.

2.1.1 Polarisation

When an incident beam interacts with matter, the polarisation state may be altered. If the incident beam is reflected off a surface, p polarised light (light polarised parallel to the reflecting surface) is preferentially reflected. For an electromagnetic wave, the polarisation is defined by the plane of oscillation of the *electric* field component. In the simplest case, the electric field component oscillates in a one dimensional plane (as shown in figure 2.1, which oscillates in the y plane) and can be considered *linearly* polarised. Elliptic and circular polarisations arise when two or more interfering sources superpose to produce an electric field whose plane of oscillation rotates in time. This results in a chiral wave oscillating in two dimensions. Linear and circular polarisations are both limiting cases of the more general, elliptic polarisation. Neither linear nor elliptic polarisations are rotationally symmetric about the axis of propagation, and therefore can be described by their orientation in the plane perpendicular to propagation (in this example, in the xy plane). Elliptic and circular polarisations also have a discernible rotation associated with the oscillation, which is described by *sense* or *handedness*. The polarisation is best illustrated by the trace of one full cycle of oscillation, viewed from the direction of propagation. Figure 2.2 shows example traces of linear, elliptic and circularly polarised beams, propagating in the z direction.

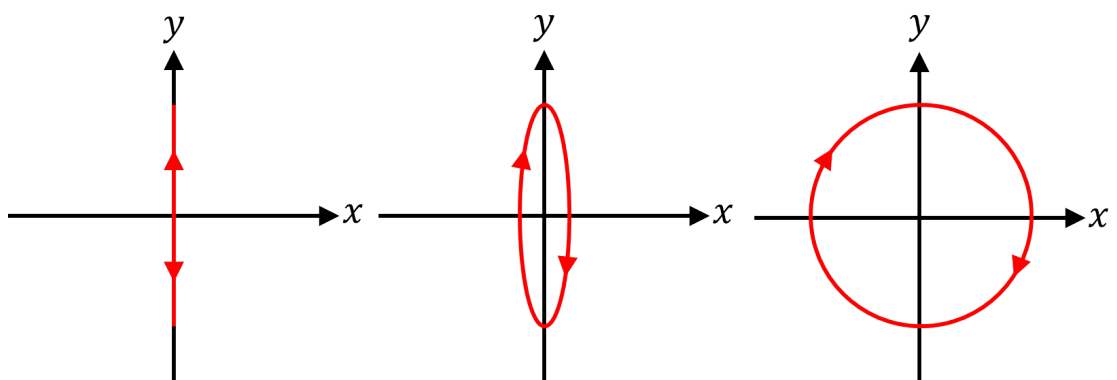


Figure 2.2: Three different polarisations as seen from the trace of one full cycle. From left to right: a linearly polarised beam, polarised in the y plane, a right-hand elliptically polarised beam, polarised in the y plane, and a right hand circular polarised beam.

Knowledge of these variables is fundamental for scattering applications, and most commonly these are described in the form of Stokes parameters.

2.2 Stokes Parameters

The four Stokes parameters, I , Q , U and V , describe fully the intensity and polarisation state of radiation [1]. Together, these parameters make up the Stokes vector. They are illustrated here using the Poincaré sphere [2], a graphical tool used to visualize polarised light.

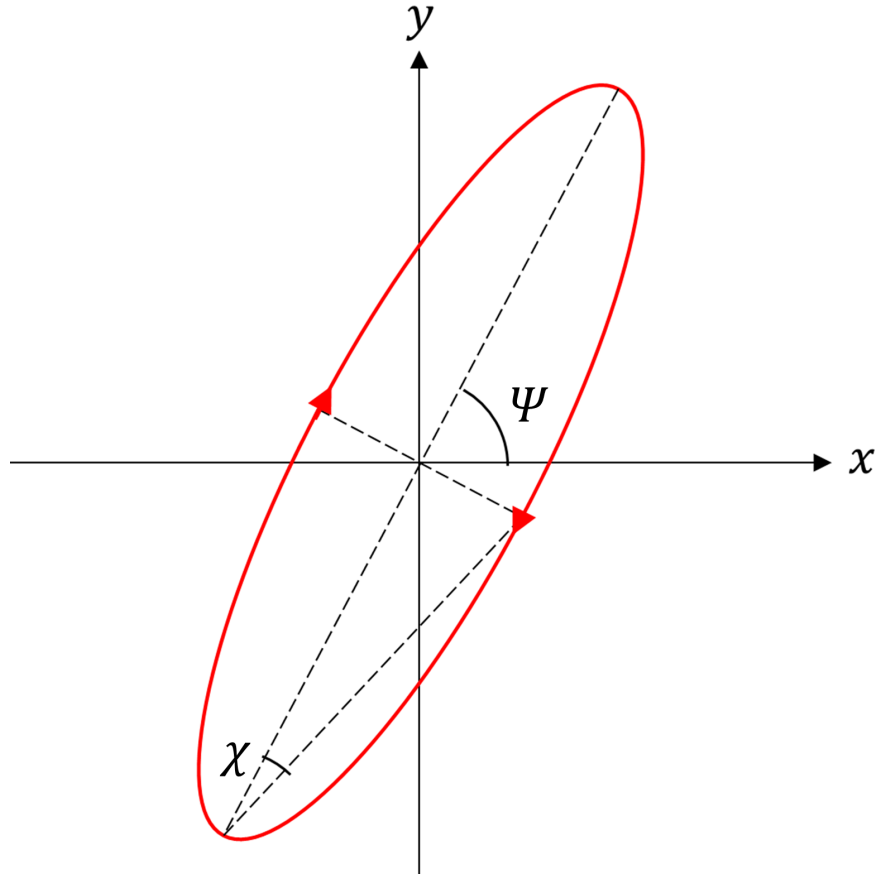


Figure 2.3: An xy view of a right hand elliptically polarised beam propagating in the z direction. The polarisation is defined by the electric field component and therefore the magnetic field component is not shown. ψ describes the orientation of the polarisation in the xy plane, and χ describes the width of the ellipse.

Figure 2.3 shows the trace of a right hand elliptically polarised beam. The total intensity, I of the beam is described by the Stokes parameter I . The other Stokes parameters are all polarisation dependent. It can be seen from the diagram, that the angle χ dictates the degree of ellipticity. As $\chi \rightarrow 45^\circ$, the ellipse becomes circular and the beam can be considered circularly polarised. As $\chi \rightarrow 0^\circ$ the ellipse becomes one dimensional and the beam can be considered linearly polarised. The angle ψ denotes the orientation of the polarisation about the xy plane. When $\psi = 90^\circ$, the beam is polarised in the y plane, whereas when $\psi = 0^\circ$, the beam is polarised in the x plane. The Stokes parameters are defined as follows [2]:

$$I = I \quad (2.2.1)$$

$$Q = Ip \cos(2\psi) \cos(2\chi) \quad (2.2.2)$$

$$U = Ip \sin(2\psi) \cos(2\chi) \quad (2.2.3)$$

$$V = Ip \sin(2\chi) \quad (2.2.4)$$

Where:

I = intensity, Wm^{-2}

p = degree of polarisation of the beam

The Stokes parameters may also be defined by the x and y components of the electric field E_x and E_y , respectively. This notation defines the Stokes parameters in terms of experimentally measurable quantities [3, 4, 5].

$$I = |E_x|^2 + |E_y|^2 \quad (2.2.5)$$

$$Q = |E_x|^2 - |E_y|^2 \quad (2.2.6)$$

$$U = 2\text{Re}(E_x E_y^*) \quad (2.2.7)$$

$$V = -2\text{Im}(E_x E_y^*) \quad (2.2.8)$$

Where E_x and E_y are the x and y components of the electric field. $|E_x|^2$ and $|E_y|^2$ are therefore the measurable intensities of light polarised in the x and y planes respectively.

2.3 Scattering by a single particle

2.3.1 The scattering phase matrix

Consider an incident beam (I_0, Q_0, U_0, V_0) , scattered by a particle. The angle that the scattered beam makes with the incident beam is known as the ‘scattering angle’, θ , defined in figure 2.4.

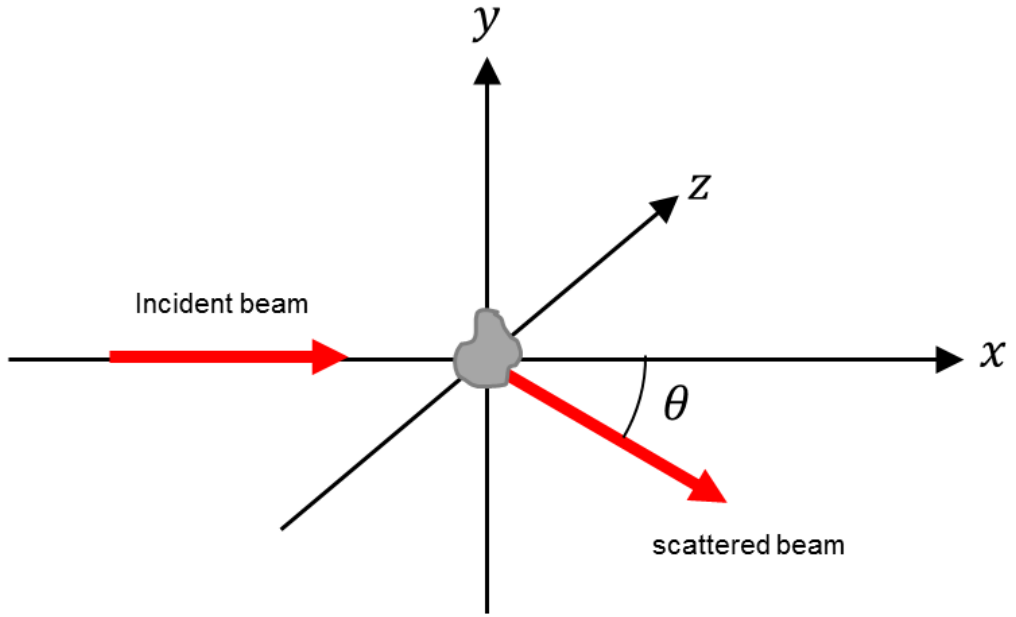


Figure 2.4: An incident beam propagating in the x direction is scattered by a nonspherical particle at the origin. The scattering angle, θ is defined as the angle between the direction of the incident and scattered beams in the scattering plane, where the scattering plane in this example is the xz plane.

The Stokes vector of the scattered beam (I_s, Q_s, U_s, V_s) , at a distance r from the scatterer, can be given by:

$$\begin{bmatrix} I_s \\ Q_s \\ U_s \\ V_s \end{bmatrix} = \frac{1}{k^2 r^2} \begin{bmatrix} P_{11} & P_{12} & P_{13} & P_{14} \\ P_{21} & P_{22} & P_{23} & P_{24} \\ P_{31} & P_{32} & P_{33} & P_{34} \\ P_{41} & P_{42} & P_{43} & P_{44} \end{bmatrix} \cdot \begin{bmatrix} I_0 \\ Q_0 \\ U_0 \\ V_0 \end{bmatrix} \quad (2.3.1)$$

Where k is the wavenumber, and matrix elements P_{ij} (where $i, j = 1, 2, 3, 4$) describe the transformation of the incident stokes parameters. The phase matrix is dependent upon the polarisation of the beam, and the orientation, size and shape of the scattering particle.

For randomly oriented particles, several symmetry relations exist and the scattering phase matrix simplifies down to 6 unique elements [6], given by:

$$\begin{bmatrix} I_s \\ Q_s \\ U_s \\ V_s \end{bmatrix} = \frac{1}{k^2 r^2} \begin{bmatrix} P_{11} & P_{12} & 0 & 0 \\ P_{12} & P_{22} & 0 & 0 \\ 0 & 0 & P_{33} & P_{34} \\ 0 & 0 & -P_{34} & P_{44} \end{bmatrix} \cdot \begin{bmatrix} I_0 \\ Q_0 \\ U_0 \\ V_0 \end{bmatrix} \quad (2.3.2)$$

2.3.2 Phase function and asymmetry parameter

The first element of the phase matrix, P_{11} is known as the *phase function*. The phase function is a normalized distribution of the scattered intensity for scattering angles 0° – 180° . To illustrate this, figure 2.5 shows a plane wave propagating in the x direction, incident upon a scattering particle centered at the origin. The beam is scattered according to the optical properties of the particle. A portion of the incident beam is scattered along the vector \mathbf{a} , denoted by the red arrow. The vector \mathbf{a} makes an angle θ with the x axis in the xz plane (the scattering plane, shaded), and an angle ϕ with the x axis in the xy plane. The light is scattered into a solid angle element $d\Omega$, where $d\Omega = d\theta d\phi$.

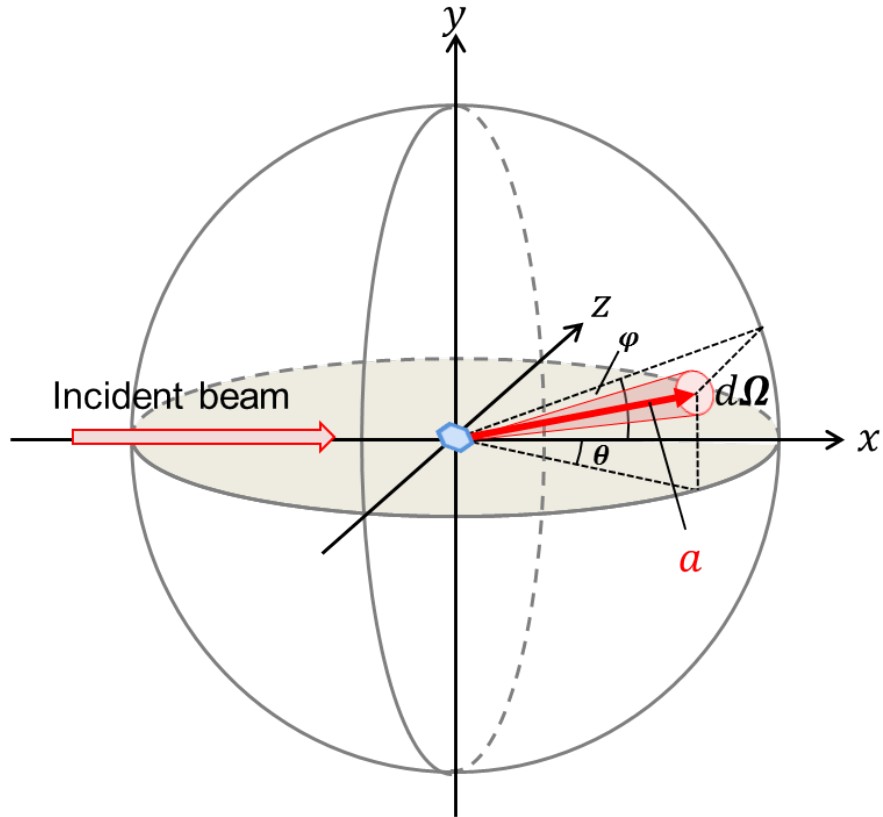


Figure 2.5: . An incident beam is scattered by a particle at the origin. The light is scattered in direction \mathbf{a} , into a solid angle element $d\Omega$. Vector \mathbf{a} makes an angle θ with the x -axis in the scattering plane (shaded), and an angle ϕ with the x axis in the xy plane. $d\Omega$ is equal to $d\theta d\phi$.

The phase function describes the normalized intensity of the scattered radiation as a function of scattering angle, θ . This distribution is normalised to 4π steradians over the sphere, and is given by:

$$\int_0^{2\pi} \int_0^{\pi} P_{11}(\theta) \sin \theta d\theta d\phi = 4\pi \quad (2.3.3)$$

Since P_{11} is not a function of ϕ , this simplifies to, and is more commonly written as:

$$\frac{1}{2} \int_0^{\pi} P_{11}(\theta) \sin \theta d\theta = 1 \quad (2.3.4)$$

The phase function describes the intensity and direction of scattered radiation, and can be used to find the asymmetry parameter, g :

$$g = \frac{1}{2} \int_0^{\pi} P_{11}(\theta) \sin \theta \cos \theta d\theta \quad (2.3.5)$$

Mathematically, the asymmetry parameter can have any value between 1 and -1 . Positive values mean that the majority of radiation is scattered in the forward direction ($\theta < 90^\circ$), whereas negative values mean that the majority of radiation is back scattered ($\theta > 90^\circ$). The asymmetry parameter allows the amount and direction of the scattered radiation to be described by a single number, rather than the full angular distribution given by the phase function. As such, the asymmetry parameter is widely used, alongside other variables, in climate modelling to describe the scattering behaviour of ice clouds. This is discussed further in sections 3.3.1 and 6.

The other elements of the scattering phase matrix contain information regarding the transformation of the incident to the scattered polarisation vectors. Although climate modelling does not currently make use of any polarisation dependent variables, the polarisation elements hold additional information regarding the microphysical properties of the scattering particle. Therefore polarisation elements are utilized in both remote sensing and in situ instrumentation, discussed further in sections 3.2.2 and 5.

2.3.3 Depolarisation

When electromagnetic radiation is reflected off a surface, electric fields polarised parallel to the plane of reflection (*p* polarised) are preferentially reflected, whereas electric fields polarised perpendicular to the plane of reflection (*s* polarised) are more likely to be refracted [7]. The polarisation may also be altered by refraction in the case of birefringent materials. In a birefringent material, the refractive index varies with respect to the orientation of the incident electric field [8, 9]. Ice is a uniaxial crystal, meaning that there is one direction of propagation where the refractive index is constant, regardless of the state of polarisation. This direction is called the optic axis, or *c* axis, defined in figure 2.6. For light propagating perpendicular to the *c* axis, the refractive index varies dependent upon the incident polarisation, whereas for light propagating parallel to the *c* axis, refractive index is constant. For light scattered by an ice crystal, every interface where reflection and/or refraction occur cause the reorientation of the incident polarisation vector. Therefore, the transformation matrix relating the incident and scattered fields hold information regarding the ray path of the beam, which can allow us to infer particle properties such as shape, size and orientation. The use of polarisation information is discussed further in section 5.

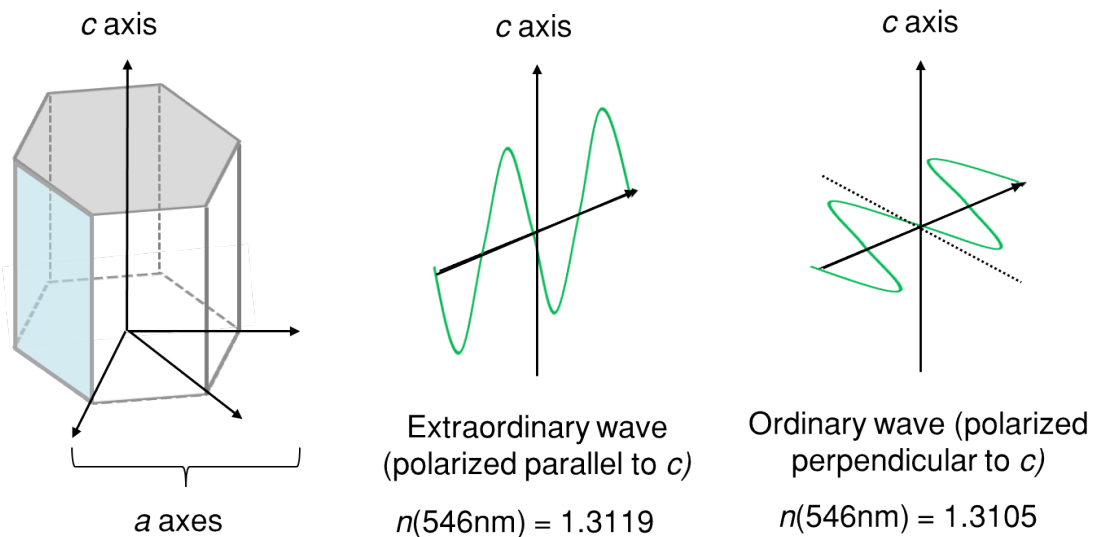


Figure 2.6: Definition of the *c* axis and *a* axes of an ice crystal: the *c* axis is parallel to the prism facet (shaded blue), whereas the *a* axes are parallel to the basal facet (shaded grey). For an E-field polarised parallel to the *c* axis (an ‘extraordinary wave’), the real refractive index, *n*, is a maximum. For an E-field polarised perpendicular to *c*, the real refractive index is a minimum. Example refractive indices given in the diagram are for a wavelength of 546 nm. For a wave propagating in the *c* direction, refractive index is not polarisation dependent.

Linear depolarisation ratio

The linear depolarisation ratio is measured by active remote sensing instruments and several in situ instruments, discussed further in section 5. Typically, a linearly polarised

beam is transmitted, and the ‘backscattered’ component is measured at near backscattering angles. The scattered beam is separated into parallel and perpendicularly polarised components (relative to the polarisation of the incident beam), and the linear depolarisation ratio is given by:

$$\delta = \frac{I_{\perp}}{I_{\parallel}} \quad (2.3.6)$$

Where:

δ = linear depolarisation ratio

I_{\perp} = perpendicularly polarised component

I_{\parallel} = parallel polarised component

2.4 Resolving the Scattering Phase Matrix

Section 2.3.1 discussed the transformation phase matrix which relates the incident stokes vector to the scattered stokes vector. These matrix elements may be calculated, or approximated, theoretically, or measured experimentally.

2.4.1 Theoretical methods

The electromagnetic approach

Maxwell’s equations form the basis of classical electrodynamics and optics [10], and are given, in differential form, as::

$$\nabla \times \mathbf{E} = -\frac{\partial \mathbf{B}}{\partial t} \quad (2.4.1)$$

$$\nabla \times \mathbf{H} = \mathbf{J} + \frac{\partial \mathbf{D}}{\partial t} \quad (2.4.2)$$

$$\nabla \cdot \mathbf{D} = \rho \quad (2.4.3)$$

$$\nabla \cdot \mathbf{B} = 0 \quad (2.4.4)$$

Where:

\mathbf{E} = electric field

\mathbf{B} = magnetic induction

t = time

\mathbf{H} = magnetic field

\mathbf{J} = current density

\mathbf{D} = electric displacement

ρ = electric charge density

Maxwell's equations are used to derive the electric field and magnetic induction field components produced by current and charge distributions. Where the electric displacement D , and magnetic field H are associated according to the constitutive relations:

$$\mathbf{D} = \epsilon_0 \mathbf{E} + \mathbf{P} \quad (2.4.5)$$

$$\mathbf{H} = \frac{\mathbf{B}}{\mu_0} - \mathbf{M} \quad (2.4.6)$$

Where:

ϵ_0 = permittivity of free space

P = electric polarisation

μ_0 = permeability of free space

M = magnetization

The material laws are valid for isotropic, homogeneous media, and the permeability and permittivity are frequency dependent. The variables in equations 2.4.1 – 2.4.4 are related by the general relations:

$$\mathbf{J} = \sigma \mathbf{E} \quad (2.4.7)$$

$$\mathbf{B} = \mu \mathbf{H} \quad (2.4.8)$$

$$\mathbf{P} = \epsilon_0 \chi \mathbf{E} \quad (2.4.9)$$

Where:

σ = conductivity

μ = permeability

χ = electric susceptibility

Coefficients σ , μ and χ are dependent upon the scattering medium.

We describe our electric field as a time-harmonic field, with angular frequency ω , as:

$$\mathbf{E}(\mathbf{r}, t) = \text{Re}\{\mathbf{E}(\mathbf{r})e^{-i\omega t}\} \quad (2.4.10)$$

Where $\mathbf{E}(\mathbf{r}, t)$ is the electric field in the time domain (real), and $\mathbf{E}(\mathbf{r})$ is the electric field in the frequency domain (complex). The angular frequency, ω is related to the wave properties: wavenumber, k , wavespeed, c , and wavelength, λ via:

$$k = \frac{\omega}{c} = 2\pi/\lambda \quad (2.4.11)$$

and the medium properties: complex refractive index, m , conductivity, σ , and permittivity, ϵ , by:

$$m = \epsilon - \frac{4\pi i\sigma}{\omega} \quad (2.4.12)$$

Defining \mathbf{E} as a time-harmonic field, and substituting equations 2.4.7, 2.4.8 and 2.4.9 into equations 2.4.1, 2.4.2, 2.4.3 and 2.4.4, we obtain Maxwell's equations in the frequency domain:

$$\nabla \cdot (\epsilon\mathbf{E}) = 0 \quad (2.4.13)$$

$$\nabla \times \mathbf{E} = -i\omega\mu\mathbf{H} \quad (2.4.14)$$

$$\nabla \cdot \mathbf{H} = 0 \quad (2.4.15)$$

$$\nabla \times \mathbf{H} = -i\omega\epsilon\mathbf{E} \quad (2.4.16)$$

Using these equations, we can describe our electromagnetic wave properties in relation to our host media. To solve Maxwell's equations for \mathbf{E} and \mathbf{B} , they must be integrated over appropriate *boundary conditions*. Consider an electric field travelling from medium 1 to medium 2, with the unit vector \mathbf{n} in the direction of propagation. For a dielectric material (one with no free surface charges), the boundary conditions tangential to the surface are

given by:

$$\mathbf{E}_1 = \mathbf{E}_2 \quad (2.4.17)$$

$$\mathbf{H}_1 = \mathbf{H}_2 \quad (2.4.18)$$

and the boundary conditions normal to the surface are given by:

$$\mathbf{D}_1 = \mathbf{D}_2 \quad (2.4.19)$$

$$\mathbf{B}_1 = \mathbf{B}_2 \quad (2.4.20)$$

Where subscripts 1 and 2 denote media 1 and 2 respectively. Methods based on electromagnetic theory must solve the Maxwell equations for an electromagnetic wave interacting with the boundaries of a scattering particle. To determine the scattered field, these solutions must also be expanded into the far field. For special cases, solutions can be found analytically, but solutions may also be found by utilizing numerical methods. These methods, along with their applications and limitations are discussed further in section 2.4.2.

The geometric optics approximation

Electromagnetic methods rely on solving Maxwell's equations either analytically or numerically. Currently, these methods cannot be applied to all particle shapes and sizes that are of interest in atmospheric science. Furthermore, methods may be computationally intensive making them impractical in the treatment of large or complex structures. Therefore, it is common in atmospheric physics to make use of the geometric optics approximation. The geometric optics approximation assumes that the energy of the electromagnetic waves propagates strongly within *ray tubes* [11]. The ray or ray tube is a geometric line along the axis of propagation of an electromagnetic wave, perpendicular to the wavefronts [12]. For a large, homogeneous scattering medium, geometric optics is considered a reasonable approximation to treat the refraction and reflection of a ray at the interface of two media as shown in figure 2.7, this is described by Snell's law:

$$m_1 \sin \theta_1 = m_2 \sin \theta_2 \quad (2.4.21)$$

Where m_1 and m_2 are the refractive indices of mediums 1 and 2 respectively, and θ_1 and θ_2 are the angles of incidence and refraction, with respect to the surface normal. When $\frac{m_1}{m_2} \sin \theta_1 > 1$ (the critical angle), the ray is reflected.

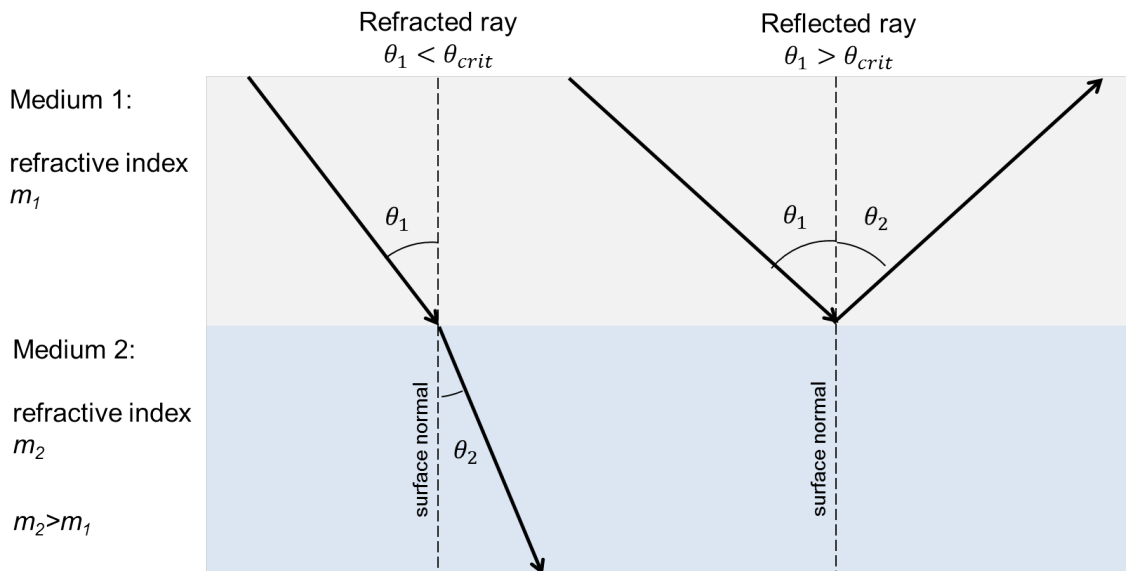


Figure 2.7: A ray travels from medium 1 to medium 2, according to Snell's law of refraction. The left hand ray path shows an incident ray, where the angle of incidence (θ_1) is less than the critical angle (θ_{crit}), the ray is therefore refracted. The ray path shown on the right hand side show the case where the angle of incidence is greater than the critical angle, at which point the ray is reflected.

The ray approximation in the geometric optics approach is used not only to find the field in the presence of a boundary, but also to find the scattered field outside of the scattering particle (in the far field). The geometric approach ignores the phase of the electromagnetic wave, and also does not treat diffraction. This approximation is useful in treating large scattering particles, although at smaller sizes relative to the wavelength, more rigorous methods should be favoured.

The physical optics approximation

The physical optics approximation provides an intermediate method between the exact electromagnetic treatment, and the geometric optics approximation. In physical optics, the internal field (inside the scattering particle) is replaced by the approximate geometric optics field in order to find the field at the particle surface. However, the external field is described using Maxwell's equations. The physical optics approximation has become more common in the treatment of atmospheric particles, specific methods are discussed further in section 2.4.2.

2.4.2 Scattering Models

As discussed in section 2.4.1, the electromagnetic scattering problem can be solved by seeking solutions to Maxwell's equations. Exact analytical solutions can be found for particular shapes, first done for homogeneous spheres (known as Lorentz-Mie theory) [13, 14]. The ease and accessibility of Lorentz-Mie theory has led to its widespread use in

atmospheric physics, requiring atmospheric particles to be approximated as spheres [15]. Whilst a spherical particle may be suitable approximation for certain particles, or certain applications, nonsphericity can have a significant impact upon the single scattering properties of a particle (discussed further in section 3.2.1). Therefore, numerical techniques are necessary in the treatment of other particle shapes.

One method which uses numerical techniques to find solutions to Maxwell's equations is the T-Matrix approach (also known as the Null Field Method). This technique finds a 'transformation matrix' relating the incident and scattered fields by matching boundary conditions for solutions to Maxwell's equations [16]. The method was initially developed for rotationally symmetric particles such as cylinders [16], and was later extended to the treatment of non-axisymmetric particles such as solid hexagonal prisms [17]. Other methods include the Finite difference Time Domain (FDTD), which discretizes the scattering particle and host media into finite volume elements for which Maxwell's equations can be solved, and the Discrete Dipole Approximation (DDA) uses a similar method by discretizing the scattering particle into a series of polarisable elements (or dipoles). Whilst the T-Matrix approach is limited to specific particle geometries, DDA and FDTD can in theory be applied for any arbitrary particle shape. However, high computational demands limit the use of electromagnetic methods for larger and more complex particles and so more approximate methods are used.

A widely used scattering code in atmospheric physics is the ray-tracing code for light scattering at polyhedral shaped particles [18], which is also used in chapters 4, 5 & 6. The ray tracing method finds the scattered Stokes vector using Snell's law (equation 2.4.21) to calculate the refraction of a ray at the particle surface. This procedure is repeated for several rays and several particle orientations to find the scattering phase matrix for a randomly oriented particle. A far-field diffraction approximation is included by treating the projected cross section of the scattering particle as a source of secondary wavelets. The Ray Tracing with Diffraction on Facets (RTDF) model is based upon the ray-tracing code and makes further corrections for diffraction [19]. Here, each facet is approximated by a series of slits which act as a source of secondary wavelets. This allows diffraction from all facets to be treated, rather than only the projected cross section. As a result, RTDF tends to yield phase functions with smoother peak features when compared to ray-tracing, more in keeping with measured results [20, 21, 22]. Methods based on geometric optics are limited to larger particle sizes which can be considered to be within the geometric optics limit (particles larger than the incident wavelength), and therefore cannot be used in the treatment of the smaller ice crystals commonly observed in cirrus. Although further techniques are being developed, there is currently no single scattering model that can be used for the treatment of cirrus as a whole, and therefore both exact and approximate methods are required.

References

- [1] Stokes, G. G. “On the Change of Refrangibility of Light”. In: *Transactions of the Cambridge Philosophical Society* 9 (1852), p. 399.
- [2] Chandrasekhar, S. *Radiative Transfer*. Dover publications, 1960, p. 25. ISBN: 0-486-60590-6.
- [3] Berry, H. G., Gabrielse, G., and Livingston, A. E. “Measurement of the Stokes parameters of light”. In: *Applied Optics* 16 (12 1977).
- [4] Clarke, D. and Grainger, J. F. *Polarized light and optical measurement*. Pergamon, 1971.
- [5] Hayman, M. and Thayer, J. P. “General description of polarization in lidar using Stokes vectors and polar decomposition of Mueller matrices”. In: *Journal of the Optical Society of America* 29 (2012), pp. 400–409. DOI: 10.1364/JOSAA.29.000400.
- [6] Hulst, H. C. Van De. *Light scattering by small particles*. Courier Corporation, 1957. ISBN: 9780486642284.
- [7] Konnen, G. P. *Polarized light in Nature*. Cambridge University Press, 1985. ISBN: 978-0521258623.
- [8] Petrenko, V. F. and Whitworth, R. W. *Physics of Ice*. Clarendon Press, 1999, pp. 219–221. ISBN: 9780198518952.
- [9] Hobbs, P. V. *Ice Physics*. OUP Oxford, 2010. ISBN: 978-0199587711.
- [10] Maxwell, J. C. *A Treatise on Electricity and Magnetism*. 3rd ed. Oxford: Clarendon, 1891.
- [11] Borovoi, A., Konoshonkin, A., and Kustova, N. “The physical-optics approximation and its application to light backscattering by hexagonal ice crystals”. In: *Journal of Quantitative Spectroscopy and Radiative Transfer* 146.July 2015 (2014), pp. 181–189. DOI: 10.1016/j.jqsrt.2014.04.030.
- [12] Smith, F. G., King, T. A., and Wilkins, D. *Optics and Photonics: An Introduction, 2nd edition*. Wiley. ISBN: 978-0-470-01783-8.
- [13] Mie, G. “Beitrage zur Optik truber Medien, speziell kolloidaler Metallosungen”. In: *Ann Phys* 25 (1908), pp. 377–445.
- [14] Debye, P. “Der Lichtdruck auf Kugeln von beliebigem Material”. In: *Ann Phys* 30 (1909), pp. 57–136.
- [15] Kyle, T. G. *Atmospheric Transmission, Emission and Scattering*. Pergamon Press, 1991. ISBN: 0 08 040287 9.
- [16] Waterman, P. C. “Matrix formulation of electromagnetic scattering”. In: *Proceedings of the IEEE* 53 (1965), pp. 805–812.

- [17] Havemann, S. and Baran, A. J. “Extension of T-matrix to scattering of electromagnetic plane waves by non-axisymmetric dielectric particles: application to hexagonal ice cylinders”. In: *Journal of Quantitative Spectroscopy and Radiative Transfer* 70 (2001), pp. 139–158.
- [18] Macke, A., Mueller, J., and Raschke, E. “Single scattering properties of atmospheric ice crystals”. In: *Journal of Atmospheric Science* 53 (1996), pp. 2813–2825.
- [19] Hesse, E., McCall, D., Ulanowski, Z., Stopford, C., and Kaye, P. H. “Application of RTDF to particles with curved surfaces”. In: *Journal of Quantitative Spectroscopy and Radiative Transfer* 110 (2009), pp. 1599–1603.
- [20] Gayet, J.-F., Auriol, F., Oshchepkov, S., Schroder, F., Duroure, C., Febvre, G., Fournol, J.-F., Crepel, O., Personne, P., and Daugereon, D. “In situ measurements of the scattering phase function of stratocumulus, contrails and cirrus”. In: *Geophysical Research Letters* 25.7 (1998), pp. 971–974.
- [21] Gayet, J.-F., Mioche, G., Shcherbakov, V., Gourbeyre, C., Busen, R., and Minikin, A. “Optical properties of pristine ice crystals in mid-latitude cirrus clouds: a case study during CIRCLE-2 experiment”. In: *Atmospheric Chemistry and Physics* 11.6 (2011), pp. 2537–2544.
- [22] Van Diedenhoven, B., Cairns, B., Fridlind, A. M., Ackerman, A. S., and Garrett, T. J. “Remote sensing of ice crystal asymmetry parameter using multi-directional polarization measurements - Part 2: Application to the Research Scanning Polarimeter”. In: *Atmospheric Chemistry and Physics* 13.6 (Mar. 2013), pp. 3185–3203. DOI: 10.5194/acp-13-3185-2013.

3.1 Ice crystal Habit

The structure of ice crystals, commonly referred to as *morphology* or *habit*, has intrigued both scientific and non-scientific communities throughout history. Their complex and symmetric aesthetic has attracted speculation about their formation mechanisms, with theories ranging from the spiritual to the scientific. Scientific studies into the formation of snow crystals began in the early 20th century, and in more recent times, ice crystal habit continues to attract scientific interest due to its impact upon the single-scattering properties of ice crystals [1, 2, 3, 4], and subsequently its role in the Earth's climate.

3.1.1 Ground based studies

Although scientific investigations into ice crystal habit did not start until the 20th century, several notable observations were made as early as the 17th century from examinations of ground level snowfall. In 1611, Johannes Kepler published 'On The Six-Cornered Snowflake', recognising the six-fold symmetry of snow crystals [5], he speculated that this symmetry may arise from the hexagonal close packing of spheres; a theory which 300 years later would be validated with the use of X-ray diffraction techniques [6]. In 1635, Rene Descartes contributed to the classification and cataloguing of ice crystal habits by detailing the structure of natural snow crystals viewed by eye [7]. Later in the century, the invention of the optical microscope allowed for more detailed viewing of ice crystal structure, and by using this technique, Robert Hooke made detailed illustrations of ground based snowflakes in 'Micrographia' as shown in figure 3.1 [8].

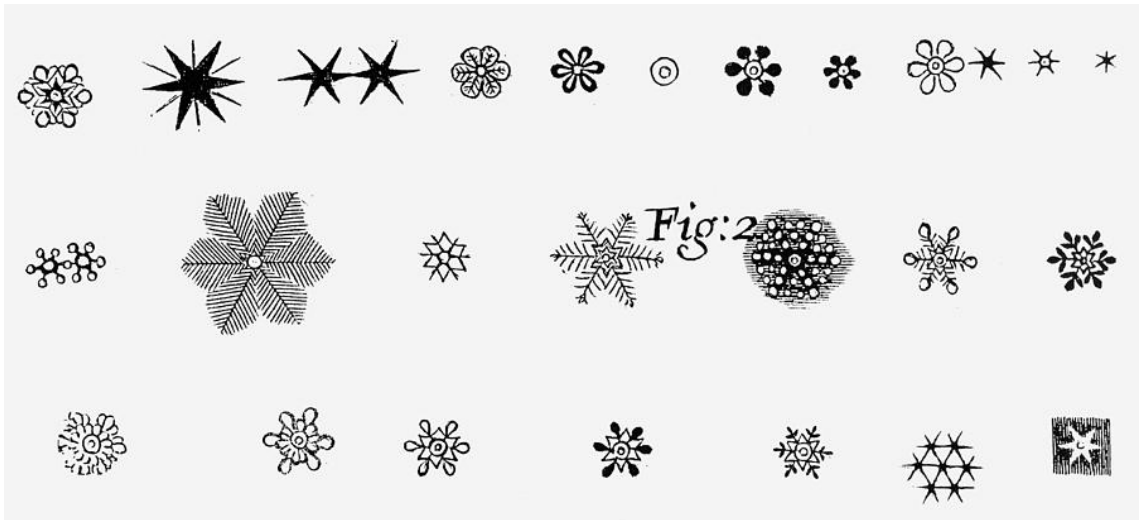


Figure 3.1: Illustrations of observed snow crystal habits by Robert Hooke, published in 'Micrographia' [8].

The advent of photography allowed real crystal images to be recorded, a craft pioneered by Wilson Bentley who photographed more than 5000 natural snow crystals collected at ground level [9]. A combination of optical microscopy and photography techniques have since been employed during ground based scientific investigations, and an extensive range of habits have been observed [10, 11]. Figure 3.2 shows some example photographs of ice crystals collected in North Dakota.



Figure 3.2: Photographs of ground based ice crystal samples. Photography by Aaron Kennedy, University of North Dakota.

Whilst photography techniques allow for high levels of detail to be captured, samples collected at ground level are not necessarily representative of the full range of habits that exist in the atmosphere. By sampling only ground level ice crystals, difficulties ensue when attempting to classify particle habit based on the environmental growth conditions (discussed further in section 3.1.4). To better understand ice as it occurs in the atmosphere, samples have to be taken in clouds using aircraft or balloon borne measurement systems.

3.1.2 In-situ studies

In the early 20th century, Weickmann collected in-situ particles from an open cockpit aircraft [12]. The collection apparatus comprised a perspex tile for collecting samples,

with an attached microscope and camera for directly imaging crystals as they were collected. In order to prevent shattering, the plastic plate was coated in a lacquer, softening the impact, and thus keeping the crystals intact. The use of the lacquer added an interesting perspective to the dataset, as when the ice crystals evaporated, the imprint was still evident on the tile. Comparing the crystal photographs and the corresponding imprints, it can be seen that many of the crystals contained indented cavities which were not visible from the photographs alone. Such indentations are potentially important for light scattering applications, discussed further in section 4. A wide range of crystal habits were photographed, including dendrites, plates, solid and hollow columns and more complex structures such as rosettes and side planes - structures which are not commonly reported at ground level.

Other than the work by Weickmann, similar imaging techniques have not been used in-situ. Subsequent work employed the use of formvar replication to image ice crystals. Formvar is a thermoplastic resin which can be dissolved in chloroform, this solution can then be used to preserve ice crystals by collecting the sample in a thin layer of the solution. As the chloroform evaporates, the resin hardens, leaving the ice crystal encased in plastic. This ‘replica’ is then viewable under an optical microscope [13]. This technique has been used for sampling in-situ in the form of both aircraft based replicators [14, 15, 16], and balloon borne replicators [17]. Whilst these replicas provide the ability to obtain high resolution crystal images, they can also suffer from artifacts, and incomplete replication causing difficulties in habit identification [13]. Furthermore the data collection efficiency is limited and the imaging and analysis is onerous when compared with modern sampling techniques.

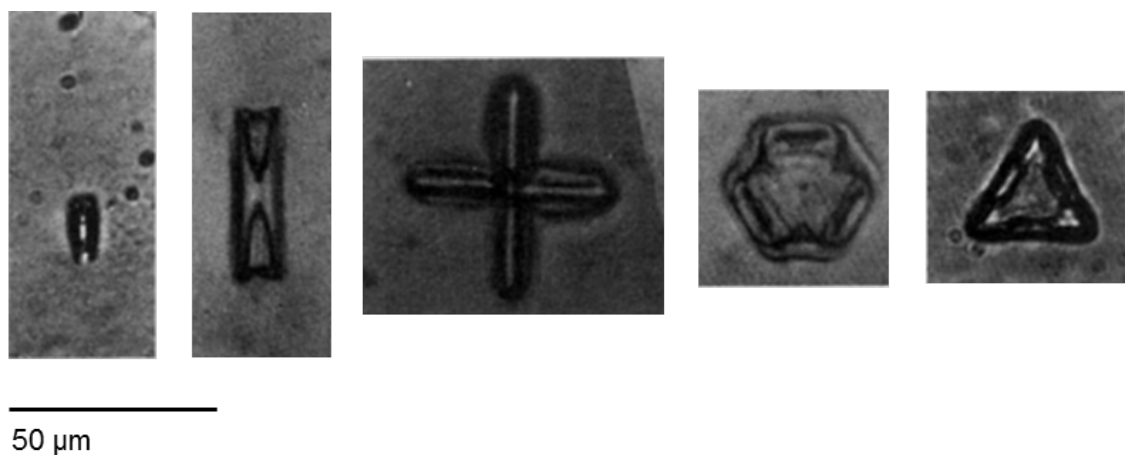


Figure 3.3: Formar images collection in-situ. Left to right: a short column, a hollow column, a budding 4 branched rosette, a plate and a trigonal ice crystal. Figure adapted from Heymsfield et al. 1986 [15].

Modern in-situ studies typically use a range of aircraft mounted instrumentation to determine various properties of ice and other atmospheric particulates. For larger particles, optical imaging probes are used, whereby the particle is illuminated by a light source opposite an array of detectors, such as a CCD array. The shadow cast on the imaging

array forms the particle image. The optical arrangement of the Stratton Park Engineering Company (SPEC) Cloud Particle Imager (CPI) is illustrated in figure 3.4. Various other imaging probes use similar optical set-ups such as the Cloud Imaging Probe (CIP) by Droplet Measurement Technologies (DMT), and the research instruments the HOLOGraphic DETector for Clouds (HOLODEC) [18] and the Particle Habit Imaging and Polar Scattering (PHIPS) probe [19]. Although technology has improved, allowing more accurate imaging, many uncertainties still exist. Habit recognition requires high detail images, and the discrete pixel size of the detector array limits the image resolution. Furthermore, out of focus images can be improperly sized [20], and diffraction fringes can interfere with correct habit classification (see figure 3.5). The HOLODEC uses digital inline holography to reconstruct these out of focus images, although these reconstructed images may lack clarity and cannot be used in the discriminating between water droplets and small ice [18]. In the case of the PHIPS instrument, the imaging laser is replaced with an incoherent light source, removing the complication of diffraction fringes ([19, 21]).

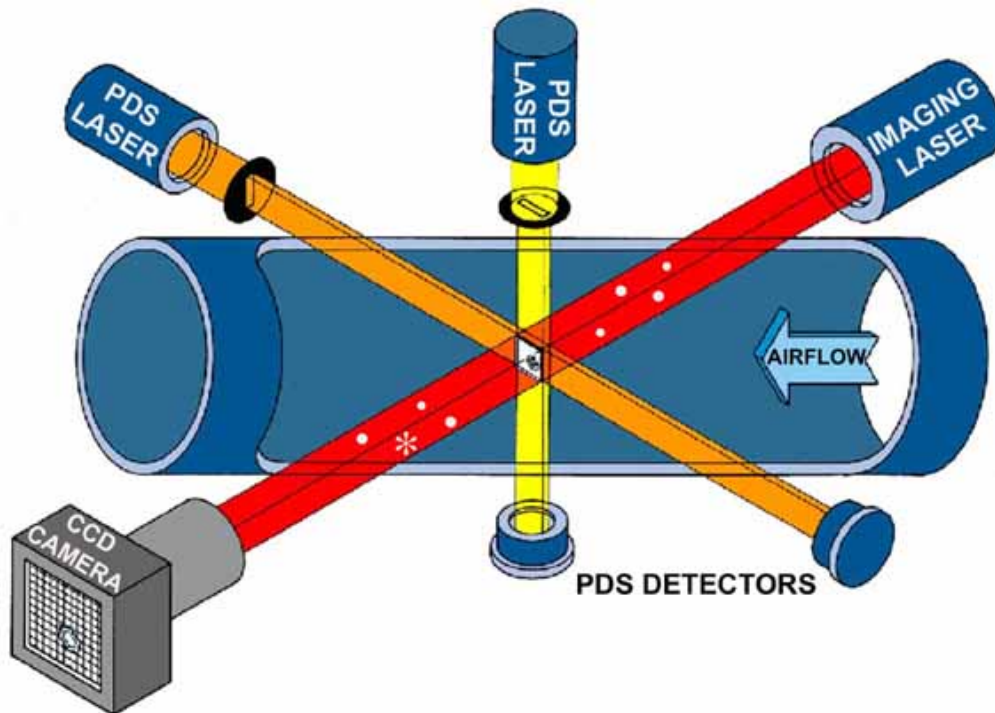


Figure 3.4: Optical imaging arrangement of the SPEC CPI. Figure reproduced courtesy of the Stratton Park Engineering Company [22].

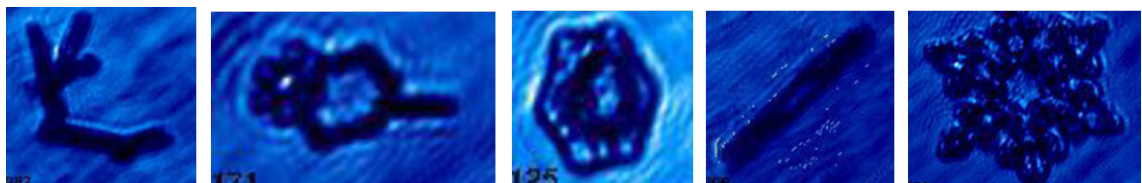


Figure 3.5: Ice crystal images taken using the CPI-v1.0 in the Manchester Ice Cloud Chamber. As a coherent light source is used, diffraction fringes are evident on the particle images, this can complicate habit recognition.

All in-situ instrumentation is flown through the air at high speed, and can cause shattering of ice crystals on the inlet of the probe as shown in figure 3.6 [23]. Larger ice particles are known to break-up and enter the sample volume, consequently causing the over-counting of small ice. Due to this, many historical particle size distributions (PSDs) measured in-situ are biased towards smaller sizes. These errors permeate into the microphysical and radiative parametrizations as further discussed in section 3.3. Attempts to remove these errors have included the introduction of anti-shatter tips, to reduce the occurrence of crystal shattering, and algorithms to remove the shattered artifacts based on particle inter-arrival time [24].

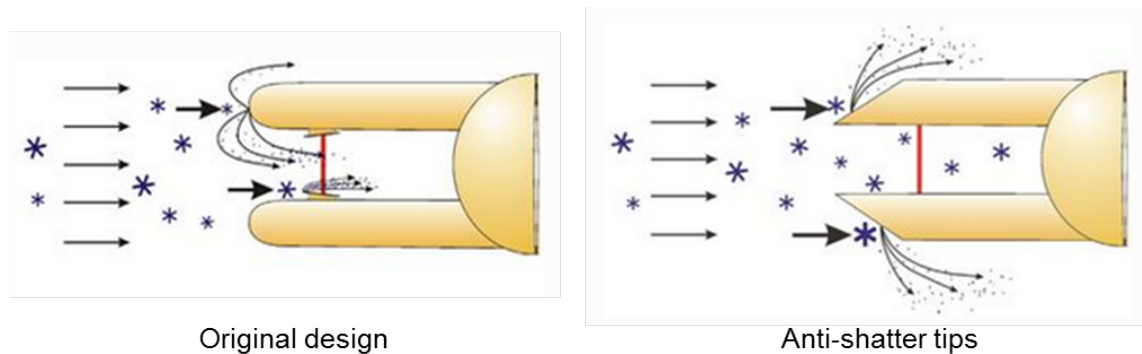


Figure 3.6: Left: original tip design: Particle shatter on the probe inlet and shattered fragments are redirected into the sample volume. Right: anti-shatter tips direct particles incident on the tips away from the sample volume. Figure courtesy of Droplet Measurement Technologies [25].

For particles below the resolution of optical imaging probes, single particle scattering probes have been used to detect and size particles. Forward scattering probes (such as the Forward Scattering Spectrometer Probe (FSSP) by Particle Measurement Systems (PMS) and the Cloud Droplet Probe (CDP) by DMT) are designed and calibrated for the sizing of homogeneous spheres based on Mie-Lorentz theory. Figure 3.7 shows the polar scattering plot (left) for a $10\ \mu\text{m}$ homogeneous sphere with a real refractive index of 1.33. The scattering pattern is related to particle size, and therefore intensity measurements in a known angular range can be used to determine the diameter of the scattering particle. Forward scattering instruments take intensity measurements from the forward scattering lobe, however, this forward scattering region falls within the oscillating Mie signal. These oscillations do not occur for nonspherical particles, and can therefore limit the applicability of the method to the sizing of inhomogeneous or nonspherical particles.

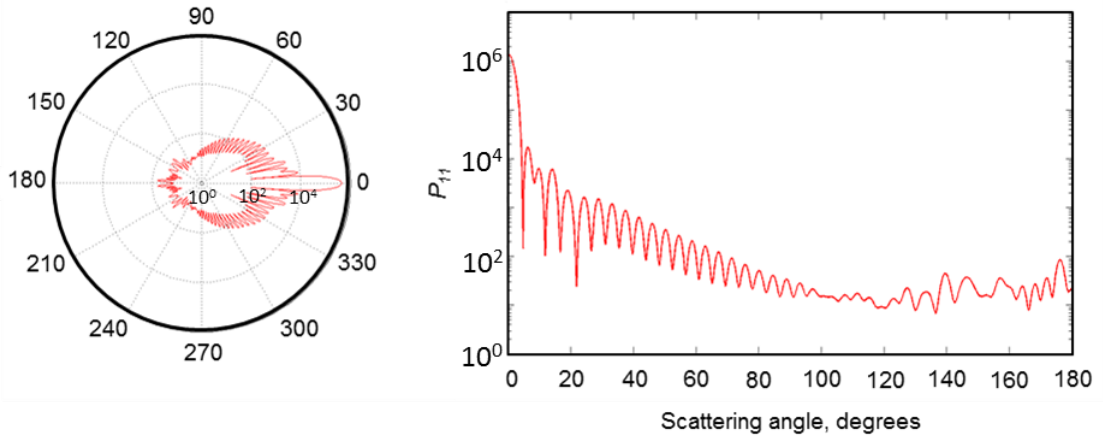


Figure 3.7: Left: A polar plot showing the scattered intensity with respect to scattering angle, the ‘forward scattering lobe’ can be seen in the 0° – 5° region. Right: a cartesian plot of the normalised scattered intensity with respect to scattering angle (phase function). Calculations are done for a $10\ \mu\text{m}$ homogeneous sphere with real refractive index 1.33, in a medium of real refractive index 1. Results are obtained using Jan Schaefer’s ‘MatScat’ code [26].

The Small Ice Detector (SID) series of instruments, developed at University of Hertfordshire, also use forward scattered light to detect and size particles [27, 28, 29]. In contrast to other forward scattering instruments, the SID uses a CCD camera to take a 2D scattering pattern in the angular range 6° – 25° . The scattering pattern is determined by a variety of particle microphysical properties including shape, roughness, hollowness, size and orientation. Due to the sensitivity to particle shape, the SID, unlike most forward scattering instruments, can effectively discriminate between spherical and nonspherical particles. Figure 3.8 shows example scattering patterns obtained from the SID-3 for a variety of particle types [30].

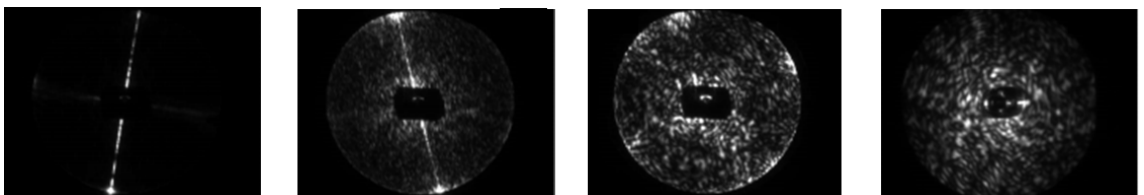


Figure 3.8: Diffraction patterns taken from the SID-3. From left to right: pristine hexagonal column, roughened hexagonal column, bullet rosette & dust grain. Images adapted from Ulanowski et al. 2014 [30].

Other than examining the 2D scattering pattern, nonsphericity of particles can be determined by taking *polarised* measurements of scattered light. As discussed in section 2.1.1, when an incident beam is scattered by a faceted particle, the polarisation can be altered due to *reflection*. For this reason, the linear depolarisation ratio, δ , (given by equation 2.3.6 in section 2.3.3) can be used to distinguish between spherical and nonspherical particles. This technique is commonly used by ground or space based LIDAR, which measures polarised reflectances at near back scattering angles to determine microphysical

properties such as thermodynamic phase, particle habit and orientation. Similar measurements can also be done on single particles using in-situ instrumentation. This is further discussed in section 5.

Summary of in-situ data

The CPI, has been used on a number of field experiments exploring tropical and mid-latitude cirrus [31, 32, 33]. As such, there exists a large body of data on particle habit collected on numerous campaigns. Mid-latitude cirrus tends to be made up of uniform cloud layers. As small particles fall through the cloud, they increase in size due to vapour deposition and aggregation. Therefore, as cloud depth increases (measured from cloud top), particle size and complexity increase. Typical particle sizes are reported from 10 μm [34] to 4000 μm [35]. In tropical cirrus, deep convection transports large aggregated crystals back to the cloud top allowing large and small crystals to coexist at small cloud depths [35]. Consequently, the PSD for mid latitude and tropical cirrus varies. There is little in-situ data for Arctic cirrus, however, it is suggested that the PSD is dominated by ‘diamond dust’ (small, pristine plates and columns), with particle sizes reported between 100 μm –1000 μm [36]. In addition to the difference in particle sizes, the habit distribution varies between different types of cirrus. Results from the EMERALD I campaign shows mid-latitude cirrus consists largely of budding rosettes and rosettes, as seen in Figure 3.9 [31]. Conversely, tropical cirrus consists largely of plates and plate aggregates [37]. Examples of ice crystals in anvil cirrus can be seen in figure 3.10. Recent studies have also shown the prevalence of small quasi-spherical particles in mid-latitude cirrus [38].

3.1.3 Laboratory studies

Whilst in-situ data is necessary for observing real cloud particles, laboratory studies contribute additional knowledge and understanding to the field. The improved ability to constrain experimental conditions allow for aspects of ice crystal growth to be studied in more detail when compared to in-situ studies. The first controlled laboratory experiment took place in a mountain lab in Hokkaido where Ukichiro Nakaya constructed a diffusion chamber and successfully grew the first artificial snowflakes on the tip of a rabbit hair filament [40]. With this set-up, a range of crystals were produced in various humidities and temperatures down to -30° . Diffusion chambers such as Nakaya’s are typically cooled from below and can therefore maintain a significant temperature gradient, making the chamber a useful tool for investigating temperature related phenomena. Similar set-ups have been used in various investigations [41, 42, 43]. Furthermore, since the growing ice crystal is supported by the filament, large growth times can be achieved, allowing for the formation of large and complex particles. However, as the ice crystal is grown directly on the filament surface, there is an argument that the resultant ice crystals can

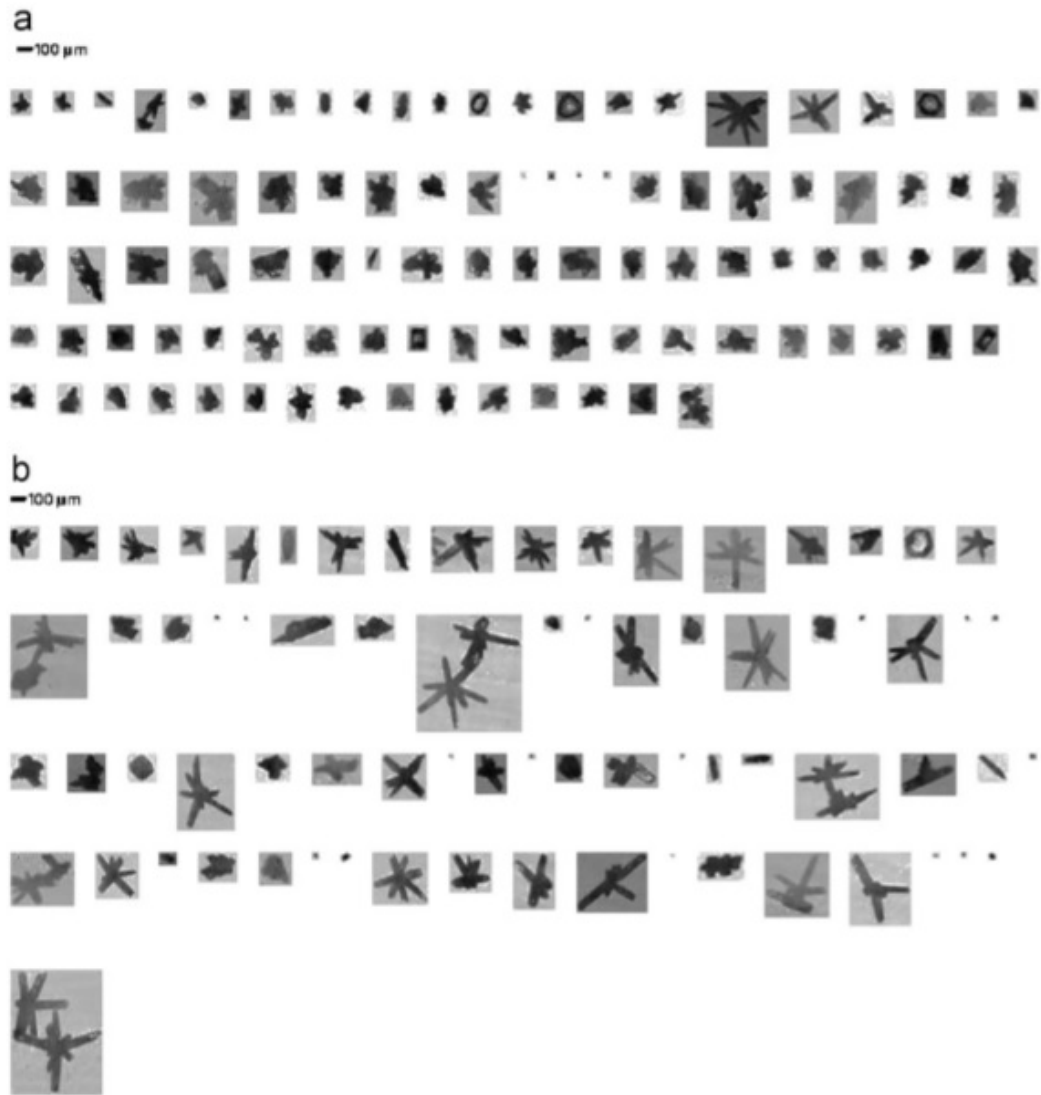


Figure 3.9: CPI images of mid-latitude cirrus particles at a) cloud top and, b) cloud bottom. Figure from Baran 2009 [39].

suffer from ‘*nucleation bias*’, whereby morphological perturbations occur due to the nucleation site [44, 45]. Although it is generally agreed that ice crystal growth is determined mainly from the environmental temperature and supersaturation (discussed further in section 3.1.4), other studies have shown growth mechanisms (and consequently habit) to be dependent upon various other factors such as electric field, nucleation mechanism and the order (or arrangement) of the protons on the ice surface [46, 47, 48, 49, 50, 44]. Consequently, it has been argued that particles grown on filaments may differ to ice crystals formed naturally [44].

A somewhat similar technique is the growth of ice crystals on a substrate. In order to create the correct growth conditions, the substrate is held at some temperature below 0°C , and the vapour is supplied from a reservoir held at a higher temperature. This technique works well in near vacuum environments and is therefore utilized for the growth of ice in a microscope sample stage [51]. Similarly to filament chambers, crystals grown on substrates may also suffer from morphological perturbations caused by nucleation bias. Fur-

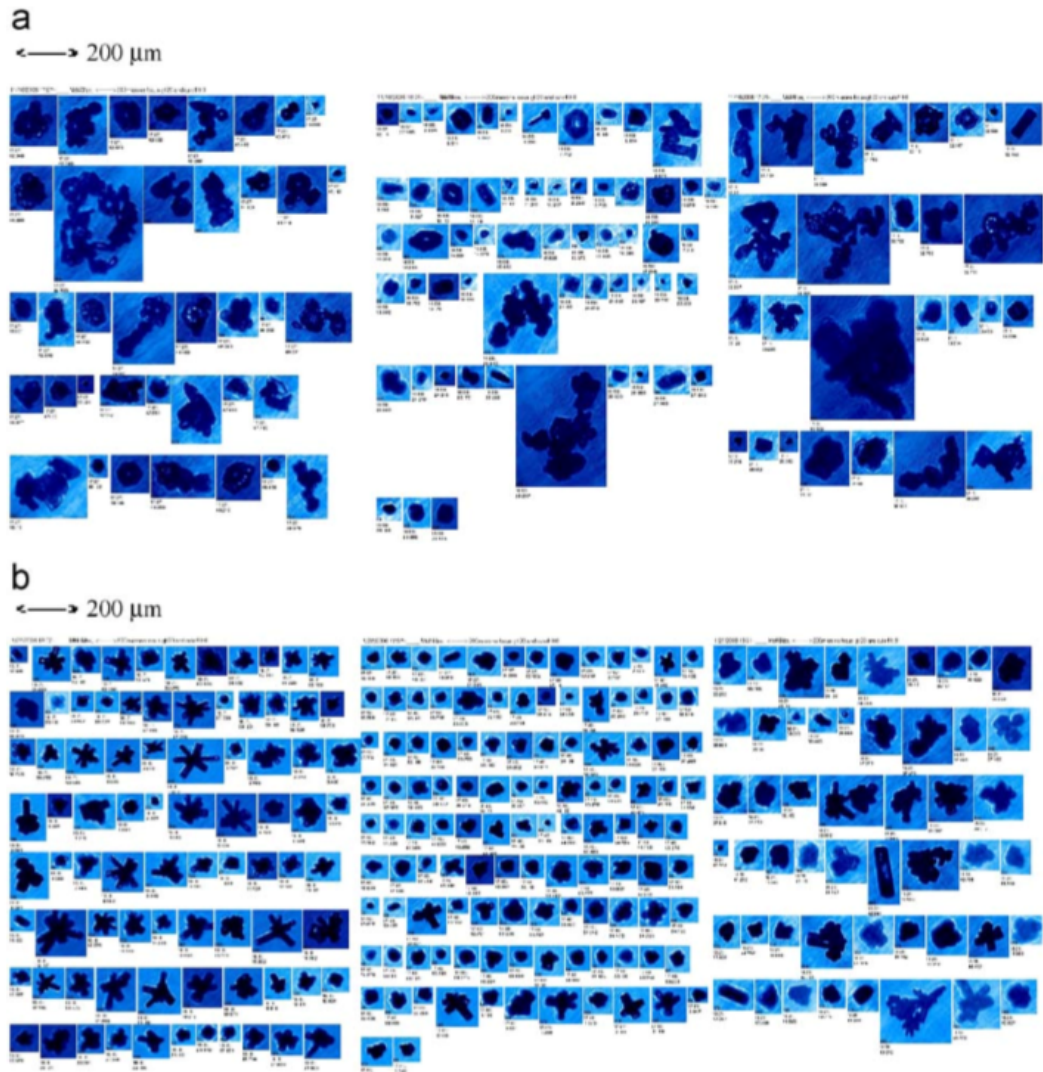


Figure 3.10: CPI images of tropical cirrus particles in a) fresh anvil and, b) aged anvil. Figure from Baran 2009 [39].

Furthermore, the low pressures required in microscope sample stages limit the environmental conditions which can be achieved and therefore the applicability of results to naturally formed ice crystals.

Both techniques discussed so far produce ice crystals growing from a stationary point, allowing for the study of individual ice crystals as a function of environmental conditions. A final technique which offers this ability is the study of single levitated ice crystals. Ice crystals can be levitated in a moving air column [52] or in an electrodynamic trap [1, 53, 54]. This technique removes the bias caused by growing ice on a substrate or filament, whilst still allowing a single particle to be isolated. A drawback of this technique is that as the crystal grows, the required levitation forces increase. Therefore, levitation experiments are limited to smaller particles, and larger, more complex crystals cannot be studied. Furthermore, the orientation of the ice crystal in the trap is not easily constrained, making imaging (and therefore habit identification) troublesome.

The most realistic way to grow ice crystals in a laboratory environment, is to grow

crystals in free fall in a cloud chamber, where a cloud chamber typically consists of a large ‘fall tube’ housed inside a cold room. The method of operation varies between cloud chambers, and between experiments, however some of the basic techniques are outlined here. The use of a cloud chamber environment allows some of the issues associated with other techniques to be addressed. To create a supersaturated environment, the cloud chamber can be humidified by the introduction of water vapour using a water boiler [55, 56], or droplet generator [57]. Typically, the vapour/droplets are allowed to freeze on the chamber walls. The required humidity can then either be achieved by introducing more water vapour/droplets, or by conducting an ‘expansion’. During an expansion, the cloud chamber is depressurised, causing the chamber temperature to drop and the ice on the chamber walls to sublime. Either technique may be used to create the desired temperature and humidity for the experiment. Once the chamber is humidified, there are a variety of techniques that can be used for nucleating ice in the chamber. A popular technique is the localised cooling of air inside the chamber using liquid nitrogen [57], dry ice [58], or compressed air [55]. An alternative is to introduce aerosol particles to the chamber to cause heterogeneous nucleation [59]. This technique removes the nucleation bias which affects filament and substrate experiments, furthermore, dependent on the size of the chamber, large growth times can be achieved, allowing for the study of large, complex and even aggregated particles [55]. Although the cloud chamber environment addresses some of the issues experienced by other techniques, the growth of ice in free fall does not allow for the isolation of single ice crystals. Therefore, cloud chamber studies are limited to the study of particle ensembles. Also, in larger cloud chambers, accurate control of humidity can not be attained, therefore precluding studies of the dependence of ice crystals evolution with respect to humidity.

3.1.4 The Morphology Diagram

For many of the studies discussed so far, the experimental aims were to classify particle habit in terms of the environmental conditions in which it was grown. As such, many of these studies produced a ‘*morphology diagram*’, depicting crystal growth as a function of temperature and supersaturation [40, 11, 42]. These diagrams are based on a variety of techniques, and although many agree at warmer temperatures, deviations start to appear at colder temperatures. In order to address these differences, a recent study constructed an extensive habit diagram, detailing the growth of ice in the temperature range 0° — 70°C and supersaturations of 0–0.6 (with respect to ice), as shown in figure 3.11 [44]. Discrepancies between previous morphology diagrams are attributed to biases in experimental techniques (as discussed in section 3.1.3), and for ground based or in situ samples, we do not know the history of the particles as they flow from one area of saturation to another. This history may significantly change the complexity and structure of the particle which cannot be accounted for in the habit diagram.

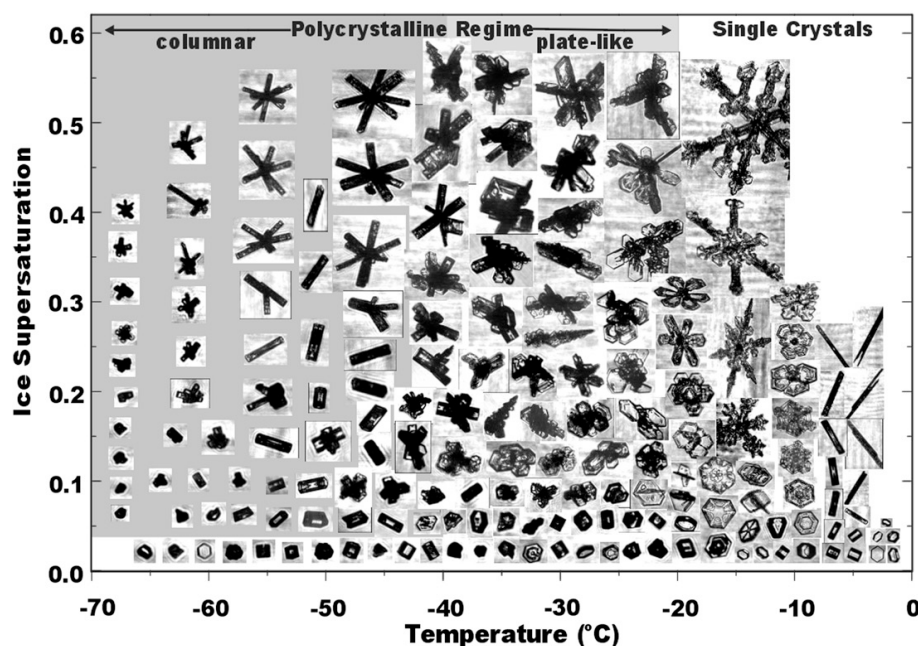


Figure 3.11: Ice crystal habit with respect to temperature and supersaturation. Figure from Bailey & Hallet 2009 [44].

3.1.5 Deviation from pristine forms

Although the comprehensive habit diagram covers a range of atmospherically relevant temperatures, we also note that ice grown in the atmosphere may be subject to changing conditions. This can result in transitional forms such as capped columns, where an existing columnar crystal is transported into an environment which encourages plate-like growth. Such transitional forms have been identified in-situ and from ground based studies [11], although cannot be placed on the habit diagram.

Aggregation

Early research recognised aggregation in observational studies and highlighted the process as an important factor in cloud evolution and precipitation [60]. Many of these early studies suggested that the process was a warm temperature phenomenon, only occurring above temperatures of -20° [61, 60, 62]. More recent investigations have shown that aggregation can also occur at much lower temperatures down to -60° [63, 64], and is seen in a variety of habits [65]. These findings support in-situ measurements as aggregates continue to be found in a number of field campaigns and laboratory studies. Results from the 2006 Tropical Warm Pool International Cloud Experiment (TWP-ICE) [66] showed that aggregates were the dominant habit for large crystals (maximum dimension $200\ \mu\text{m}$) in anvil cirrus. The large degree of aggregation found in electrically active storms led to the suggestion that electric fields aid the process of aggregation [63], later supported by laboratory experiments [55]. Although aggregation is clearly prominent in electrically active systems, aggregates are found in cirrus of all varieties [31, 67, 63, 68, 37]. The

aggregation process alters the ice crystal maximum dimension, and the particle size distribution (PSD). This contribution impacts upon the bulk scattering properties of cirrus and therefore aggregation cannot be overlooked in cirrus models.

Surface Roughness

A further deviation from the pristine form, not generally identifiable from traditional imaging techniques, is that of surface roughness as shown in figure 3.12. In-situ measurements of the asymmetry parameter, g , (discussed in section 2.3.2) consistently give values smaller than those calculated by habit models [69, 70]. Furthermore, laboratory studies have shown that roughened particles may reflect up to twice as much solar radiation compared with equivalent smooth particles [71]. Therefore, the discrepancy between measured and modelled results is accredited to rough particle surfaces, which is considered to be one of the most influential factors on the phase function and asymmetry parameter of ice crystals [72].

The roughness of a surface is influenced by the Helmholtz free energy, A . The Helmholtz free energy has two contributions:

$$A = E - TS \quad (3.1.1)$$

Where:

A = Helmholtz free energy / J

E = Surface energy / J

T = Temperature / K

S = Surface entropy / JK⁻¹

The surface energy, E , favours a smooth surface with the lowest number of available bonds. The surface entropy, S , favours a rough surface with a large amount of dangling bonds. The relative contributions of entropy and energy vary with temperature. The contribution of surface energy is greater at lower temperatures, whereas the contribution of surface entropy is greater at higher temperatures [73]. Therefore, it follows that a growing crystal surface will have a higher degree of roughness at higher temperatures. However, as discussed in Section 3.1.4, the growth of ice crystals is governed by more parameters than simply temperature.

Obvious difficulties exist when faced with the challenge of measurement and characterisation of a rough ice surface. The use of a Scanning Electron Microscope (SEM) requires the ice crystal to be coated in a conductive medium before imaging. This requires the preservation of the ice crystal, for example in formvar, prior to the additional conduc-

tive coating. Consequently, some surface information may be lost in this process. An alternative method is the Variable Pressure SEM (VP-SEM). This allows the ice crystal to be grown inside the sample stage, allowing for surface growth to be monitored over time as a function of selected parameters (temperature, pressure, supersaturation). Studies using a VP-SEM showed significant differences in the roughness of hexagonal ice crystals undergoing growth compared with those ablating [51]. This result suggests that the reflectivity of a cirrus cloud is higher when the particles are ablating, and thus reflectivity can be directly linked with cloud age. Although a significant finding, the applicability of the result to real ice particles must be examined. The maximum pressure attainable in the sample stage is far lower than a typical cirrus ice particle would experience. Also, the technique requires crystals to be grown on a filament or substrate, causing possible morphological perturbations. These limitations impact upon the validity of VP-SEM analysis for the representation of real atmospheric ice.

Due to the difficulty in measuring surface roughness, there is no equivalent in-situ data. However, the introduction of new probes such as the Small Ice Detector (SID) make use of known relationships to infer surface roughness. The SID takes two dimensional scattering patterns of small ($10\ \mu\text{m}$) ice particles (discussed in section 3.1.2). 2D scattering patterns from rough surfaces exhibit speckle-like features, and the speckle size is related to the degree of surface roughness (see figure 3.8). Therefore the SID has the capability of distinguishing between particles with surfaces of varying degrees of roughness.

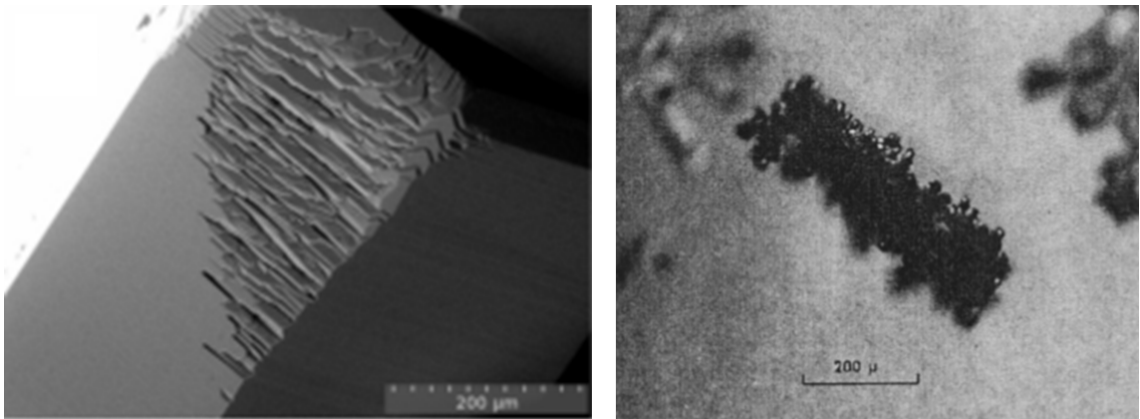


Figure 3.12: Left: a rough ice surface imaged in a VP-SEM sample stage. Right: A heavily rimed ice crystal observed during in situ studies by Ono 1969 [14].

Scalene and trigonal particles

Many studies have noted that ice crystals commonly deviate from expected six-fold symmetry. Crystals with three-fold symmetry have been observed in both laboratory and field studies [74, 58, 42, 12]. It is theorized that such symmetry arises due to a stacking fault in the crystal lattice [74]. This change in symmetry has been shown to affect the single scattering properties [74], although they have yet to be included in radiative parametrizations.

3.2 Single Scattering by Ice Crystals

3.2.1 Theoretical Studies

In order to model light scattering by ice crystals, the ice crystal shape must be represented in a scattering model. An overview of available scattering models is given in section 2.4.2. Each scattering model has limitations to its applicability: for models using electromagnetic methods, solutions may only be attainable for specific particle geometries or for limited size parameters. Although DDA and BEM can be applied to any complex shape, the computational intensity of electromagnetic techniques may limit their usage. For this reason, models using electromagnetic methods are generally used for the treatment of small particles which are generally assumed to have simple, pristine forms. Models based on geometric optics have fewer limitations and therefore more complex ice crystals can be represented. However, due to the extensive range of crystal habits, even the more complex particle models are mere idealizations.

Idealized Particles

Ray tracing results from simple shapes (such as ellipsoids and circular cylinders), were compared against results from the more realistic hexagonal column, in order to determine their usefulness in ice particle modelling [75]. In the case of the ellipsoid and cylinder, computations of side scattering were similar to that of a hexagonal column. However, forward and backscattering differed significantly. In all cases, the simplified shapes gave higher values for asymmetry parameter than hexagonal columns, and in most cases, halo features as would be seen with hexagonal models were not observed. Considering that models for hexagonal columns give higher asymmetry parameters than measured results, this study concluded that ellipsoids and cylinders are not adequately representative of atmospheric ice crystals. The use of the simple hexagonal column is still widespread, although more accurate geometries are sought to represent a variety of ice crystal habits.

Aggregated Particles

Aggregated particles are observed both in-situ and in laboratory experiments and can make up a significant proportion of the ice contained in a cloud [38, 66, 63]. As such, aggregate models have been constructed in several studies [76, 77, 37, 68, 67], and are commonly used in habit mixture models [78, 79]. The compact column aggregate [77], adequately predicts asymmetry parameter and has as such been favoured in a number of habit mixture models. However, the relationship between particle mass, m , and maximum dimension, D , of the aggregate followed $m \propto D^3$ as opposed to the generally accepted relation $m \propto D^2$ [67, 80, 78]. In order to adhere to these microphysical relationships, the ‘compactness’ of the aggregate must be varied. One study used CPI images from TWP-ICE [66] to construct models of aggregated particles, shown in figure 3.13 [37].

The aggregates were described by three parameters: the aggregation index, AI , the area ratio, A_r , and the normalized projected area A_n . The aggregation index was introduced to describe the compactness of the aggregate. Mathematically the AI is defined as ‘the sum of the distances between the centres of mass of all plates divided by the sum of the distances between the centres of mass of all the plates when they lie on a straight line’ and can have values between 0 (fully compact) and 1 (ideal chain). The area ratio is defined as the average projected area, divided by the area of circumscribed circle. The normalized projected area is defined as the orientation-averaged projected area for the aggregate, divided by the average projected area of an aggregate with $AI = 1$ [37]. The aggregate models were used to compute single scattering properties using Macke’s ray tracing code [81]. The scattering phase function, P_{11} , asymmetry parameter, g , and single scattering albedo, ω_0 , were calculated as function of AI , A_R and A_n , at three wavelengths. The findings were that, for non-absorbing wavelengths, the asymmetry parameter increases with increasing plate size. Aggregates with more compact shapes (low AI) exhibit reduced forward scattering and enhanced lateral and backscattering. A difference in AI of 0.44, caused a difference in g of 6.89%.

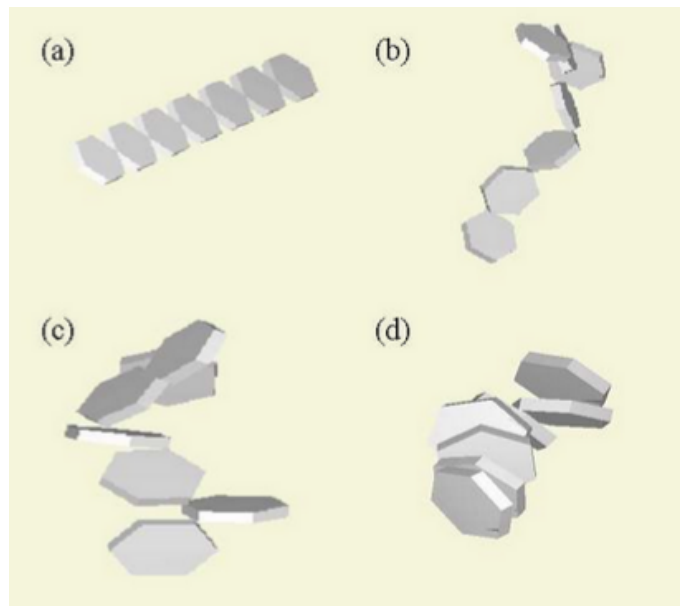


Figure 3.13: Models of plate aggregates with varying aggregation index, AI . a) $AI = 1$, b) $AI = 0.81$, c) $AI = 0.6$ and d) $AI=0.4$. Figure from Um & McFarquhar 2009 [37].

Rough and Nonspherical Particles

As discussed in Section 3.1.2, 2D imaging probes are subject to limited resolution. When imaging smaller particles, edges appear rounded and particles are often misclassified as spherical. Although some instrumentation can distinguish between spherical and nonspherical particles, exact shapes of small ice particles are not well defined. This uncertainty about the true nature of small ice has led to the widespread use of spherical geometries for the representation of small ice. For these small, quasispherical particles, the forward scattering region is dominated by diffraction, and is therefore least sensitive to

particle shape (see figure 3.7). At larger scattering angles, general effects of nonsphericity are noted such as the suppression of rainbow and glory features [82]. When these single scattering properties are used to model bulk optical properties, the assumption of sphericity can lead to a significant underestimate of the cloud albedo [83, 84]. Therefore, more accurate representations of small ice and other atmospheric particulates are sought. Suggested representations for quasispherical cirrus particles include Chebyshev particles [85], gaussian random spheres [86, 87], droxtals [88], the budding bucky ball [89] and the koch fractal crystal [81] (figure 3.14).



Figure 3.14: Representation of nonspherical particles. a) chebyshev particle, b) gaussian random sphere, c) droxtal, d) budding bucky ball, e) koch fractal crystal. Figures adapted from Um & McFarquhar 2011 [89], and Macke et al. 1996 [81].

Many of these quasispherical particle models are formed by the deformation of the surface of a sphere. This deformation of the particle surface can be used not only in creating nonspherical particles, but in creating roughened surfaces on larger particles such as hexagonal prisms. This has been done by discretizing the ice surface into a number of small facets, and tilting the facets [77]. The facets were tilted using a first-order Gram-Charlier series. This particular series was chosen because it had previously been used to model sea surfaces [90], which were thought to be suitable approximations to rough ice surfaces based on SEM observations [91]. Although rough ice surfaces can be modelled, the most common use of ‘roughness’ is that of a distortion parameter available in Macke’s ray tracing code [81]. The addition of ‘distortion’ tilts the outgoing ray between 0° and some maximum (based on the selected amount of distortion between 0 and 1), thus approximating the effects of a rough particle surface. The general effects of modelled roughness, or distortion, are to lower the asymmetry parameter and smooth out halo features.

Hollow Particles

As discussed in Section 3.1.5, measured asymmetry parameters are consistently lower than modelled values. The use of roughness in models typically lowers the asymmetry parameter to more realistic values [72, 92, 71]. Ray tracing results from hollow column geometries have also shown a decrease in asymmetry parameter when compared with solid columns [93]. However, a more recent study used similar geometries in a more rigorous, physical optics approach and found that the main effect of the cavity was to reduce backscattering, therefore *increasing* the asymmetry parameter. This study also

showed that the presence of a cavity affected the polarisation dependent elements of the phase matrix, with hollow columns exhibiting lower linear depolarisation ratios when compared to solid columns [94].

Particles with inclusions

In addition to the cavities seen in hollow columns, observations have been made of particles with *inclusions*, such as embedded air bubbles or solid particles [10, 12]. Ice crystals with internal scatterers have been modelled in various studies, and the general effect of inclusions is found to be a reduction in asymmetry parameter in conjunction with a smoothing of the phase function [95]. In the case of embedding soot, or other absorbing particles, the net effect is an *increase* in asymmetry parameter due to the additional absorption. Similarly to the use of surface roughness, the use of inclusions yields single scattering results comparable to those measured in-situ or in the laboratory. Because of this, an Inhomogeneous Hexagonal Monocrystal (IHM), was proposed as a ‘radiatively equivalent model’ to represent bulk optical properties of cirrus. The geometry of the IHM could be tuned to suitably represent not only scattered intensities, but also polarisation properties based on observed values [96].

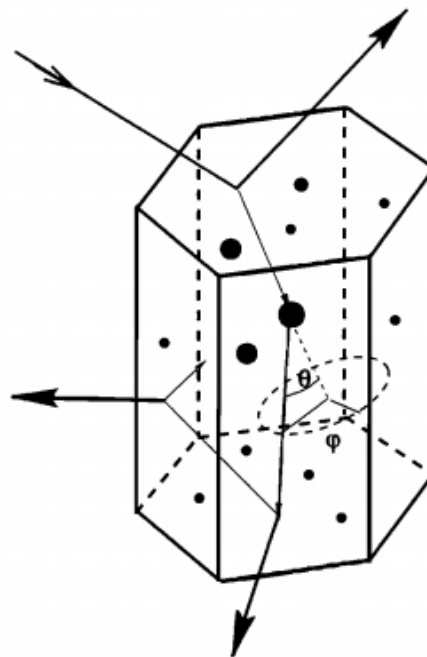


Figure 3.15: The Inhomogeneous Hexagonal Monocrystal: a hexagonal prism is embedded with internal scatterers to alter the single scattering properties of the prism. Figure from Labonnote et al. 2001 [96].

3.2.2 Single Scattering Measurements

In-situ Studies

As discussed in section 3.1.2, there exist a range of scattering probes for the detection and sizing of cloud particles. Whilst many of these are used simply for particle sizing based on a spherical particle approximation, other probes are capable of measuring various scattering properties to determine microphysical properties other than size.

The polar nephelometer is an in-situ instrument capable of measuring the phase function of a scattering particle [97]. The optical arrangement is illustrated in figure 3.16. Particles entering the sample volume scatter light onto an array of photodetectors. The measured intensities are then used to calculate the phase function and asymmetry parameter. Due to the high flow velocities and small sample volume, the scattering particle spends a limited time in the sample volume. Due to this, the ‘phase function’ measurement for a single particle is not representative of random crystal orientations. For this reason, phase function measurements from the polar nephelometer are generally reported as averaged phase functions, taken from several particles. The polar nephelometer has been used in various campaigns [98, 99, 100, 19, 70, 38, 101], and although halo features have been measured [98], in-situ measurements generally yield smoother phase functions, and lower asymmetry parameters than those predicted by models. In addition to the polar nephelometer, the PHIPS probe, mentioned previously, combines particle imaging with a measurement of the scattering phase function with a similar optical arrangement to the polar nephelometer [21].

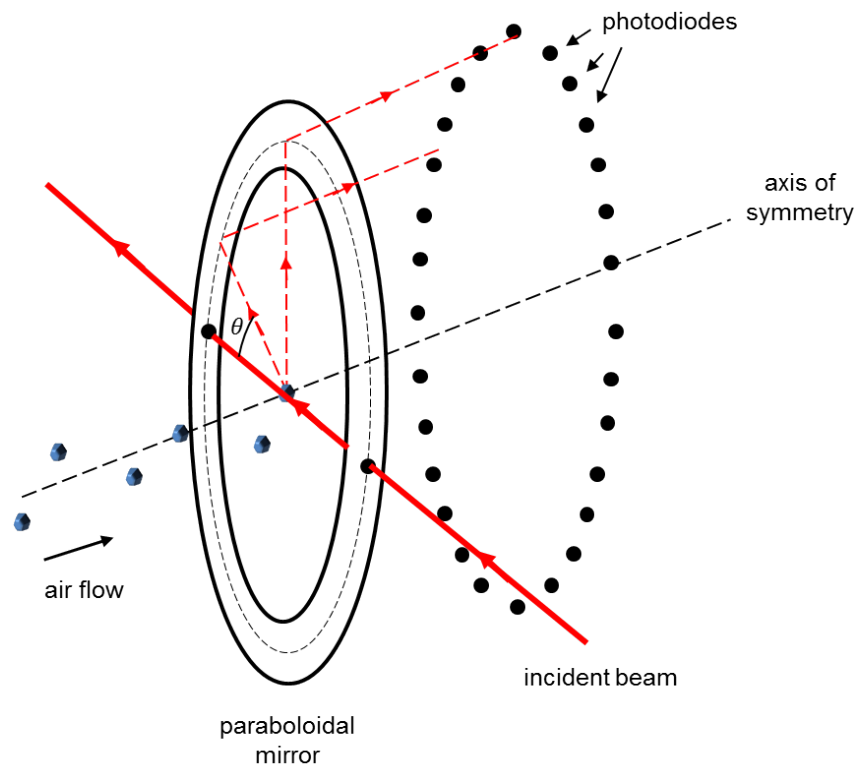


Figure 3.16: Optical set-up of a polar nephelometer. Particles enter the probe in an air flow where they pass through a 800nm laser beam. Light scattered in the plane of the paraboloidal mirror is reflected onto an array of photodiodes where the intensity is measured. The measured intensities at different scattering angles is used to produce a phase function. Figure adapted from Gayet et al. 1997 [97].

As discussed in section 2.3.2, the phase function is an important quantity for climate modelling as it determines the total amount and direction of scattered light. In climate models this is typically represented by the asymmetry parameter (section 2.3.2), which is essentially a parametrization for the phase function, defined by equation 2.3.5. The Cloud Integrating Nephelometer (CIN) measures the asymmetry parameter, but not the phase function. The optical arrangement of the CIN is illustrated in figure 3.17. The use of cosine masks optically integrates the phase function, allowing the asymmetry parameter to be derived. The CIN has also been used in a number of field campaigns, and has also found that in-situ measurements of asymmetry parameter are lower than those predicted by models [69, 102].

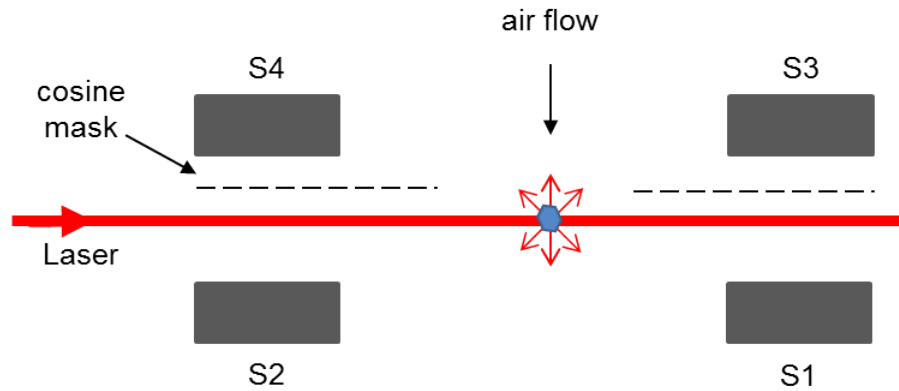


Figure 3.17: Optical arrangement of the Cloud Integrating Nephelometer (Gerber Scientific Inc., Reston, Virginia). Particles in an air flow are passed through a sample volume where they are illuminated by a laser. Four photomultipliers (S1-4) are used to measure the intensity of scattered light. S1 and S3 measure forward scattered light, whereas S2 and S4 measure backward scattered light. Cosine masks are used to weight the measurements of S3 and S4 with respect to scattering angle. Figure adapted from Gerber et al. 2000 [69].

Measurements of the phase function and/or asymmetry parameter are useful in the field of climate science as asymmetry parameter is one of the main optical properties used to describe particles in a radiative parametrization (see section 3.3.3). Whilst the polarisation dependent elements of the phase matrix are not as yet used in the prediction of radiative fluxes in the atmosphere, polarised measurements can discriminate certain microphysical features and are therefore a powerful tool in microphysical instrumentation. The linear depolarisation ratio (equation 2.3.6) is commonly measured by ground and space based LIDAR, and used to determine thermodynamic phase, particle habit and particle orientation [103, 104, 105, 106, 70, 107]. In addition to remote sensing, certain in-situ instrumentation also have capabilities to take polarised measurements. DMT produced an Aerosol Particle Spectrometer with Depolarization (APSD), which measures the linear depolarization ratio for light collected between 140° and 170° for the purpose of determining nonsphericity or particle roughness. For larger particles, the CAS-DPOL [108] and the CPSD (both by DMT) use similar optical arrangements to measure LDR at near backscattering angles for the purpose of discriminating between water droplets and ice. The linear depolarisation properties of ice crystals and the relevant instrumentation is discussed further in section 5.

Laboratory Studies

Whilst in situ data is crucial in understanding scattering properties of real atmospheric particulates, laboratory studies allow for controlled investigations. In particular, this can help with the correct characterization of particle habit, and accessibility means that alternative measurement techniques may be used. Section 3.1.3 discussed some of the difficulties in creating and classifying ice crystals in a laboratory environment and the same

difficulties apply when conducting laboratory based scattering measurements of ice crystals, although several more factors have to be addressed. The growth of ice on filaments or substrates are generally unsuitable for scattering measurements as the filament/substrate will produce its own scattered field, making the scattered field from the ice crystal difficult to determine. Instead, scattering measurements are better suited to particles suspended in air, either levitated or in free fall.

Due to the difficulty of dealing with small particles, early studies used microwave analog techniques to study scattering by nonspherical particles. This method used microwave radiation and millimeter size targets on the assumption that preserving the size parameter would also preserve the scattering properties. Results were then extrapolated to different wavelengths and particle sizes [109, 110, 111]. A newer analogue technique for the investigation of single scattering by ice crystals uses realistically sized targets grown from sodium fluorosilicate [112, 71]. These crystals have similar optical properties to ice and can be grown in geometries representative of cirrus ice crystals, such as simple hexagonal columns and bullet rosettes. The use of realistically sized targets allows experiments to be conducted at the wavelength of interest, without the need to extrapolate results.

For experiments on real particles, levitation techniques benefit from the ability to attribute measured scattering properties with a single particle. For electrostatically levitated particles, an issue with the levitation technique is constraining the orientation of the ice particle. Measurements from randomly oriented particles are desirable for measurements of the phase function or asymmetry parameter. However, under electrodynamic levitation, the ice crystal has a tendency to spin about one axis. This tendency is useful in the measurement of scattering by horizontally or vertically aligned particles [1], although achieving full randomization is preferable for measuring phase matrix elements. Furthermore, levitation techniques are limited to small particle sizes, and some studies have struggled to characterize the scattering particle in detail [53, 54].

For measurements of larger particles, ensemble measurements can be conducted in cloud chambers. The creation of ice in a cloud chamber is discussed in section 3.1.3. Once the ice is created, different techniques can be used to take scattering measurements. A common approach is the application of aircraft instrumentation into the laboratory, such as the polar nephelometer [57], or the PHIPS [21] to measure phase functions, and the HOLIMO [113] to measure linear depolarisation ratio. These instruments work in much the same way that they do in-situ, however, the particles are drawn through the instruments via a pump. By doing so, much slower air speeds are used (compared with in-situ measurements), and therefore laboratory based experiments are less likely to suffer from particle shattering [114]. In the polar nephelometer, a stream of particles is drawn through the sample volume and one particle is sampled at a time, results are then generally averaged over several particles. In a cloud chamber environment, larger optical arrangements can be used to increase the sample volume, and measure scattering from an ensemble of particles instantaneously. Although several particles may occupy the sample volume, if

particle concentrations and sizes are sufficiently small, effects of multiple scattering can be considered negligible [115]. The application of a scanning detector can then be used to take phase function measurements from a cloud of particles. One such set-up is illustrated in figure 3.18 [56]. The rotating detector is used to measure scattered intensity at different scattering angles whilst additional detectors monitor the incident and attenuated beam. From these measurements, phase function and asymmetry parameter can be calculated. As a single detector is used for angular measurements, the full phase function is not taken instantaneously and therefore measurements are sensitive to the temporal homogeneity of the cloud. A similar approach has been used in laboratory experiments presented in this thesis and are discussed further in sections 4 and 5.

Similar to in-situ studies, laboratory studies have measured smoother phase functions, with diminished halo features compared to those predicted by theory [1, 56, 115]. In addition to this, laboratory measured linear depolarisation ratios tend to be smaller than those predicted by theory [113, 21]. As phase functions are not well predicted using current particle geometries, we see that further laboratory studies are necessary for the improvement of these particle models, and for testing the ability of scattering models to produce realistic results.

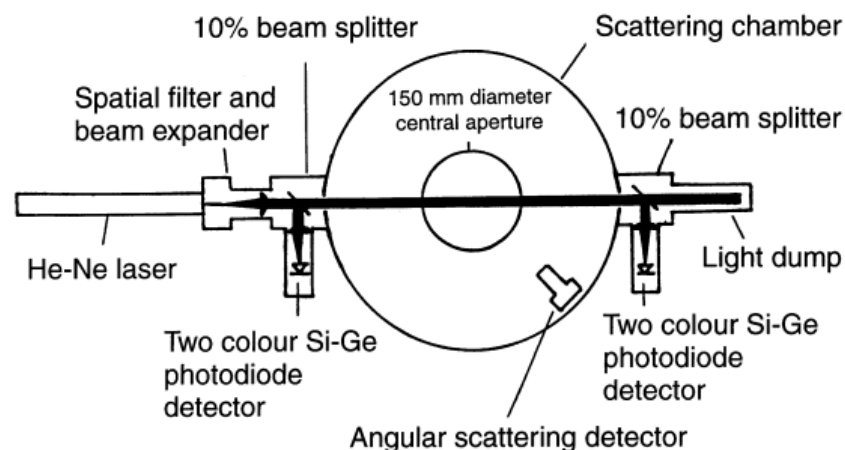


Figure 3.18: Application of scanning detector optics to measure the phase function from an ensemble of particles in a laboratory cloud chamber. A laser beam is directed through a cloud of particles, which scatter the beam in all directions. 10% Beam splitters are used to measure the intensity of the incident and attenuated beam (and therefore extinction), and a rotating detector measures scattered intensity at different scattering angles. Figure from Saunders et al. 1998 [56].

3.3 Application of Single Scattering Properties to Climate Prediction

3.3.1 General Circulation Models

General Circulation Models (GCMs) are used for future projections of the global climate. Early models focused only on circulation in the ocean or atmosphere [116], although modern models combine both atmospheric and oceanic processes [117, 118, 119, 120]. In modern GCMs, the Earth-Atmosphere-Ocean system is discretized into grid boxes with a horizontal resolution of 250–600km, 10–20 layers in the atmosphere and up to 30 layers in the ocean [121]. Similar, higher resolution, GCMs are used for regional climate and weather forecasting, but the computational demands make them unsuitable for global, long term predictions such as projections of mean global temperature. Cloud processes operate on scales from microns to thousands of kilometers. The sub grid scale processes can have a large effect on the climate and therefore must be taken into account in the GCM. This is done in the form of a *parametrization*. A parametrization describes the statistical effect of the sub grid scale processes on the mean state of the grid box. Such parametrizations exist for various physical processes.

3.3.2 Ice cloud Microphysical Parametrizations

Microphysical parametrizations use GCM predicted variables in order to predict parameters which govern the initiation, growth and precipitation of cloud particles. Such processes include ice nucleation, droplet activation, ice crystal capacitance/sublimation, fall speed, and Particle Size Distribution. Such variables are crucial in climate modelling as they affect dynamics (latent heating and cooling due to vapour growth/evaporation and freezing), surface precipitation (due to varying fall speeds, particle mass and concentration) and cloud optical properties. Observational and theoretical studies have shown that power laws can be used to describe the mass, m , of ice particles with respect to their maximum dimension, D , [67]. Earlier parametrizations used $m \propto D^3$ relationships, although newer research has shown theoretically that aggregated particles follow the mass-dimensional relationship $m \propto D^2$ [67, 45]. In addition to particle mass, observational data has been used to derive relationships for particle area ratio, A_r [35]. The area ratio gives the ice particle cross sectional area as a function of its maximum diameter. This study derived several relationships for a variety of cirrus sampled in-situ, and the averaged $A_r(D)$ relationships for showed little variation for different geographical locations. However, the $A_r(D)$ relationship was found to vary with vertical height.

These relationships are of importance for various processes, however they are of particular interest here due to their bearing on the optical properties of the cloud. In a GCM, these optical properties are parametrized separately in the *radiative* parametrization.

3.3.3 Radiative Parametrizations

A common approach in climate models is to relate the bulk optical properties to the diagnostic variable *effective diameter*, D_e , and GCM prognostic variables Ice Water Content and/or temperature [122, 123]. The effective diameter for water, ice or mixed phase clouds is given by given by equation 3.3.1 [124]:

$$D_e = \frac{3}{2} \frac{WC}{\rho \sum_i n_i A_i} \quad (3.3.1)$$

Where:

WC = Water Content

ρ = density of ice or liquid water

A_i = the mean cross sectional area in bin i

n_i = number concentration in bin i

The use of D_e is generally suitable for the parametrization of water clouds and at solar wavelengths where the bulk properties of cirrus become largely independent of PSD. However, this becomes unreliable for ice clouds at more absorbing wavelengths [125, 126, 127, 78, 128], and for frequencies in the microwave, where it has been shown that optical properties cannot be uniquely defined by D_e and the Ice Water Content (IWC) [127]. For ice clouds, the optical properties are also dependent upon the shape of the PSD, which is not accounted for in D_e based schemes as they tend to be physically inconsistent with the microphysical scheme and may assume different PSDs [128]. Recent parameterizations have bypassed the need for D_e by coupling the optical parameterization directly to the GCM prognostic variable IWC [78]. In order to make the microphysical and optical schemes physically consistent, it has also been argued that particles used in the optical parameterization should adhere to the same mass-dimensional and area ratio-dimensional power laws as assumed in the microphysical scheme [128, 78]. As discussed in section 3.1, ice crystals in cirrus cloud contain a myriad of shapes and sizes with further deviations in the form or roughness, inclusions and internal structure. Each of these variations can have a significant impact upon the scattering behaviour of the ice crystal. In order to predict bulk optical properties, we need to construct geometric models to accurately represent ice particles and their scattering properties, and couple these models to GCM prognostic variables (IWC, T) and variables from the microphysical scheme (PSD). Whilst earlier radiative parametrizations used single geometries such as cylinders or hexagonal columns [123], current parametrizations favour mixtures of particle geometries, known as ‘habit-mixture models’.

Habit Mixture Models

It has been shown that habit mixture models better follow the derived mass dimensional power laws [79, 129], compared with single particle models. For satellite retrievals from MODIS, a 9 element habit mixture model is used [79]. These elements are shown in figure 3.19.

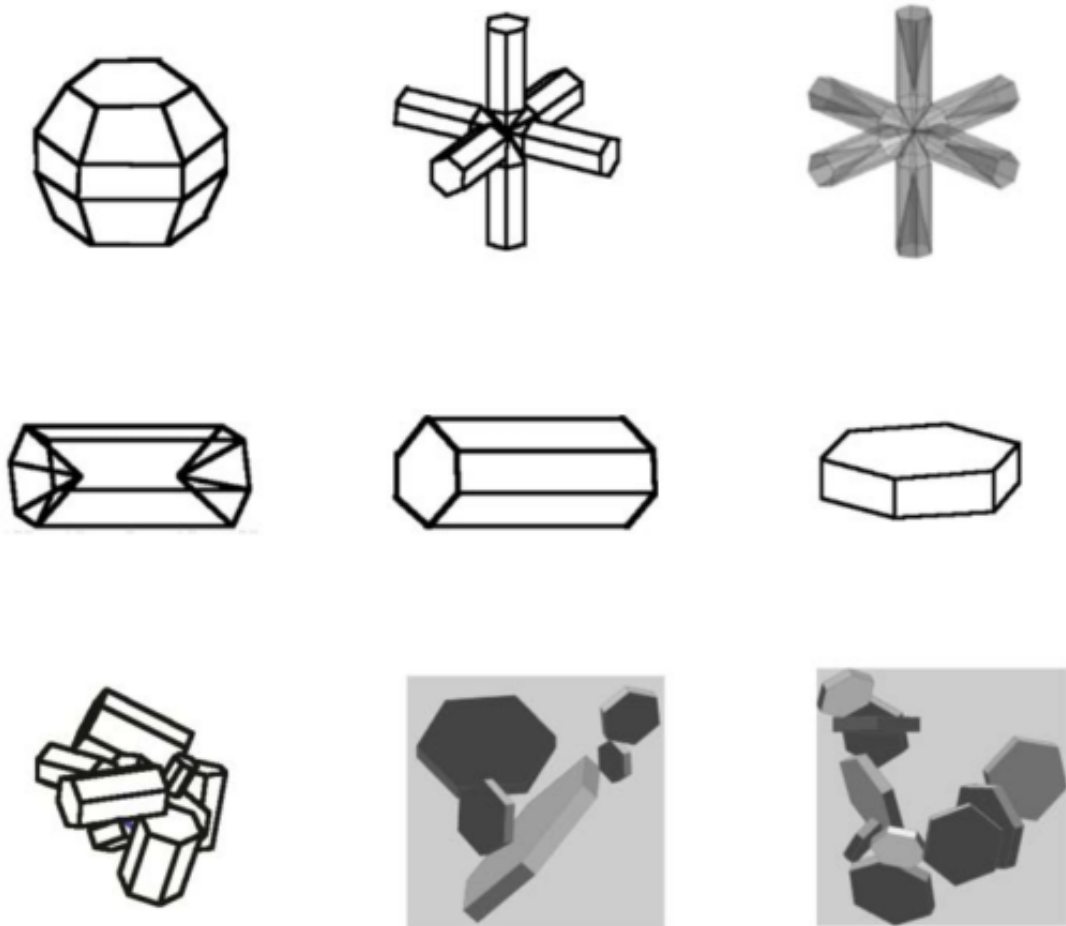


Figure 3.19: Current particle models used for MODIS satellite retrievals from Baum et al. 2005 [79].

The Baum model comprises (left to right, top to bottom): the droxtal, the bullet rosette, the hollow bullet rosette, the hollow column, the solid column, the plate, the compact column aggregate, the compact plate aggregate and the spatial plate aggregate. This is a size dependent model, with habit weightings determined by in-situ measured PSDs.

An alternative to the Baum model is the ensemble model [130]. The ensemble model takes into account the sedimentation process as discussed in Section 3.1.2, whereby crystal size and complexity increases with cloud depth. The ensemble model consists of six elements, illustrated in figure 3.20.

The ensemble model uses six particle geometries as shown in figure 3.20. The ensemble model becomes increasingly complex with cloud depth. Simple hexagonal columns

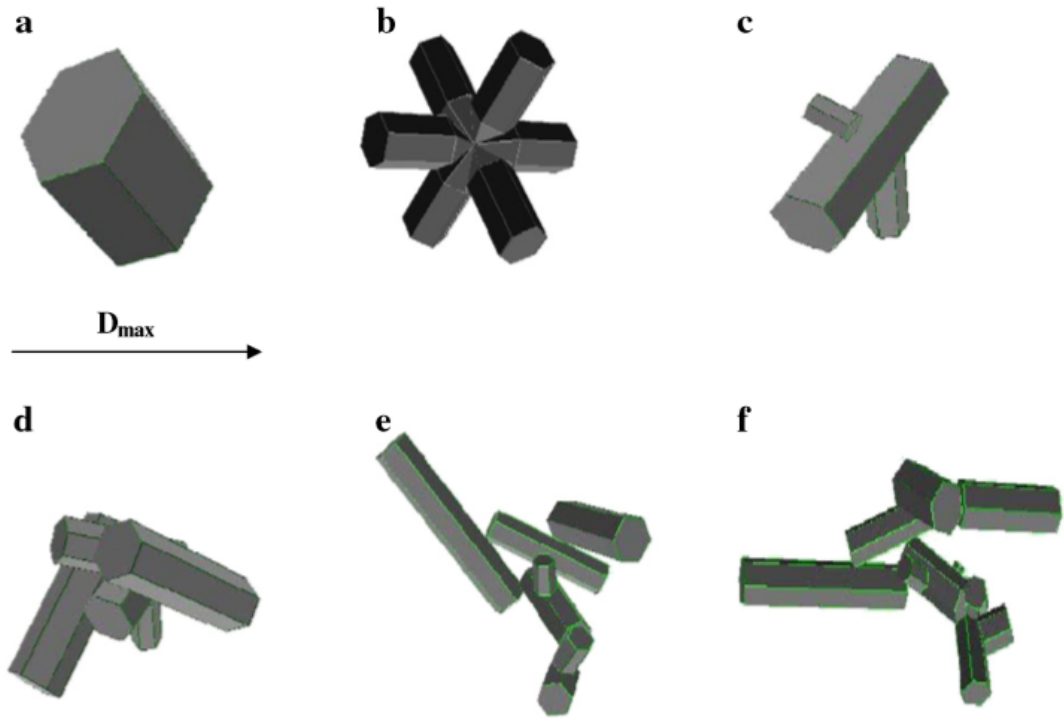


Figure 3.20: Elements of the ensemble model. a) the hexagonal column, b) the bullet rosette, c) the three branched hexagonal aggregate, d) the compact five branched hexagonal aggregate, e) the eight element chain like hexagonal aggregate and f) the ten element chain like hexagonal aggregate. Figure from [130].

occur at the cloud top, but as cloud depth increases, other columns are attached arbitrarily until the most complex shape, the ten element aggregate is created. This ensemble is weighted based on parameterized PSDs based on IWC measurements [131]. This model has shown to predict optical depth and IWC to within experimental uncertainties [39, 129]. As both the Baum and ensemble model obey mass dimensional relationships, they are suitably consistent across the electromagnetic spectrum and can therefore be used to predict both long-wave and short-wave fluxes and radiances [128, 129]. The ensemble model has also been shown to predict radar reflectivity and microwave brightness temperatures see for instance [132]. Radiative parametrizations are discussed further in section 6.

References

- [1] Bacon, N. J. and Swanson, B. D. “Laboratory measurements of light scattering by single levitated ice crystals”. In: *Journal of Atmospheric Science* 57 (2000), pp. 2094–2104.
- [2] Key, J. R., Yang, P., Baum, B. A., and Nasiri, S. “Parameterization of shortwave ice cloud optical properties for various particle habits”. In: *Journal of Geophysical Research* 107 (2002), p. D13.
- [3] Yang, H., Dobbie, S., Herbert, R., Connolly, P., Gallagher, M., Ghosh, S., Al-Jumur, S. M. R. K., and Clayton, J. “The effect of observed vertical structure, habits, and size distributions on the solar radiative properties and cloud evolution of cirrus clouds”. In: *Quarterly Journal of the Royal Meteorological Society* 0 (2011), pp. 1–14.
- [4] Macke, A., Francis, P. N., Mcfarquhar, G. M., and Kinne, S. “The Role of Ice Particle Shapes and Size Distributions in the Single Scattering Properties of Cirrus Clouds”. In: *Journal of the Atmospheric Sciences* 55 (1998), pp. 2874–2883.
- [5] Kepler, J. *On The Six-Cornered Snowflake*. Oxford University Press, 1611.
- [6] Dowell, L. G., Moline, S. W., and Rinfret, A. P. “A low-temperature X-ray diffraction study of ice structures formed in aqueous gelatin gels”. In: *Biochimica et Biophysica Acta* 59.1 (May 1962), pp. 158–167.
- [7] Frank, C. F. “Descartes’ Observations on the Amsterdam Snowfalls of 4,5,6 and 9 February 1634”. In: *Journal of Glaciology* 13 (1974), p. 535.
- [8] Hooke, R. *Micrographia: or, Some physiological descriptions of minute bodies made by magnifying glasses*. London: J. Martyn and J. Allestry, 1665.
- [9] Bentley, W. A. “Photographing Snowflakes”. In: *Popular Mechanics Magazine* 37 (1922), pp. 309–312.
- [10] Walden, V. P., Warren, S. G., and Tuttle, E. “Atmospheric ice crystals over the Antarctic Plateau in winter”. In: *Journal of Applied Meteorology* 42 (2003), pp. 1391–1405.
- [11] Magono, C. and Lee, C. W. “Meteorological Classification of Snow Crystals”. In: *Journal of the Japanese Society of Snow and Ice* 24 (1962), pp. 33–37. DOI: 10.5331/seppyo.24.33.
- [12] Weickmann, H. *Die Eisphase in der Atmosphäre*. Berichte des Deutschen Wetterdienstes in der US-Zone. Dt. Wetterdienst in der US-Zone, 1949.
- [13] Griggs, J. D. and Jayaratne, E. R. “The Replication of Ice Crystals Using Formvar: Techniques and Precautions”. In: *Journal of Atmospheric and Oceanic Technology* 3.3 (Sept. 1986), pp. 547–551.

- [14] Ono, A. “The shape and riming properties of ice crystals in natural clouds”. In: *Journal of Atmospheric Science* 26 (1969), pp. 138–147.
- [15] Heymsfield, A. J. “ice particles in a cirriform cloud at -83 and implications for polar stratospheric clouds”. In: *Journal of the Atmospheric Sciences* 43.8 (1986), pp. 851–855.
- [16] Mossop, S. C. and Heffernan K. J. “Studies of ice crystals in natural clouds”. In: *J. Rech. Atmos.* 3 (1967), pp. 45–64.
- [17] Miloshevich, L. M. and Heymsfield, A. J. “A balloon-borne continuous cloud particle replicator for measuring vertical profiles of cloud microphysical properties: instrument design, performance, and collection efficiency analysis”. In: *Journal of Atmospheric and Oceanic Technology* 14 (1997), 753–768.
- [18] Fugal, J. P. and Shaw, R. A. “Cloud particle size distributions measured with an airborne digital in-line holographic instrument”. In: *Atmospheric Measurement Techniques Discussions* 2 (2009), pp. 659–688. DOI: 10 . 5194 / amt d - 2 - 659-2009.
- [19] Abdelmonem, A., Schnaiter, M., Amsler, P., Hesse, E., Meyer, J., and Leisner, T. “First correlated measurements of the shape and light scattering properties of cloud particles using the new Particle Habit Imaging and Polar Scattering (PHIPS) probe”. In: *Atmospheric Measurement Techniques* 4.10 (Oct. 2011), pp. 2125–2142. DOI: 10 . 5194 / amt - 4 - 2125-2011.
- [20] Connolly, P. J., Flynn, M. J., Ulanowski, Z., Choulaton, T. W., Gallagher, M. W., and Bower, K. N. “Calibration of the cloud particle imager probes using calibration beads and ice crystal analogs: The depth of field”. In: *Journal of Atmospheric and Oceanic Technology* 24 (2007), pp. 1860–1879. DOI: 10 . 1175 / JTECH2096 . 1.
- [21] Schnaiter, M., Schon, R., Mohler, O., Saathoff, H., and Wagner, R. “Backscattering linear depolarization ratio of laboratory generated ice clouds composed of pristine and complex-shaped ice crystals.” In: *10th International Conference on Light Scattering by Non-spherical Particles*. 2007, pp. 193–196.
- [22] Stratton Park Engineering Company. *CPI theory of operation*. 2012. URL: <http://www.specinc.com/cpi-operation>.
- [23] Korolev, A. V., Emery, E. F., Strapp, J. W., Cober, S. G., Isaac, G. A., Wasey, M., and Marcotte, D. “Small Ice Particles in Tropospheric Clouds: Fact or Artifact? Airborne Icing Instrumentation Evaluation Experiment”. In: *Bulletin of the American Meteorological Society* 92.8 (Aug. 2011), pp. 967–973. DOI: 10 . 1175 / 2010BAMS3141 . 1.

- [24] Field, P. R., Heymsfield, A. J., and Bansemer, A. “Shattering and particle interarrival times measured by optical array probes in ice clouds.” In: *Journal of Atmospheric and Oceanic Technology* 23 (2006), pp. 1357–1371.
- [25] Droplet Measurement Technologies. *Anti-Shatter Tips for Cloud Imaging Probe (CIP), Cloud Combination Probe (CCP) or Cloud, Aerosol, and Precipitation Probe (CAPS)*. 2015. URL: www.dropletmeasurement.com/korolev-tips.
- [26] J. Schaefer. *MatScat*. 2012. URL: www.scattport.org/index.php/programs-menu/mie-type-codes-menu/517-matscat.
- [27] Hirst, E., Greenaway, R. S., Field, P. R., and Johnson, D. W. “Discrimination of micrometre-sized ice and supercooled droplets in mixed phase clouds”. In: *Atmos. Environ.* 35 (2001), pp. 33–47.
- [28] Cotton, R., Osborne, S., Ulanowski, Z., Hirst, E., Kaye, P. H., and Greenaway, R. S. “The Ability of the Small Ice Detector (SID-2) to Characterize Cloud Particle and Aerosol Morphologies Obtained during Flights of the FAAM BAe-146 Research Aircraft”. In: *Journal of Atmospheric and Oceanic Technology* 27.2 (Feb. 2010), pp. 290–303. DOI: 10.1175/2009JTECHA1282.1.
- [29] Ulanowski, Z., Hirst, E., Kaye, P. H., and Greenaway, R. “Retrieving the size of particles with rough and complex surfaces from two-dimensional scattering patterns”. In: *Journal of Quantitative Spectroscopy and Radiative Transfer* (2012), pp. 2457–2464. DOI: 10.1016/j.jqsrt.2012.06.019.
- [30] Ulanowski, Z., Kaye, P. H., Hirst, E., Greenaway, R. S., Cotton, R. J., Hesse, E., and Collier, C. T. “Incidence of rough and irregular atmospheric ice particles from Small Ice Detector 3 measurements”. In: *Atmospheric Chemistry and Physics* 14 (2014), pp. 1649–1662. DOI: 10.5194/acp-14-1649-2014.
- [31] Gallagher, M. W., Connolly, P. J., Whiteway, J., Figueras-Nieto, D., Flynn, M., Choullarton, T. W., Bower, K. N., Cook, C., Busen, R., and Hacker, J. “An overview of the microphysical structure of cirrus clouds observed during EMERALD-1”. In: *Quarterly Journal of the Royal Meteorological Society* 131 (2005), pp. 1143–1169.
- [32] Vaughan, G., Bower, K., Schiller, C., MacKenzie, A. R., Peter, T., Schlager, H., Harris, N. R. P., and May, P. T. “SCOUT-O3/ACTIVE: High-altitude Aircraft Measurements around Deep Tropical Convection”. In: *Bulletin of the American Meteorological Society* 89.5 (May 2008), pp. 647–662. DOI: 10.1175/BAMS-89-5-647.

- [33] Protat, A., McFarquhar, G. M., Um, J., and Delanoe, J. “Obtaining Best Estimates for the Microphysical and Radiative Properties of Tropical Ice Clouds from TWP-ICE In Situ Microphysical Observations”. In: *Journal of Applied Meteorology and Climatology* 50.4 (Apr. 2011), pp. 895–915. DOI: 10.1175/2010JAMC2401.1.
- [34] Vogelmann, A. M. and Ackerman, T. P. “Relating Cirrus Cloud Properties to Observed fluxes: a Critical Assessment”. In: *Journal of the Atmospheric Sciences* 52 (1995), pp. 4285–4301.
- [35] Heymsfield, A. J. and Miloshevich, L. M. “Parameterizations for the Cross-Sectional Area and Extinction of Cirrus and Stratiform Ice Cloud Particles”. In: *Journal of Atmospheric Science* 60 (2003), pp. 936–956.
- [36] Lawson, R. P., Baker, B. A., Zmarzly, P., O’Connor, D., Mo, Q., Gayet, J.-F., and Shcherbakov, V. “Microphysical and Optical Properties of Atmospheric Ice Crystals at South Pole Station”. In: *Journal of Applied Meteorology and Climatology* 45 (2006), pp. 1505–1524.
- [37] Um, J. and Mcfarquhar, G. M. “Single-scattering properties of aggregates of plates”. In: *Quarterly Journal of the Royal Meteorological Society* 304. February (2009), pp. 291–304. DOI: 10.1002/qj.
- [38] Gayet, J.-F., Mioche, G., Bugliaro, L., Protat, A., Minikin, A., Wirth, M., Dornbrack, A., Shcherbakov, V., Mayer, B., Garnier, A., and Gourbeyre, C. “On the observation of unusual high concentration of small chain-like aggregate ice crystals and large ice water contents near the top of a deep convective cloud during the CIRCLE-2 experiment”. In: *Atmospheric Chemistry and Physics* 12 (2012), pp. 727–744.
- [39] A. J. Baran. “A review of the light scattering properties of cirrus”. In: *Journal of Quantitative Spectroscopy and Radiative Transfer* 110.14-16 (Sept. 2009), pp. 1239–1260. DOI: 10.1016/j.jqsrt.2009.02.026.
- [40] U. Nakaya. *Snow Crystals: Natural and Artificial*. Harvard University Press, 1954.
- [41] B. J. Mason. “Snow crystals, natural and man made”. In: *Contemporary Physics* 33 (1992), pp. 227–43.
- [42] Bailey, M. and Hallet, J. “Growth rates and habits of ice crystals between -20°C and -70°C”. In: *Journal of the Atmospheric Sciences* 61 (2004), pp. 514–544.
- [43] V. J. Schaefer. “Silver and Lead Iodides as Ice-Crystal Nuclei”. In: *Journal of Meteorology* 11 (1954), pp. 417–419.
- [44] Bailey, M. P. and Hallett, J. “A Comprehensive Habit Diagram for Atmospheric Ice Crystals: Confirmation from the Laboratory, AIRS II, and Other Field Studies”. In: *Journal of Atmospheric Science* 66.9 (2009), pp. 2888–2899.

- [45] Westbrook, C. D., Hogan, R. J., and Illingworth, A. J. “The capacitance of pristine ice crystals and aggregate snowflakes”. In: *Journal of the Atmospheric Sciences* 65 (2008). DOI: 10.1175/2007JAS2315.1.
- [46] Pan, D., Liu, L-M., Tribello, G. A., Slater, B., Michaelides, A., and Wang, E. “Surface energy and surface proton order of the ice Ih basal and prism surfaces”. In: *Journal of Physics: Condensed Matter* 22.7 (2010), p. 074209.
- [47] Vali, G. “Ice nucleation - Theory”. In: *NCAR/ASP 1999 Summer Colloquium*. 1999.
- [48] Bacon, N. J., Baker, M. B., and Swanson, B. D. “Initial stages in the morphological evolution of vapour-grown ice crystals: A laboratory investigation”. In: *Quarterly Journal of the Royal Meteorological Society* 129 (Apr. 2003), pp. 1903–1927. DOI: 10.1256/qj.02.04.
- [49] Bartlett, J. T., Anthony, P., and Mason, B. J. “The Growth of Ice Crystals in an Electric Field”. In: *Zeitschrift fur Angewandte Mathematik und Physik* 14.5 (1963), pp. 599–610.
- [50] Libbrecht, K. and Tanusheva, V. “Electrically Induced Morphological Instabilities in Free Dendrite Growth”. In: *Physical Review Letters* 81.1 (July 1998), pp. 176–179. DOI: 10.1103/PhysRevLett.81.176.
- [51] Pfalzgraff, W. C., Hulscher, R. M., and Neshyba, S. P. “Scanning electron microscopy and molecular dynamics of surfaces of growing and ablating hexagonal ice crystals”. In: *Atmospheric Chemistry and Physics* 10.6 (Mar. 2010), pp. 2927–2935. DOI: 10.5194/acp-10-2927-2010.
- [52] Rukuta, N. and Takahashi, T. “The growth of atmospheric ice crystals: a summary of findings in vertical supercooled cloud tunnel studies”. In: *Journal of the Atmospheric Sciences* 56 (1999), pp. 1963–1979.
- [53] A. Pluchino. “Observations of halo scattering from single ice crystals”. In: *Optics Letters* 11.5 (1986), pp. 276–278. DOI: 10.1364/OL.11.000276.
- [54] A. Pluchino. “Scattering photometer for measuring single ice crystals and evaporation and condensation rates of liquid droplets”. In: *Journal of the Optical Society of America A* 4.3 (1987), pp. 614–620. DOI: 10.1364/JOSAA.4.000614.
- [55] Connolly, P. J., Emersic, C., and Field, P. R. “A laboratory investigation into the aggregation efficiency of small ice crystals”. In: *Atmospheric Chemistry and Physics* 12.4 (Feb. 2012), pp. 2055–2076. DOI: 10.5194/acp-12-2055-2012.
- [56] Saunders, C., Rimmer, J., Jonas, P., Arathoon, J., and Liu, C. “Preliminary laboratory studies of the optical scattering properties of the crystal clouds”. In: *Annales Geophysicae* 16 (1998), pp. 618–627.

- [57] Barkey, B., Bailey, M., Liou, K.-N., and Hallett, J. “Light-scattering properties of plate and column ice crystals generated in a laboratory cold chamber”. In: *Applied Optics* 41.27 (Sept. 2002), pp. 5792–5796.
- [58] Schaefer, V. J. “The Production of Ice Crystals in a Cloud of Supercooled Water Droplets”. In: *Science* 104 (Nov. 1946), pp. 457–459. DOI: 10.1126/science.104.2707.457. URL: <http://www.ncbi.nlm.nih.gov/pubmed/17787489>.
- [59] Schnaiter, M., Kaye, P. H., Hirst, E., Ulanowski, Z., and Wagner, R. “Exploring the surface roughness of small ice crystals by measuring high resolution angular scattering patterns.” In: *AAPP* 89.1 (2011), pp. 5–8. DOI: 10.1478/C1V89S1P084.
- [60] Holser, C. L., Jensen, D. C., and Goldshlak, L. “On the Aggregation of Ice Crystals to form Snow”. In: *Journal of Meteorology* 14 (1957), pp. 415–420.
- [61] Nakaya, U. and Matsumoto, A. “Evidence of the existence of a liquid-like film on ice surfaces”. In: *Snow, Ice and Permafrost Establishment. Res. Paper* 4 (1953), pp. 1–6.
- [62] Rogers, D. C. *The aggregation of natural ice crystals*. Laramie, Wyo. Dept. of Atmospheric Resources, University of Wyoming, 1974.
- [63] Connolly, P. J., Saunders, C. P. R., Gallagher, M. W., Bower, K. N., Flynn, M. J., Choulaton, T. W., Whiteway, J., and Lawson, R. P. “Aircraft observations of the influence of electric fields on the aggregation of ice crystals”. In: *Quarterly Journal of the Royal Meteorological Society* 131.608 (Apr. 2005), pp. 1695–1712. DOI: 10.1256/qj.03.217.
- [64] Field, P. R. and Heymsfield, A. J. “Aggregation and scaling of ice crystal size distributions”. In: *Journal of the Atmospheric Sciences* 60 (2003), pp. 544–560.
- [65] Kajikawa, M. and Heymsfield, A. J. “Aggregation of ice crystals in cirrus”. In: *Journal of the Atmospheric Sciences* 46 (1989), pp. 3108–3121.
- [66] May, P. T., Mather, J. H., Vaughan, G., Bower, K. N., Jakob, C., McFarquhar, G. M., and Mace, G. G. “The tropical warm pool international cloud experiment”. In: *Bulletin of the American Meteorological Society* 89.5 (May 2008), ES21–ES23. DOI: 10.1175/BAMS-89-5-May.
- [67] Westbrook, C. D., Ball, R. C., Field, P. R., and Heymsfield, A. J. “Theory of growth by differential sedimentation, with application to snowflake formation”. In: *Physical review. E, Statistical, nonlinear, and soft matter physics* 70 (Aug. 2004), p. 021403.
- [68] Um, J. and McFarquhar, G. M. “Single-Scattering Properties of Aggregates of Bullet Rosettes in Cirrus”. In: *Journal of Applied Meteorology and Climatology* 46 (2007), pp. 757–775. DOI: 10.1175/JAM2501.1.

- [69] Gerber, H., Takano, Y., Garrett, T. J., and Hobbs, P. V. “Nephelometer measurements of the asymmetry parameter, volume extinction coefficient, and backscatter ratio in Arctic clouds”. In: *Journal of Atmospheric Science* 1999 (2000), pp. 3021–3034.
- [70] Lampert, A., Ehrlich, A., Dornbrack, A., Jourdan, O., Gayet, J.-F., Mioche, G., Shcherbakov, V., Ritter, C., and Wendisch, M. “Microphysical and radiative characterization of a subvisible midlevel Arctic ice cloud by airborne observations – a case study”. In: *Atmospheric Chemistry and Physics* 9.8 (Apr. 2009), pp. 2647–2661. DOI: 10.5194/acp-9-2647-2009.
- [71] Ulanowski, Z., Hesse, E., Kaye, P. H., and Baran, A. J. “Light scattering by complex ice-analogue crystals”. In: *Journal of Quantitative Spectroscopy and Radiative Transfer* 100.1–3 (2006), pp. 382–392. DOI: 10.1016/j.jqsrt.2005.11.052.
- [72] Baum, B. A., Yang, P., Hu, Y.-X., and Feng, Q. “The impact of ice particle roughness on the scattering phase matrix”. In: *Journal of Quantitative Spectroscopy and Radiative Transfer* 111.17-18 (Nov. 2010), pp. 2534–2549. DOI: 10.1016/j.jqsrt.2010.07.008.
- [73] Libbrecht, K. G. “The physics of snow crystals”. In: *Reports on Progress in Physics* 68.4 (Apr. 2005), pp. 855–895. DOI: 10.1088/0034-4885/68/4/R03.
- [74] Murray, B. J., Salzmann, C. G., Heymsfield, A. J., Dobbie, S., Neely, R. R., and Cox, C. J. “Trigonal ice crystals in Earth’s atmosphere”. In: *Bulletin of the American Meteorological Society* (2014). DOI: 10.1175/BAMS-D-14-00017.1.
- [75] Macke, A. and Mishchenko, M. I. “Applicability of regular particle shapes in light scattering calculations for atmospheric ice particles”. In: *Applied Optics* 35 (1996), pp. 4291–4296.
- [76] Xie, Y., Yang, P., Kattawar, G. W., Baum, B. A., and Hu, Y. “Simulation of the optical properties of plate aggregates for application to the remote sensing of cirrus clouds.” In: *Applied Optics* 50.8 (2011), pp. 1065–81.
- [77] Yang, P. and Liou, K. N. “Single-scattering properties of complex ice crystals in terrestrial atmosphere”. In: *Contr. Atmos. Phys.* 71 (1998), pp. 223–248.
- [78] Baran, A. J., Hill, P., Furtado, K., Field, P., and Manners, J. “A Coupled Cloud Physics-Radiation Parameterization of the Bulk Optical Properties of Cirrus and its Impact on the Met Office Unified Model Global Atmosphere 5.0 Configuration”. In: *Journal of Climate* November (June 2014), p. 140625124737000. DOI: 10.1175/JCLI-D-13-00700.1.

- [79] Baum, B. A., Heymsfield, A. J., Yang, P., and Bedka, S. T. “Bulk scattering properties for the remote sensing of ice clouds. Part I: Microphysical data and models”. In: *Journal of Applied Meteorology* 44 (2005), pp. 1885–1895.
- [80] Cotton, R. J., Field, P. R., Ulanowski, Z., Kaye, P. H., Hirst, E., Greenaway, R. S., Crawford, I., Crosier, J., and Dorsey, J. “The effective density of small ice particles obtained from in situ aircraft observations of mid-latitude cirrus”. In: *Quarterly Journal of the Royal Meteorological Society* 139.676 (2013), pp. 1923–1934.
- [81] Macke, A., Mueller, J., and Raschke, E. “Single scattering properties of atmospheric ice crystals”. In: *Journal of Atmospheric Science* 53 (1996), pp. 2813–2825.
- [82] Mishchenko, M. I., Travis, L. D., and Mackowski, D. W. “T-matrix computations of light scattering by nonspherical particles: A review”. In: *Journal of Quantitative Spectroscopy and Radiative Transfer* 55 (May 1996), pp. 535–575. DOI: 10.1016/0022-4073(96)00002-7.
- [83] Yang, P. and Liou, K. -N. “Light Scattering and Absorption by Nonspherical Ice Crystals”. In: *Light Scattering Reviews*. Ed. by A. A. Kokhanovsky. Springer-Praxis, 2006. Chap. 2, pp. 31–71.
- [84] Kinne, S. and Liou, K. -N. “The effects of the nonsphericity and size distribution of ice crystals on the radiative properties of cirrus clouds”. In: *Atmospheric Research* 24 (1989), pp. 273–284.
- [85] Mugnai, A. and Wiscombe, W. J. “Scattering from nonspherical Chebyshev particles. I: cross sections, single-scattering albedo, asymmetry factor, and backscattered fraction”. In: *Applied optics* 25 (1986), pp. 1235–1244.
- [86] Muinonen, K. and Erkkila, H. “Scattering of light by concave-hull-transformed Gaussian particles”. In: *10th International Conference on Light Scattering by Non-spherical Particles*. 2007, pp. 125–128.
- [87] Veihelmann, B., Nousiainen, T., Kahnert, M., and Zande, W.J. “Light scattering by small feldspar particles simulated using the Gaussian random sphere geometry”. In: *Journal of Quantitative Spectroscopy and Radiative Transfer* 100.1-3 (2006), pp. 393–405. DOI: 10.1016/j.jqsrt.2005.11.053.
- [88] Yang, P., Baum, B. A., Heymsfield, A. J., Hu, Y. X., Huang, H. L., Tsay, S. C., and Ackerman, S. “Single-scattering properties of droxtals”. In: *Journal of Quantitative Spectroscopy and Radiative Transfer* 79–80 (2003), pp. 1159–1169. DOI: 10.1016/S0022-4073(02)00347-3.
- [89] Um, J. and McFarquhar, G. M. “Dependence of the single-scattering properties of small ice crystals on idealized shape models”. In: *Atmospheric Chemistry and Physics* 11 (2011), pp. 3159–3171. DOI: 10.5194/acp-11-3159-2011.

- [90] Cox, C. and Munk, W. “Measurement of the Roughness of the Sea Surface from Photographs of the Sun’s Glitter”. In: *Journal of the Optical Society of America* 44.11 (1954), pp. 838–850. DOI: 10.1364/JOSA.44.000838.
- [91] Cross, J. D. “Study of the surface of ice with a scanning electron microscope”. In: *Physics of ice. Proceedings of the International Symposium on Physics of Ice*. Plenum Press, 1968.
- [92] Liu, C., Panetta, R. L., and Yang, P. “The effects of surface roughness on the scattering properties of hexagonal columns with sizes from the Rayleigh to the geometric optics regimes”. In: *Journal of Quantitative Spectroscopy and Radiative Transfer* 129 (2013), pp. 169–185. DOI: 10.1016/j.jqsrt.2013.06.011.
- [93] Schmitt, C. G., Iaquinta, J., Heymsfield, A. J., and Iaquinta, J. “The Asymmetry Parameter of Cirrus Clouds Composed of Hollow Bullet Rosette - Shaped Ice Crystals from Ray-Tracing Calculations”. In: *Journal of Applied Meteorology and Climatology* 45.July (2006), pp. 973–981.
- [94] Yang, P., Zhang, Z., Kattawar, G. W., Warren, S. G., Baum, B., Huang, H-L., Hu, Y. X., Winker, D., and Iaquinta, J. “Effect of Cavities on the Optical Properties of Bullet Rosettes: Implications for Active and Passive Remote Sensing of Ice Cloud Properties”. In: *Journal of Applied Meteorology and Climatology* 47.9 (2008), pp. 2311–2330.
- [95] Macke, A., Mishchenko, M. I., and Cairns, B. “The influence of inclusions on light scattering by large ice particles”. In: *Journal of Geophysical Research* 101 (1996), pp. 23311–23316.
- [96] Baran, A. J. and Labonnote, L. C. “On the reflection and polarization properties of ice cloud”. In: *Journal of Quantitative Spectroscopy and Radiative Transfer* 100 (2006), pp. 41–54.
- [97] Gayet, J. F., Crepel, O., Fournol, J. F., and Oshchepkov, S. “A new airborne polar Nephelometer for the measurements of optical and microphysical cloud properties. Part I: Theoretical design”. In: *Annales Geophysicae* 15.4 (1997), pp. 451–459. DOI: 10.1007/s00585-997-0451-1.
- [98] Auriol, F., Gayet, J. F., and Febvre, G. “In situ observation of cirrus scattering phase functions with 22 and 46 halos: Cloud field study on 19 February 1998”. In: *Journal of the Atmospheric Sciences* (Feb. 2001), pp. 3376–3390.
- [99] Gayet, J. F., Auriol, F., Oshchepkov, S., Schroder, F., Duroure, C., Febvre, G., Fournol, J. F., Crepel, O., Personne, P., and Daugereon, D. “In situ measurements of the scattering phase function of stratocumulus, contrails and cirrus”. In: *Geophysical Research Letters* 25.7 (1998), pp. 971–974.

- [100] McFarquhar, G. M., Um, J., and Jackson, R. “Small Cloud Particle Shapes in Mixed-Phase Clouds”. In: *Journal of Applied Meteorology and Climatology* 52.5 (May 2013), pp. 1277–1293. DOI: 10.1175/JAMC-D-12-0114.1.
- [101] Gayet, J.-F., Mioche, G., Shcherbakov, V., Gourbeyre, C., Busen, R., and Minikin, A. “Optical properties of pristine ice crystals in mid-latitude cirrus clouds: a case study during CIRCLE-2 experiment”. In: *Atmospheric Chemistry and Physics* 11.6 (2011), pp. 2537–2544.
- [102] Mcfarquhar, G. M., Freer, M., Um, J., McCoy, R., and Bolton, W. “Remote Sensing and In-Situ Observations of Arctic Mixed-Phase and Cirrus Clouds Acquired During Mixed-Phase Arctic Cloud Experiment : Atmospheric Radiation Measurement Uninhabited Aerospace Vehicle Participation Cirrus Observations - Remote Sensing”. In: *Fifteenth ARM Science Team Meeting*. 2005.
- [103] Schotland, R. M., Sassen, K., and Stone, R. “Observations by lidar of linear depolarization ratios for hydrometeors”. In: *Journal of Applied Meteorology* 10 (1971), pp. 1011–1017.
- [104] Noel, V., Chepfer, H., Ledanois, G., Delaval, A., and Flamant, P. H. “Classification of particle effective shape ratios in cirrus clouds based on the lidar depolarization ratio”. In: *Applied optics* 41.21 (2002), pp. 4245–4257. DOI: 10.1364/AO.41.004245.
- [105] V. Noel. “Classification of particle shapes from lidar depolarization ratio in convective ice clouds compared to in situ observations during CRYSTAL-FACE”. In: *Journal of Geophysical Research* 109.D24 (2004), p. D24213. DOI: 10.1029/2004JD004883.
- [106] Chen, W. -N., Chiang, C. -W., and Nee, J. -B. “Lidar ratio and depolarization ratio for cirrus clouds”. In: *Applied optics* 41.30 (2002), pp. 6470–6476. DOI: 10.1364/AO.41.006470.
- [107] Stephens, G. L., Vane, D. G., Boain, R. J., Mace, G. G., Sassen, K., Wang, Z., Illingworth, A. J., O’Connor, E. J., Rossow, W. B., Durden, S. L., Miller, S. D., Austin, R. T., Benedetti, A., and Mitrescu, C. “the Cloudsat Mission and the A-Train”. In: *Bulletin of the American Meteorological Society* 83.12 (Dec. 2002), pp. 1771–1790. DOI: 10.1175/BAMS-83-12-1771.
- [108] Baumgardner, D. “The cloud, aerosol and precipitation spectrometer (CAPS): a new instrument for cloud investigations”. In: *Atmos. Res.* 59-60 (2001), pp. 251–264.
- [109] Greenberg, J. M., Pedersen, N. E., and Pedersen, J. C. “Microwave Analog to the Scattering of Light by Nonspherical Particles”. In: *Journal of Applied Physics* 32.2 (1961), pp. 233–242.

- [110] Zerull, R. and Giese, R. H. *Microwave analog studies*. Ed. by T. Gehrels. University of Arizona Press, 1974, pp. 901–915.
- [111] B. A. S. Gustafson. “Microwave analog to light scattering measurements: A modern implementation of a proven method to achieve precise control”. In: *Journal of Quantitative Spectroscopy and Radiative Transfer* 55.5 (1996). Light Scattering by Non-Spherical Particles, pp. 663–672. DOI: 10.1016/0022-4073.
- [112] Ulanowski, Z., Hesse, E., Kaye, P. H., Baran, A. J., and Chandrasekhar, R. “Scattering of light from atmospheric ice analogues”. In: *Journal of Quantitative Spectroscopy and Radiative Transfer* 79-80 (2003), pp. 1091–1102. DOI: 10.1016/S0022-4073(02)00342-4.
- [113] Amsler, P., Stetzer, O., Schnaiter, M., Hesse, E., Benz, S., Moehler, O., and Lohmann, U. “Ice crystal habits from cloud chamber studies obtained by in-line holographic microscopy related to depolarization measurements”. In: *Applied Optics* 48.30 (Oct. 2009), pp. 5811–22.
- [114] Vidauure, G. and Hallet, J. “Particle Impact and Breakup in Aircraft Measurement”. In: *Journal of Atmospheric and Oceanic Technology* 26 (2008), pp. 972–983. DOI: 10.1175/2008JTECHA1147.1.
- [115] Smedley, A. R. D., Webb, A. R., and Saunders, C. P. R. “Application of a diode array spectroradiometer to measuring the spectral scattering properties of cloud types in a laboratory”. In: *Atmospheric Chemistry and Physics* 7 (2007), pp. 5803–5813.
- [116] N. A. Phillips. “The general circulation of the atmosphere: A numerical experiment”. In: *Quarterly Journal of the Royal Meteorological Society* 82.352 (1956), pp. 123–164. DOI: 10.1002/qj.49708235202.
- [117] Collins, W. D., Rasch, P. J., Boville, B. A., Hack, J. J., Williamson, D. L., Kiehl, J. T., Briegleb, B., Bitz, C., Lin, S. -J., Zhang, M., and Dai, Y. “Description of the NCAR Community Atmosphere Model (CAM 3.0)”. In: *Ncar/Technical Note* June (2004), p. 214.
- [118] P. Lynch. “The origins of computer weather prediction and climate modeling”. In: *Journal of Computational Physics* 227.7 (2008), pp. 3431–3444. DOI: 10.1016/j.jcp.2007.02.034.
- [119] *Met Office Seasonal and Climate Models*. 2014. URL: <http://www.metoffice.gov.uk/research/modelling-systems/unified-model/climate-models>.

- [120] Walters, D. N., Brooks, M. E., Boutle, I. A., Melvin, T. R. O., Stratton, R. A., Wells, H., Williams, K. D., Bushell, A. C., Copsey, D., Earnshaw, P. E., Gross, M. S., Hardiman, S. C., Harris, C. M., Heming, J. T., Klingaman, N. P., Levine, R. C., Manners, J., Martin, G. M., Milton, S. F., Mittermaier, M. P., Morcrette, C. J., Riddick, T. C., Roberts, M. J., Sanchez, C., Selwood, P. M., Smith, C., Tennant, W. J., Vosper, S. B., Vidale, P. L., Wilkinson, J. M., Wood, N., Woolnough, S. J., and Xavier, P. K. “The Met Office Unified Model Global Atmosphere 6.0/6.1 and JULES Global Land 6.0/6.1 configurations, in preparation”. In: ().
- [121] Intergovernmental Panel on Climate Change. *What is a GCM?* 2013. URL: www.ipcc-data.org/guidelines/pages/gcm_guide.html.
- [122] Bozzo, A., Maestri, T., Rizzi, R., and Tosi, E. “Parameterization of single scattering properties of mid-latitude cirrus clouds for fast radiative transfer models using particle mixtures.” In: *Geophysical Research Letters* 35 (2008), p. L16809.
- [123] Fu, Q., Sun, W. B., and Yang, P. “Modeling of scattering and absorption by non-spherical cirrus ice particles at thermal infrared wavelengths.” In: *Journal of Atmospheric Science* 56 (1999), pp. 2937–2947.
- [124] “The definition and significance of an effective radius for ice clouds”. In: *Journal of the Atmospheric Sciences* 55 (1998), 2039–2052.
- [125] D. L. Mitchell. “Effective diameter in radiative transfer: General definition, applications and limitations”. In: *Journal of the Atmospheric Sciences* 59 (2002), pp. 2330–2346.
- [126] A. J. Baran. “The dependence of cirrus infrared radiative properties on ice crystal geometry and shape of the size distribution function”. In: *Quarterly Journal of the Royal Meteorological Society* 131 (2005), pp. 1129–1142. DOI: 10.1256/qj.04.91.
- [127] Mitchell, D. L., Lawson, R. P., and Baker, B. “Understanding effective diameter and its application to terrestrial radiation in ice clouds”. In: *Atmospheric Chemistry and Physics* 11 (2011), pp. 3417–3429.
- [128] A. J. Baran. “From the single-scattering properties of ice crystals to climate prediction: A way forward”. In: *Atmospheric Research* 112 (2012), pp. 45–69.
- [129] Baran, A. J., Bodas-Salcedo, A., Cotton, R., and Lee, C. “Simulating the equivalent radar reflectivity of cirrus at 94 GHz using an ensemble model of cirrus ice crystals: a test of the Met Office global numerical weather prediction model”. In: *Quarterly Journal of the Royal Meteorological Society* 137.659 (2011), pp. 1547–1560. DOI: 10.1002/qj.870.
- [130] Baran, A. and Labonnote, L. C. “A self-consistent scattering model for cirrus. I: The solar region”. In: *Quarterly Journal of the Royal Meteorological Society* 1912 (2007), pp. 1899–1912. DOI: 10.1002/qj.

- [131] Field, P. R., Heymsfield, A. J., and Bansemer, A. “Snow size distribution parameterization for midlatitude and tropical ice cloud.” In: *Journal of Atmospheric Science* 64 (2007), pp. 4346–4365.
- [132] Baran, A. J., Cotton, R., Furtado, K., Havemann, S., Labonnote L.-c., Marengo, F., Smith, A. J., and Thelen J.-C. “A self-consistent scattering model for cirrus II: The high and low frequencies”. In: *Quarterly Journal of the Royal Meteorological Society* 140 (2014), pp. 1039–1057. DOI: 10.1002/qj.2193.

Paper 1: ‘Laboratory Investigations into scattering properties of hollow ice particles’

This manuscript was published in the Journal of Quantitative Spectroscopy and Radiative Transfer, volume 157 (2015) pages 106–118.

4.1 Summary

As described in section 1.1, cirrus clouds are a large source of uncertainty in climate modelling. In a radiative parametrization, the bulk optical properties of clouds are typically described using the asymmetry parameter, g , among other variables. The asymmetry parameter is derived from the phase function, P_{11} (described in section 2.3.2). This paper measures the phase function, and consequently asymmetry parameter, of five ice clouds generated in a laboratory cloud chamber. Each of the five clouds were found to contain a predominant crystal habit (solid columns, hollow columns, solid plates or complex plates), with a narrow distribution of size. One of the main findings of the paper is the difference in internal structure between hollow columns grown at -7° and those grown at -30° . Microscope measurements were used to create new particle geometries for use in scattering models. Experimental measurements are then compared to predictions from ray tracing and Ray Tracing with Diffraction on Facets.

4.2 Author contributions

The initial set up of the equipment was conducted by Helen Smith, with help and guidance from Andrew Smedley. This included the alteration of previous equipment, the building of new equipment, and the set up of measurement instrumentation and software. The experiments and data analysis were then conducted by Helen Smith.

Using observations from the experiments, particle geometries were constructed by Helen Smith with the help of Paul Connolly. Ray Tracing simulations from these models were found by Helen Smith, and RTDF simulations were found by Evelyn Hesse.

The manuscript was prepared by Helen Smith, but all coauthors have contributed to the drafting process. The entire investigation was conducted under the general guidance of Ann Webb, Paul Connolly and Anthony Baran who have offered help and advice throughout.

The paper is published in the Journal of Quantitative Spectroscopy and radiative Transfer, and copyright remains with the journal.

Cloud chamber laboratory investigations into scattering properties of hollow ice particles

Helen R. Smith^{a,1}, Paul J. Connolly^a, Anthony J. Baran^b, Evelyn Hesse^c,
Andrew R. D. Smedley^a, Ann R. Webb^a

^a*The University of Manchester, Oxford Road, Manchester, M13 9PL*

^b*Met Office, Exeter, UK*

^c*University of Hertfordshire, Hatfield, Hertfordshire, AL10 9AB*

Abstract

Measurements are presented of the phase function, P_{11} , and asymmetry parameter, g , of five ice clouds created in a laboratory cloud chamber. At -7°C , two clouds were created: one comprised entirely of solid columns, and one comprised entirely of hollow columns. Similarly at -15°C , two clouds were created: one consisting of solid plates and one consisting of hollow plates. At -30°C , only hollow particles could be created within the constraints of the experiment. The resulting cloud at -30°C contained short hollow columns and thick hollow plates. During the course of each experiment, the cloud properties were monitored using a Cloud Particle Imager (CPI). In addition to this, ice crystal replicas were created using formvar resin. By examining the replicas under an optical microscope, two different internal structures were identified. The internal and external facets were measured and used to create geometric particle models with realistic internal structures. Theoretical results were calculated using both Ray Tracing (RT) and Ray Tracing with Diffraction on Facets (RTDF). Experimental and theoretical results are compared to assess the impact of internal structure on P_{11} and g and the applicability of RT and RTDF for hollow columns.

Keywords: asymmetry parameter, hollowness, ice crystal, ray tracing, RTDF, phase function

Email address: `helen.smith-8@postgrad.manchester.ac.uk` (Helen R. Smith)

1. Introduction

The role of clouds in the Earth’s radiation budget is still considered one of the biggest uncertainties in predicting climate change today [1]. Ice clouds are of particular interest as the large range of ice crystal size, shape and complexity gives rise to considerable variabilities in their net radiative effect [2, 3, 4]. In addition to this, cirrus has an extensive global coverage of 30%, with coverage in the tropics reaching 60–70% [5].

Ice crystal habit has been an area of scientific curiosity for centuries [6, 7, 8], with many studies of natural snow crystals noting the wide variety of crystal morphologies. In the 1930s, the first controlled laboratory investigations into crystal habit were conducted, where crystal growth was observed over a variety of conditions [9]. These findings were presented in the form of a morphology diagram, describing ice crystal habit as a function of temperature and supersaturation. Since then, observations from numerous laboratory and field studies have built on the original morphology diagram, with several other particle habits discovered over a larger range of temperatures and supersaturations [10, 11]. In order to identify ice crystal habit, laboratory based experiments have used a variety of techniques including photography, formvar replicas, and cloud probes [12, 13, 14, 15, 16]. Although some in-situ studies have used replication techniques [17, 18], in-situ habit information is mostly gathered with the use of 2D imaging probes such as the Stratton Park Engineering Company (SPEC) Cloud Particle Imager (CPI) (see section 2.2.1) [19]. The CPI is capable of determining the habits and sizes of particles in the size range 10–2000 μm and as such it has been used in determining the habit and size distributions of various cloud types in several field experiments [20, 21, 22, 23, 18, 19, 24, 25, 26]. However, the ability to accurately determine habit from CPI images is hampered by particle orientation and the limited resolving power of the probe.

The variety in particle size and shape poses many challenges in the modelling of scattering by ice crystals. Multiple studies have highlighted the importance of crystal habit upon the scattering properties [27, 28, 29, 30, 31, 32, 33, 34]. Simplified shapes such as cylinders and spheroids were found to be inadequate approximations [35], and the more accurate simple hexagonal column still predicts higher asymmetry parameters and more prominent halo features than those observed from satellite and aircraft data [36, 37, 38, 39, 40, 41]. The featureless phase functions are known to be related to crystals with mesoscopic surface roughness, aggregates and parti-

cles with inclusions. Consequently, surface roughness and internal structure have gained recognition as important factors in the scattering properties of ice crystals [42, 43, 44, 45, 46, 47]. These small scale features cannot be accurately determined from cloud probe images and consequently may be overlooked in particle models. Although approximations to observed surface roughness are often used, details of the inclusions have yet to be accounted for in particle models since suitable measurements have not previously been available.

There have been a number of theoretical studies of idealized surface roughness. By creating rough surfaces in the particle model by tilting facet mantles, or by distorting the outgoing ray paths, results from these studies agree that ice particle roughness leads to a general decrease in asymmetry parameter in addition to a more featureless phase function [31, 48]. However, a recent paper showed that the mantle tilting method does not replicate idealized surface roughness for high values of roughness [49]. Experimental difficulties mean that direct measurements of ice surface roughness are scarce. In general, the surface roughness of ice crystals is beyond the capabilities of optical microscopy, and the coating techniques required for electron microscopy mean that the ice surface cannot be directly imaged. Recently, however, the Variable Pressure Scanning Electron Microscope (VP-SEM) has proved successful in measuring ice surface roughness [50]. One study used the Small Ice Detector version 3 (SID-3) to obtain two dimensional scattering patterns from ice crystals [51]. By making use of the relationship between surface energy and roughness, these scattering patterns may be used to estimate ice crystal roughness. This technique has the ability to distinguish between particles of varying degrees of roughness and has been used in-situ for the classification of naturally occurring ice crystals [45].

Similar to surface roughness, internal structure is also known to influence the scattering properties of ice crystals. One theoretical study modelled cavities using hexagonal based pyramids which were identified by CPI particle images [52]. Ray Tracing results from these models showed a reduction in asymmetry parameter for hollow particles at certain aspect ratios. Another study used a similar particle model based on photomicrograph images of hollow rosettes at the South Pole [53]. In their study, a more rigorous physical optics approach was used which showed a general increasing trend in the asymmetry parameter for hollow particles [53]. Both of these studies used comparable internal structures based on different particle images. Similar indentations can be seen from a number of experiments [10, 54]. Other sources

show varied and complex cavities [17, 55], the structure of which are difficult to determine using two dimensional images and may be missed entirely with instruments of limited resolution. This results in over-idealized geometries being used for hollow ice crystals in particle models. As the single scattering properties are known to be sensitive to particle habit, it is probable that the faithful representation of internal geometry is also necessary. Further laboratory investigations are therefore pivotal in determining internal structure and its impact upon the single scattering properties, and to test light scattering models.

2. Experimental set-up

2.1. Cloud Chamber

The experiments presented in this paper were conducted in the Manchester Ice Cloud Chamber (MICC), as previously described [56]. The cloud chamber consists of a 10m tall fall tube of 1m diameter. The chamber is housed in three stacked cold rooms capable of reaching temperatures down to -55°C . The set-up used in this experiment is shown in figure 2.1.

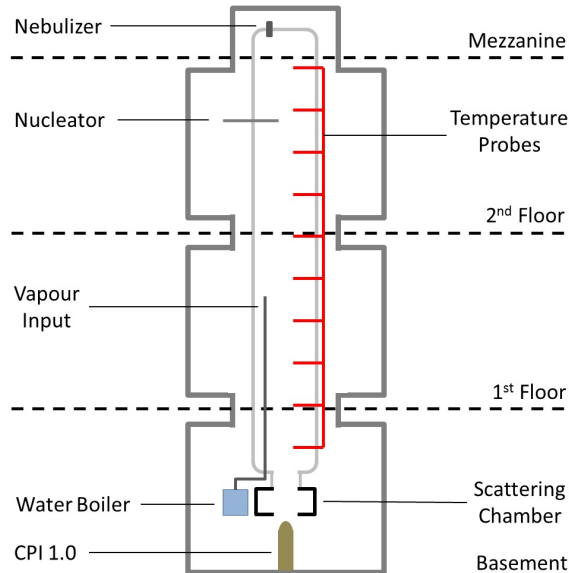


Figure 1: Schematic of the Manchester Ice Cloud Chamber. A 10m tall fall tube is housed in three cold rooms over three stories. Various access points allow the addition of liquid water and vapour, and a compressed air line is used to nucleate ice in the cloud.

At the top of the chamber, a Schlick Form 5 two-substance nebulizer was used to create a cloud of supercooled liquid water droplets. The micrometer scale on the nebulizer allowed the size and concentration of water droplets to be controlled. Approximately 1m below the nebulizer, ice was nucleated in the cloud using a compressor expansion technique [16, 57, 56]. To employ this technique, a solenoid valve was used to open and close a compressed air line. When the valve was opened, the compressed air expanded adiabatically, thus cooling the local environment to below the homogeneous nucleation temperature and forcing the formation of ice. In these experiments, the solenoid valve was opened and closed periodically in order to provide a steady flux of ice nuclei. Water vapour was input at the midpoint of the chamber via a water boiler, therefore the ice crystals continued to grow as they fell through the chamber. All experiments were conducted at ambient atmospheric pressure (1010mbar).

It is known from previous studies that the ice crystal habit is dependent on temperature and supersaturation [9, 10]. From certain habit diagrams, it is clear that certain temperature ranges produce particular habits [58]. It is also evident that the ice crystal structure becomes more complex with increasing supersaturation, allowing for the formation of hollow columns and sector plates above water saturation. Therefore, in order to create a variety of solid and hollow habits in the ice cloud chamber, the temperature and humidity had to be altered. The temperature of the chamber was set and maintained by selecting the cold room temperatures. The temperature inside the chamber was found to be stable within $\pm 1.5^\circ$. However, the supersaturation is dependent upon a number of factors and could not be as easily constrained. Two methods were used to vary the supersaturation: changing the ice crystal concentration, and altering the vapour input. By decreasing the ice crystal concentration, or by increasing the amount of water vapour, the supersaturation was increased. The ice crystal concentration was controlled by the droplet input and the nucleator frequency, whereas the vapour input was controlled by a variable power supply. By altering these inputs, clouds of predominantly hollow or particles were achieved. Using this experimental set-up, the profile of the cloud was vertically inhomogeneous inside the chamber and therefore representative measurements of relative humidity could not be taken.

2.2. Cloud Measurement

2.2.1. CPI

Inside the scattering section (described in section 2.3), a Cloud Particle Imager (CPI) samples the cloud as it falls out of the chamber [59]. The CPI has been used in numerous laboratory and field studies [22, 60, 61]. The probe takes 2D images of the ice crystals which are then processed using CPIview. CPIview gives information on particle size, habit and concentration. In these experiments, the CPI was used to monitor ice crystal concentration.

2.2.2. Ice Crystal Replicas

In addition to the CPI, the cloud was monitored using ice crystal replicas. These are made using a 0.6% solution of polyvinyl formal (C_3H_7), commonly known as formvar, in chloroform. This solution was chilled in the cold room prior to collecting samples. The solution was applied to microscope slides which were placed in the cloud chamber to collect falling ice crystals. The slides were left to dry in a sealed bell jar filled with desiccant in order to minimise the production of artefacts. The ice crystals which fall on the microscope slide are encompassed by the formvar solution, as the chloroform evaporates, the ice crystal is preserved in a formvar shell [62]. Once dry, the ice crystal replicas were examined under an optical microscope. The dimensions of both internal and external facets were measured using a microscope graticule. These measurements were used to construct geometric particle models with realistic internal structures, discussed in section 3.

2.3. Scattering Chamber

The scattering experiments were conducted in a separate scattering chamber, which was attached to a sampling port at the bottom of the cloud chamber. Figure 2.3 shows a cross-sectional view of the scattering chamber.

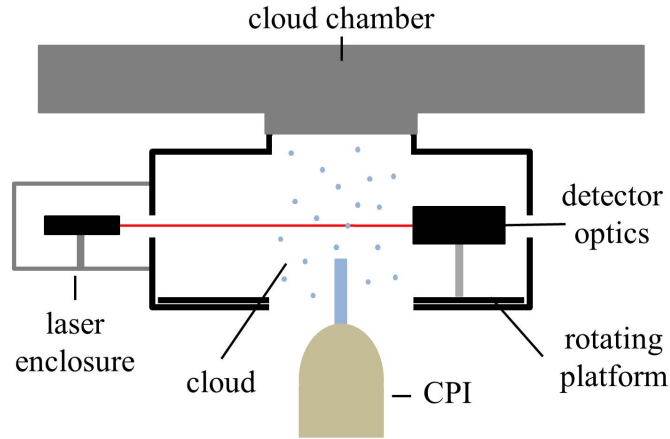


Figure 2: Vertical cross-sectional schematic of the scattering chamber. The laser is directed through the cylindrical cloud of diameter 0.3m. The detector optics rotate around the central axis of the cloud, collecting scattered light

The scattering chamber has been previously described in several papers [57, 16, 15]. However, a brief description is given here. The chamber is a cylindrical enclosure of diameter 0.45m and height 0.3m. A 0.3m opening at the top of the scattering chamber attaches to the bottom of the cloud chamber, and an opening at the bottom allows the cloud to fall through freely. The lasers are mounted outside the chamber in a temperature controlled box, and the beams are directed through the centre of the chamber. The base of the scattering chamber contains a motor controlled rotating platform with an angular resolution of 0.19° per step. The detector optics were mounted on the rotating platform in the same plane as the lasers, at a distance of 0.06m from the centre of the scattering section. Consequently, the measured intensities are considered to be in the far-field.

2.4. Optical Set up

The optical set-up is shown via a plan view of the scattering chamber in figure 3.

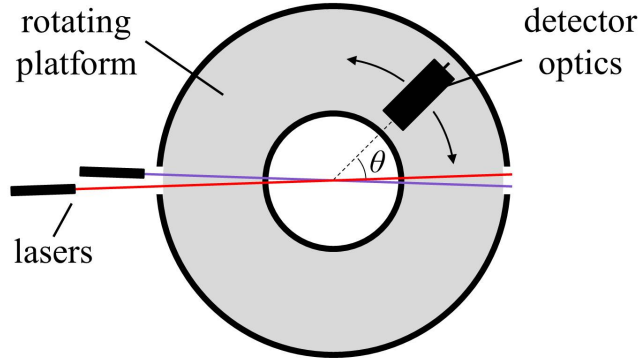


Figure 3: Plan view of the optical set-up. The grey disc represents the rotating platform at the bottom of the scattering chamber, the detector optics were fixed onto this. The detector rotated around a vertical axis at the centre of the chamber, and hence the centre of the cloud. (Not to scale)

The experiment used two 5mW diode lasers: a Taurus 635 nm red laser, and an Electra portable 405 nm violet laser, both manufactured by laserglow technologies. The degree of polarization of the red and violet lasers were measured to be 0.91 and 0.87 respectively. The lasers were oriented so they were linearly polarized at 45° to the scattering plane.

The intensities of the red and violet lasers were monitored over experimental temperatures for several hours in order to determine the stability of the power of the input beam. The intensities were measured to be stable to within 3.1% and 2.8%, respectively. The divergence of the red and violet beams were measured to be $< 1.2\text{mrad}$ and $< 0.5\text{mrad}$, respectively. As the maximum path length of each laser was $< 0.3\text{m}$, the divergence of the lasers was not further considered. The detector optics had a field of view of 1.0° , as the distance from the detector optics to the centre of the scattering volume was $< 0.06\text{m}$, this divergence was also considered negligible and was not further considered.

In order to utilize both wavelengths in each experiment, the lasers were directed through the centre of the scattering section, separated by an angle of 0.94° (5 steps) as shown in figure 3. By offsetting them in this way, the scattered intensity could then be measured for each laser simultaneously, although the red and violet signals corresponded to different scattering angles. The detector optics consisted of a planoconvex lens with a focal length of

0.10m. A fibre optic was placed at the focal length, and a collar was placed before the lens, restricting the field of view to 1.0° . The detector optics fed into an Ocean Optics S2000 CCD array spectrometer which measured the intensity of the scattered light. The spectrometer has a wavelength range of 200–850nm over 2048 pixels. The low dynamic range of the instrument required the additional use of neutral density filters to record high intensities in the $0\text{--}10^\circ$ range. Beyond this, the integration time of the instrument was altered in order to measure varying intensities of scattered light. Corrections for filters, integration time and dark current are applied in post processing.

2.4.1. Measurements

Each measurement was taken over the course of a minute and therefore corresponds to an ensemble of particles passing through the scattering volume. During each measurement, the detector was stationary. It was then moved 5 steps and the next measurement was taken. This process was repeated every 0.95° between angles 0.38° to 150.4° ; beyond this, the detector optics intersected the laser beam and thus no useful data could be collected for $\theta > 150^\circ$. The measured intensity corresponds to a scattering volume, V , defined in this paper as the volume of the laser which falls within the field of view of the detector optics (shown in figure 4).

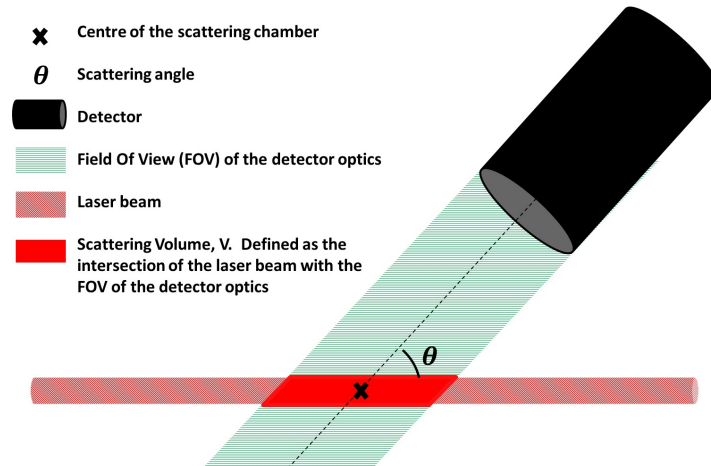


Figure 4: The scattering volume, V , is the volume in which the laser intersects the field of view of the detector optics. Only light scattered in the plane of the detector optics from within the scattering volume is observed. The measured signal is therefore proportional to V , which is a function of scattering angle, θ .

The scattering volume changes depends upon the position of the detector, and is therefore a function of angle, θ , where θ is the angle subtended by the straight through beam and the detector optics. Only light scattered within this volume is seen by the detector optics and as such the measured intensity is proportional to V . In order to correct for this, the measured intensity is divided by the scattering volume in order to get the scattered intensity per unit volume.

2.5. Particle Orientation

Ice particles are observed to fall preferentially with their major axis perpendicular to direction of propagation [63, 64]. The amount by which they deviate from this orientation can be described by the tilt angle. As particles become larger and more elongated, the tilt angles decrease and the particles become more preferentially oriented.

The flow field inside the scattering volume was modelled using the Partial Differential Equation toolbox in Matlab 2014b. In order to do this, the cold room environment was modelled using Neumann boundary conditions for solid objects and Dirichlet conditions for the inlet tube to the CPI, which had a known flow speed. In these experiments, the inlet tube to the CPI lies $\sim 1\text{cm}$ below the scattering volume (figure 4). The resultant flow field is shown in figure 5a. The average ice crystal fall speeds were estimated to be $\sim 0.25\text{ms}^{-1}$ [65]). The net movement of the crystal is then approximated by adding the velocities of the flow field to the crystal fall speeds. Assuming that the major axis of the ice crystal is oriented orthogonal to the direction of propagation, the deviation of the axis or orientation from the horizontal is estimated. These angular deviations are estimated to be between -81° and 81° , the distribution of orientations is shown in figure 5b. It was also assumed that the ice crystals maintain a rotational degree of freedom about their minor axis. Other factors such as ambient shears are likely to cause may cause additional deviations from the estimated orientation. For the purposes of this experiment, orientation was treated as random.

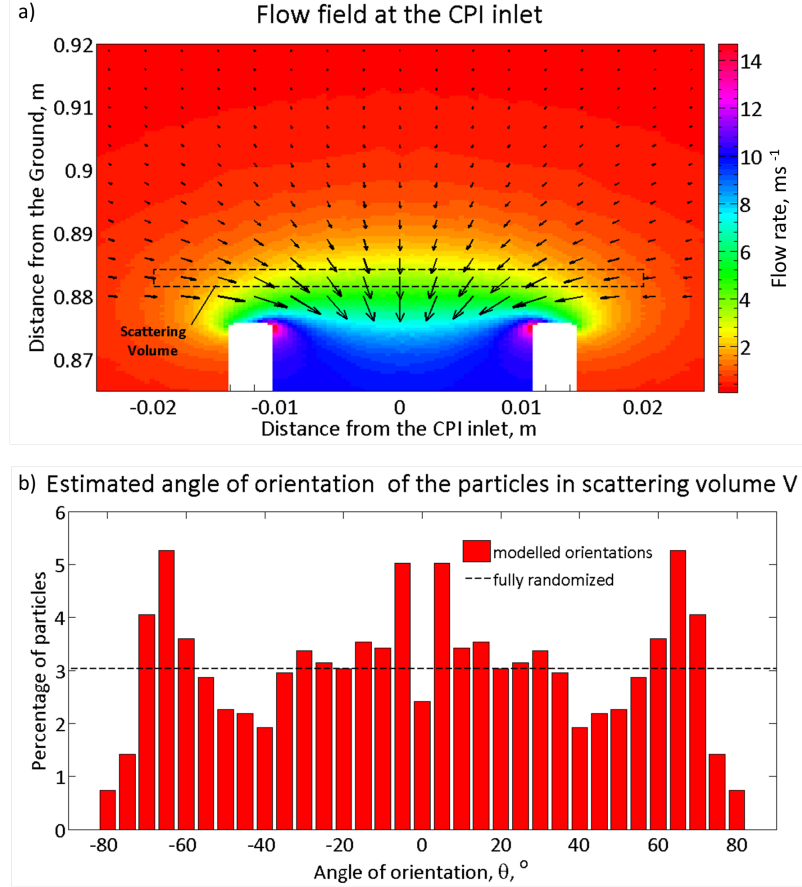


Figure 5: Modelled flow field at the CPI inlet and estimated ice crystal orientations, expressed as the angle the major axis of the ice crystal makes to the horizontal.

2.6. Obtaining the scattering phase function, P_{11}

The red and violet lasers are partially linearly polarized at an angle of 45° to the scattering plane. The degree of polarization of each laser was measured to be 0.91 and 0.87, respectively. Therefore the incident Stokes parameters are given by:

$$I_{0(v)} \cdot \begin{bmatrix} 1 \\ 0 \\ p_v \\ 0 \end{bmatrix}, \text{ and } I_{0(r)} \cdot \begin{bmatrix} 1 \\ 0 \\ p_r \\ 0 \end{bmatrix}$$

Where:

$I_{0(v)}$ = Intensity of the violet laser, Wm^{-2}

$I_{0(r)}$ = Intensity of the red laser, Wm^{-2}

p_v = degree of polarization of the violet laser

p_r = degree of polarization of the red laser

In order to calculate the Stokes parameter of the scattered wave, we assume that the particles in the scattering volume are randomly oriented, as discussed in section 2.5. By making this assumption, the Stokes parameter of the scattered wave can be given by [66]:

$$\begin{bmatrix} I \\ Q \\ U \\ V \end{bmatrix} = \frac{I_0}{k^2 r^2} \begin{bmatrix} P_{11} & P_{12} & 0 & 0 \\ P_{12} & P_{22} & 0 & 0 \\ 0 & 0 & P_{33} & P_{34} \\ 0 & 0 & -P_{34} & P_{44} \end{bmatrix} \cdot \begin{bmatrix} 1 \\ 0 \\ p \\ 0 \end{bmatrix} \quad (1)$$

Where:

I_0 = Intensity of the incident beam, Wm^{-2}

k = wavenumber

r = distance from the scattering particle to the detector, m

$$\begin{bmatrix} I \\ Q \\ U \\ V \end{bmatrix} = \frac{I_0}{k^2 r^2} \begin{bmatrix} P_{11} \\ P_{12} \\ p \times P_{33} \\ -p \times P_{34} \end{bmatrix} \quad (2)$$

and therefore:

$$I \propto P_{11} \quad (3)$$

Where I is the total scattered intensity as a function of angle θ . Therefore the measured intensities described in section 2.4 can be normalised to 4π in order to obtain the phase function P_{11} , according to:

$$\int_0^\pi P_{11}(\theta) \sin \theta d\theta = 2 \quad (4)$$

As we cannot measure beyond $\theta = 150.4^\circ$, modelled data were used to fill in the range 150.4° to 180° . Images of the formvar replicas were analysed in

order to create suitable particle models for each cloud. In all experiments, it was found that each cloud consisted of only one crystal habit, although the aspect ratio was found to change with particle size. Here, the aspect ratio is defined as the ratio of the length of the prism face to the length of the basal face. Particles with an aspect ratio > 1 are considered to be column-like, whereas particles with an aspect ratio < 1 are considered to be plate-like. A habit mixture model was created that was based on one habit but several sizes and aspect ratios. Details of the composition of each cloud can be found in section 3. Both Ray Tracing [31] and RTDF were tested (see section 3.1). RTDF differs from conventional geometric optics by considering diffraction at facets in addition to diffraction at the projected cross-section. Therefore, RTDF better describes the size dependence, especially for small and intermediate size parameters [67]. RTDF phase functions were used to normalise the measured results. The data were normalised as follows:

$$f \times \int_0^{150.4^\circ} I_{sca}(\theta) \sin \theta d\theta + \int_{150.4^\circ}^{180^\circ} m(\theta) \sin \theta d\theta = 2 \quad (5)$$

Where $m(\theta)$ is the modelled data and f is a scaling factor required to normalise the phase function. The normalised intensity, $I_{sca}(\theta) \times f$ is then plotted as a function of θ . The asymmetry parameter, g , is defined as:

$$g = \frac{1}{2} \int_0^{180^\circ} P_{11}(\theta) \sin \theta \cos \theta d\theta \quad (6)$$

For the measured phase functions, the asymmetry parameter was found by using $P_{11} = I_{sca}(\theta) \times f$ in the range $\theta = 0.38^\circ$ to 150.4° and using the modelled values of P_{11} in the range $\theta = 150.4^\circ$ to 180° .

3. Results

3.1. Theoretical Results

Measurements from the formvar replicas (figure 6) were used to create geometric models, which represented internal structure.

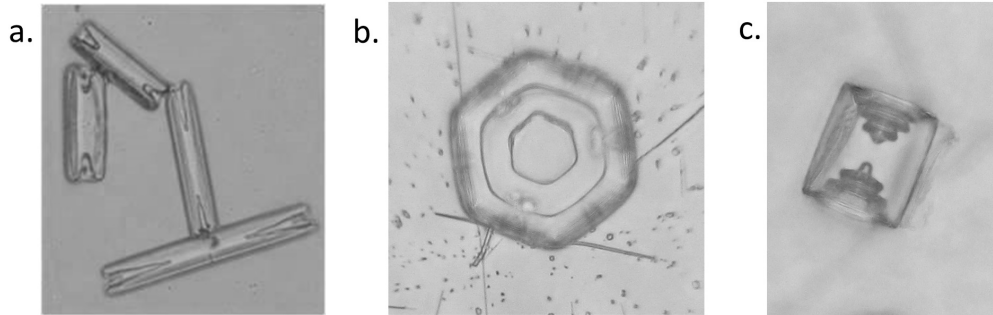


Figure 6: Formvar replicas showing typical structures of hollow particles at a. -7°C , b. -15°C and c. -30°C .

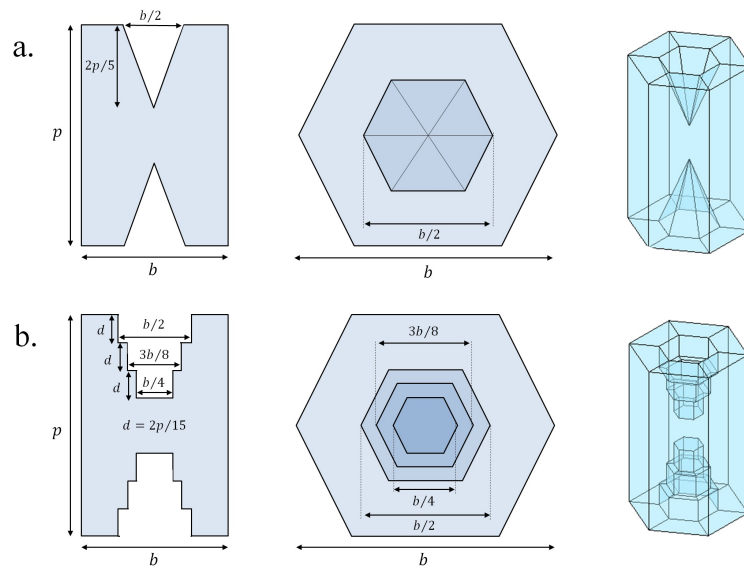


Figure 7: Construction of the particle models based on formvar replicas. a) shows the construction of a typical hollow column as observed at -7°C and b) shows the construction of a typical hollow column as observed at -30°C . From left to right: cross sectional view taken parallel to the prism face, plan view as seen from the basal face, and 3D model.

Experiments at $T = -7^{\circ}\text{C}$ and $T = -30^{\circ}\text{C}$ both produced columnar habits in agreement with established habit diagrams [10]; however, there were notable differences between the columns grown at -30°C and the columns grown

at -7°C . At -30°C (figure 6c) the columns showed a stepped internal structure. Whereas at -7°C (figure 6a) the columns showed a simpler internal structure.

When viewed from the basal face, each indentation of the stepped hollow column had hexagonal symmetry. Based on averaged measurements, each indentation was constructed by three hexagonal columns of descending size. The size of the basal faces measured $b/2$, $3b/8$ and $b/4$ respectively, where b is the length of the basal facet of the ice crystal. The depth of each indentation measured $2p/15$ where p is the length of the prism facet of the ice crystal. The columns created at -7°C could not be viewed from the basal face due to the tendency of the ice crystals to lie with their prism facets parallel to the microscope slide. It was assumed that these indentations also retained hexagonal symmetry and therefore they were modelled using hexagonal based pyramids. Each indentation had a base width of $b/2$ and a height of $2p/5$. At -15°C the plates (figure 6b) could not be viewed from their prism face due to their orientation. Although the thickness of the plates could be estimated using CPI images, the vertical profile of the internal structure could not be investigated in detail. From the formvar images, the internal structure of plates appeared similar to the structure of the stepped columns seen at -30°C , although the structure became increasingly complex as the plates increased in size. For this reason, plates were modelled using the same geometry as the stepped column with a thickness of $15\mu\text{m}$ based on observations from the CPI.

3.1.1. Results from Ray Tracing and Ray Tracing with Diffraction on Facets

Three example columns were constructed in order to directly compare the effects of each indentation: one solid column, one hollow column with a pyramidal cavity (as observed at -7°C), and one hollow column with stepped internal structure (as observed at -30°C). Each column measured $100\mu\text{m}$ (prism face) by $50\mu\text{m}$ (basal face), and each indentation measured $40\mu\text{m}$ in depth. The phase function and asymmetry parameter were found using both Ray Tracing and RTDF, for a wavelength of 635nm and a complex refractive index of $1.3085 + (1.04 \times 10^{-8})i$ [68]. All modelled results presented in this paper are based on random orientations. Results using the two methods are presented in figure 8 and table 1.

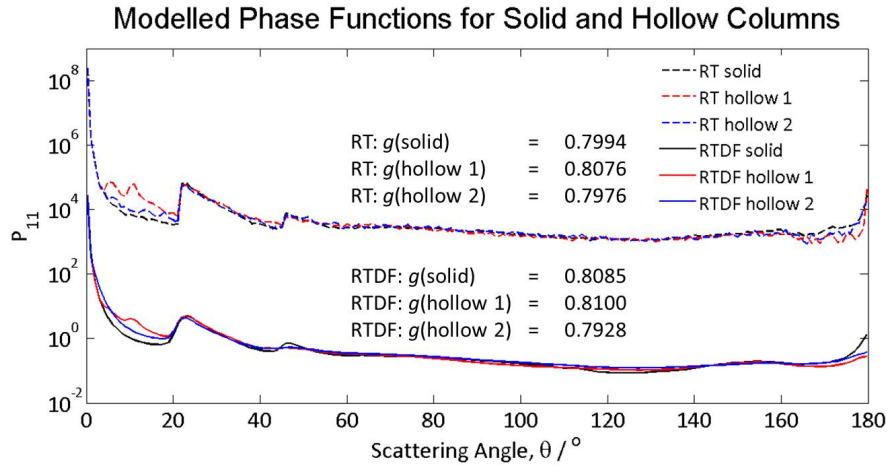


Figure 8: Ray Tracing and RTDF results for solid columns and both types of hollow columns. 'Hollow 1' denotes the typical hollow structure as seen at -7°C , as depicted in figure 7a. 'Hollow 2' denotes the typical hollow structure as seen at -30°C , as depicted in figure 7b. The results from Ray Tracing are offset by 10^4 in order to present both models on the same graph.

	Ray Tracing		RTDF	
	g	% dev.	g	% dev.
Solid	0.7994		0.8085	
Hollow 1	0.8076	1.03	0.8100	0.12
Hollow 2	0.7976	-0.23	0.7928	-1.94

Table 1: Modelled asymmetry parameters for solid columns and both types of hollow columns for a prism length of $100\mu\text{m}$ and a basal length of $50\mu\text{m}$. 'Hollow 1' corresponds to the typical internal structure seen at -7°C , and 'Hollow 2' corresponds to the typical internal structure seen at -30°C , '% dev.' gives the percentage deviation of the modelled asymmetry parameter of the hollow models from the modelled asymmetry parameter of the solid models.

Comparing the RT and RTDF results in figure 8, one notable difference is the increased scattering between about 3° and 20° observed for hollow column 1. The phase function of hollow column 1 has two additional peaks at $\sim 4.7^{\circ}$ and 9.5° , which are due to ray paths sketched in figure 9. Ray path A corresponds to the halo for the prism angle of 15.14° . Path B is similar, but the ray re-enters the crystal and goes through a second deflection. Therefore, the complete deflection angle is about twice the deflection angle

for ray path A. This increase in forward scattering leads to a noticeably higher asymmetry parameter for hollow column 1 when compared with the solid column. Due to the stepped indentation of hollow column 2, which only includes additional 90° prism angles, there is only a small increase in forward scattering compared to the solid column. In this case, the reduction in the 22° halo, in addition to the increase in scattering in the $120\text{--}140^\circ$ region leads to an overall decrease in asymmetry parameter. Therefore, the asymmetry parameter of hollow column 2 is rather similar to that of the solid column.

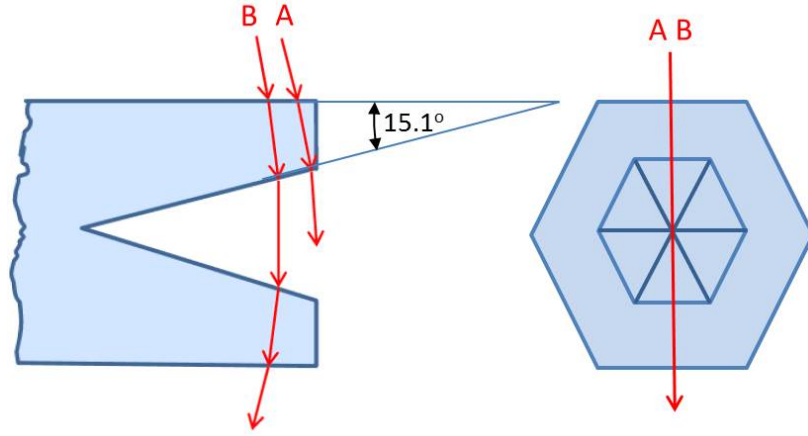


Figure 9: Schematic of ray paths causing additional halos in hollow column 1 compared to a solid column: $\sim 4.7^\circ$ (path A), $\sim 9.5^\circ$ (path B).

To compare the two scattering models, the ratios of the RT phase functions to the RTDF phase functions are plotted in figure 10. The RTDF phase functions are similar to RT; however, the peaks are broadened due to diffraction on facets. Due to this, some of the intensity of the 22° halo peak is moved towards smaller scattering angles. For all particles, scattering close to 180° is significantly smaller for RTDF when compared with RT, particularly in the case of the hollow columns. Overall, these deviations result in a 1.4% increase in the RTDF predicted asymmetry parameter for the solid column when compared to RT. For hollow column 1, RTDF predicts an asymmetry parameter 0.12% larger than RT. This increase is rather small, which is most likely due to a reduction of the RTDF forward scattering peak at $\theta = 0.25^\circ$ because of the smaller area of parallel basal facet components. The RTDF

forward scattering peak is slightly more reduced for hollow column 2 when compared with RT, presumably due to the segmentation of the basal facets into smaller components causing stronger diffraction as well as additional ray paths. This results in a 2% lower asymmetry parameter for hollow column 2 compared to the solid column when using RTDF.

Ratios of RT phase functions to RTDF phase functions for solid and hollow columns

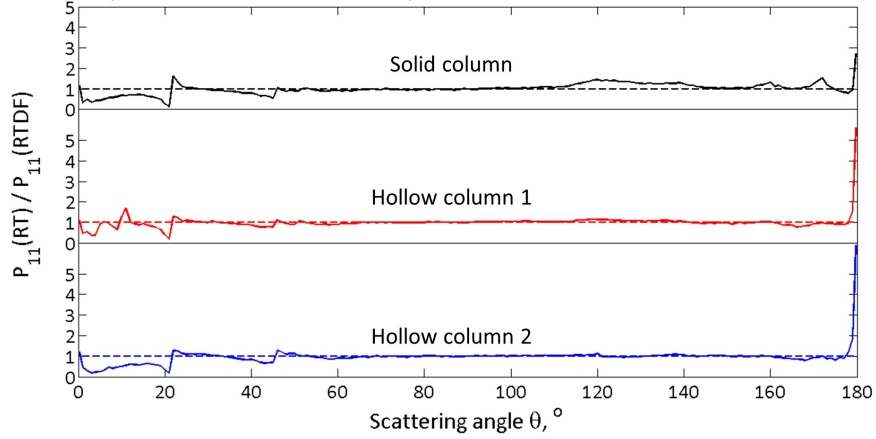


Figure 10: Ratios of the RT phase functions to RTDF phase functions for solid and hollow columns

3.2. Experimental Results

Five experiments were conducted. In order to produce different habits, several input variables were changed. Three temperatures were chosen in order to cover different habit regimes. Ice crystal concentration and vapour input were varied in order to alter the relative humidity in the chamber. The input parameters are summarised in table 2.

Experiment	Temperature °C	Ice Crystal Concentration, l^{-1}	Predominant Habit	Size Range μm
1	-7	10000	Solid Column	10–170
2	-7	2500	Hollow Column	20–280
3	-15	5000	Solid Plate	10–290
4	-15	1000	Hollow Plate	20–290
5	-30	1000	Hollow Plate/Columns	10–140

Table 2: Summary of input parameter and cloud properties for each experiment.

3.2.1. Particle Size Distributions

Particle size distributions were measured from the formvar replicas. These results are presented in figure 11.

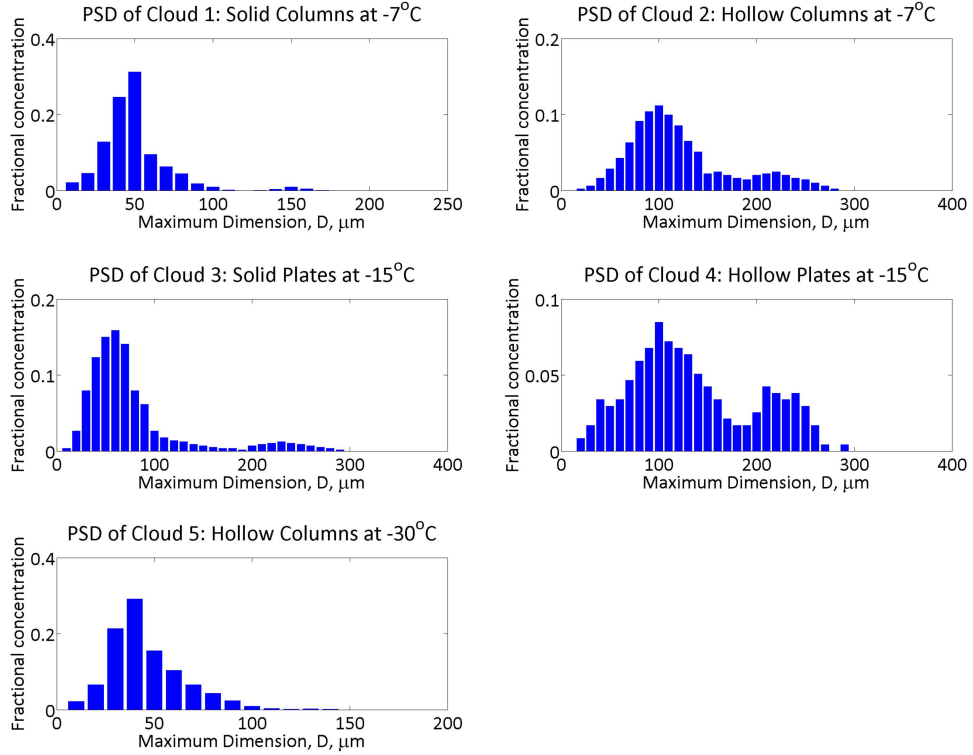
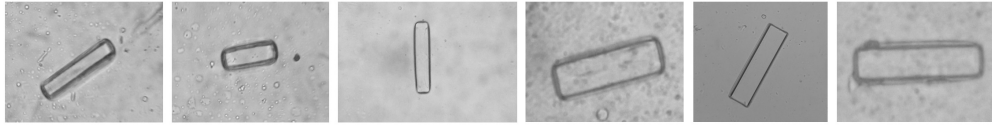


Figure 11: Particle size distributions for the five clouds created during these experiments. Approximately 1000 formvar images were analysed for each cloud.

3.2.2. Particle Habits

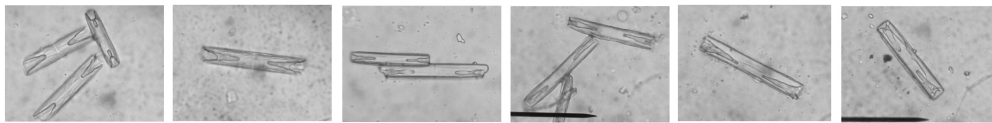
The formvar replicas were also used to determine the particle habits. It was found that each cloud consisted of one particle habit, with a range of sizes and aspect ratios. Typical particle habits are shown in figure 3.2.2.

Cloud 1: -7°C Solid Columns



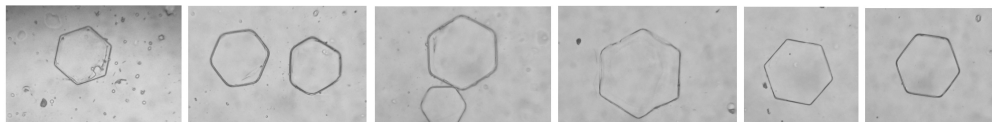
100µm

Cloud 2: -7°C Hollow Columns



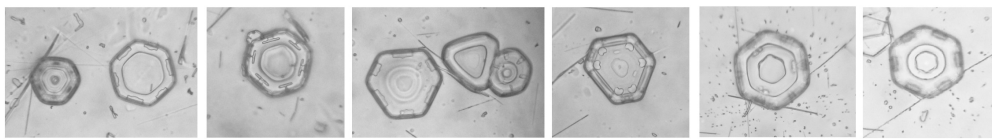
100µm

Cloud 3: -15°C Solid Plates



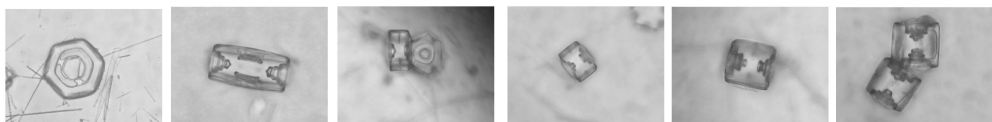
100µm

Cloud 4: -15°C Hollow Plates



100µm

Cloud 5: -30°C Hollow Columns and Plates



100µm

Figure 12: Formvar replicas showing typical habits observed during the five experiments.

The aspect ratios were measured from the ice crystal replicas. Due to the tendency for plates to land with their basal face parallel to the microscope slide, the aspect ratio of plates was not measured. The measured aspect ratios with respect to maximum particle dimension is given in figure 13. Maximum crystal dimension is defined as $\sqrt{p^2 + b^2}$, where p and b are the

dimensions of the prism and basal facets respectively.

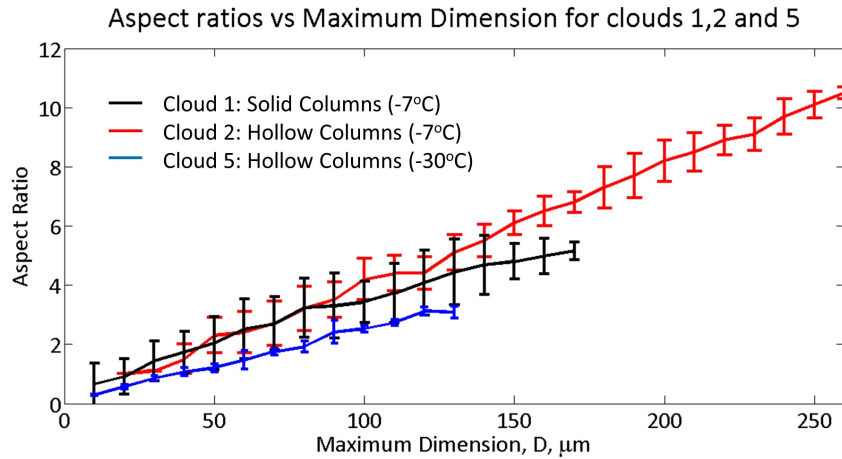


Figure 13: Aspect ratios of hollow and solid columns based on measurements from formvar replicas

These size distributions and aspect ratios were used to construct habit mixture models for each cloud. For clouds 3 and 4, the aspect ratios could not be measured due to the orientation of the crystals. From CPI images, the thickness of the plates was estimated to be $15\mu\text{m}$. This thickness was used for all plate sizes. The particle models were used in both RT and RTDF.

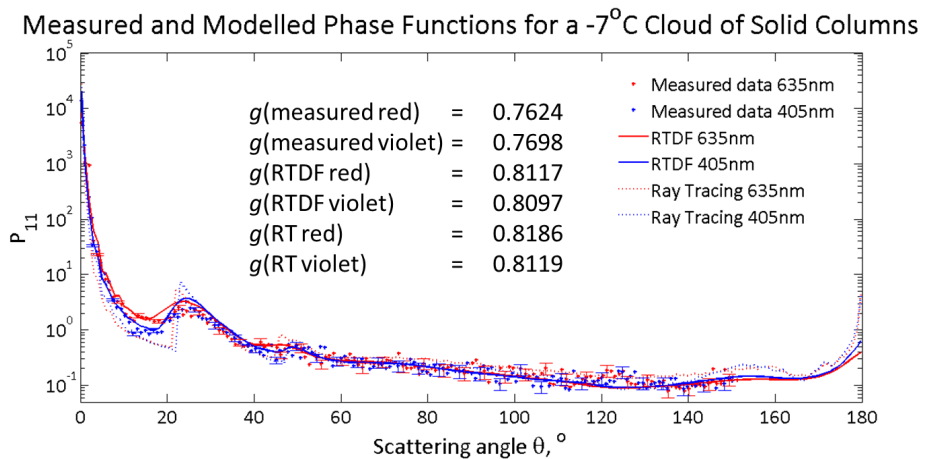


Figure 14: Measured and modelled phase functions for solid columns at -7°C

Measured and Modelled Phase Functions for a -7°C Cloud of Hollow Columns

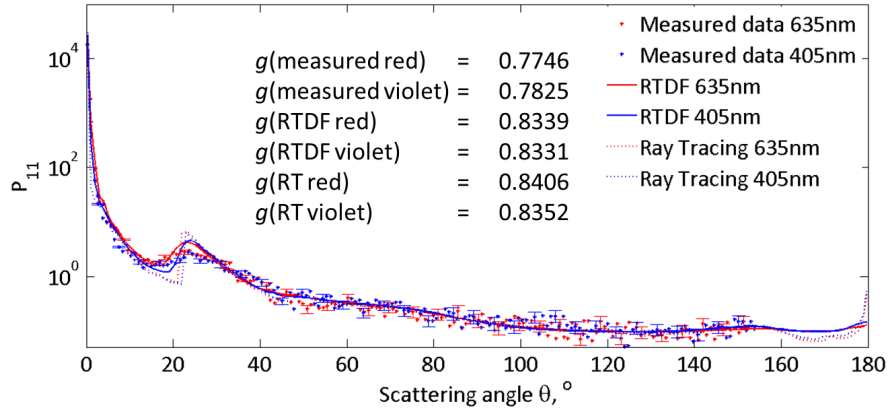


Figure 15: Measured and modelled phase functions for hollow columns at -7°C

Measured and Modelled Phase Functions for a -15°C Cloud of Solid Plates

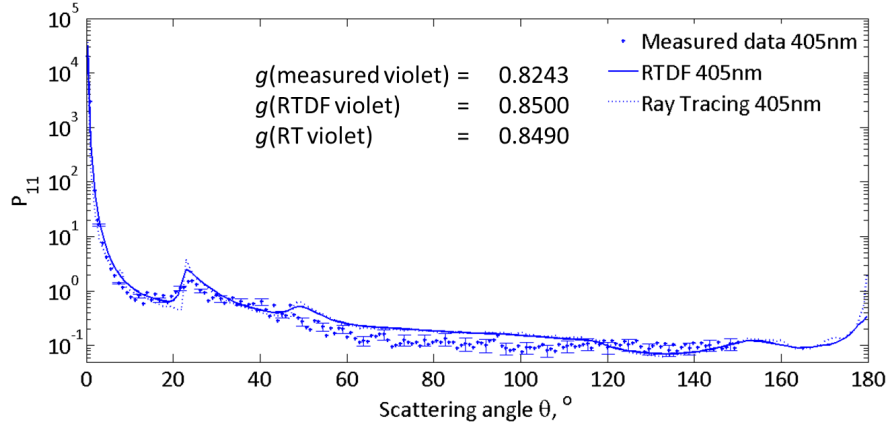


Figure 16: Measured and modelled phase functions for solid plates at -15°C . Intensity measurements from the red laser are unavailable for this experiment.

Measured and Modelled Phase Functions for a -15°C Cloud of Hollow Plates

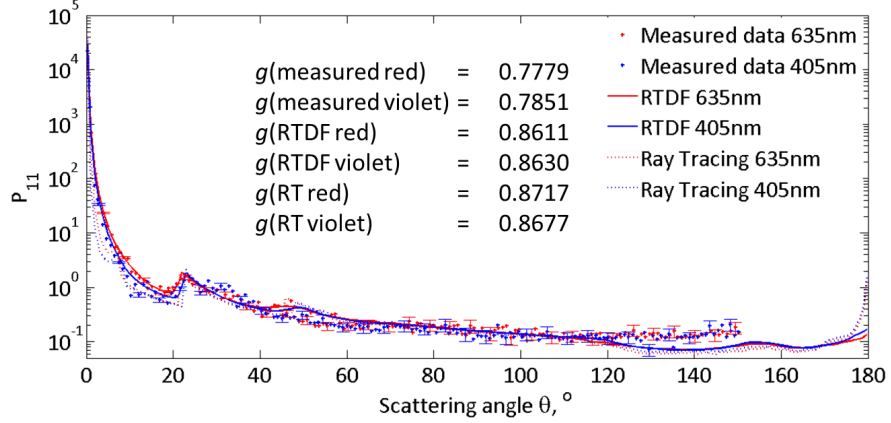


Figure 17: Measured and modelled phase functions for hollow plates at -15°C

Measured and Modelled Phase Functions for a -30°C Cloud of Hollow Columns

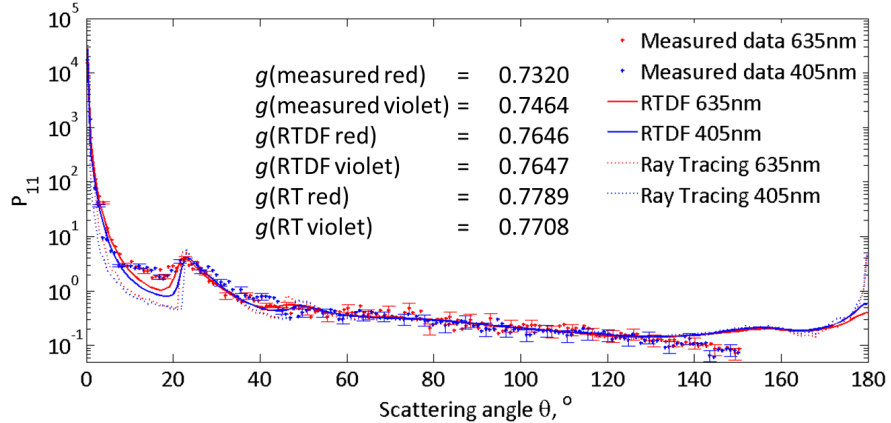


Figure 18: Measured and modelled phase functions for a cloud of cold hollow columns and hollow plates at -30°C

4. Discussion

In figures 14–18, it can be seen that there are random variations, or noise, in the measured phase functions. This can be attributed, in part, to low signal to noise ratios, where ‘signal’ is defined as the measured intensity, and ‘noise’ is defined as the background intensity. At larger angles where the

scattered intensity was weak, typical signal to noise ratios were ~ 2 . As the lasers were diode lasers with inherently short coherence lengths, the noise cannot be attributed to laser speckle. Each experiment was repeated four times in order to gain average measurements. The average signal to noise ratios and standard deviations for all experiments are given in table 3.

Angular Range, $^{\circ}$	0–10	10–30	30–50	50–70	70–90	90–110	110–130	130–150
SNR	14.32	6.95	5.52	4.31	2.48	2.15	1.98	2.01
Standard Deviation, %	4	9	14	17	23	26	24	24

Table 3: Average Signal to Noise Ratios (SNR) and standard deviations (as a percentage of the mean) of the intensity measurements used to obtain the phase functions.

A summary of the measured and modelled asymmetry parameters is given in table 4.

	Cloud 1		Cloud 2		Cloud 3		Cloud 4		Cloud 5	
	g	% dev.								
measured (red)	0.7623		0.7746				0.7779		0.7320	
measured (violet)	0.7698		0.7825		0.8243		0.7851		0.7464	
RTDF (red)	0.8117	6.48	0.8339	7.66			0.8611	10.70	0.7646	4.45
RTDF(violet)	0.8097	5.19	0.8331	6.47	0.8500	3.13	0.8630	9.93	0.7647	2.45
RT (red)	0.8186	7.40	0.8406	8.52			0.8717	12.05	0.7789	6.41
RT (violet)	0.8119	5.47	0.8352	6.74	0.8490	2.99	0.8677	10.52	0.7708	3.27

Table 4: Measured and modelled asymmetry parameters for all experiments. ‘% dev.’ gives the percentage deviation of the modelled result from the measured result.

For cloud 1, solid columns at -7°C , there is little difference between the asymmetry parameters predicted by Ray Tracing and RTDF. Both RT and RTDF over-predict the asymmetry parameter by 5.2–7.4%. However, differences are easily seen in the phase function (figure 14). Compared to measured results, Ray Tracing over-predicts the 22° halo and over-predicts scattering in the $140\text{--}150^{\circ}$ range. It also under-predicts scattering in the $0\text{--}10^{\circ}$ range. By comparison, the 22° halo predicted by RTDF is smaller and smoother, fitting within the errors of measured results.

For cloud 2, hollow columns at -7°C , both models over-predict the asymmetry parameter by 6.5–8.5%. The halo feature predicted by Ray Tracing is significantly reduced when compared to the solid column model, however the halo is still sharper than measured results, leading to an under-prediction of scattering in the $10\text{--}20^{\circ}$ range and an over-prediction of scattering in the $20\text{--}30^{\circ}$ range. By comparison, the shape of the halo feature predicted by RTDF is much smoother, although the peak is still over-predicted.

Both plate clouds (clouds 3 and 4) show a significant deviation between the measured and modelled phase functions in the 120° – 150° range. This may be due to the inaccurate modelling of plate particles. As described in section 3.1, the prism facet of plate habits could not be measured from the formvar replicas. Based on CPI images, it was decided to model all plates with a thickness of $15\mu\text{m}$. The modelled phase functions all exhibit a trough feature between 120° – 150° , which is not seen for columnar habits. This deviation may be caused, in part, by the under-prediction of the thickness of the plates. In addition to this, it can be seen from figure 12 that the hollow plates produced in cloud 4 had additional features protruding from the prism facets, the particles in cloud 3 had rounded edges, and both clouds contained scalene particles. Omitting these features in the model may cause deviations from the measured results. Comparing the measured results for clouds 3 and 4, we observe a reduction in asymmetry parameter for cloud 4 when compared with cloud 3. However, the modelled results show an increase in asymmetry parameter for cloud 4 when compared to cloud 3. This is due to the change in aspect ratio of the particles. The hollow plate cloud was created at a higher humidity than the solid plate cloud by increasing the vapour input to the chamber. This created the hollow particles as seen in figure 3.2.2, however the ice crystals also exhibited smaller aspect ratios and therefore they cannot be directly compared.

For cloud 5, hollow columns at -30°C , there is a significant deviation in the results in the 140 – 150° range. As described with respect to the plate clouds (clouds 3 and 4), this may be due to a non-representative selection of the size and aspect ratio of the particles. The particles collected in cloud 5 had typical aspect ratios close to one, and therefore both orientations were seen in the formvar replicas. However, if thin, plate-like particles were present in the cloud, they may have oriented on the microscope slides with their basal facet parallel to the slide. In this case, the aspect ratio could not be measured and was therefore not recorded. Due to this, the range of predicted aspect ratios may have been skewed to larger sizes. There is also a deviation from modelled data in the 10 – 20° range, which may be caused by particle roughness, which is known to smooth out halo features. Alternatively it could be caused by particles with more numerous indentations. Each indentation is modelled by three steps based on averaged measurements. However, particles with more or less steps have been observed. The presence of additional step features could cause light to leave the particle at shallower angles, causing increased scattering in the 10 – 20° range.

5. Conclusions

The cavities of hollow ice particles were found to have differing structures at different temperatures, and the structure of the cavity was found to influence the single scattering properties of the particles.

In section 3.1, solid and hollow particle models were tested using RT and RTDF in order to determine the effects of two types of indentation. It was found that the two types of indentations had differing effects. For the hollow particle based on particles seen at -7°C , both RT and RTDF predict an increase in the asymmetry parameter compared to a solid column of the same aspect ratio 1. For the hollow particle model with the stepped internal structure, both RT and RTDF predict a decrease in asymmetry parameter compared with a solid column of the same aspect ratio. In all cases, RT and RTDF over-predict the asymmetry parameter. As an average across all experiments, RT over-predicts the asymmetry by 6.8%, whereas RTDF over-predicts asymmetry parameter by 6.11 %. The phase functions predicted by RT showed more prominent halo features than those predicted by RTDF. Both of the hollow particle models caused a reduction in the 46° halo when using the RTDF model, however these features remained prominent when using RT. The phase functions predicted from RTDF show less deviation from measured results compared with RT, particularly in the halo regions and the forward scattering range.

Due to experimental conditions, roughness and hollowness cannot be entirely separated. In all experiments, it is possible that surface roughness contributed to diminished halo features, which were typically over-predicted by the models. Surface roughness is also known to reduce the asymmetry parameter [45], which may explain the discrepancy between measured and modelled results. Due to this, measured asymmetry parameters from these experiments may be larger than field experiments due to more constrained lab conditions and restricted growth times leading to more pristine particles.

Acknowledgements

This work was funded by the Natural Environment Research Council (NERC) in conjunction with a CASE studentship from Met Office. We also acknowledge funding from the NERC ACID-PRUF programme, grant code NE/I020121/1.

References

- [1] Intergovernmental Panel on Climate Change, 2013: The Physical Science Basis: Contribution of Working Group 1 to the Fifth Assessment Report of the IPCC. Cambridge University Press, Cambridge
- [2] Zhang, Y., Macke, A. & Albers, F. Effect of crystal size spectrum and crystal shape on stratiform cirrus radiative forcing. *Atmos. Res.* 1999, 52, 59–75
- [3] Liou, K. N. & Takano, Y. Light scattering by nonspherical particles: remote sensing and climatic implications. *Atmos. Res.* 1994, 31, 271–98
- [4] Baran, A. J. From the single-scattering properties of ice crystals to climate prediction: A way forward. *Atmos. Res.* 2012, 112, 45–69
- [5] Sassen, K., Wang, Z. & Liu, D. Global distribution of cirrus clouds from CloudSat/Cloud-Aerosol Lidar and Infrared Pathfinder Satellite Observations (CALIPSO) measurements. *J. Geophys. Res.* 2008, 113, D00A12
- [6] Descartes, R., Tremblay, J-M. (trans.) *The Météors.* 2002 www.classiques.uqac.ca/classiques/Descartes/meteores/meteores.html
- [7] Kepler, J. *On the six cornered snowflake* (Oxford: Clarendon) 1966
- [8] Mason, B. J. Snow crystals, natural and man made. *Contemp. Phys.* 1992, 33, 227–43
- [9] Nakaya, U. *Snow Crystals: Natural and Artificial.* Harvard University Press. 1954
- [10] Bailey, M. P. & Hallett, J. A Comprehensive Habit Diagram for Atmospheric Ice Crystals: Confirmation from the Laboratory, AIRS II, and Other Field Studies. *J. Atmos. Sci.* 2009, 66, 2888–2899
- [11] Bailey, M. & Hallet, J. Growth rates and habits of ice crystals between -20°C and -70°C . *J. Atmos. Sci.* 2004, 61, 514–44
- [12] Miloshevich, L. M. & Heymsfield, A. J. A balloon-borne continuous cloud particle replicator for measuring vertical profiles of cloud microphysical properties: instrument design, performance, and collection efficiency analysis. *J. Atmos. Ocean. Technol.* 1997, 14, 753–768

- [13] Barkley, B., Bailey, M., Liou, K.-N. & Hallet, J. Light-scattering properties of plate and column ice crystals generated in a laboratory cold chamber. *Appl. Opt.* 2002, 41, 5792–5796
- [14] Rimmer, J. S. & Saunders, C. P. R., Extinction measurements and single scattering albedo in the 0.5 to 1.05 μm range for a laboratory cloud of hexagonal ice crystals. *Atmos. Res.* 1998, 49, 177–188
- [15] Saunders, C., Rimmer, J., Jonas, P., Arathoon, J. & Liu, C. Preliminary laboratory studies of the optical scattering properties of the crystal clouds. *Annales Geophysicae* 1998, 16, 618–627
- [16] Smedley, A. R. D., Webb, A. R. & Saunders, C. P. R. Application of a diode array spectroradiometer to measuring the spectral scattering properties of cloud types in a laboratory. *Atmos. Chem. Phys.* 2007, 7, 5803–5813
- [17] Weickmann, H. *Die Eisphase in der Atmosphere*. Royal Aircraft Establishment, Farnborough. 1947
- [18] Heysfield, A. & Miloshevich, L. Parameterizations for the Cross-Sectional Area and Extinction of Cirrus and Stratiform Ice Cloud Particles. *J. Atmos. Sci.* 2003, 60, 936–956
- [19] Lawson, R. P., Baker, B. A., Zmarzly, P., O’Connor, D., Mo, Q., Gayet, J.-F. & Shcherbakov, V. Microphysical and Optical Properties of Atmospheric Ice Crystals at South Pole Station. *J. Appl. Meteor. Clim.* 2006, 45, 1505–1524
- [20] Um, J. & Mcfarquhar, G. M. Single-scattering properties of aggregates of plates. *QJRMS.* 2009, 304, 291–304
- [21] Gayet, J.-F., Mioche, G., Bugliaro, L., Protat, A., Minikin, A., Wirth, M., Dörnbrack, A., Shcherbakov, V., Mayer, B., Garnier, A. & Goubeyre, C. On the observation of unusual high concentration of small chain-like aggregate ice crystals and large ice water contents near the top of a deep convective cloud during the CIRCLE-2 experiment. *Atmos. Chem. Phys.* 2012, 12, 727–744
- [22] Gallagher, M. W., Connolly, P. J., Whiteway, J., Figueras-Nieto, D., Flynn, M., Choulaton, T. W., Bower, K. N., Cook, C., Busen, R. &

- Hacker, J. An overview of the microphysical structure of cirrus clouds observed during EMERALD-1. *QJRMS*. 2005, 131, 1143–1169
- [23] Vogelmann, A. M. & Ackerman, T. P. Relating Cirrus Cloud Properties to Observed fluxes: a Critical Assessment. *J. Atmos. Sci.* 1995, 52, 4285–4301
- [24] McFarquhar, G. M., Yang, P., Macke, A. & Baran, A. J. A new parameterization of single scattering solar radiative properties for tropical anvils using observed ice crystal size and shape distributions. *J. Atmos. Sci.* 2002, 59, 2458–2478
- [25] McFarquhar, G. M., Heymsfield, A. J., Macke, A., Iaquina, J. & Aulenchbach, S. M. Use of observed ice crystal sizes and shapes to calculate mean-scattering properties and multispectral radiances: CEPEX April 4, 1993, case study. *J. Geophys. Res.* 1999, 104, 31763
- [26] Lindqvist, H., Muinonen, K., Nousiainen, T., Um, J., McFarquhar, G. M., Haapanala, P., Makkonen, R. & Hakkarainen, H. Ice-cloud particle habit classification using principal components. *J. Geophys. Res.* 2012, 117, D16206
- [27] Key, J. R., Yang, P., Baum, B. A. & Nasiri, S. Parameterization of short-wave ice cloud optical properties for various particle habits. *J. Geophys. Res.* 2002, 107(D13)
- [28] Yang, H., Dobbie, S., Herbert, R., Connolly, P., Gallagher, M., Ghosh, S., Al-Jumur, S. M. R. K. & Clayton, J. The effect of observed vertical structure, habits, and size distributions on the solar radiative properties and cloud evolution of cirrus clouds. *QJRMS*. 2011, 0, 1–14
- [29] Macke, A., Francis, P. N., Mcfarquhar, G. M. & Kinne, S. The Role of Ice Particle Shapes and Size Distributions in the Single Scattering Properties of Cirrus Clouds. *J. Atmos. Sci.* 1998, 55, 2874–2883
- [30] Bacon, N. J. & Swanson, B. D. Laboratory measurements of light scattering by single levitated ice crystals. *J. Atmos. Sci.* 2000, 57, 2094–2104
- [31] Macke, A., Mueller, J. & Raschke, E. Single scattering properties of atmospheric ice crystals. *J. Atmos. Sci.* 1996, 53, 2813–2825

- [32] Yang, P. & Liou, K. N. Geometric-optics-integral-equation method for light scattering by nonspherical ice crystals. *Appl. Opt.* 1996, 35, 6568–6584
- [33] Baran, A. J., Watts, P. D. & Francis, P. N. Testing the coherence of cirrus microphysical and bulk properties retrieved from dual-viewing multispectral satellite radiance measurements. *J. Geophys. Res.* 1999, 104, 31673-83
- [34] Baran, A. J. & Labonnote, L. C. On the reflection and polarization properties of ice cloud. *JQSRT.* 2006, 100, 41–54
- [35] Macke, A. & Mishchenko, M. I. Applicability of regular particle shapes in light scattering calculations for atmospheric ice particles. *Appl. Opt.* 1996, 35, 4291–4296
- [36] Gerber, H., Takano, Y., Garrett, T. J. & Hobbs, P. V. Nephelometer measurements of the asymmetry parameter, volume extinction coefficient, and backscatter ratio in arctic clouds. *J. Atmos. Sci.* 2000, 57, 3021–3034
- [37] Lampert, A., Ehrlich, A., Dornbrack, A., Jourdan, O., Gayet, J.-F., Mioche, G., Shcherbakov, V., Ritter, C. & Wendisch, M. Microphysical and radiative characterization of a subvisible midlevel Arctic ice cloud by airborne observations - a case study. *Atmos. Chem. Phys.* 2009, 9, 2647–2661
- [38] Gayet, J.-F., Mioche, G., Shcherbakov, V., Goubeyre, C., Busen, R. & Minikin, A. Optical properties of pristine ice crystals in mid-latitude cirrus clouds: a case study during CIRCLE-2 experiment. *Atmos. Chem. Phys.* 2011, 11, 2537–2544
- [39] Garrett, T. J., Gerber, H., Baumgardner, D. G., Twohy, C. H. & Weinstock, E. M. Small, highly reflective ice crystals in low-latitude cirrus. *Geophys. Res. Lett.* 2003, 30(21), 2132
- [40] Garrett, T. J., Navarro, B. C., Twohy, C. H., Jensen, E. J., Baumgardner, D. G., Bui, P. T., Gerber, H., Herman, R. L., Heymsfield, A. J., Lawson, P., Minnis, P., Nguyen, L., Poellot, M., Pope, S. K., Valero, F. P. J. & Weinstock, E. M. Evolution of a Florida Cirrus Anvil. *J. Atmos. Sci.* 2005, 62, 2352–2372

- [41] Van Diedenhoven, B., Cairns, B., Fridlind, A. M., Ackerman, A. S. & Garrett, T. J. Remote sensing of ice crystal asymmetry parameter using multi-directional polarization measurements - Part 2: Application to the Research Scanning Polarimeter. *Atmos. Chem. Phys.* 2013, 13, 3185–3203
- [42] Yang, P., Hong, G., Kattawar, G., Minnis, P. & Hu, Y. Uncertainties associated with the surface texture of ice particles in satellite-based retrieval of cirrus clouds: part II - effect of particle surface roughness on retrieved cloud optical thickness and effective particle size. *IEEE transaction on Geoscience and Remote Sensing.* 2008, 46(7), 1948–1957
- [43] Schmitt, C. G. & Heymsfield, A. J. On the Occurrence of Hollow Bullet Rosette- and Column-Shaped Ice Crystals in Midlatitude Cirrus. *J. Atmos. Sci.* 2007, 64, 4514–4519
- [44] Neshyba, S. P., Lowen, B., Benning, M., Lawson, A. & Rowe, P. M. Roughness metrics of prismatic facets of ice. *J. Geophys. Res.* 2013, 118, 3309–3318
- [45] Ulanowski, Z., Kaye, P. H., Hirst, E., Greenaway, R. S., Cotton, R. J., Hesse, E. & Collier, C. T. Incidence of rough and irregular atmospheric ice particles from Small Ice Detector 3 measurements. *Atmos. Chem. Phys.* 2014, 14, 1649–1622
- [46] Shcherbakov, V., Gayet, J-F., Baker, B. A. & Lawson, R. P. Light scattering by single natural ice crystals. *J. Atmos. Sci.* 2006, 63, 1513–1525
- [47] Shcherbakov, V., Gayet, J-F., Jourdan, O., Strm, J. & Minikin, A. Light scattering by single ice crystals of cirrus clouds. *Geophys. Res. Lett.* 2006, 33, L15809
- [48] Yang, P. & Liou, K-N. Single-scattering properties of complex ice crystals in terrestrial atmosphere. *Contr. Atmos. Phys.* 1998, 71, 223–48
- [49] Liu, C., Panetta, R. L. & Yang, P. The effects of surface roughness on the scattering properties of hexagonal columns with sizes from the Rayleigh to the geometric optics regimes. *JQSRT.* 2013, 129, 169–185

- [50] Pfalzgraff, W. C., Hulscher, R. M. & Neshyba, S. P. Scanning electron microscopy and molecular dynamics of surfaces of growing and ablating hexagonal ice crystals. *Atmos. Chem. Phys.* 2010, 10, 2927–2935
- [51] Schnaiter, M., Kaye, P. H., Hirst, E., Ulanowski, Z. & Wagner, R. Exploring the surface roughness of small ice crystals by measuring high resolution angular scattering patterns. *AAPP.* 2011, 89(1), 5-8
- [52] Schmitt, C. G., Iaquinta, J., Heymsfield, A. J. & Iaquinta, J. The asymmetry parameter of cirrus clouds composed of hollow bullet rosette-shaped ice crystals from ray-tracing calculations. *J. Appl. Meteor. Clim.* 2006, 45, 973–981
- [53] Yang, P., Zhang, Z., Kattawar, G. W., Warren, S. G., Baum, B. A., Huang, H.-L., Hu, Y. X., Winker, D. & Iaquinta, J. Effect of cavities on the optical properties of bullet rosettes: implications for active and passive remote sensing of ice cloud properties. *J. Appl. Meteor. Clim.* 2008, 47, 2311–2330
- [54] Heymsfield, A. J., Bansemer, A., Field, P. R., Durden, S. L., Stith, J. L., Dye, J. E., Hall, W. & Grainger, C. A. Observations and parameterizations of particle size distributions in deep tropical cirrus and stratiform precipitating clouds: results from in-situ observations in TRMM field campaigns. *J. Atmos. Sci.* 2002, 59, 3457–3491
- [55] Mason, B. J. *The physics of clouds.* Clarendon Press, Oxford. 1957
- [56] Connolly, P. J., Emersic, C. & Field, P. R. A laboratory investigation into the aggregation efficiency of small ice crystals. *Atmos. Chem. Phys.* 2012, 12, 2055–2076
- [57] Rimmer, J. S. & Saunders, C. P. R. Radiative scattering by artificially produced clouds of hexagonal plate ice crystals. *Atmos. Res.* 1997, 45, 153–164
- [58] Libbrecht, K. G. *The physics of snow crystals.* *Reports on Progress in Physics.* 2005, 68, 855–895
- [59] Connolly, P. J., Flynn, M. J., Ulanowski, Z., Choulaton, T. W., Gallagher, M. W. & Bower, K. N. Calibration of the Cloud Particle Imager

- probes using calibration beads and ice crystal analogs: the depth of field. *J. Atmos. Ocean. Technol.* 2007, 24, 1860–1879
- [60] Vaughan, G., Bower, K., Schiller, C., MacKenzie, A. R., Peter, T., Schlager, H. Harris, N. R. P. & May, P. T. SCOUT-O3/ACTIVE: high-altitude aircraft measurements around deep tropical convection. *Bull. Amer. Meteor. Soc.* 2008, 89, 647–662
- [61] Protat, A., McFarquhar, G. M., Um, J. & Delano, J. Obtaining best estimates for the microphysical and radiative properties of tropical ice clouds from TWP-ICE in situ microphysical observations. *J. Appl. Meteor. Clim.* 2011, 50, 895–915
- [62] Griggs, D. J. & Jayarante, E. R. The replication of ice crystals using formvar: techniques and precautions. *J. Atmos. Ocean. Technol.* 1986, 3, 547–551
- [63] Platt, C. M. R. Lidar backscatter from horizontal ice crystal patterns. *J. Appl. Meteor.* 1978, 17, 482-8.
- [64] Chepfer, H., Brogniez, G., Goloub, P., Breon, F. M., & Flamant, P. H. Observations of horizontally oriented ice crystals in cirrus clouds with POLDER-1/ADEOS-1. *JQSRT.* 1999, 63, 521-543
- [65] Heymsfield, A. J. & Westbrook, C. D. Advances in the estimation of ice particle fall speeds using laboratory and field measurements. *J. Atmos. Sci.* 2010, 67, 2469–2484
- [66] van de Hulst, H. C. *Light Scattering by Small Particles.* John Wiley & Sons, New York, 1957
- [67] Hesse, E., McCall, D., Ulanowski, Z. Stopford, C. & Kaye, P. H. Application of RTDF to particles with curved surfaces. *JQSRT.* 2009, 110, 1599–1603
- [68] Warren, S. G. & R. E. Brandt, *Optical constants of ice from the ultraviolet to the microwave: A revised compilation,* *J. Geophys. Res.* 2008, 113, D14220

Paper 2: Exact and near backscattering measurements of the linear depolarisation ratio of various crystal habits generated in a laboratory cloud chamber.

This manuscript was submitted to the ELS-XV special issue of the Journal of Quantitative Spectroscopy and Radiative Transfer and is currently under review.

5.1 Summary

The following paper investigates the backscattering linear depolarization ratio (LDR) of various ice crystal habits. As discussed in section 2.1.1, polarised scattering is a valuable tool in the measurement of microphysical properties by either remote or in-situ instrumentation. Experiments were conducted in the Manchester Ice Cloud Chamber where LDR was measured for a variety of particle habits including solid and hollow columns, dendrites and plates. Geometric particle models were created and used to predict LDR using a Ray Tracing code. A comparison between measured and modelled results show that Ray Tracing over-predicts LDR compared with measured results, however, the use of a more realistic geometric particle model significantly reduced LDR predictions, closing the gap between measured and modelled results.

5.2 Author contributions

The design and set up of the optical measurement system was conducted by Helen Smith with the help of advice from Ann Webb, Paul Connolly and Anthony Baran. Measurements and data analysis were completed by Helen Smith.

The particle geometries used for modelling were created for Paper 1 by Helen Smith and Paul Connolly. Slight alterations to the geometries were made for this investigation by Helen Smith.

The manuscript was prepared by Helen Smith, and all coauthors contributed to the drafting process. The entire investigation was conducted under the general supervision of Ann Webb, Paul Connolly and Anthony Baran.

Exact and near backscattering measurements of the linear depolarisation ratio of various ice crystal habits generated in a laboratory cloud chamber

Helen R Smith^{a,1}, Paul J Connolly^a, Ann R Webb^a, Anthony J Baran^b

^a*The University of Manchester, Oxford Road, Manchester, UK*

^b*Met Office, Exeter, UK*

Abstract

Ice clouds were generated in the Manchester Ice Cloud Chamber (MICC), and the backscattering linear depolarisation ratio, δ , was measured for a variety of habits. To create an assortment of particle morphologies, the humidity in the chamber was varied throughout each experiment, resulting in a range of habits from the pristine to the complex. This technique was repeated at three temperatures: -7°C , -15°C and -30°C , in order to produce both solid and hollow columns, plates, sectorised plates and dendrites. A linearly polarised 532 nm continuous wave diode laser was directed through a section of the cloud using a non-polarising 50:50 beam splitter. Measurements of the scattered light were taken at 178° , 179° and 180° , using a Glan-Taylor prism to separate the co- and cross- polarised components. The intensities of these components were measured using two amplified photodetectors and the ratio of the cross- to co- polarised intensities were measured to find the linear depolarisation ratio. In general, it was found that Ray Tracing over-predicts the linear depolarisation ratio. However, by creating more accurate particle models which better represent the internal structure of ice particles, discrepancies between measured and modelled results (based on Ray Tracing) were reduced.

Keywords: linear depolarisation ratio, cirrus, hollowness, polarisation, ray tracing, back scattering, ice crystal

Email address: h.smith20@herts.ac.uk (Helen R Smith)

1. Introduction

The recent meeting of the Intergovernmental Panel on Climate Change highlighted the role of clouds in the Earth's atmosphere as one of the biggest uncertainties in predicting climate change today [1]. One such cloud type that adds to the uncertainty in predicting climate change is cirrus. This is because the net radiative effect of cirrus can be positive or negative, and the direction and magnitude of this forcing is highly sensitive to the microphysical properties of the constituent ice particles [2, 3, 4]. Such particle properties are typically investigated with the use of Optical Array Probes (OAPs), which use optical arrays to capture 2 dimensional particle images. OAPs include the Stratton Park Engineering Company's Cloud Particle Imager (CPI) [5], and 2 Dimensional Stereo probe (2D-S) [6], and the Cloud Imaging Probe (CIP) and Precipitation Imaging Probe (PIP) by Droplet Measurement Technologies (DMT) [7]. These probes have been used both in situ and in laboratory experiments for the counting, sizing and habit classification of ice particles [8, 9, 10, 11]. Although successful in characterizing larger particles, the discrete pixel size of the array limits the image resolution, meaning that smaller particles (below 80 μm) cannot be accurately categorized. Small ice crystals in cirrus can be influential on the bulk optical properties of the cloud and therefore the accurate counting and sizing of these smaller particles is crucial [11]. Furthermore, the measurement of other atmospheric particulates is necessary, not only for determining their optical properties but also due to their role in cloud formation and evolution [12, 13, 14]. These small particles cannot be measured using OAPs and therefore other techniques must be employed.

In addition to imaging probes, there currently exists a range of in situ instrumentation, which use singly-scattered light to determine information about the scattering particle. Forward scattering probes, such as the Forward Scattering Spectrometer Probe (FSSP) by Particle Measurement Systems (PMS) [15, 16], and the Cloud Droplet Probe (CDP) by DMT [17], measure scattered intensities in a given angular range in the forward direction. These measurements are used to count and size particles based on a Mie approximation for homogeneous spheres. Ice and aerosol particles are generally nonspherical and may also be inhomogeneous, thus limiting the accuracy of forward scattering probes for the sizing of nonspherical particles. The ability to determine particle asphericity is a useful tool, not only for particle sizing but for the determination of thermodynamic phase (by

discriminating droplets from small ice). One probes which can differentiate between spherical and nonspherical particles is the Small Ice Detector 3 (SID-3). Whilst this instrument also gathers forward scattered light in the 6° – 25° range, the optical array is used to capture the 2 dimensional scattering pattern. This pattern can be used not only to size the particle, but also to estimate the particle habit and surface roughness [18, 19]. Near backscattered light is also measured by certain in situ instrumentation such as DMT’s CAS-DPOL [20], and Cloud Particle Spectrometer with Polarization Detection (CPSPD) [21] instruments, which measure the linear depolarisation ratio of the scattered light [22, 23]. Ice particles depolarise the incident light by internal reflection, effectively rotating the vibration plane of the incident beam. Therefore faceted particles such as ice are more strongly depolarising than water droplets, with measurements of linear depolarisation ratio typically an order of magnitude higher for ice clouds compared with water clouds [24, 25]. Measurements from the CAS-DPOL and CPSPD can therefore be used for determining particle asphericity, and in the discrimination of liquid water from ice. Further to in situ instrumentation, ground and space based remote sensing rely on scattered signals to determine particle properties [26, 27, 28, 29, 30]. The backscattering linear depolarisation ratio has long been used by LIDAR instruments/analysis to determine the thermodynamic phase, size, orientation and habit of cloud particles.

Each of the instruments discussed so far use measurements of scattered light to determine microphysical properties based on comparisons to current theoretical or observational data. However, discrepancies between measured and modelled results exist. LIDAR measurements of linear depolarisation ratio in cirrus are typically lower than those predicted by theory [31]. These observations have previously been attributed to preferential crystal orientation and the presence of liquid water [31]. However, interpretations of these data usually rely on simulations from Ray Tracing, where highly idealized particles are assumed [27]. Particle complexities such as inclusions, cavities and surface roughness are known to affect the single scattering properties of ice particles [32, 33, 34, 35, 36]. Theoretical studies have shown that indentations on the basal facets (frequently seen in laboratory, in situ and ground based studies in the form of ‘hollow’ columns) act to significantly reduce the linear depolarisation ratio [37, 38]. Similar results were shown during laboratory experiments in the Aerosol Interaction and Dynamics in the Atmosphere (AIDA) chamber where low depolarisation ratios of 0.1–0.15 were recorded using the Scattering Intensity Measurement for the Optical detec-

tion of icE (SIMONE) instrument for a cloud comprised predominantly of hollow columns [39]. By comparison, a cloud composed of solid crystals was measured to have significantly higher depolarisation ratios of 0.3 [39]. By incorporating these particle cavities (along with further complexities such as inclusions and particle roughness) geometric particle models may be improved, thus yielding more realistic values of linear depolarisation ratio from Ray Tracing simulations.

From the current literature, we see that different scattering angles, and different elements of the scattering phase matrix can hold information about particular microphysical properties. Therefore the development and use of scattering instrumentation (both in situ and remote) may contribute a plethora of useful information to supplement data gathered from 2D imaging probes. Of interest here is the linear depolarisation ratio which is typically measured at near back-scattering angles to determine particle sphericity (and thus discriminate between ice and liquid water). Further controlled measurements are therefore useful in examining the sensitivity of linear depolarisation ratio on various microphysical characteristics, and also to test the ability of scattering models to recreate these results. In the work presented here, the linear depolarisation ratios were measured experimentally for a variety of ice crystal habits at scattering angles of 178° , 179° and 180° at temperatures between -7°C and -30°C . Measured depolarisation ratios are presented for several habits including solid and hollow columns, plates, sectorised plates and dendrites. These results are compared with modelled results from Ray Tracing [40], and the applicability of this scattering model is discussed.

2. Methods

2.1. Experimental Methods

2.1.1. Production of the Cloud

This work was conducted in the Manchester Ice Cloud Chamber (MICC) as described in previous papers [32, 10]. The cloud chamber is a 10 m tall by 1 m diameter cylindrical fall tube which is housed over three floors, in three stacked cold rooms. The chamber can maintain temperatures down to -50°C , and the temperature is monitored via 10 equidistant thermocouples which are placed along the length of the chamber.

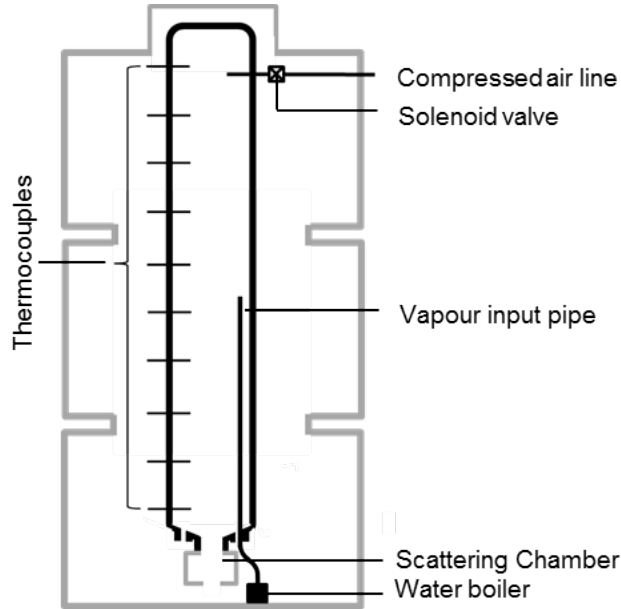


Figure 1: The Manchester Ice Cloud Chamber (MICC) and set-up for experiments.

For this particular experiment, the chamber is humidified using a water boiler, which introduces water vapour near the centre of the chamber as shown in figure 1. After the chamber has been humidified, the boiler is switched off; ice is then nucleated at the top of the chamber using the ‘air popper’ technique [32, 10, 41]. The air popper utilizes a solenoid valve connected to a compressed air line. When the valve is opened, the air expands adiabatically, causing localised cooling down to about -80°C [10], therefore causing the nucleation of ice. These nuclei fall through the chamber, growing at the expense of the water vapour, before falling out of the sampling port at the bottom. The particles then fall into a scattering chamber, where the optical measurements are taken. As time increases, the vapour in the chamber is depleted, causing a drop in humidity, and we see a change in particle habit with respect to time. Due to the vertical inhomogeneity of this set-up, representative values of humidity could not be taken, and therefore emphasis is given to particle habit, rather than the environmental conditions responsible for their formation. For each experiment, the temperature is kept constant.

2.1.2. Classification of Particle Habit

To determine particle habit, formvar replicas were taken every 60 s throughout the course of the experiment. To do this, a 1 % weight to volume solution of formvar in chloroform was made. The solution was applied to microscope slides on which crystals were collected from the base of the cloud chamber. Each slide typically captured hundreds of ice crystals, these were later photographed under an optical microscope. Using the microscope graticule, the lengths of the basal, b , and prism facets, p , were measured. Aspect ratio, α , and maximum dimension, D , were then calculated using:

$$\alpha = p/b \quad (1)$$

and

$$D = \sqrt{p^2 + b^2} \quad (2)$$

where:

p = length of the prism facet

b = length of the basal facet

α = aspect ratio

D = maximum dimension

For plate-like particles, which tended to fall with basal facets parallel to the microscope slide, the lengths of the prism facets could not be measured with the microscope graticule. Instead, the microscope was focussed on the top and bottom facets of the crystals respectively, and the vernier scale on the microscope was used to estimate plate thickness.

2.1.3. Scattering chamber & Optical Se-up

Optical measurements were taken in the ‘scattering chamber’ which was placed at the bottom of the cloud chamber. The scattering chamber is a

0.8 m×0.8 m×0.4 m container, with a 0.3 m opening at the top which was attached to a cloud chamber sample port as shown in figure 1. A rotating platform was mounted at the bottom of the scattering chamber, on which the detector optics were mounted. A plan view of the set-up is given in figure 2. A fan was placed beneath the scattering chamber in order to encourage the randomization of particle orientation.

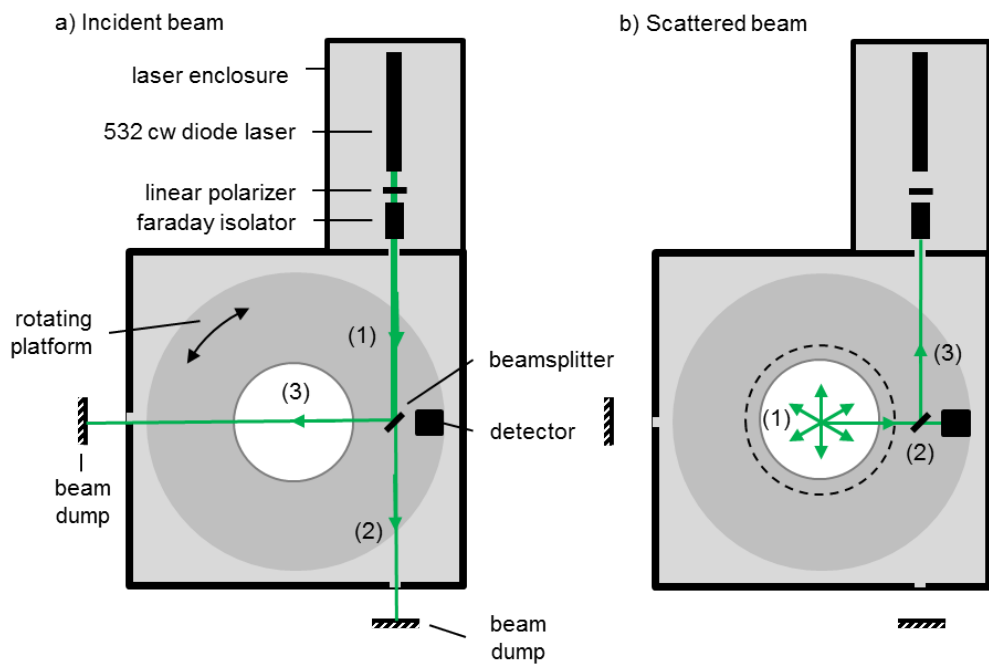


Figure 2: Figure (a) shows the set-up of the optical elements in the scattering chamber, and the path of the incident beam. The laser beam was passed through a polariser and isolator (1), before falling incident on the beamsplitter. The transmitted beam (2) was extinguished, whilst the reflected beam (3) passed through the chamber, before it was also extinguished. Figure (b) shows the path of the scattered beam: cloud particles fell through the area bounded by the dotted line, light was scattered in all directions (1), the directly backscattered portion fell incident on the beamsplitter (2), where the reflected portion (3) was diverted by the isolator, and the transmitted portion was measured by the detector. The detector was fixed to the rotating platform, allowing the measurement angle to be changed. The beamsplitter was attached to a fixed platform and therefore remains stationary.

The laser source used in these experiments was a Hercules 2000 532 nm diode laser from laserglow technologies. The laser was housed in a temperature and humidity controlled enclosure outside of the scattering chamber. The beam was firstly passed through a wire grid polariser, thus polarising the beam perpendicular to the scattering plane. The beam was then directed through a faraday isolator, which prevents back reflections from re-entering the laser. The beam then exited the laser enclosure and entered the scattering chamber, where it fell upon a 50:50 non polarising pellicle beam splitter, mounted at 45° to the incident beam. The beam splitter directed the reflected beam through the cloud, whilst the transmitted beam was extinguished on a beam stop at the far side of the chamber. The reflected beam was scattered by cloud particles in the sample volume. The use of a non polarising beam splitter allowed 50% of the light scattered at 180° to be transmitted back through the beam splitter without altering the polarisation, thus allowing the measurement of linear depolarisation ratio at exactly 180°. Measurements were also taken at 179° and 178°. The portion of directly back scattered light which was reflected by the beam splitter was diverted via the faraday isolator and therefore did not re-enter the laser. The detector head collected scattered light in a solid angle element of 0.035 sr. Inside the detector head, a Glan-Taylor polarisation cube separated the scattered light into *s* and *p* components. The two components were focused down via two plano-convex lenses onto two fibre optic heads. The fibre optic cables were connected at the other end to two amplified Si photodetectors, which measured the intensity of the two components. The linear depolarisation ratio was found by taking the ratio of the perpendicular and parallel components of the scattered light, where parallel and perpendicular are defined relative to the incident beam:

$$\delta = \frac{I_{\perp} - I_{\perp(bg)}}{I_{\parallel} - I_{\parallel(bg)}} \quad (3)$$

where:

δ = Linear depolarisation ratio

I_{\perp} = Intensity of the perpendicular component

$I_{\perp(bg)}$ = Background intensity of the perpendicular component

I_{\parallel} = Intensity of the parallel component

$I_{\parallel(bg)}$ = Background intensity of the parallel component

As various optical elements can be affected by environmental conditions, care was taken to mitigate the effects of temperature and humidity on the optical components. Where possible, equipment was housed in the laser enclosure (which was actively heated, and dried using desiccant), or in the case of the photodetectors, housed outside of the cold room entirely. The beam splitter and detector head were required to be mounted inside the scattering chamber, so low voltage heating elements were applied to the mounting posts, and small fans were used to create a local air flow over the optical surfaces. This approach was found to remove/prevent condensation which would have affected polarisation measurements.

2.2. Calibration of the Photodetectors

Two broadband (320–1100nm) Thorlabs Si Transimpedance Amplified Photodetectors were used to measure the parallel and perpendicular polarised components of the scattered beam. Each photodetector outputs a voltage (V), which is a function of the incident light power (P), wavelength responsivity (R), and gain (G), given by:

$$V = P \cdot R(\lambda) \cdot G \quad (4)$$

These experiments use a single 532 nm radiation source, and therefore, knowledge of the full spectral responsivity, $R(\lambda)$, is not required. Instead, a combined responsivity-gain value, $G(\lambda = 532)$, was found for each of the two photodetector systems, including the effect of their collection optics. As the laser itself does not have a calibrated output, the gain was measured via a cross-calibration against an Ocean Optics S2000 CCD spectrometer system with direct input optics, which was calibrated independently against a NIST-traceable FEL 1kW lamp. To find the gain for each photodetector system, the laser beam was split using a 50:50 pellicle beam splitter, and the reflected and transmitted beams were directed to the calibrated Ocean Optics collection optics, and the photodetector collection optics, respectively. Both sets of collection optics were placed equidistant from the beamsplitter, and aligned with the input beam by using target centered alignment optics to match the back reflections with the incident beam. A faraday isolator was used to prevent back reflections from re-entering the laser. This procedure was repeated

using various neutral density filters to verify that the gains determined were stable across the measurable intensity range. This was again repeated for the second photodetector system. The calibration set-up is shown in figure 3.

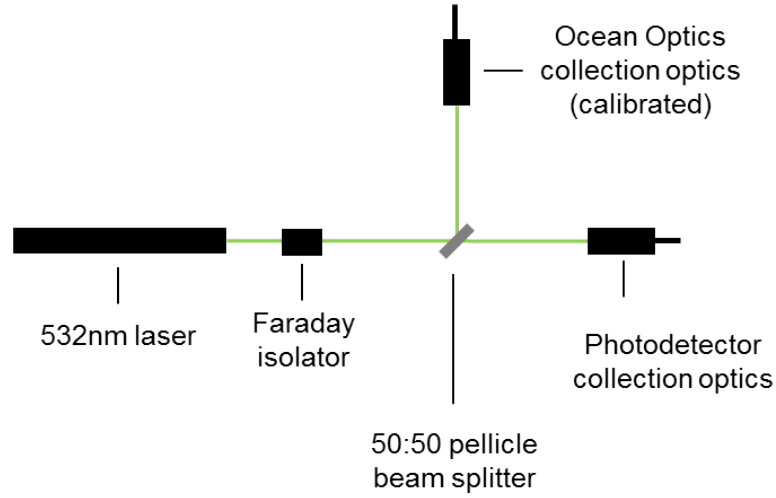


Figure 3: The laser beam is directed onto a 50:50 pellicle beam splitter, aligned at 45° to the incident beam. The reflected 50% of the beam is directed onto the calibrated Ocean Optics CCD spectrometer collection optics, and the transmitted beam is directed onto the photodetector collection optics. The measured intensity from the calibrated instrument is used to find the gain of the non-calibrated photodetector system.

The combined responsivity-gain is given by:

$$G(\lambda = 532\text{nm}) = \frac{I_m - I_{m(bg)}}{V - V_{(bg)}} \quad (5)$$

where:

I_m = Measured intensity from the CCD array spectrometer

$I_{m(bg)}$ = Measured background intensity from the CCD array spectrometer

V = Photodetector output voltage

$V_{(bg)}$ = Photodetector background voltage

Any systematic errors in the Ocean Optics calibration and in the cross-calibration set-up will be removed by taking the ratio of the two photodetector channels to find the linear depolarisation ratio. In the experimental set-up, the two sets of photodetector collection optics were combined with a glan-taylor cube as described in section 2.1.3. In this set-up, the measured gains for each detector were then confirmed by rotating the laser's plane of polarisation and ensuring the expected ratios were produced.

2.3. Computational Methods

Three particle models were used to describe typical geometries identified in the cloud chamber [32]. This includes the solid hexagonal prism, the hollow hexagonal prism with pyramidal indentations (henceforth referred to as the ‘hollow 1’ geometry), and hollow hexagonal prism with stepped hexagonal indentations (henceforth referred to as the ‘hollow 2’ geometry) as shown in figure 4.

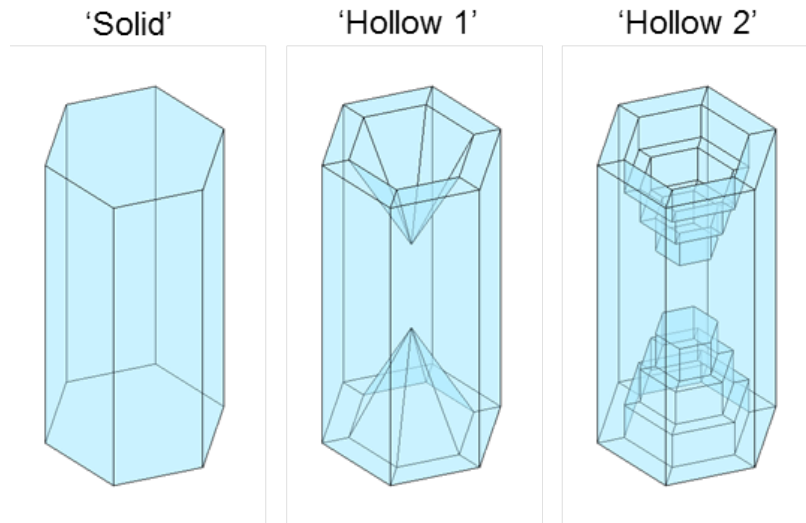


Figure 4: From left to right: solid hexagonal model, hollow hexagonal model with pyramidal indentations (‘hollow 1’), hollow hexagonal model with stepped indentations (‘hollow 2’). Details of model construction can be found in Smith et. al. 2015. [32].

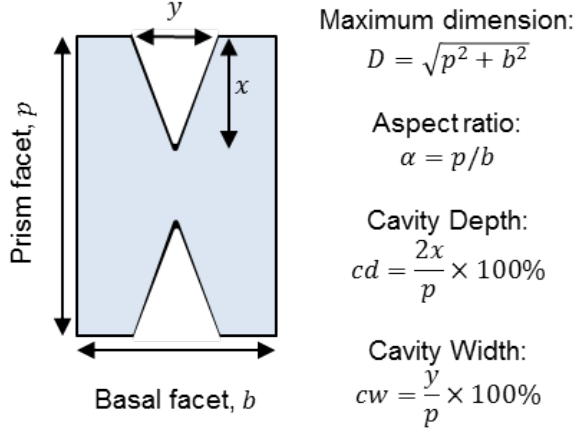


Figure 5: Definitions of maximum dimension, aspect ratio, cavity depth and cavity width.

The particles are constructed according to the maximum dimension, D , aspect ratio, α , cavity width, cw , and depth, cd , as shown in figure 5, where the cavity width and depth are defined as percentages of the prism and basal facets, respectively. By changing these variables, the particle models can cover a wide range of crystal morphologies as observed during the experiments. The particle models were used in a ray tracing code [40], with a wavelength of 532 nm and a complex refractive index of $1.3117 + (1.409 \times 10^{-9})i$ [42]. The ray tracing code outputs phase matrix elements, and therefore we must define the linear depolarisation ratio in terms of these. The intensity and polarisation of a beam can be described by its Stokes vector, (I, Q, U, V) , where I gives the intensity and Q, U and V together describe the ellipticity, orientation and sense of the polarisation. The Stokes vector for a beam scattered by a randomly oriented particle is related to the Stokes vector of the incident beam by [43]:

$$\begin{bmatrix} I_s \\ Q_s \\ U_s \\ V_s \end{bmatrix} = \frac{1}{k^2 r^2} \begin{bmatrix} P_{11} & P_{12} & 0 & 0 \\ P_{12} & P_{22} & 0 & 0 \\ 0 & 0 & P_{33} & P_{34} \\ 0 & 0 & -P_{34} & P_{44} \end{bmatrix} \cdot \begin{bmatrix} I_0 \\ Q_0 \\ U_0 \\ V_0 \end{bmatrix} \quad (6)$$

where:

k = wavenumber

r = distance from the scatterer to the observer

P_{ij} = Phase Matrix elements

$I_{0,s}$ = Incident and scattered intensities, respectively

$Q, U, V_{0,s}$ = Stokes vectors describing polarisation for the incident and scattered beams, respectively.

In this experiment, the beam is linearly polarised in the y plane, and therefore the incident Stokes vector can be given by:

$$\begin{bmatrix} I_0 \\ Q_0 \\ U_0 \\ V_0 \end{bmatrix} = I_0 \begin{bmatrix} 1 \\ -1 \\ 0 \\ 0 \end{bmatrix} \quad (7)$$

Putting this into equation 6, gives:

$$\begin{bmatrix} I_s \\ Q_s \\ U_s \\ V_s \end{bmatrix} = \frac{I_0}{k^2 r^2} \begin{bmatrix} P_{11} & P_{12} & 0 & 0 \\ P_{12} & P_{22} & 0 & 0 \\ 0 & 0 & P_{33} & P_{34} \\ 0 & 0 & -P_{34} & P_{44} \end{bmatrix} \cdot \begin{bmatrix} 1 \\ -1 \\ 0 \\ 0 \end{bmatrix} \quad (8)$$

giving:

$$\begin{bmatrix} I_s \\ Q_s \\ U_s \\ V_s \end{bmatrix} = \frac{I_0}{k^2 r^2} \begin{bmatrix} P_{11} - P_{12} \\ P_{12} - P_{22} \\ 0 \\ 0 \end{bmatrix} \quad (9)$$

So the Stokes vectors of the scattered light can be given by:

$$I_s = \frac{I_0}{k^2 r^2} (P_{11} - P_{12}) \quad (10)$$

$$Q_s = \frac{I_0}{k^2 r^2} (P_{12} - P_{22}) \quad (11)$$

$$U_s = 0 \quad (12)$$

$$V_s = 0 \quad (13)$$

The intensities in the x and y planes are given by:

$$I_x = \frac{1}{2} (I_s + Q_s) \quad (14)$$

$$I_y = \frac{1}{2} (I_s - Q_s) \quad (15)$$

As the incident beam is polarised in the y plane, the linear depolarisation ratio is given as:

$$\delta = \frac{I_x}{I_y} = \frac{I_s + Q_s}{I_s - Q_s} \quad (16)$$

In terms of the phase matrix elements, this can be expressed as:

$$\delta = \frac{P_{11} - P_{22}}{P_{11} - 2P_{12} + P_{22}} \quad (17)$$

We make use of equation 17 to find the linear depolarisation ratio from the ray tracing simulations of P_{11} , P_{12} and P_{22} . The ray tracing model cannot simulate direct forward or backscattering and has minimum and maximum scattering angles of 0.25° and 179.75° respectively. Therefore we cannot directly compare the exact backscattering measurements with modelled results.

3. Results

3.1. Experimental Results

Experiments were conducted at three temperatures: -7°C , -15°C and -30°C . In each experiment, particle habit in the scattering volume was found to change with respect to time due to the drop in humidity in the cloud chamber. As discussed in section 2, reliable humidity measurements could not be taken in this and therefore emphasis is given to particle habit rather than humidity. Formvar replicas were taken every minute throughout the course of each experiment, yielding several hundred replicas per experiment. The replicas were then examined under a microscope to measure the maximum dimension, aspect ratio, cavity type, cavity depth and cavity width. These values were then used to create particle models for use in the ray tracing code, so that measured and modelled results could be compared. Details of the model constructions can be found in [32]. Each data point presented for modelled data represents results from *one* particle geometry. That is, the average particle geometry as observed from microscope measurements at a particular point in time for each experiment (as defined in figures 7, 10 and 13).

3.1.1. Experiments at -7°C

Photographs of the formvar replicas from -7°C experiments are shown in figure 6. We see that the initial crystals grown during these experiments had large indentations, which appear pyramidal in shape. Crystals grown later in the experiment became less hollow, with cavity depth reducing, and cavity structure becoming slightly more complex. Eventually, ice crystals grown at the end of the experiment were entirely solid. Averaged structures

based on microscope observations are given in figure 7. These numeric values were used to construct particle models, which were used in ray tracing. The linear depolarisation ratio was measured at 178° , 179° and 180° , and it was modelled at 178° , 179° and 179.75° . Measured and modelled results are shown in figure 8.

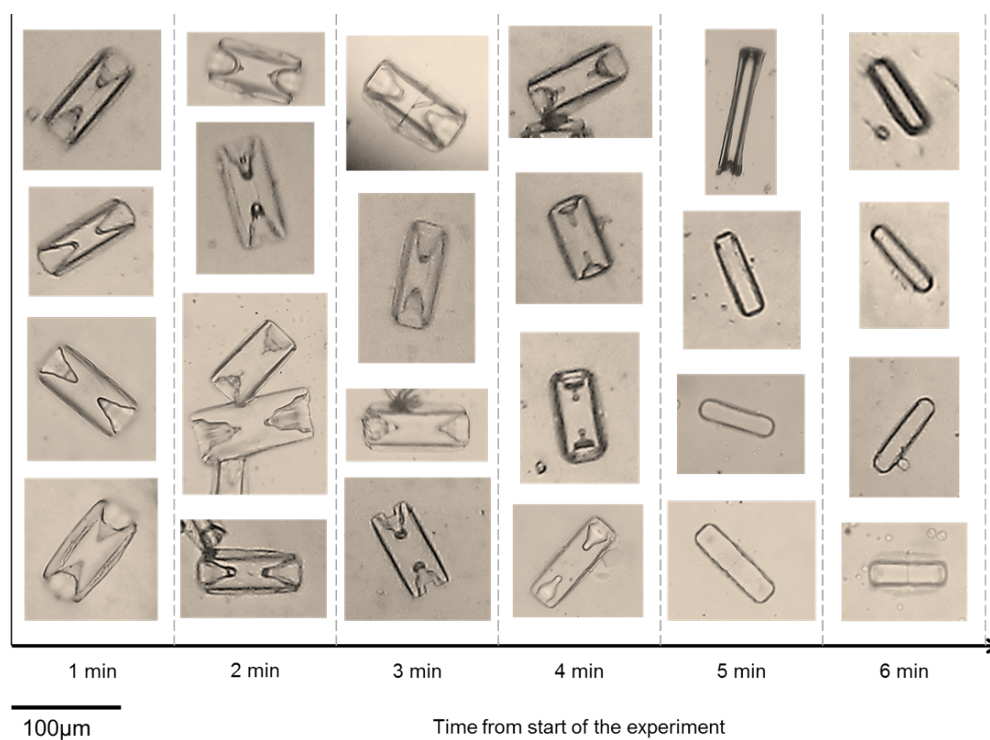


Figure 6: Photographic images of formvar replicas collected during experiments conducted at -7°C , plotted against time from nucleation.

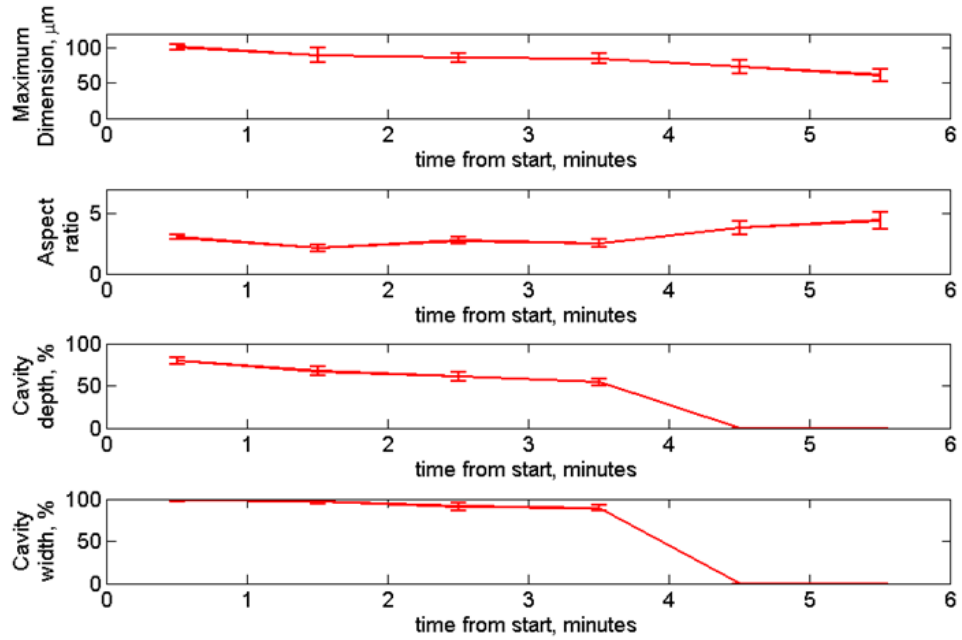


Figure 7: Mean measured maximum dimension, aspect ratio, cavity depth and cavity width for replicas collected during experiments at -7°C , plotted with respect to time.

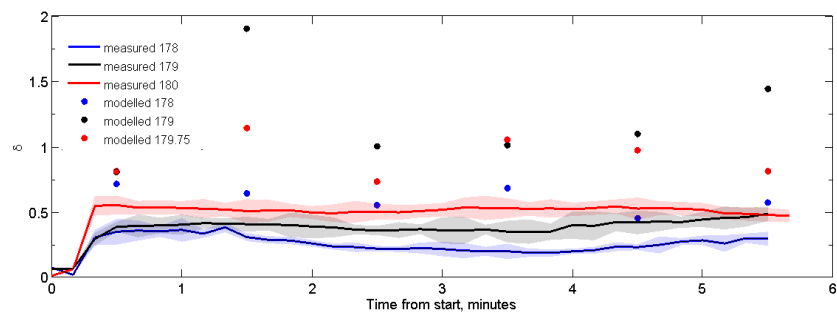


Figure 8: Measured and modelled linear depolarisation ratios of solid and hollow columns produced at -7°C . Standard deviations of measured results are shown as shaded regions.

3.1.2. Experiments at -15°C

Photographs of the formvar replicas from the -15°C experiments are shown in figure 9. Similarly to the -7°C experiments, we see that the crystal habits become more pristine with time. Initial crystal samples show some dendritic features, whereas later crystals are simpler sectorial plates. Crystals grown at the end of the experiment are simple solid plates. Again, several hundreds of crystal replicas were measured, these data are summarised in figure 10. Measured and modelled linear depolarisation ratios are given in figure 11.

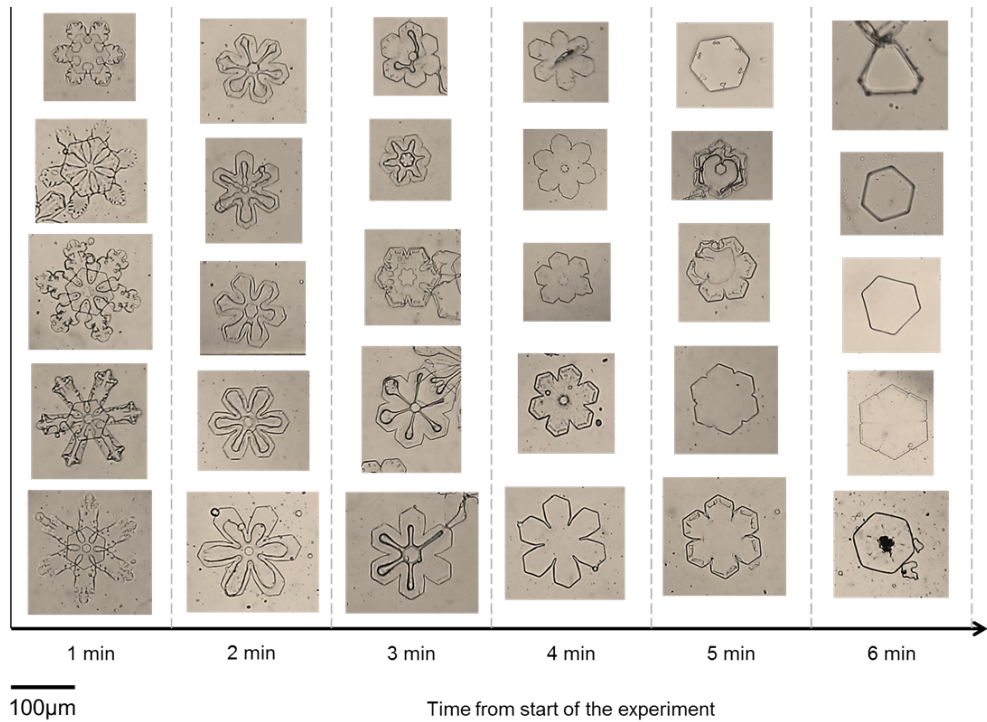


Figure 9: Photographic images of formvar replicas collected during the -15°C experiments, plotted against time from nucleation.

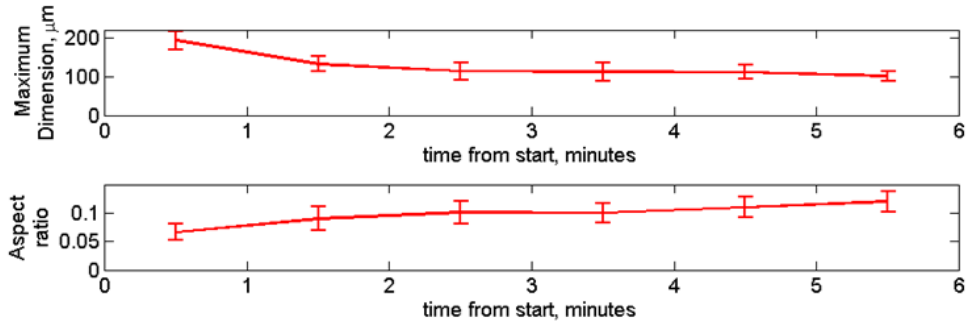


Figure 10: Mean measured maximum dimension, aspect ratio, cavity depth and cavity width for the -15°C experiments, plotted with respect to time.

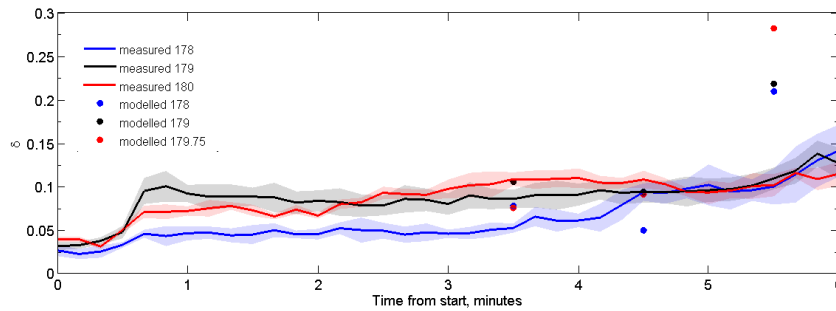


Figure 11: Measured and modelled linear depolarisation ratios of dendrites/sectorised plates/plates. Standard deviations of measured results are shown as shaded regions.

3.1.3. Experiments at -30°C

Photographs of the formvar replicas from the -30°C experiments are shown in figure 12. Unlike the previous two experiments, all crystals imaged during this experiment have similar internal structures, with barely any solid crystals being imaged. During the first minute of the experiment, the cloud consisted only of droplets, but after two minutes the cloud became entirely glaciated. Initial crystal samples show hollow crystals with stepped cavities. Later samples also show similar cavities, however there is a noticeable change

in the aspect ratio. A summary of crystal measurements is given in figure 13, and measured and modelled linear depolarisation ratios are given in figure 14.

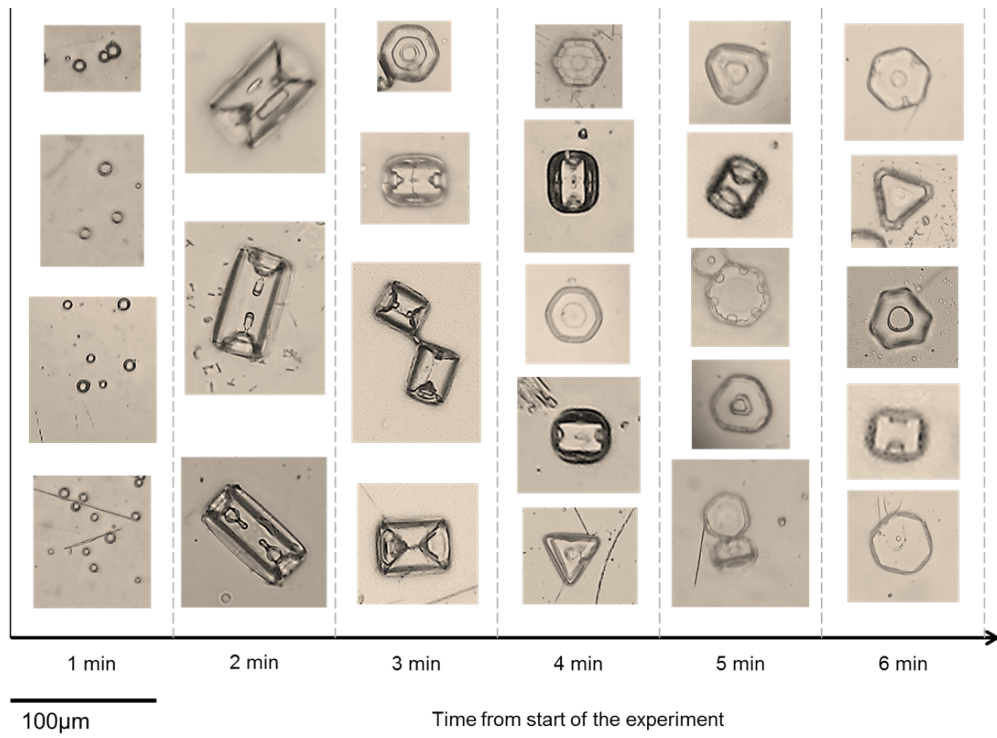


Figure 12: Photographic images of formvar replicas collected during the -30°C experiments, plotted against time from nucleation.

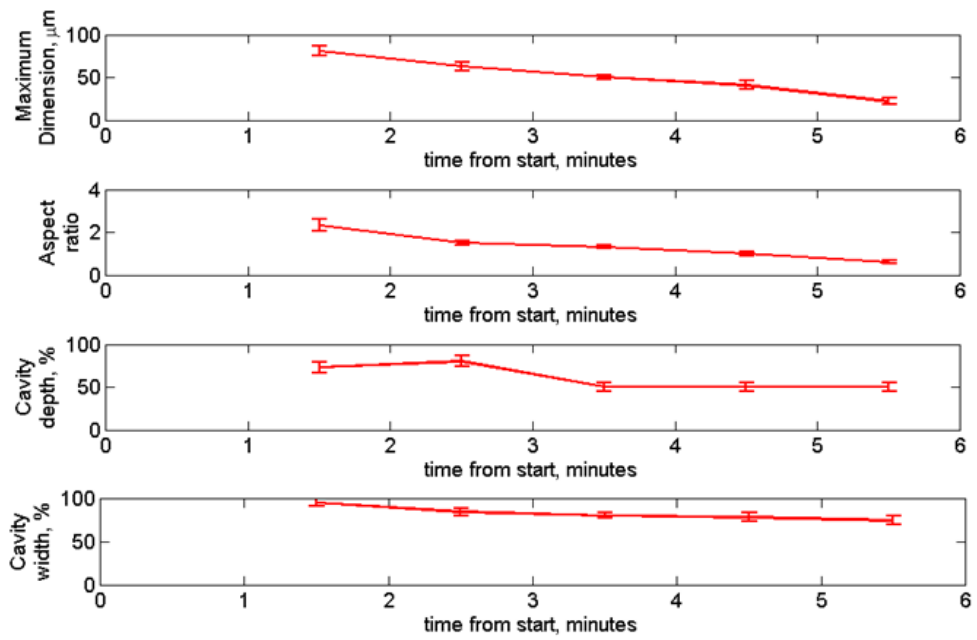


Figure 13: Mean measured maximum dimension, aspect ratio, cavity depth and cavity width for the -30°C experiments, plotted with respect to time.

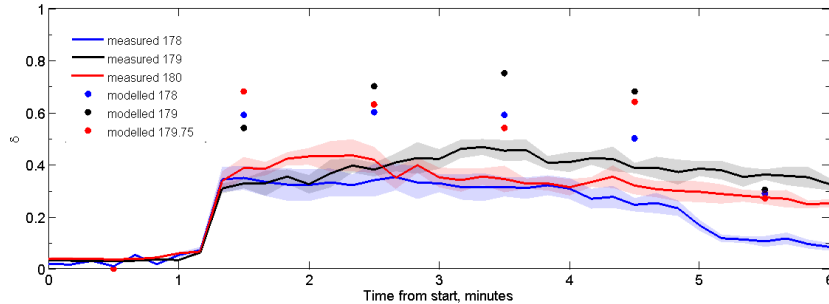


Figure 14: Measured linear depolarisation ratios at 178° , 179° and 180° (solid line), and modelled values from ray tracing. Standard deviations of measured results are shown as shaded regions.

3.2. Computational results

Several variables have already been highlighted as factors in the linear depolarisation ratio of ice crystals, including: aspect ratio, indentations (cavities), and surface roughness. Such variables are intrinsically linked and can therefore not be isolated in real experiments. Therefore, the individual effects of aspect ratio, cavity depth, cavity width and distortion are investigated theoretically.

3.2.1. Effect of aspect ratio on linear depolarisation ratio

Linear depolarisation ratio was calculated for three types of crystal geometry: solid hexagonal prisms, hollow hexagonal prisms with pyramidal cavities, and hollow hexagonal prisms with hexagonal cavities. The maximum dimension was set to a constant of $100\ \mu\text{m}$, the cavity depth and width were set to 50% and 80%, respectively, and the aspect ratio was varied. The left hand plot in figure 15 shows the near backscattering simulations of the three crystal geometries with respect to aspect ratio. We see in general that the hollow 2 particles are less sensitive to changes in aspect ratio, whereas both the solid prisms and the hollow 1 particles show a greater range in depolarisation at near backscattering angles. Although this paper focuses on the backscattering linear depolarisation ratio, the ray tracing code outputs

phase matrix elements for the angular range 0.25° – 179.75° , therefore the linear depolarisation ratio over the full angular range is discussed. The right hand plot in figure 15 shows the linear depolarisation ratios over all angles for all three crystal geometries with varying aspect ratio. We see that the hollow 1 particle shows the greatest variation in linear depolarisation ratio at forward scattering angles where it appears to be very sensitive to aspect ratio.

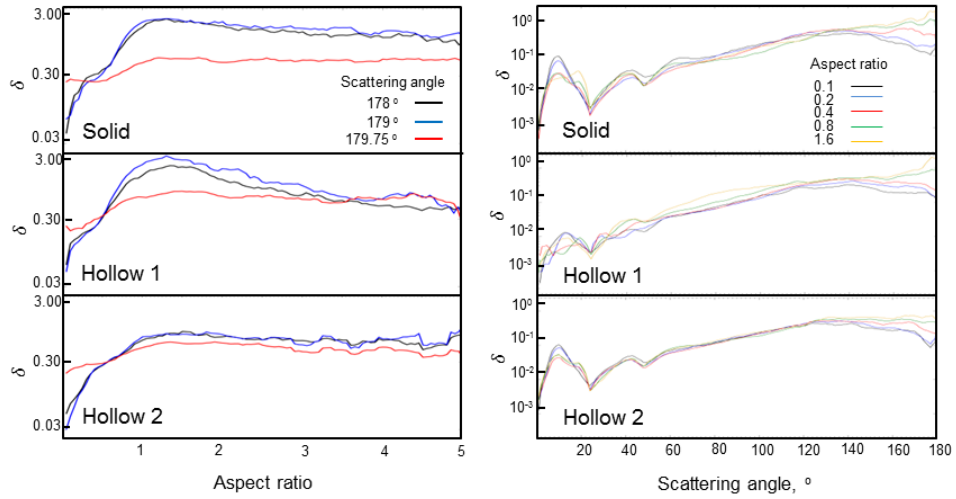


Figure 15: Left: linear depolarisation ratios at near backscattering angles (178° , 179° and 179.75°) for solid (top), hollow 1 (middle) and hollow 2 (bottom) crystals at varying aspect ratios. Right: linear depolarisation ratios between 0.25° – 179.75° for solid (top), hollow 1 (middle) and hollow 2 (bottom) crystals at aspect ratios of 0.1, 0.2, 0.4, 0.8 and 1.6

3.2.2. Effect of cavity depth on linear depolarisation ratio

In this paper, we present two geometries for the internal structure of hollow ice crystals. The ‘hollowness’ is defined as the length of both cavities expressed as a percentage of the length of the prism facet. To investigate the effect of cavity depth on the linear depolarisation ratio, Ray Tracing results were computed for particles of varying degrees of hollowness, from 0% to 97.5%. Since it is evident that linear depolarisation ratio is sensitive to aspect ratio, particularly for aspect ratios less than 1, these calculations were repeated for particles of aspect ratios of 0.2, 0.4, 0.8 and 1.6. For these

calculations the maximum dimension was fixed at $100\ \mu\text{m}$, and the cavity width was fixed at 80%. Figure 16 shows the modelled, near backscattering linear depolarisation ratios for the two hollow particles with varying cavity depths.

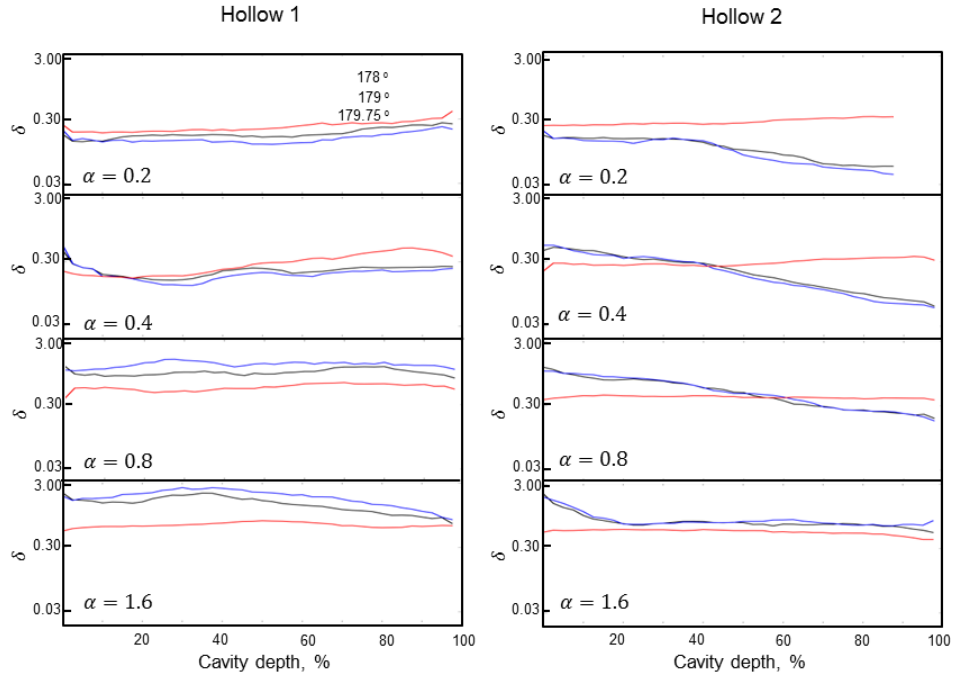


Figure 16: Modelled near backscattering linear depolarisation ratios of two hollow cavity types with varying cavity depth and aspect ratio. The left hand side shows results from the hollow 1 particle (pyramidal cavities), whereas the right hand side shows results from the hollow 2 particle (stepped cavities).

From figure 16, we see that for the hollow 1 particle (pyramidal cavities), there is no obvious correlation between cavity depth and linear depolarisation ratio. By comparison, for the hollow 2 particle, we see a general decrease in linear depolarisation ratio with respect to cavity depth at scattering angles of 178° and 179° . However, at 179.75° , the linear depolarisation seems insensitive to cavity depth. Figure 17 shows the modelled linear depolarisation ratios for the full range of scattering angles calculated (0.25° – 179.75°).

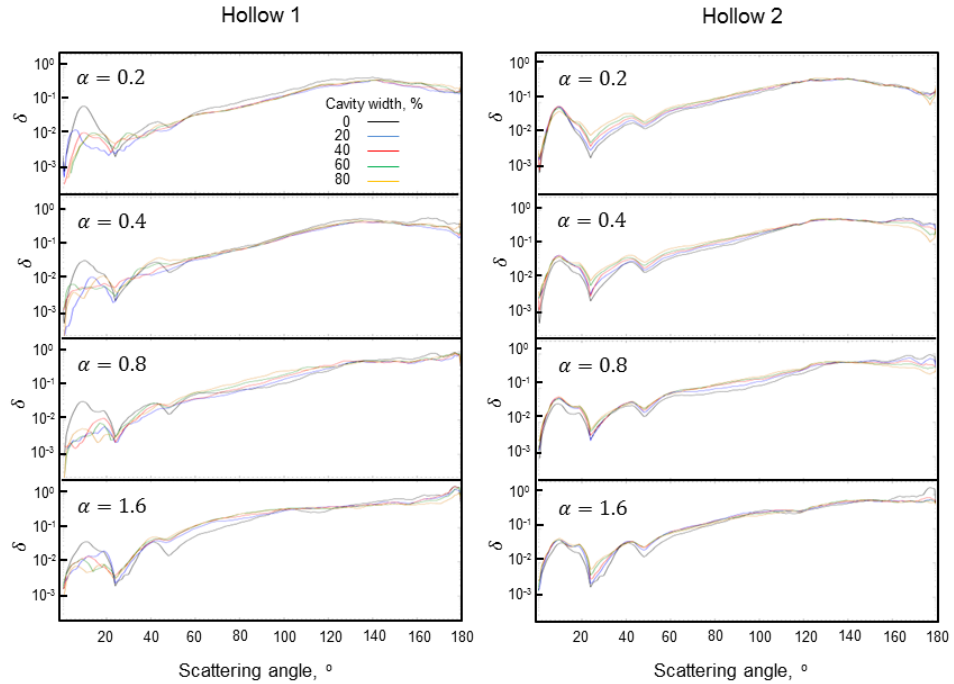


Figure 17: Modelled linear depolarisation ratios for two types of hollow column with varying aspect ratio and cavity depth. The left column shows results from the hollow 1 geometry (pyramidal indentations), and the right column shows results from the hollow 2 geometry (stepped indentations). Different traces represent cavity depths of 0, 20, 40, 60 and 80%.

From figure 17 we see that the 0° – 20° region is particularly sensitive to the presence of pyramidal indentations, with an evident drop in linear depolarisation ratio. However, the same effect is not observed for particles with stepped cavities. It can also be seen that, at larger scattering angles ($\geq 160^\circ$), the linear depolarisation ratio is more sensitive to changes in the stepped cavity, when compared with the pyramidal cavity.

3.2.3. Effect of cavity width on linear depolarisation ratio

In addition to the cavity depth, simulations were also run for particles of varying cavity width. For these calculations, the maximum dimension was again set to $100\ \mu\text{m}$, the cavity depth was set to 50%, and the cavity width was varied in 5% increments from 0% to 95%. Simulations were run for as-

pect ratios of 0.2, 0.4, 0.8 and 1.6.

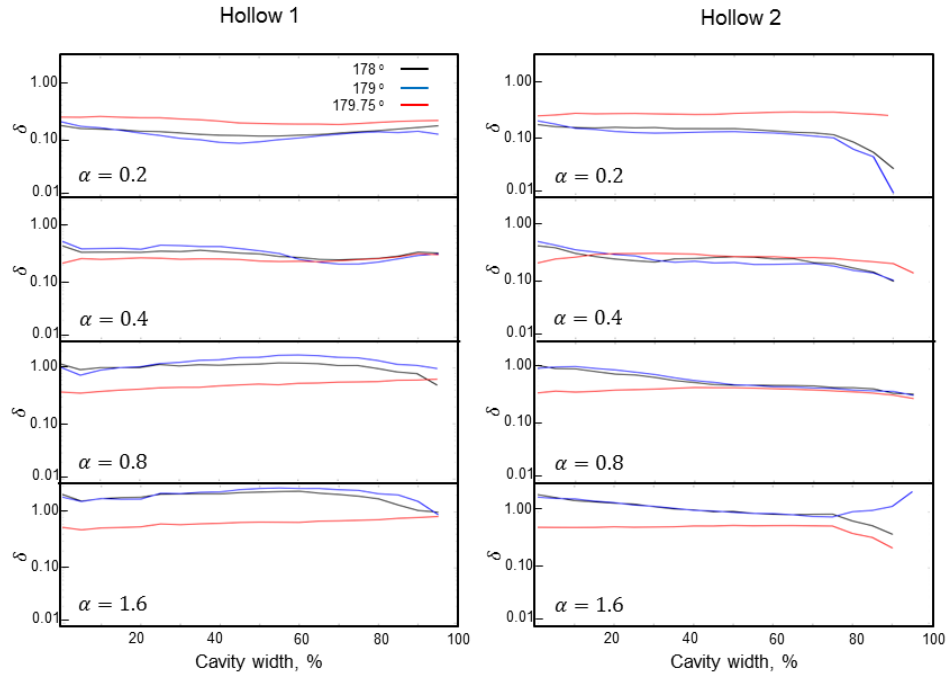


Figure 18: Modelled near backscattering linear depolarisation ratios of two hollow cavity types with varying cavity width and aspect ratio. The left hand side shows results from the hollow 1 particle (pyramidal cavities), whereas the right hand side shows results from the hollow 2 particle (stepped cavities).

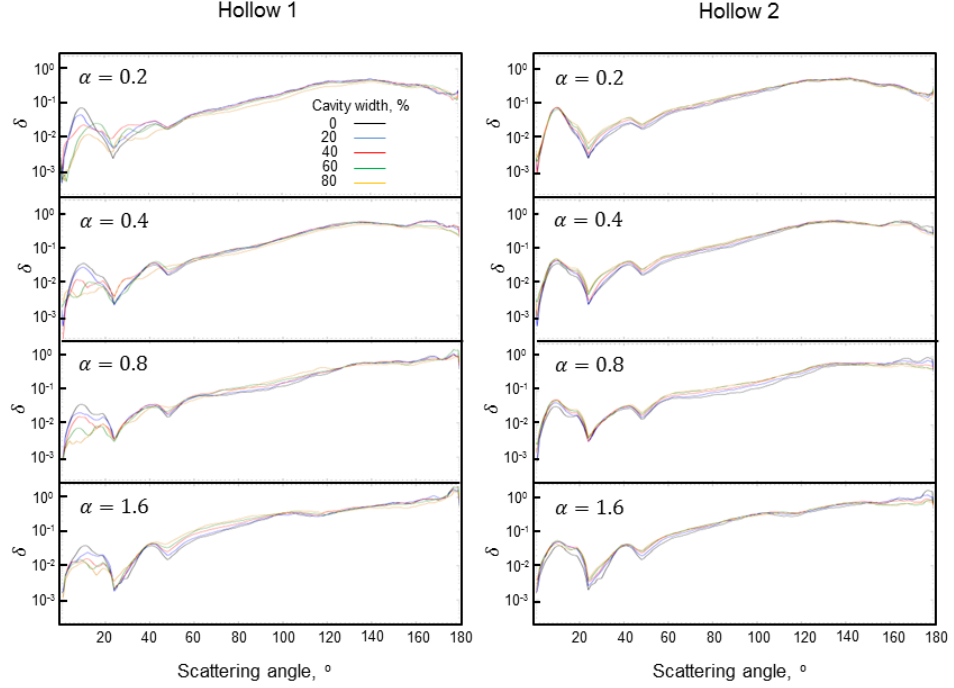


Figure 19: Modelled linear depolarisation ratios for two types of hollow column with varying aspect ratio and cavity depth. The left column shows results from the hollow 1 geometry (pyramidal indentations), and the right column shows results from the hollow 2 geometry (stepped indentations). Different traces represent cavity widths of 0, 20, 40, 60 and 80%.

From figure 18, we see that there is little dependence on the cavity width for the linear depolarisation ratio of hollow 1 particles. On the other hand, hollow 2 particles show a general decrease in linear depolarisation ratio with respect to increasing cavity width. Similarly to simulations investigating the cavity depth, we again see that the forward scattering region (0° – 50°) is affected by the cavity width of the hollow 1 particles, although the same effect is not observed for the hollow 2 particles.

3.2.4. Effect of distortion on linear depolarisation ratio

To approximate the effect of surface roughness, simulations were run with varying values of the distortion parameter, s . The distortion parameter approximates surface roughness by tilting the surface normal for an incoming

ray. The tilt angle is defined by a random number up to a maximum, which is defined by the distortion parameter [40]. However, it has been shown that by using uniformly distributed tilt angles, the angular scattering intensities are poorly modelled. Therefore we use a modified code where the probability distribution function of the tilt angles is described by a Weibull distribution [44, 45]. Similar to previous simulations, the maximum dimension was set to $100\ \mu\text{m}$, the cavity depth was set to 50%, and the cavity width was set to 80%. Simulations were run for aspect ratios of 0.2, 0.4, 0.8 and 1.6. Firstly we investigate the effects of distortion on the linear depolarisation ratios of solid columns, shown in figure 20.

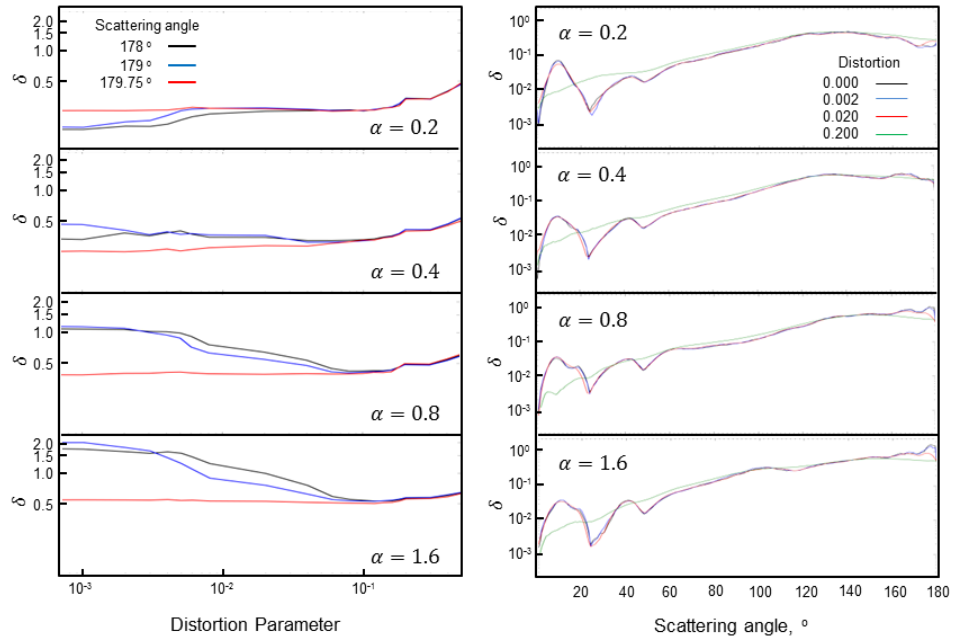


Figure 20: Modelled linear depolarisation ratios for solid columns with varying values of distortion and aspect ratio. The left column shows near backscattering linear depolarisation ratios (178° , 179° and 179.75°) with varying distortion. The right columns shows linear depolarisation ratios in the angular range 0.25° – 179.75° for solid columns with distortion parameters of 0, 0.002, 0.02 and 0.2.

From figure 20 (left), we see that for the weakly depolarising plate-like particles ($\alpha = 0.2, 0.4$), the use of distortion causes a general increasing

trend in the linear depolarisation ratio for near backscattering angles. As the aspect ratio increases, and the prisms become more strongly depolarising ($\alpha = 0.8, 1.6$), we see a general decrease in linear depolarisation ratio for scattering angles 178° and 179° for small values of distortion. For aspect ratios of 0.8 and 1.6, the linear depolarisation ratios at scattering angles 178° and 179° reach a minimum at a distortion parameter of ≈ 0.12 , before increasing again. These minima correspond to maximum decreases in predicted linear depolarisation ratio at near-backscattering angles of 61% and 73% for aspect ratios of 0.8 and 1.6 respectively (compared with simulations with zero distortion).

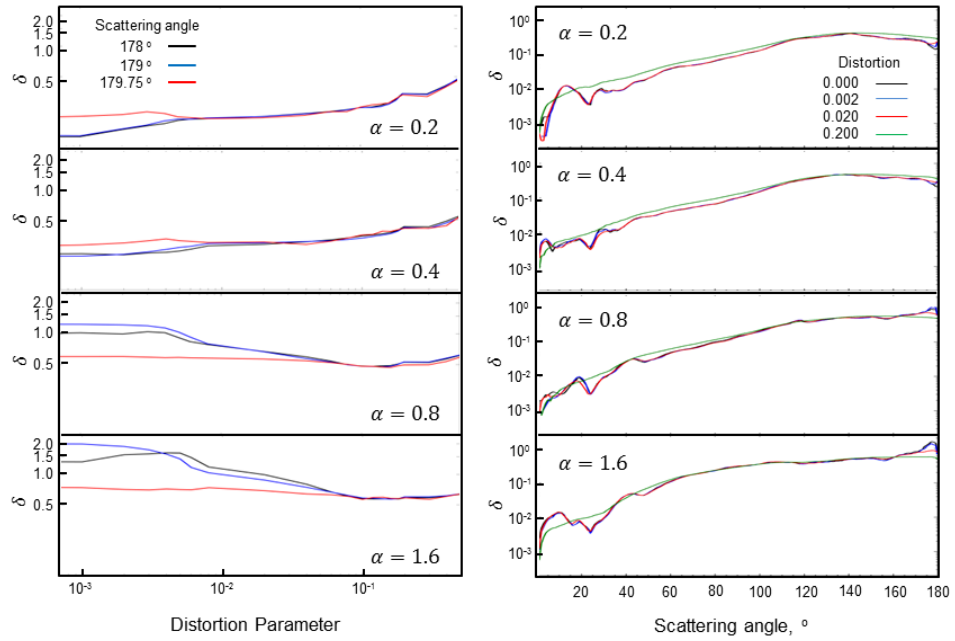


Figure 21: Modelled linear depolarisation ratios for hollow 1 columns with varying values of distortion and aspect ratio. The left column shows near backscattering linear depolarisation ratios (178° , 179° and 179.75°) with varying distortion. The right column shows linear depolarisation ratios in the angular range 0.25° – 179.75° for hollow 1 columns with distortion parameters of 0, 0.002, 0.02 and 0.2.

The same calculations were done for hollow 1 type columns, presented in figure 21. From this we see similar results to those obtained using solid

columns (figure 20). Again, the weakly depolarising particles ($\alpha = 0.2, 0.4$) show a general increasing trend in linear depolarisation with the use of distortion. For the more strongly depolarising particles ($\alpha = 0.8, 1.6$), we again see an initial decrease in the linear depolarisation ratio, reaching minimum values at a distortion parameter of ≈ 0.14 . These minimum values correspond to maximum decreases in predicted linear depolarisation ratio of 60% and 71% for aspect ratios of 0.8 and 1.6 respectively (for near backscattering angles).

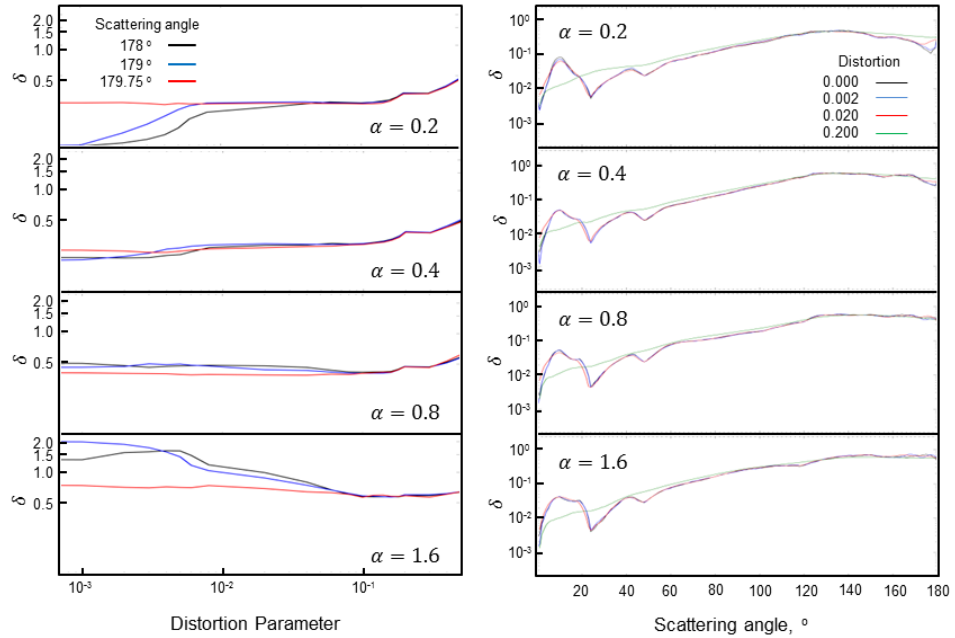


Figure 22: Modelled linear depolarisation ratios for hollow 2 columns with varying values of distortion and aspect ratio. The left column shows near backscattering linear depolarisation ratios (178° , 179° and 179.75°) with varying distortion. The right column shows linear depolarisation ratios in the angular range 0.25° – 179.75° for hollow 2 columns with distortion parameters of 0, 0.002, 0.02 and 0.2.

Figure 22 show the ray tracing calculations for hollow 2 type columns with varying degrees of distortion. Similar to both the solid columns and hollow 1 columns, plate like particles ($\alpha = 0.2, 0.4$) show a general increasing trend in linear depolarisation ratio with the use of distortion. For the more strongly

depolarising particles ($\alpha = 0.8, 1.6$), the use of very small distortion values ($s < 0.005$) causes a initial increase in linear depolarisation ratio. Beyond this, increasing the distortion parameter causes a reduction in the linear depolarisation ratio, down to a minimum value at $s = 0.12$, at which point the linear depolarisation begins to increase. These minimum values correspond to maximum decreases in predicted near-backscattering linear depolarisation ratios of 16% and 17% for aspect ratios 0.8 and 1.6 respectively. Therefore we see that the use of distortion on the hollow 2 column has a weaker impact on the linear depolarisation ratio when compared to solid or hollow 1 columns.

The right-hand columns of figures 20, 21 and 22 shows the linear depolarisation ratios of the three crystal geometries with distortion values of 0, 0.002, 0.02 and 0.2 over the full angular range computed by the ray tracing code. For all three particle types, we see that the use of distortion has a significant effect on forward scattering regions with notable differences seen around the halo regions.

4. Conclusions

Measurements of the linear depolarisation ratio at exact and near backscattering angles were taken for various ice crystal habits. Results are presented here and compared with simulations from Ray Tracing. In general, it is found that modelled results from Ray Tracing over-predict the linear depolarisation ratio when compared to measured results. This is particularly true for the experiments conducted at -7°C where particles had large aspect ratios, and were either solid, or contained pyramidal cavities. On average for this experiment, differences between measured and modelled results were $\approx 120\%$. Section 3.2.4 discusses the use of the distortion parameter to approximate surface roughness. For columnar particles, the use of the distortion parameter can lower the predicted linear depolarisation ratio which may explain, in part, the discrepancies between measured and modelled results.

At -15°C , experimental and modelled results agree well for large plates and sectorised plates observed between 3 and 5 minutes (9), however, for the smaller, pristine plates observed at the end of the experiments, modelled results largely over-predicted linear depolarisation ratio by up to 200%. Unlike the experiments conducted at -7°C , the modelled results cannot be improved with the use of distortion. For plate like particles, the use of the distortion parameter causes an increase in the predicted linear depolarisation ratio (see

figures 20,21 and 22). For such weakly depolarising particles, increasing the complexity of the particle by using distortion will cause linear depolarisation ratio to increase, due to the wave undergoing many more interactions. The discrepancy between measured and modelled results in this case may be due to the rounded particle edges as observed in figure 9, or other complexities not yet represented in the particle model.

For experiments conducted at -30°C , all particles were found to have stepped internal structures, so these were modelled using the ‘hollow 2’ geometry. Again, modelled results over-predicted the linear depolarisation compared to measurements, but average differences were reduced to just 30%. In this experiment, particle habits transition from column-like to plate-like over time. Although distortion could be used to reduce the predicted linear depolarisation ratio of the initial columnar particles, it could not be applied to reduce the linear depolarisation ratio of plate-like particles observed towards the end. Similarly to the -15°C experiments, the discrepancy between measured and modelled results could be explained, in part, by the rounded edges of the particles, both external and internal.

It is known that there are limitations to the geometric optics approach and its applicability for the treatment of polarised scattering has been questioned [46]. This is important for those applying these techniques for the determination of cloud/aerosol properties. Indeed, results from this paper show large differences between measured and modelled results when assuming pristine solid hexagons, and hexagons with pyramidal cavities (figures 8 & 11). However, when the stepped hollow column is assumed, the predictions of linear depolarisation ratio become much more realistic (figure14). Figures 16 and 18 show a general decreasing trend in the linear depolarisation ratio with increasing cavity depth and cavity width, respectively. Although the particle models are based on measurements from crystal replicas, errors in the measurement of cavity depth and width may in part explain the discrepancy between measured and modelled results. This result serves to highlight the sensitivity of the scattering properties on small scale features. Whilst limitations of geometric optics are known, if more accurate scattering models are not applicable for larger and more complex crystal geometries, then geometric optics may be a suitable approximation when the particle geometries are better represented.

In addition to the backscattering region, ray tracing simulations show sensitivities to cavities at smaller scattering angles. In particular, the linear

depolarisation ratio in the 0° – 20° region for a hollow 1 column is significantly lower than for a solid column. This difference is less significant for the hollow 2 column. For the hollow 1 column, the linear depolarisation ratio in the forward scattering region also shows sensitivity to the cavity depth and width as shown in figures 17 and 19. This sensitivity is not evident for the hollow 2 column, which appears more sensitive to changes in the cavity size at near backscattering angles as shown in figures 16 and 18. These dependencies may be used for the development of in situ instrumentation to measure linear depolarisation ratios at not only near backscattering angles, but at smaller angles too.

Although the results presented here focus on particle hollowness, other complexities are known to affect depolarisation, such as surface roughness, particle inclusions, and further deviations which have been observed are currently overlooked [35, 36]. From the formvar images, we can clearly see that many of the particles exhibit rounded edges, this is particularly true for the indentations of the stepped hollow particles 12. This particle rounding is a likely contributor to the low values of linear depolarisation measured in these experiments. Further to the basal cavities presented here, indentations are often observed protruding from the prism facets, although their geometry is currently undetermined. There are also instances of scalene and trigonal particles in several of these experiments, which has also been noted in situ [47, 48]. By incorporating these observed complexities, more physically representative particle models can be created and used to yield more reliable results from ray tracing calculations.

Acknowledgments

This work was funded by a Doctoral Training Grant (DTG) from the Natural Environment Research Council (NERC) in conjunction with a CASE award from Met Office UK. We would also like to acknowledge funding from the NERC ACID-PRUF program, Grant code NE/I020121/1, which supported experiments conducted in the Manchester Ice Cloud Chamber.

References

- [1] IPCC, The Physical Science Basis: Contribution of Working Group 1 to the fifth assessment report of the IPCC, Cambridge University Press, 2013.

- [2] M. Wendisch, P. Pilewskie, J. Pommier, S. Howard, P. Yang, A. J. Heymsfield, C. Schmitt, D. Baumgardner, B. Mayer, Impact of cirrus crystal shape on solar spectral irradiance: A case study for subtropical cirrus, *Journal Of Geophysical Research* 110. doi:10.1029/2004JD005294.
- [3] Y. Zhang, A. Macke, F. Albers, Effect of crystal size spectrum and crystal shape on stratiform cirrus radiative forcing, *Atmospheric Research* 52 (1999) 59–75.
- [4] A. J. Baran, A review of the light scattering properties of cirrus, *Journal of Quantitative Spectroscopy and Radiative Transfer* 110 (14-16) (2009) 1239–1260. doi:10.1016/j.jqsrt.2009.02.026.
- [5] R. P. Lawson, B. A. Baker, P. Zmarzly, D. O’Connor, Q. Mo, J.-F. Gayet, V. Shcherbakov, Microphysical and Optical Properties of Atmospheric Ice Crystals at South Pole Station, *Journal of Applied Meteorology and Climatology* 45 (2006) 1505–1524.
- [6] R. P. Lawson, D. O’Connor, P. Zmarzly, K. Weaver, B. Baker, Q. Mo, H. Jonsson, The 2D-S (stereo) probe: Design and preliminary tests of a new airborne, high-speed, high-resolution particle imaging probe, *Journal of Atmospheric and Oceanic Technology* 23 (1997) (2006) 1462–1477. doi:10.1175/JTECH1927.1.
- [7] D. Baumgardner, H. Jonsson, W. Dawson, D. O’Connor, R. Newton, The cloud, aerosol and precipitation spectrometer: a new instrument for cloud investigations, *Atmospheric Research* 5960 (2001) 251–264. doi:10.1016/S0169-8095(01)00119-3.
- [8] D. P. Grosvenor, T. W. Choularton, T. Lachlan-Cope, M. W. Gallagher, J. Crosier, K. N. Bower, R. S. Ladkin, J. R. Dorsey, In-situ aircraft observations of ice concentrations within clouds over the antarctic peninsula and larsen ice shelf, *Atmospheric Chemistry and Physics* 12 (23) (2012) 11275–11294. doi:10.5194/acp-12-11275-2012.
- [9] M. W. Gallagher, P. J. Connolly, J. Whiteway, D. Figueras-Nieto, M. Flynn, T. W. Choularton, K. N. Bower, C. Cook, R. Busen, J. Hacker, An overview of the microphysical structure of cirrus clouds

Paper 3: Using Laboratory and Field Observations to constrain a single habit shortwave optical parametrization for cirrus

This manuscript is intended to be submitted to Atmospheric Research.

6.1 Summary

The following paper uses laboratory observations from Papers 1 & 2 to apply a new geometric particle model to a radiative parametrization for cirrus cloud. The stepped hollow column (as described in sections 4 and 5) is tested as a single habit model to represent cirrus in a Global Circulation Model (GCM). In order to make the parametrization physically consistent with the microphysical scheme, the particle aspect ratio, α , is varied as a function of maximum particle dimension, D , such that it adheres to the same mass-dimensional, $m(D)$, and area-ratio-dimensional, $A_r(D)$, relationships. The parametrization is implemented into the GA6 configuration of the Met Office Unified Model and results are compared to the current operational model and a more recent habit-mixture model.

6.2 Author contributions

This work was conducted at Met Office under the main supervision of Anthony Baran, with additional supervision from Ann Webb and Paul Connolly. Helen Smith was responsible for the derivation of the aspect ratio-dimensional relationships and the construction of the geometric models used for the parameterizations. Single scattering properties were computed by Helen Smith (Ray Tracing and T-matrix), Anthony Baran (T-matrix) and

Evelyn Hesse (RTDF), and the bulk optical properties were calculated by Helen Smith. The parameterized fits were then found by Anthony Baran, and these were implemented into the GCM by Peter Hill.

The manuscript was prepared by Helen Smith, and all coauthors have contributed to in the drafting process.

Using laboratory and field measurements to constrain a single habit shortwave optical parameterization for cirrus

Helen R Smith^{a,1}, Anthony J Baran^b, Evelyn Hesse^c, Peter G Hill^b, Paul J Connolly^a, Ann Webb^a

^a*The University of Manchester, Oxford Road, Manchester, UK*

^b*Met Office, Exeter, UK*

^c*University of Hertfordshire, College Lane, Hatfield, AL10 9AB*

Abstract

A single habit parameterization for the shortwave optical properties of cirrus is presented. The parameterization utilizes a hollow particle geometry, with stepped internal cavities as identified in laboratory and field studies. This particular habit was chosen as both experimental and theoretical results show that the particle exhibits lower asymmetry parameters when compared to solid crystals of the same aspect ratio. The aspect ratio of the particle was varied as a function of maximum dimension, D , in order to adhere to the same physical relationships assumed in the microphysical scheme in a configuration of the Met Office atmosphere-only global model, concerning particle mass, size and effective density. Single scattering properties were then computed using T-Matrix, Ray Tracing with Diffraction on Facets (RTDF) and Ray Tracing (RT) for small medium and large size parameters respectively. The scattering properties were integrated over 28 Particle Size Distributions as used in the microphysical scheme. The fits were then parameterized as simple functions of Ice Water Content for 6 shortwave bands. The parameterization was implemented into the GA6 configuration of the Met Office unified model along with the current operational longwave parameterization.

Keywords: cirrus, parametrization, climate model

Email address: `helen.smith-8@postgrad.manchester.ac.uk` (Helen R Smith)

1. Introduction

In 2013, the Intergovernmental Panel on Climate Change (IPCC) concluded that the coupling of clouds with the Earth’s atmosphere is the largest uncertainty faced in predicting climate change today [1]. One such cloud type that contributes to this uncertainty is cirrus due to their extensive global coverage of about 30%, with coverage reaching 60–80% in the tropics [2]. Furthermore, cirrus has diverse microphysical properties, containing a multitude of particle habits which range in size over several orders of magnitude. This variety in size, shape and complexity poses many difficulties for the accurate representation of ice cloud in climate models. The range in size means that currently no one method can be used to calculate the single scattering properties of ice crystals, and a variety of scattering models are needed. The range in shape also poses many challenges, and it is well established that the particle habit significantly impacts upon the single scattering properties of ice crystals [3, 4, 5, 6]. The representation of single ice particles for scattering calculations has improved significantly over the years. Early studies used very simplified shapes such as spheres and cylinders, but these were found to be inadequate approximations for the treatment of ice crystals [7]. More realistic representations of particle habits such as bullet rosettes and aggregates have been constructed [8, 9, 10, 6, 11], and are commonly used in habit mixture models to represent cirrus. In addition to particle habit, small scale features such as surface roughness, inclusions and hollowness have gained recognition as potentially important contributors to the scattering behaviour [12, 13, 14] of ice crystals. Theoretical results show that hollow hexagonal crystals exhibit a general increasing trend in the asymmetry parameter, suggesting that hollow crystals reflect less than their solid counterparts [13]. On the contrary, it has been shown that rough particles could reflect up to twice the radiation when compared with pristine crystals [15]. The asymmetry parameter is typically over predicted in scattering models compared with results estimated from in-situ measurements [16, 17]. However, these in-situ results could have been affected by particle shattering on the inlets of the microphysical probes, thereby artificially decreasing the size and asymmetry parameter [18].

To mimic naturally occurring surface roughness, many theoretical studies make use of the distortion parameter, which approximates surface roughness by tilting the facets of the ice crystal in the scattering model [19]. This

method yields smoother phase functions with lower asymmetry parameters than when roughness is not accounted for. Another method used is that of particle inclusions: the incorporation of inclusions into the ice crystal model also smooths peak features such as ‘halos’ and ‘ice bows’, and reduces the asymmetry parameter, yielding more realistic values [20, 21, 22, 10]. For optical parameterizations, many studies make use of a range of particle habits [23, 24, 10], although the distortion parameter is still widely used as a proxy for surface roughness. Other studies suggest that with the use of distortion, ice clouds can be represented entirely by hexagonal prisms of varying aspect ratio, negating the need to represent the full range of crystal habits [25].

Whilst the single scattering properties of cirrus ice particles are affected by micro-scale features, the bulk optical properties of cirrus are also affected by macro-scale properties such as cloud optical depth, ice mass in the cloud column and particle size distribution (PSD). As such, the cirrus net radiative effect is sensitive to the various assumptions made in the microphysical scheme. Typically, in a GCM, the bulk optical properties of clouds are parameterized in terms of the diagnostic variable *effective diameter*, D_e , as a function of the Ice Water Content (IWC) and/or environmental temperature (T) [24, 26]. Effective diameter of the PSD is given by [27]:

$$D_e = \frac{3}{2} \frac{WC}{\rho \sum_i n_i A_i} \quad (1)$$

Where:

WC = Water Content

ρ = density of ice or liquid water

A_i = the mean cross sectional area in bin i

n_i = number concentration in bin i

The use of effective diameter assumes that the bulk-optical properties are uniquely defined by D_e and either IWC and/or T , but it has been shown that they are also dependent upon the shape of the PSD [28, 29]. This dependency is not accounted for in D_e based schemes as they tend to be physically inconsistent with the microphysical scheme [5], consequently the microphysical

and radiative parameterizations may assume different PSDs. Whilst the use of D_e is generally valid for water clouds, the relationship becomes unreliable for ice clouds and for more absorbing wavelengths [30, 29, 28, 11, 5]. Recent parameterizations have bypassed the need for D_e by coupling the optical parameterization directly to the GGM prognostic variable IWC [11]. In order to make the microphysical and optical schemes physically consistent, it has also been argued that particles used in the optical parameterization should adhere to the same mass-dimensional and area ratio-dimensional power laws as assumed in the microphysical scheme [5, 11].

The parameterization presented in this paper (referred to as `hex_cav` from this point forward) uses single hollow hexagonal columns of varying aspect ratios (i.e. ratio of length to radius) to represent cirrus ice crystals across all size ranges as these were commonly observed in recent cloud chamber studies [31]. By varying the aspect ratio, particles are fitted within observed ranges of mass and area-ratio relationships as a function of maximum dimension (defined as the diagonal between the basal faces of the column) in order to satisfy the assumed microphysics power laws assumed in the cloud physics scheme of the Met Office 6.0 configuration. The construction of the particle model is discussed in section 2.1. The single scattering properties are determined using various scattering models for 26 particle sizes across 54 wavelengths in the short-wave only. Single scattering properties were calculated with and without the use of the distortion parameter and therefore `hex_cav` is split into two parameterizations: `hex_cav1` (without distortion) and `hex_cav2` (with distortion), this is further discussed in section 2.3. Bulk optical properties are then found by integrating the single scattering properties over 28 Particle Size Distributions (PSDs) (section 2.4). The bulk properties are used in the GA6 configuration of the Met Office Unified Model along with the current operational long-wave parameterization (section 2.5). The GCM is used to simulate the annual twenty year short-wave fluxes at the top of the atmosphere and the corresponding zonal mean temperatures and specific humidities. Results are compared against the current operational model [32], from here on referred to as `Edwards2007`, and the CERES observations [33, 34]. The `hex_cav2` predicted zonal mean temperatures and specific humidities are compared against the ERA-Interim re-analysis product [35]. Comparisons are also made with the recent Baran (2014) parameterization, from here on referred to as `Baran2014` [11].

2. Methods

2.1. Particle Model

The hollow column used in this parameterization is based upon particles observed during laboratory experiments conducted in the Manchester Ice Cloud Chamber (MICC) [31]. Hollow ice crystals have been observed in many lab and field studies [36, 37, 38]. Images from these experiments show that the hollow columns have cavities which are pyramidal in structure, which have been modelled in theoretical studies [39, 13]. When using a rigorous improved geometric approach, the general effect of these pyramidal cavities was to increase the asymmetry parameter [13]. Laboratory experiments in the MICC found ice crystals grown at -30°C tended to have stepped hexagonal intrusions as seen in figure 1. There was little variation in the geometry of the cavities at this temperature, and no solid columns were observed. Similar structures can be seen from Weickmann’s work which catalogued photographs of ice crystals collected in-situ [40].

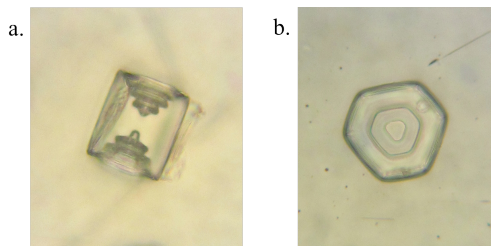


Figure 1: Formvar replicas of typical habits of ice crystals found at -30° in the Manchester Ice cloud chamber. Viewed from a. the prism face, and b. the basal face.

In order to create a particle model based on formvar replicas, similar to the one shown in figure 1, an optical microscope was used to take measurements of the crystal facets, averaged values were then used to create a particle model for use in scattering simulations. The construction of the particle model is shown in figure 2.

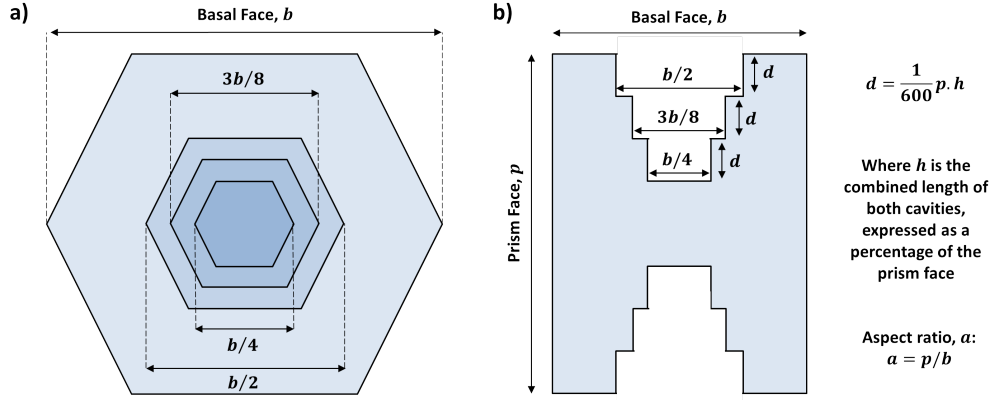


Figure 2: Particle model construction based on average measurements from formvar replicas. Figure a) shows a plan view of the particle from the basal facet, and figure b) shows a cross sectional view of the particle, taken parallel to the prism facet where b and p are the lengths of the basal and prism facets respectively. d is the depth of each cavity, and h is the total combined length of both cavities expressed as a percentage of p .

This particular particle model was chosen for the parameterization because modelled results show that the stepped hollow column causes a reduction in asymmetry parameter compared with a solid column of the same maximum dimension and aspect ratio, in contrast to the pyramidal hollow column which causes a general increase [31]. Therefore, the hollow column model offers a way of obtaining smaller asymmetry parameters other than the use of distortion or by embedding air or aerosol inclusions within the volume of the ice. Figure 3 shows phase functions and asymmetry parameters for the stepped hollow column model, calculated using both RT and RTDF (this latter model takes into account internal diffraction not accounted for by classical geometric optics [41]) at a wavelength of 632nm. The hollow particle model was set up as shown in 2, with basal and prism facets measuring 50 and 100 μm respectively, and a hollowness, h , of 80%. From figure 3 it can be seen that ray tracing over predicts the halo peaks relative to RTDF but predicts the same g values as RTDF. However, in this paper we prefer to apply the most physically appropriate model, which is RTDF.

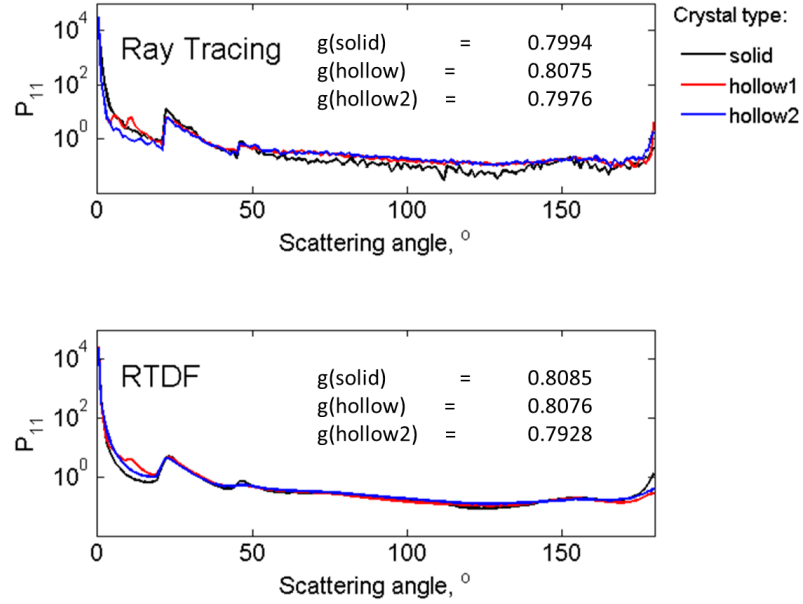


Figure 3: Modelled phase functions of solid and hollow hexagonal columns using Ray Tracing (top) and RTDF (bottom). Hollow 1 is a particle with a pyramidal cavity, whereas hollow 2 is a particle with a stepped internal cavity as shown in figure 2.

To utilize this model in the optical parameterization, the aspect ratio is varied as a function of maximum particle dimension in order to fit within observed mass-dimensional and area ratio-dimensional relationships. In this paper, we define maximum particle dimension, D , as:

$$D = \sqrt{b^2 + p^2} \quad (2)$$

Where:

D = maximum particle dimension

p = dimension of the prism facet

b = dimension of the basal facet

and the aspect ratio α , is defined as:

$$\alpha = p/b \tag{3}$$

2.1.1. Area Ratio-Dimensional Relationships

The area ratio, A_r , is defined as the ratio of the particle’s projected cross-sectional area to the area of a circumscribed circle having a diameter equal to the maximum dimension of the particle.

Observed $A_r(D)$ relationships

Area ratio is a shape sensitive parameter, and is therefore sensitive to particle habit. Consequently, observed $A_r(D)$ laws vary between cloud types. Relationships have been found for various cloud types including mixed-habit cirrus, mixed phase clouds and tropical anvils [42, 43, 44]. For this parameterization, we fit the particles to $A_r(D)$ relationships observed in mixed habit cirrus [42]. This data represents 10 profiles through midlatitude, continental and synoptic cirrus, acquired over 3 field experiments. The combined profile follows the relationship:

$$A_r = 0.18 \times D^{-0.271} \tag{4}$$

Where D is the maximum particle dimension in cm. This relationship is derived from observations in the size range 0.004–0.320 cm, giving area ratios between 0.8 and 0.25.

2.2. Mass-Dimensional Relationships

In addition to $A_r(D)$ relations, the particles used in the parameterization must also adhere to observed mass-dimensional power laws. Cirrus ice crystals are observed to obey the following mass-dimensional relationship [45]:

$$M(D) = (0.026 \pm 0.012)D^2 \tag{5}$$

In the range $D > 70 \mu\text{m}$

Where:

$M(D)$ = mass of the ice particle, kg

In the size range $D \leq 70 \mu\text{m}$, ice particles were found to have a constant effective density, given by:

$$\rho_{ICE} = 700 \pm 135 \text{ kgm}^{-3} \quad (6)$$

Where the effective density of ice, ρ_{ICE} , is defined as the mass of the ice crystal, divided by the volume of a sphere with diameter equal to the maximum particle dimension D .

For the hollow particle model used, equations were derived to characterize the relationships between the aspect ratio, the area ratio (A_r), mass (M) and effective density (ρ_{ICE}). These equations were fitted to the observed relationships as given in equations 4, 5 and 6. Particles could not be fitted exactly to both mass and area ratio relationships, therefore weighted averages are taken in order to fit the particle models within observed ranges. A full derivation is given in Appendix A.

The chosen aspect ratios fit within observed area-ratio and effective density values in the range $D > 70 \mu\text{m}$ as shown in figure 4. The maximum ice effective density that is achievable with the hollow particle model is 384.9 kg m^{-3} , which is below the observed range, and subsequently particles $< 70 \mu\text{m}$ cannot be fitted within observed values.

2.3. Single Scattering Calculations

The single scattering properties for each of the 26 particles were calculated using either T-Matrix, RT or RTDF for 54 wavelengths in the short wave between $0.2 \mu\text{m}$ and $5 \mu\text{m}$. The wavelengths and refractive indices can be found in Appendix B. For intermediate and large size parameters, RTDF

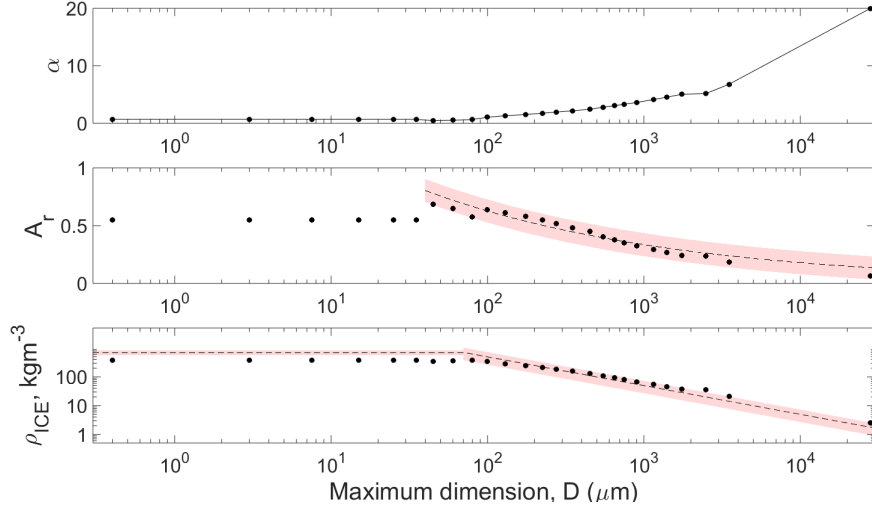


Figure 4: The top graph shows the chosen aspect ratios used for this parametrization. The second graph shows the corresponding area ratios of the chosen particles, and the shaded region shows the observed range. The bottom graph shows the corresponding ice effective density of the chosen particles, and the shaded region shows observed ranges.

of hollow hexagonal columns (as described in section 2.1) was used. In general, the applicable limit of RTDF was found to be $x > 110$, where x is the size parameter defined as $\pi D/\lambda$, where D is the maximum dimension of the particle and λ is the wavelength. However, due to the varying aspect ratio and consequently the change in size of the internal facets, the applicable limits of each scattering model were not well defined. These limits were found by comparing phase function outputs from the three scattering models. At transitional sizes (sizes between small, intermediate and large size parameters), the phase functions were found to be largely similar but below/above these, they were found to deviate. Therefore the limits were defined where the different scattering models showed good agreement. By doing so, the scattering model for each particle size and wavelength was decided on a case by case basis. At smaller size parameters, RT of solid hexagonal prisms was used, and below this, T-Matrix for solid hexagonal columns was used [46]. A chart of the chosen models with respect to particle size and wavelength can be found in Appendix C. For RT and RTDF, each simulation used 5×10^4 particle orientations and 5×10^7 incident rays. For each of the 26 particles, the single scattering properties (asymmetry parameter, single scattering albedo,

extinction cross section and scattering cross section) were calculated for 54 wavelengths in the short-wave ranging from 0.2 μm to 5.0 μm , using complex refractive indices from [47]. These calculations form the basis of the hex_cav1 parameterization.

In order to diminish the 22° halo, the simulations were also run with distortion. Distortion values of 0.1, 0.2, 0.3 and 0.4 were tested for an example column of maximum dimension 100 μm , aspect ratio 2 and wavelength 632 nm (figure 5). A distortion value of 0.4 was found to completely remove the halo feature and therefore a second set of single scattering values were calculated, forming the basis of the hex_cav2 parameterization. This distortion value was chosen as the halo peak is completely removed, therefore producing a featureless phase function similar to those observed in situ [22]. For hex_cav2, the large values of distortion used caused the outgoing ray paths to be significantly deviated. Near the particle edges, this bending of the outgoing ray path can cause outgoing rays to re-enter the space occupied by the crystal. This can cause errors where the ray is not correctly defined as being either in the scattering particle or the host medium, and the particle can no longer be considered a closed system. This issue limits the applicable size range of RTDF.

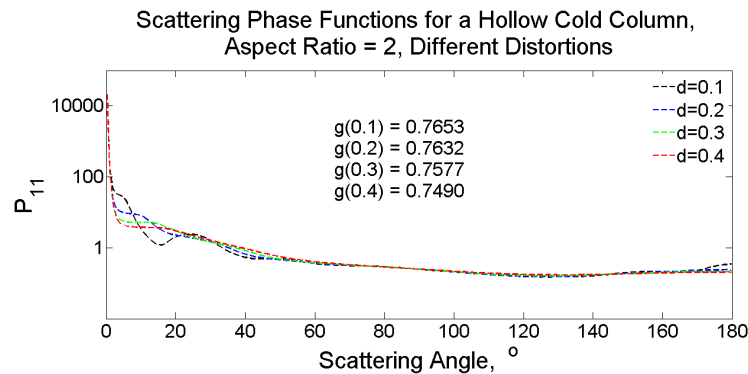


Figure 5: Phase functions of the stepped hollow column, aspect ratio 2, with varying values of distortion. Simulations were run using RTDF, with a wavelength of 635 nm. Halo features are evident for distortion values of 0.1, 0.2 and 0.3, but not for 0.4. Therefore a distortion value of 0.4 was used to remove these features.

2.4. Bulk Scattering Properties

In order to calculate the bulk scattering properties, we use 28 PSDs as parameterized in [48], and used by [11], referred to as Field2007 from this point

forward. This parameterization is based on in-situ measurements of more than 10000 PSDs over temperatures ranging from 0°C to -60°C . Field2007 improves upon earlier parameterizations as it covers a larger and therefore more representative temperature range. Furthermore, the Field2007 parameterization filters out shattered particles by analysis of ice crystal inter-arrival times, thus reducing the bias caused by shattering artefacts which is known to have affected historic PSDs [49]. Generally, bulk optical properties are related to the microphysical scheme through the use of the diagnosed variable, D_e , as discussed in section 1. Instead, we directly couple the bulk optical properties to the prognostic variable IWC.

In order to calculate the bulk scattering properties for each of these PSDs, firstly, the single scattering properties are interpolated onto size bins in each PSD, where the number of size bins in each PSD was 500 and these ranged in size between about $0.4\ \mu\text{m}$ to $28\ 000\ \mu\text{m}$. The single scattering properties at each bin size were then integrated over the PSD, thus finding a weighted average of each property. The scattering and extinction cross sections (β_{sca} and β_{ext} , respectively) are weighted by the mass of cloudy air per unit volume (in units of kg m^{-3}). This yields the mass scattering and mass extinction coefficients (K_{sca} and K_{ext} , respectively), which describe the scattering and extinction cross sections per unit mass of cloudy air. The bulk asymmetry parameter was then found by weighting with respect to scattering cross section. These weightings give bulk optical values consistent with the Met Office Unified Model definitions. In the Met Office global model the bulk scattering and extinction coefficients are represented by the mass scattering and extinction coefficients per unit mass of cloudy air, and so the units are $\text{m}^2 \text{kg}^{-1}$. The values of each of the bulk scattering properties are plotted as a function of wavelength for each of the 28 PSDs, these can be seen in Appendix D.1 and Appendix D.2 for parameterizations `hex_cav1` and `hex_cav2`, respectively. These are used to find parameterized fits for g , K_{ext} , K_{sca} and ω_0 for the 6 short wave bands used in the Met Office configuration 6 atmosphere only model. A table of these fits can be found in Appendix E.

2.5. Implementation in the GCM

The `hex_cav1` and `hex_cav2` short-wave properties are used, assuming the current Edwards et. al, 2007 [32] parameterization applied to the long-wave. This is done so that any changes in the short-wave is entirely attributable to the parametrization presented in this paper. In the climate model runs that follow, the Edwards et. al. 2007 parametrization is used as the control

model [32]. The bulk scattering properties are implemented into the GA6 configuration of the Met Office atmosphere only unified model. This is used to simulate the annual twenty year short-wave fluxes (fluxes averaged over 20 one year intervals) at the top of the atmosphere and the corresponding zonal mean temperatures and specific humidities. Details of the GA6 configuration can be found in [50]. The microphysical and radiation schemes can be found in [51] and [52] respectively.

3. Results

3.1. Comparison of Bulk Scattering Properties

In this section, we compare the bulk scattering properties predicted by the `hex_cav` parameterizations with the Edwards2007 parametrization and the recent Baran2014 parametrization. The Edwards2007 model is an effective diameter based scheme, with D_e as a function of temperature. Both `hex_cav` models and Baran2014 have no temperature dependence so instead we compare bulk scattering properties at set temperatures of 200K, 230K and 270K with respect to ice mass mixing ratio between 1.0×10^{-7} and 1.0×10^{-3} kg kg^{-1} as these ranges are found in the GA6 model. We compare results for short-wave band 1 and band 5 (0.2–32 μm and 1.19–2.38 μm , respectively), therefore contrasting a weakly absorbing band with a more absorbing one.

Mass Extinction Coefficient

Figures 6, 7 and 8 show the mass extinction coefficient for `hex_cav1`, Baran 2014, and Edwards 2007. From these figures we see that the `hex_cav` model has the lowest extinction at all fixed values of temperature for short-wave band 1. Results from short-wave band 5 and from `hex_cav2` were found to be similar, these are not shown for reasons of brevity.

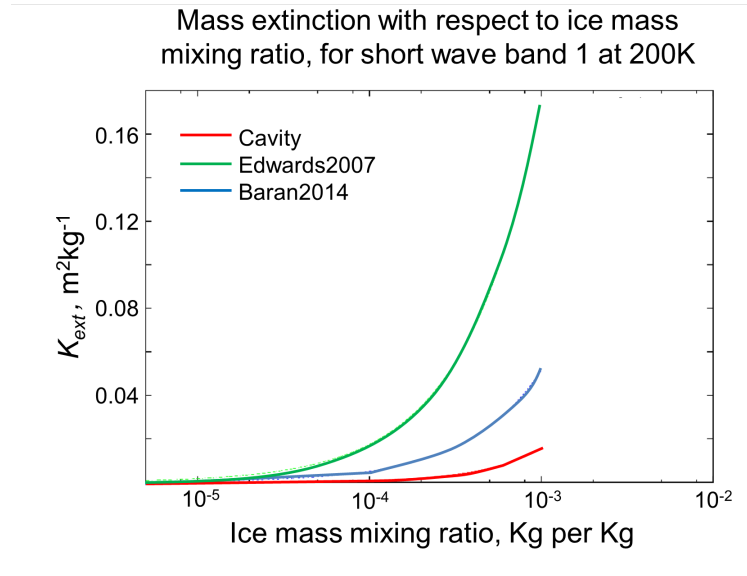


Figure 6: Mass extinction plotted against ice mass mixing ratio as predicted by hex_cav1, Edwards2007 and Baran2014 at a temperature of 200 K.

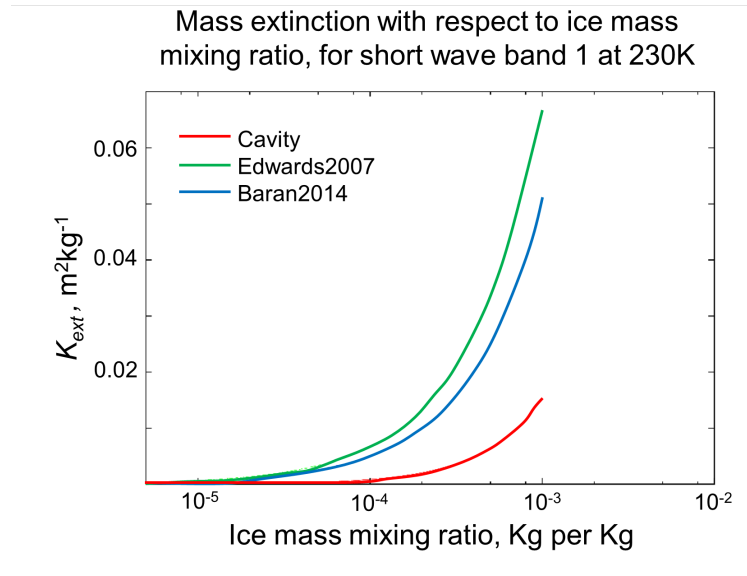


Figure 7: Mass extinction plotted against ice mass mixing ratio as predicted by hex_cav1, Edwards2007 and Baran2014 at a temperature of 230 K.

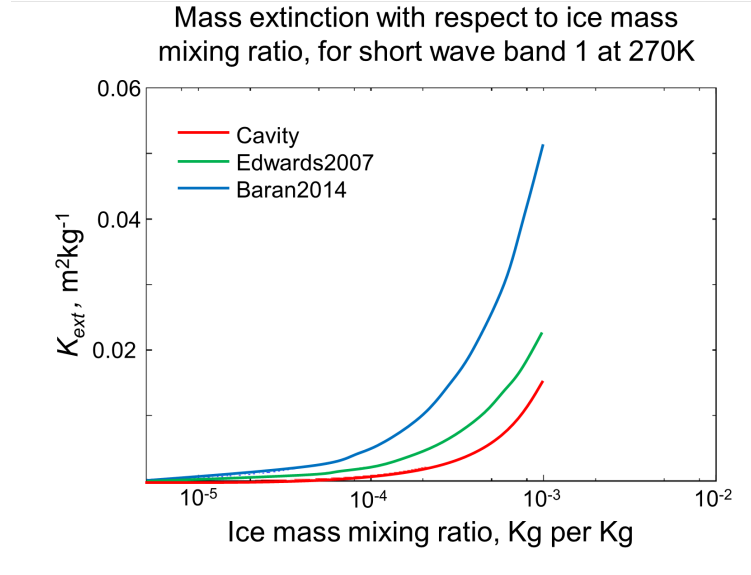


Figure 8: Mass extinction plotted against ice mass mixing ratio as predicted by hex_cav1, Edwards2007 and Baran2014 at a temperature of 270 K.

Asymmetry Parameter

Figures 9 and 10 show asymmetry parameters for Edwards2007, Baran2014, hex_cav1 and hex_cav2 at $T = 200\text{K}$ for short-wave bands 1 and 5, respectively. We see that for the Edwards2007 control model, asymmetry parameter is invariant with respect to ice mass mixing ratio as the aspect ratio of the particle does not change with particle size. However, the asymmetry values for Edwards2007 do vary slightly with temperature, whilst Baran2014 and the hex_cav parameterizations remain constant, as a function of temperature. For the more absorbing case (figure 10), we see that the hex_cav2 parameterization is closest to the fully randomised Baran2014 model. At this band, the asymmetry parameters predicted by Edwards2007 changes significantly as a function of temperature due to the larger (and therefore more absorbing) ice crystals, but still remain invariant with respect to ice mass mixing ratio.

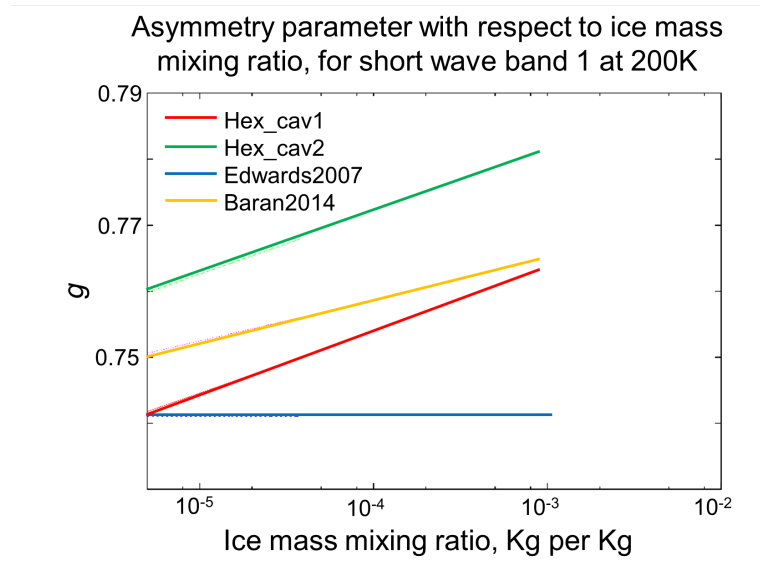


Figure 9: Asymmetry parameter plotted against ice mass mixing ratio for Edwards2007, Baran2014, hex_cav1 and hex_cav2, for short wave band 1 at 200K.

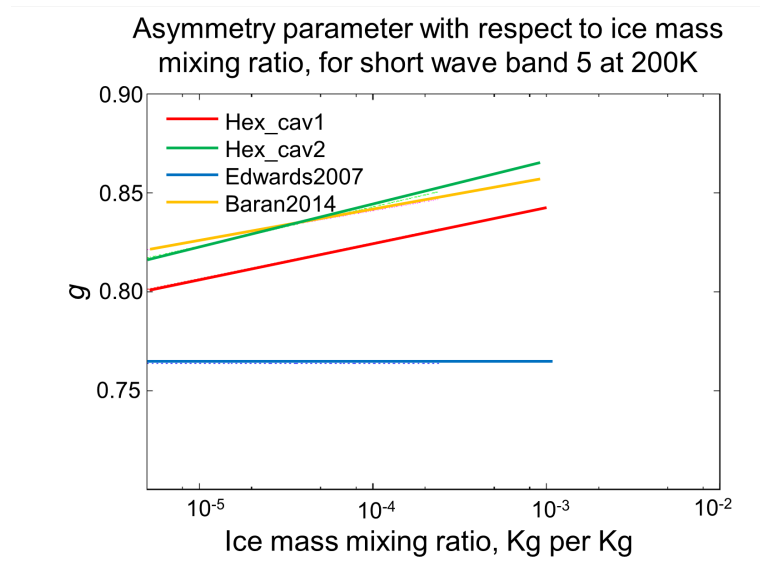


Figure 10: Asymmetry parameter plotted against ice mass mixing ratio for Edwards2007, Baran2014, hex_cav1 and hex_cav2, for short wave band 5 at 200K.

Single Scattering Albedo

Figures 11, 12 and 13 show single scattering albedos for Edwards2007, Baran2014, hex_cav1 and hex_cav2 at temperatures of 200, 230 and 270K respectively. At short-wave band 1, $\omega_0 \approx 1$, so instead we concentrate on the more absorbing short-wave band 5. The Edwards2007 ω_0 values are larger than both the Baran2014 and the hex_cav models. Both hex_cav values of ω_0 increase with ice mass mixing ratio due to the decrease in volume absorption.

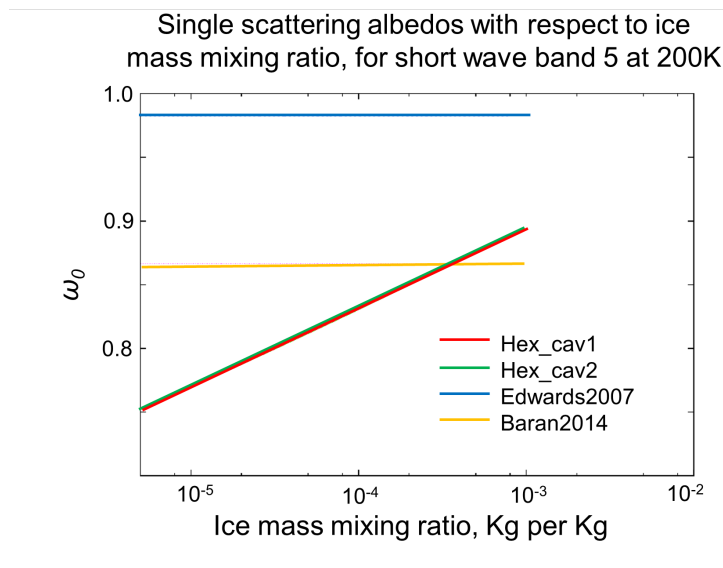


Figure 11: Single scattering albedos plotted against ice mass mixing ratio, as predicted by hex_cav, Edwards2007 and Baran2014 at $T = 200\text{K}$.

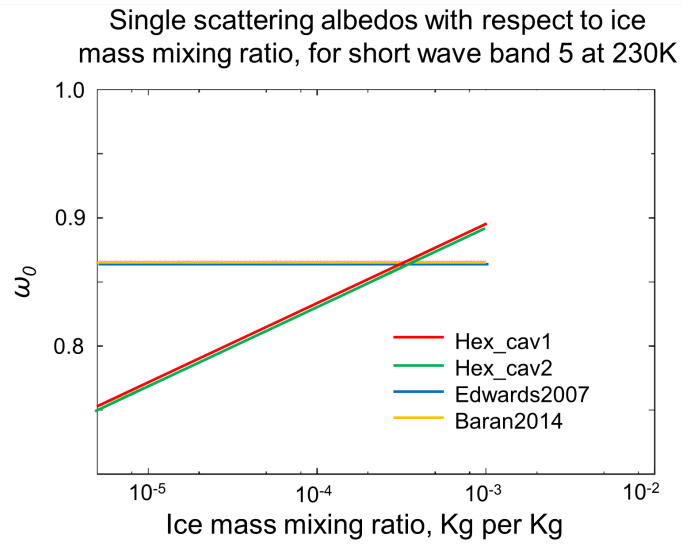


Figure 12: Single scattering albedos plotted against ice mass mixing ratio, as predicted by hex_cav, Edwards2007 and Baran2014 at $T = 230\text{K}$.

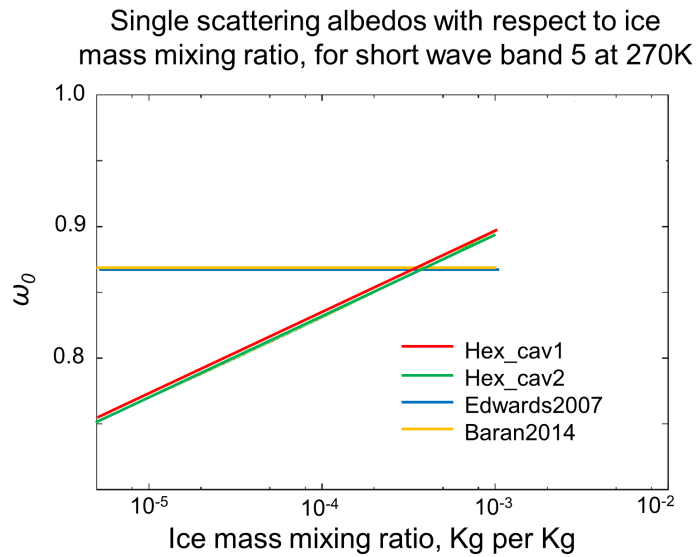


Figure 13: Single scattering albedos plotted against ice mass mixing ratio, as predicted by hex_cav, Edwards2007 and Baran2014 at $T = 270\text{K}$.

3.2. GCM simulations

This section shows results from hex_cav1 and hex_cav 2 from the GA6 configuration of the Met Office unified model, compared with the Edwards2007 control model and CERES observations.

Figures 14 and 15 show the twenty-year averaged annual down-welling and up-welling short-wave flux at top-of-atmosphere (TOA) as predicted by the hex_cav2 parameterization, respectively. The TOA downwelling short-wave flux is defined as the short-wave irradiance that reaches the Earth's surface from the model top of atmosphere (80 km). Differences between the two parameterizations in predicting the downwelling and upwelling fluxes at top-of-atmosphere can be seen in Figures 14b and 15b, respectively. Results from hex_cav1 were found to be similar and are therefore not shown for reasons of brevity. We see differences between the hex_cav parameterization and Edwards2007 are highest around the tropics and the southern ocean. When compared with observations, we see that the control model generally under predicts down-welling flux, except in the southern ocean where it tends to be over predicted. On the contrary, the hex_cav2 parameterization tends to over predict down-welling flux when compared with observations, particularly in the tropics and southern ocean. However, there are regional improvements to be seen in the hex_cav prediction of TOA fluxes. Improvements can be seen over the Atlantic, and parts of the Pacific Ocean. Converse to this, figures 15c and 15d show that the Edwards et al. 2008 and hex_cav2 parameterizations generally over predict and under predict the upwelling short-wave flux at TOA, respectively.

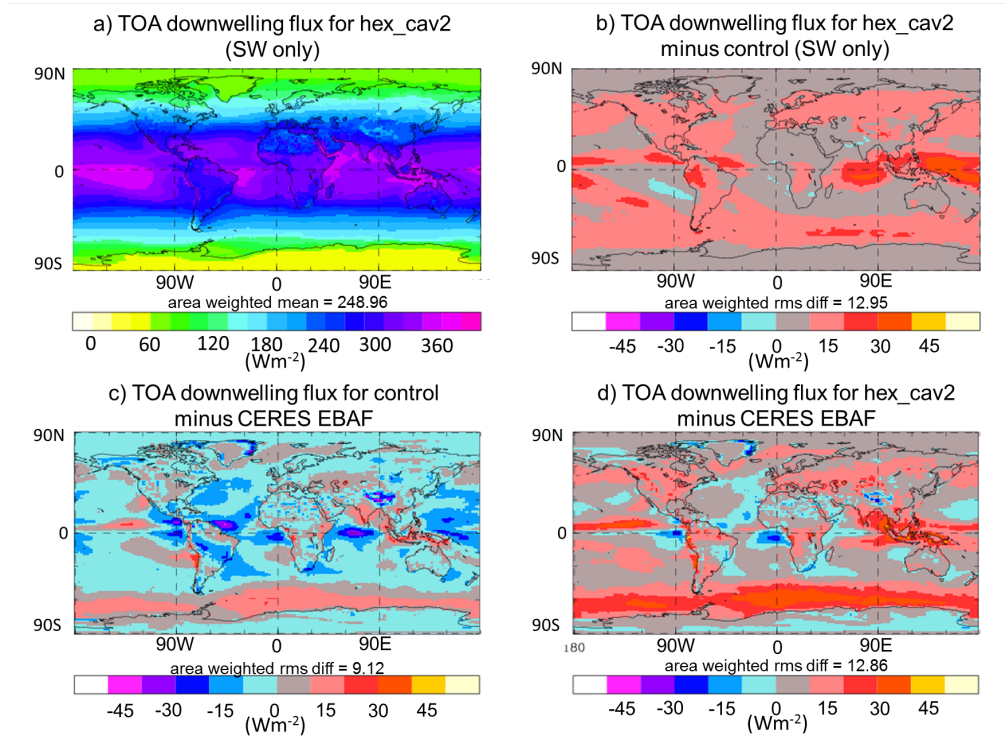


Figure 14: Annual short-wave down-welling flux at top of atmosphere. Clockwise from top left: predictions from hex_cav2, hex_cav2 minus control model, hex_cav2 minus observations, control model minus observations.

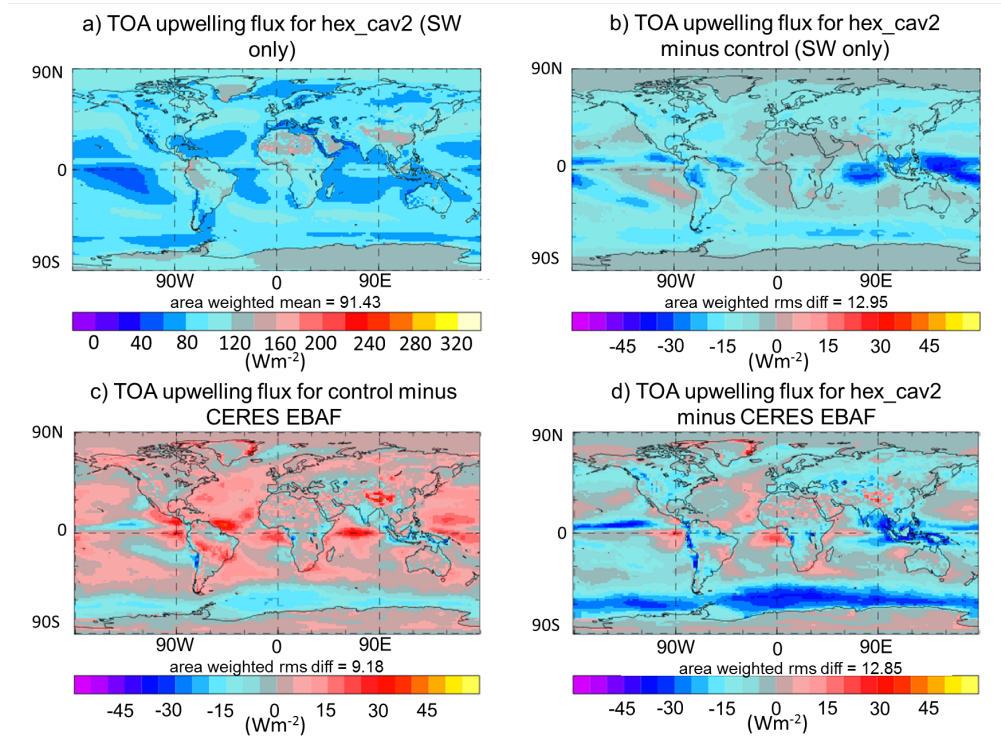


Figure 15: Annual short-wave up-welling flux at top of atmosphere. Clockwise from top left: predictions from hex_cav2, hex_cav2 minus control model, hex_cav2 minus observations, control model minus observations.

Figure 16 shows the zonal mean temperatures predicted by the Edwards et al. (2008) and hex_cav2 parameterizations. From this it can be seen that the under prediction of reflected short-wave flux in the tropics (as seen in figures 14 and 15) leads to the warming of the tropical troposphere by about 1K and cooling of the stratosphere by about 0.5K. Over the North pole this results in a significant reduction in the warming relative to the control model, and over the South Pole there is a reduction in the cooling relative to the control. This warming over the tropics leads to an increase in the specific humidity relative to the control, reducing the dry bias in the upper tropical troposphere (shown in figure 17).

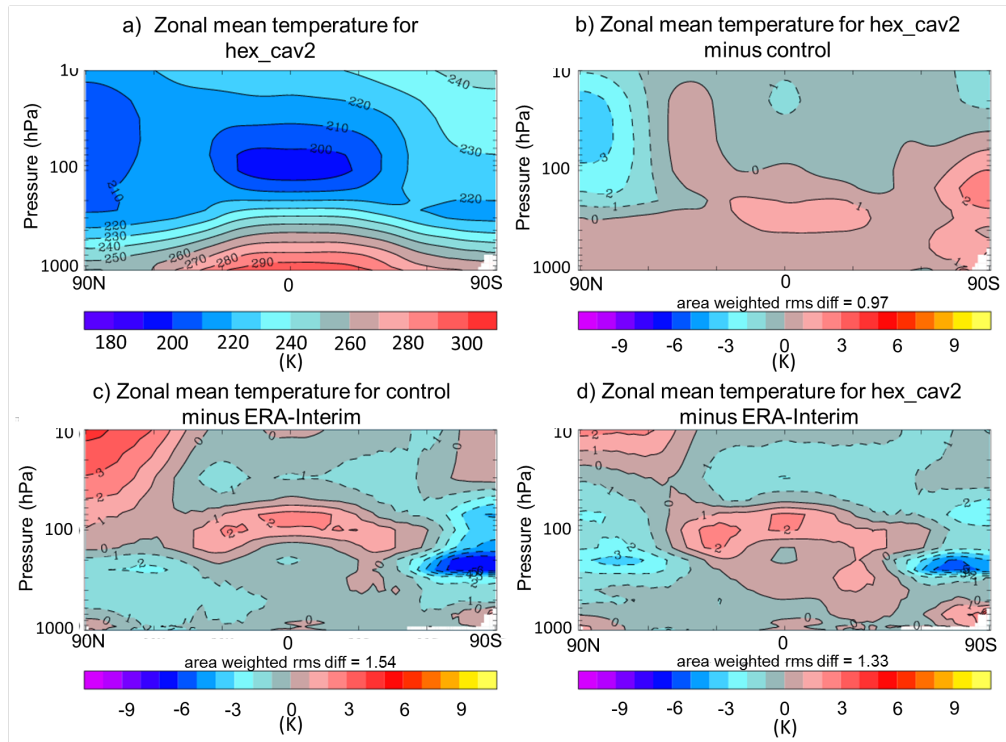


Figure 16: Zonal mean temperatures predicted by the hex_cav2 parameterization. Clock-wise from top left: predictions from hex_cav2, hex_cav2 minus control model, hex_cav2 minus observations, control model minus observations.

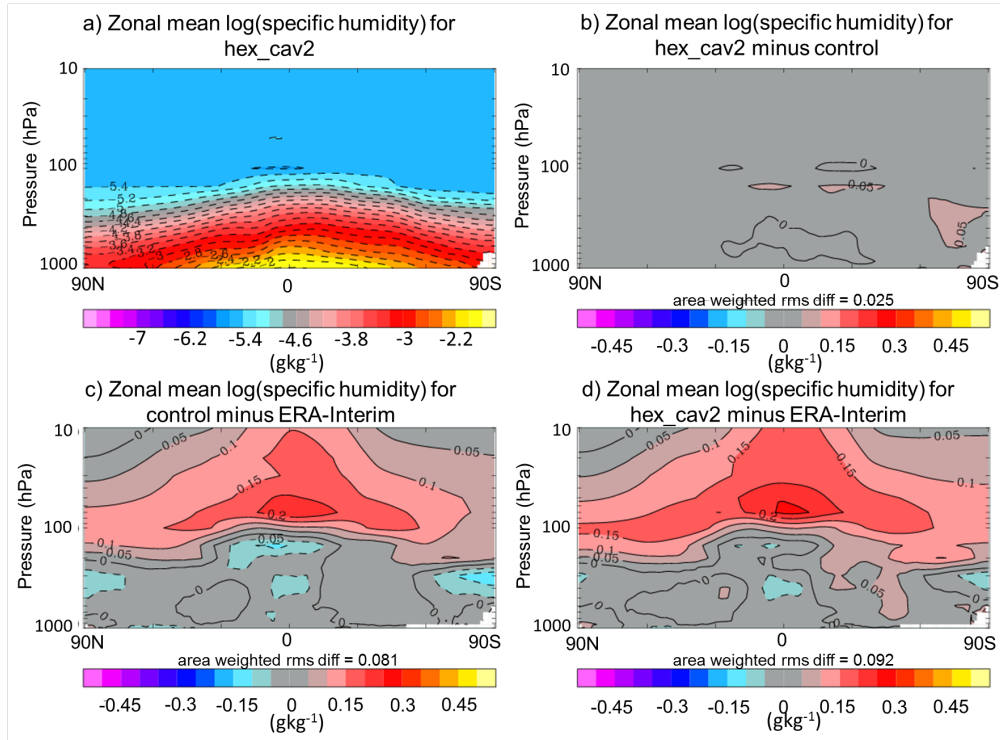


Figure 17: Zonal mean specific humidity predicted by the hex_cav2 parameterization. Clockwise from top left: predictions from hex_cav2, hex_cav2 minus control model, hex_cav2 minus observations, control model minus observations.

4. Conclusions

It has been argued that, to properly model the optical properties of cirrus ice clouds, the individual particle models used must adhere to observed mass-dimensional and area ratio dimensional relationships. By maintaining these relationships, the optical parameterization not only becomes physically consistent with the microphysics scheme (in which these relationships are assumed), but should ensure that the predicted ice mass and projected areas are accurate. In this paper, we have investigated the ability of a single particle geometry (in this case a hollow hexagonal column) to fit within these constraints.

In order to fit a hexagonal prism (whether solid or hollow) to observed area ratios, preferentially oriented particles had to be assumed, as described

in Appendix A. This resulted in very large aspect ratios of up to 20 being assumed. Despite the assumption of preferential orientation for the selection of particle aspect ratio, single scattering properties were found using randomly oriented particles, as required by the GCM. In comparison to preferential orientation, the projected area in random orientation is reduced, which is particularly significant for larger aspect ratios. Therefore the use of such large, and unrealistic aspect ratios caused much lower predictions of mass extinction coefficient compared with other parameterizations, as shown in figures 6, 7 and 8. Although the use of the hollow particle model reduced the asymmetry parameter compared with an equivalent solid model, this reduction in asymmetry parameter was eclipsed by the very small mass extinction values. Therefore, more short-wave radiation will be transmitted to Earth, which is evident in figures 14 and 15, where we can see that hex_cav2 underpredicts the reflected short-wave radiation at TOA. The effect of this is to warm the tropical troposphere (figure 16). This highlights the sensitivity of the climate to small changes in the microphysical properties of ice clouds and it is therefore pivotal to construct parameterizations that are microphysically consistent. Furthermore, it is crucial to evaluate microphysical properties of cirrus and the single scattering properties of individual ice particles.

Overall, the predictions of TOA short wave flux, zonal mean temperature and zonal mean specific humidity differ from observations more so than than the current operational model. However, there are regional improvements that can be seen. For upwelling and downwelling flux, improvements on the current model are seen over the North Atlantic, Indian and much of the Pacific Ocean. For both the zonal mean temperature and zonal mean specific humidity, although biases in the tropical tropopause are increased, biases in the polar regions are decreased. These regional improvements may correspond to areas containing smaller particles, and therefore the larger particles have had little influence on the region. Alternatively, it is known that the orientation of ice crystals in the atmosphere is not fully randomized [53]. Factors such as gravitational sedimentation can cause preferential orientation of ice crystals, particularly for $\alpha \ll 1$ or $\alpha \gg 1$ [54]. In convective systems, electric fields can also cause preferential alignment [55]. In these cases, the projected area, and hence mass extinction of the ice crystals would be larger than for randomly oriented particles. Therefore the assumption of random orientation in the GCM may lead to larger biases in regions where orientation is not negligible. In figures 15 and 14 we see that the largest biases in hex_cav2 occur in the southern ocean and over tropical Asia. The derivation

of the area-ratio dimensional relationship is based on data collected in situ via cloud probes. These data are also orientation dependent, and may be affected by particle orientation in the sample volume. Data from a variety of cirrus are used to generate a globally averaged relationship, which may be more representative of certain regions compared with others.

The results suggest that a single hexagonal prism cannot be used to approximate ice of all sizes. As seen in figure 4, the particle could not be fitted to the high values of ice effective density as observed for smaller particles. In order to conserve the ice mass for such particles, quasi-spherical particles might be a better approximation [56], allowing for higher area ratios to be achieved. As for large particles, the use of very elongated hexagonal prisms leads to under-predictions in orientation-averaged projected area. These particles may be better represented by spatial aggregate models, which can achieve the low values of area ratio required, but are less sensitive to particle orientation. The stepped hollow particle may be incorporated into such a habit mixture model as it has been observed in both field and lab studies [40]. In laboratory studies, clouds below -25° are found to contain almost exclusively stepped hollow particles. Therefore, it is likely that such structures occur frequently in cirrus ice cloud, however the internal structures are often unseen with current measurement techniques. In laboratory studies, such structures are only observed at lower temperatures with particle aspect ratios close to unity, rarely exceeding $\alpha = 3$. Consequently, the elongated particles used in `hex_cav` are unlikely to be physically representative of large ice crystals. They may however be physically representative of small ice particles and could in future be incorporated into parameterizations based on habit mixtures.

In current habit mixture models, perturbations from the pristine form are often treated with the use of distortion as a proxy for surface roughness, or by the use of inclusions. Whilst these methods may yield values of scattered intensity close to observations, they may overlook other properties of the scattered light. Measurements from the A-train now provide us with polarization measurements from ice cloud, and it has been shown that particles with similar phase functions may differ significantly with respect to degree of linear polarisation [57, 58, 59]. It has also been shown in laboratory studies that hollow particles are more weakly depolarizing compared with solid crystals [60]. In this case, roughness proxies may not be representative of various micro-scale features such as cavities, inclusions, and real surface roughness.

Appendix A. Derivation of aspect ratio equations

Fitting the model to observed $A_r(D)$ relationships

Appendix A.0.1. Randomly Oriented Particles

For a solid convex particle, the average projected cross section is given by $S/4$. Where S is the particle surface area. Although the hollow particle is concave, the projected area is not influenced by the concavities, and therefore the same equation can be applied. For a randomly oriented hexagonal prism, the average projected area is given by:

$$A_{average} = \frac{D^2(12\alpha + 3\sqrt{3})}{16(1 + \alpha^2)} \quad (\text{A.1})$$

and the area ratio is given by:

$$A_{r_average} = \frac{12\alpha + 3\sqrt{3}}{4\pi(1 + \alpha^2)} \quad (\text{A.2})$$

Appendix A.0.2. Preferentially Oriented Particles

In reality, elongated ice particles tend to fall preferentially with their largest projection perpendicular to the direction of propagation [61, 62], although vertically aligned prism facets have also been observed [63]. As such, columns fall preferentially with their prism facet parallel to the ground, whereas plates fall preferentially with their basal facet parallel to the ground.

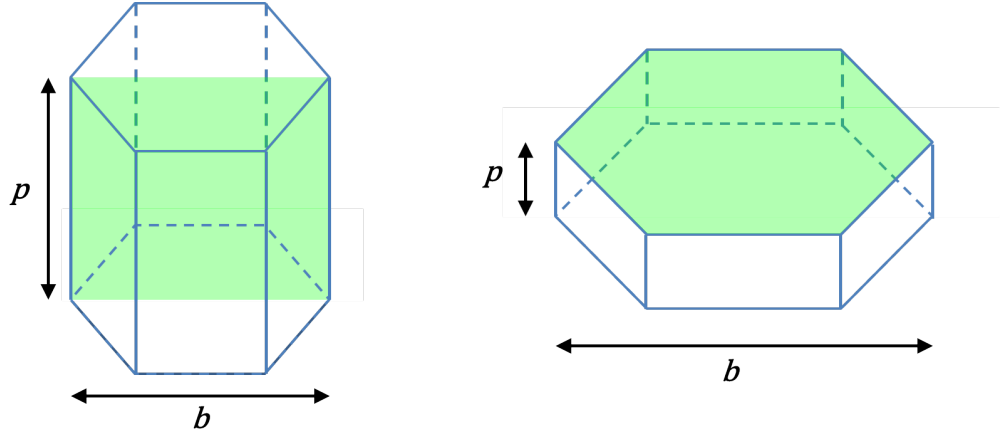


Figure A.18: Projected area of a hexagonal prism when oriented like a column (left) and a plate (right). Green shaded areas represent projected cross sections.

For column-oriented particles, the projected cross section is given by:

$$A_{column} = \frac{D^2 \alpha}{1 + \alpha^2} \quad (\text{A.3})$$

and the area ratio is given by:

$$A_{r_column} = \frac{4\alpha}{\pi(1 + \alpha^2)} \quad (\text{A.4})$$

For plate-oriented particles, the projected cross section is given by:

$$A_{plate} = \frac{3\sqrt{3}}{8} \times \frac{D^2}{(1 + \alpha^2)} \quad (\text{A.5})$$

and the area ratio is given by:

$$A_{r_plate} = \frac{3\sqrt{3}}{2\pi(1 + \alpha^2)} \quad (\text{A.6})$$

The area ratios for preferential and random orientations are plotted against aspect ratio in figure A.19.

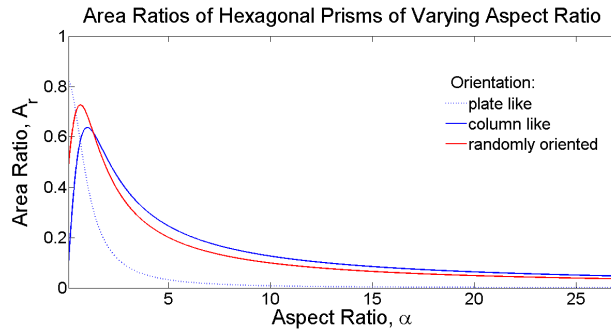


Figure A.19: Area ratio plotted against aspect for randomly oriented and preferentially oriented hexagonal columns.

By assuming a randomly oriented particle, the maximum area ratio for a hexagonal column is 0.7271. However, observed $A_r(D)$ relationships exceed this, with a maximum value of 0.8. In order to achieve this value, we must assume oriented plates. Therefore the two orientation specific relationships are used rather than the randomly oriented one.

If we extend the $A_r(D)$ relation to cover the full size range used in this parameterization (0.4-28127 μm) we get a range of values of A_r from 2.8–0.1360. Physically, the area ratio for a hexagonal column cannot exceed 0.8270, and therefore this observational relationship cannot be extrapolated to smaller particles. As D tend to infinity, A_r tends asymptotically towards 0. So in theory, the relationship can be extrapolated to larger sizes.

For plate-oriented prisms, we can equate equations A.6 and 4 to get:

$$\alpha = \sqrt{4.59D^{0.271} - 1} \quad (\text{A.7})$$

For column-oriented prisms we equate equations A.4 and 4 to get:

$$\alpha = \frac{1 + \sqrt{1 - 4(0.045\pi D^{-0.271})^2}}{0.09\pi D^{-0.271}} \quad (\text{A.8})$$

Below $D = 100 \mu\text{m}$, equation A.8 does not yield real results, and therefore all particles $< 100 \mu\text{m}$ are assumed to be oriented plates.

Appendix A.1. Fitting the particles to $M(D)$ relationships

For the hollow column used in this parameterization, the mass is given by:

$$M(D) = \rho \frac{3\sqrt{3}}{8} \left(1 - \frac{29h}{19200}\right) \alpha(1 + \alpha^2)^{-3/2} D^3 \quad (\text{A.9})$$

Where:

M = particle mass, kg

ρ = density of ice, kgm^{-3}

h = hollowness described as the combined length of both cavities, expressed as a percentage of the length of prism facet, p

Varying the hollowness caused little difference in the particle mass, and therefore a constant hollowness of 80% was assumed, as commonly observed in cloud chamber investigations [31]. In order to fit the hollow particle to observed mass-dimensional relationships, we equate equations 5 and A.9 to get:

$$D = 4.91 \times 10^{-5} \times \frac{1}{\alpha} (1 + \alpha^2)^{3/2} \quad (\text{A.10})$$

The relationship between α and D is approximated by a 10th degree polynomial:

$$\alpha = \sum_{n=0}^{10} c_n D^n \quad (\text{A.11})$$

Where c_n are the polynomial coefficients, given in table A.1.

n	c_n
10	-2.15×10^{18}
9	4.97×10^{17}
8	-4.93×10^{16}
7	2.75×10^{15}
6	-9.45×10^{13}
5	2.07×10^{12}
4	-2.9×10^{10}
3	2.53×10^8
2	-1.33×10^6
1	4820
0	0.45702

Table A.1: Coefficients of D^n for equation A.11.

Equations A.7 and A.8 relate the aspect ratio and the maximum dimension of the hollow column in order to adhere to observed area ratio-dimensional relationships, whilst equation A.11 relates aspect ratio and maximum dimension in order to obey observed mass-dimensional power laws. These equations are not in agreement and therefore the aspect ratio cannot be fitted exactly to both observed relationships. Instead, we take a weighted average in order to fit the values within observed ranges. It was found that a 50:50 weighting gave the best agreement for sizes $>70 \mu\text{m}$. In the size range $40\text{--}70 \mu\text{m}$, a 65:35 weighting was used ($M(D):A_r(D)$). These weightings were chosen as they produced the most amount of crystals within the observed ranges of $M(D)$ and $A_r(D)$. For particles below $40 \mu\text{m}$, there is no established $A_r(D)$ relationship and so particles are fitted using only the $M(D)$ relationship.

These equations were used to find the aspect ratios of 26 particles ranging in size from 0.4 to $28\,127 \mu\text{m}$, given in table A.2.

Maximum Dimension, $D / \mu\text{m}$	Aspect Ratio, α
0.4	0.7070
3.0	0.7070
7.5	0.7070
15	0.7070
25	0.7070
35	0.7070
45	0.4546
60	0.5294
80	0.6626
100	1.0585
130	1.3235
175	1.5361
225	1.7582
275	1.9540
350	2.1834
450	2.5289
550	2.8103
650	3.0682
750	3.3072
900	3.6362
1150	4.1212
1400	4.5433
1750	5.0525
2500	5.9192
3500	6.7936
28127	20.0000

Table A.2: Aspect ratios and maximum dimensions of the 26 particles used in the `hex_cav` parametrizations. For particles $\leq 80\mu\text{m}$, plate orientation is assumed, for particles $\geq 80\mu\text{m}$, column orientation is assumed.

Appendix B. Wavelengths and Refractive Indices

Wavelength, μm	Refractive Index	
	Real	Imaginary
0.2000	1.392800	5.56713×10^{-11}

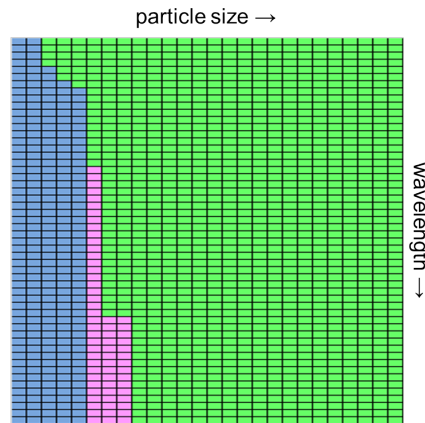
0.2250	1.365500	2.00000×10^{-11}
0.2750	1.342400	2.00000×10^{-11}
0.3500	1.324900	2.00000×10^{-11}
0.4250	1.317400	3.63700×10^{-10}
0.5506	1.311000	2.28900×10^{-09}
0.6500	1.307900	1.54500×10^{-08}
0.8700	1.303800	2.40000×10^{-07}
0.9500	1.302300	6.02000×10^{-07}
1.5000	1.300700	2.17000×10^{-06}
1.1500	1.299000	2.29000×10^{-06}
1.2500	1.297100	1.29000×10^{-05}
1.3500	1.295100	1.39000×10^{-05}
1.4500	1.292700	2.09989×10^{-04}
1.5750	1.290000	3.48150×10^{-04}
1.7250	1.285500	1.68527×10^{-04}
1.8500	1.280700	1.33900×10^{-04}
1.9250	1.277000	7.40456×10^{-04}
1.9750	1.275300	1.52800×10^{-03}
2.0500	1.272400	1.37261×10^{-03}
2.1500	1.266300	4.02500×10^{-04}
2.2500	1.258200	2.03500×10^{-04}
2.3500	1.248200	4.59100×10^{-04}
2.5000	1.227000	7.53000×10^{-04}
2.6500	1.187900	1.08640×10^{-03}
2.7500	1.130600	6.63631×10^{-03}
2.8120	1.065700	3.24500×10^{-02}
2.8380	1.038600	5.05150×10^{-02}
2.8620	1.004500	8.07060×10^{-02}
2.8880	0.968194	0.135300
2.9630	0.999010	0.338455
2.9870	1.020340	0.393300
3.0130	1.057470	0.467790
3.0370	1.125900	0.554000
3.0620	1.232660	0.614721

3.0880	1.380050	0.606245
3.1120	1.482150	0.547166
3.1380	1.633600	0.372000
3.1620	1.609840	0.413616
3.1880	1.642780	0.323409
3.2250	1.633010	0.215358
3.2750	1.640800	0.158000
3.3500	1.536070	6.34018×10^{-02}
3.4500	1.476900	2.61700×10^{-02}
3.5500	1.435780	1.19682×10^{-02}
3.6500	1.409200	7.75963×10^{-03}
3.7750	1.385000	6.96600×10^{-03}
3.9250	1.368700	9.68000×10^{-03}
4.1000	1.352600	1.47100×10^{-02}
4.3000	1.343000	2.13900×10^{-02}
4.5000	1.344000	3.17900×10^{-02}
4.7000	1.347280	2.04653×10^{-02}
4.9000	1.337900	1.34700×10^{-02}
5.0000	1.332500	1.24000×10^{-02}

Table B.3: wavelengths and refractive indices used for single scattering calculations

Appendix C. Scattering Models used

a) Scattering Models for hex_cav1



b) Scattering Models for hex_cav2

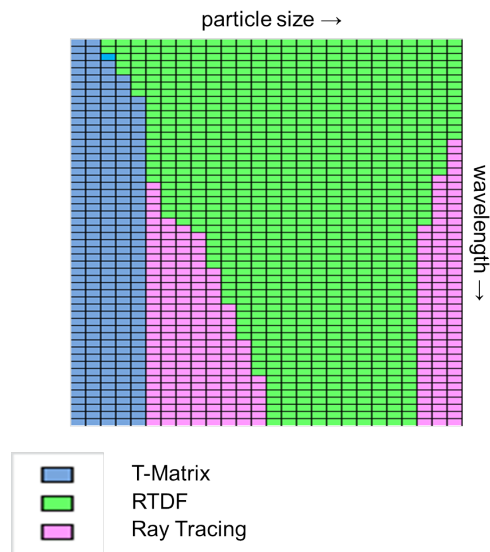


Figure C.20: Scattering models used for differing values of wavelength and particle size, for parametrizations hex_cav1 and hex_cav2. Particle size increases from left to right, numeric values can be found in table A.2. Wavelength increases from top to bottom, numeric values can be found in table B.3.

Appendix D. Bulk optical properties

Appendix D.1. Bulk properties for *hex_cav1*

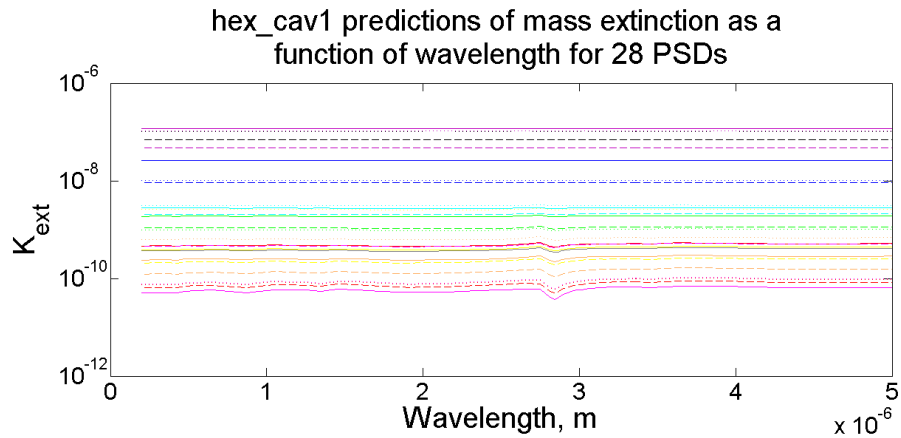


Figure D.21: Bulk K_{ext} values calculated using the *hex_cav1* parameterization. Each trace represents a different PSD from Field2007.

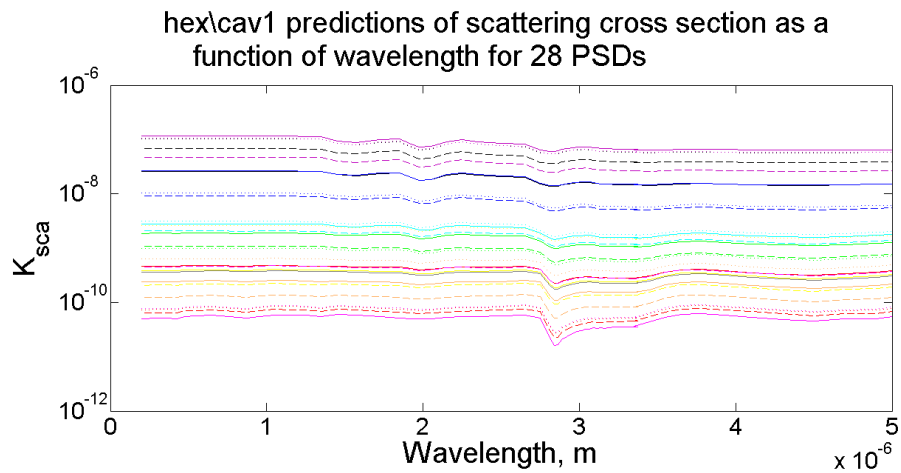


Figure D.22: Bulk K_{sca} values calculated using the *hex_cav1* parameterization. Each trace represents a different PSD from Field2007.

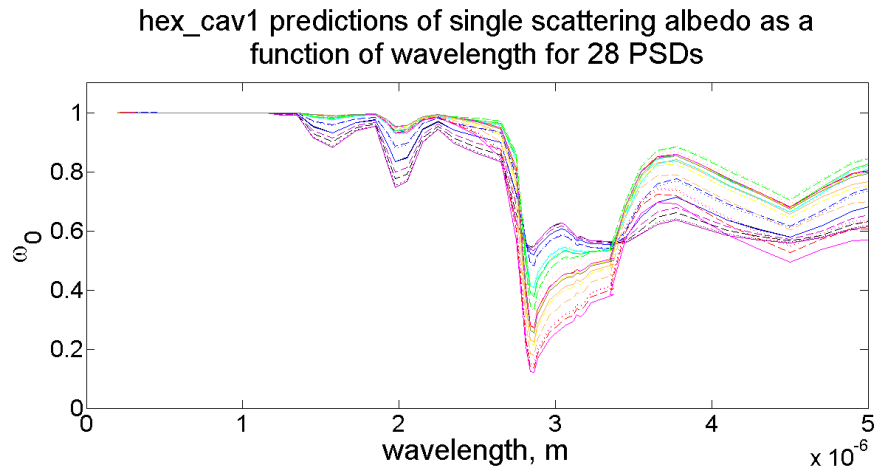


Figure D.23: Bulk ω_0 values calculated using the hex_cav1 parameterization. Each trace represents a different PSD from Field2007.

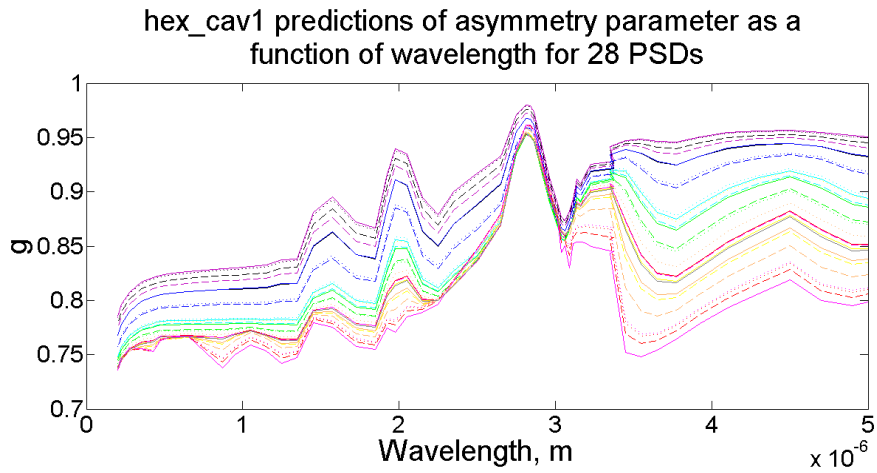


Figure D.24: Bulk g values calculated using the hex_cav1 parameterization. Each trace represents a different PSD from Field2007.

Appendix D.2. Bulk properties for *hex_cav2*

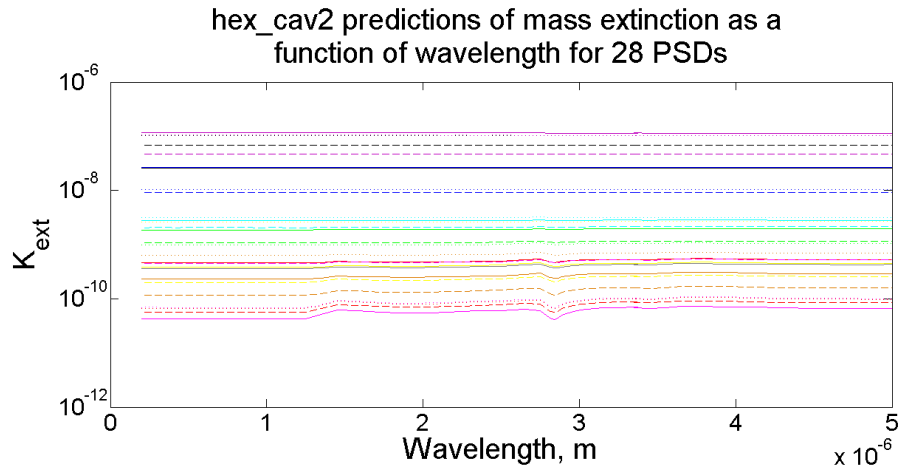


Figure D.25: Bulk K_{ext} values calculated using the *hex_cav2* parameterization. Each trace represents a different PSD from Field2007.

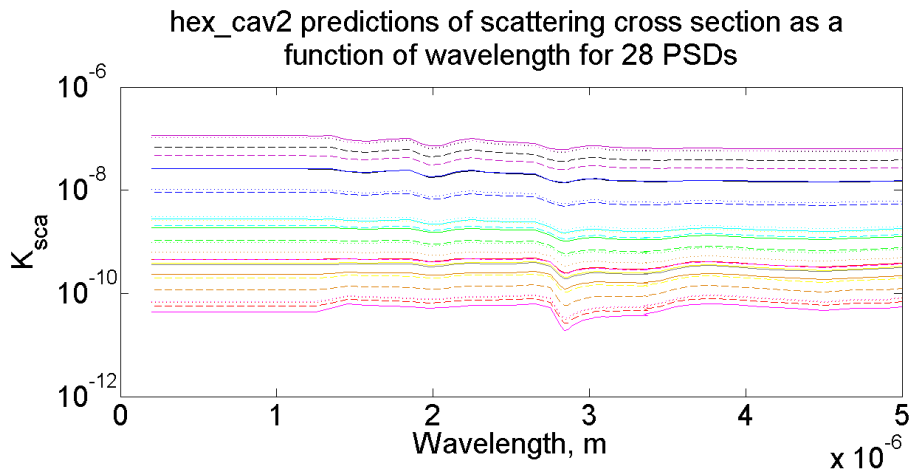


Figure D.26: Bulk K_{sca} values calculated using the *hex_cav2* parameterization. Each trace represents a different PSD from Field2007.

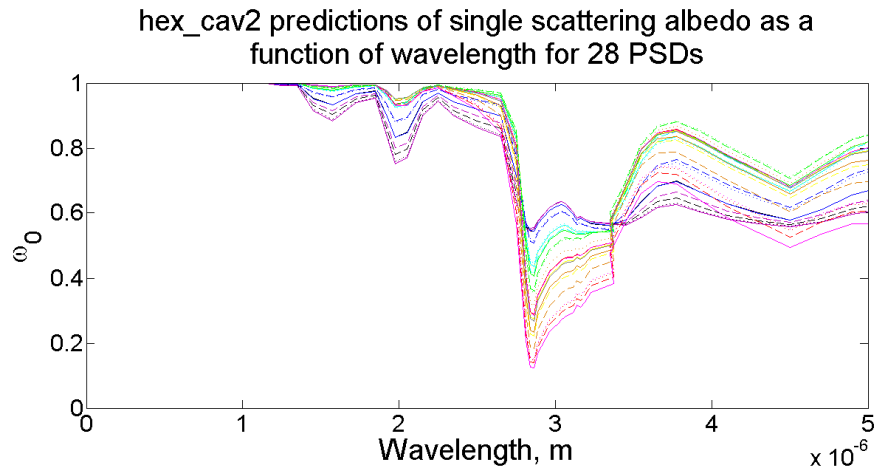


Figure D.27: Bulk ω_0 values calculated using the hex_cav2 parameterization. Each trace represents a different PSD from Field2007.

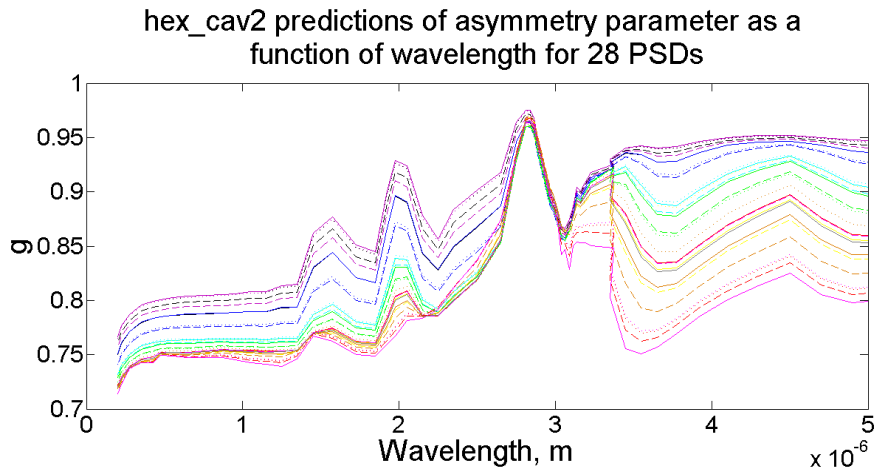


Figure D.28: Bulk g values calculated using the hex_cav2 parameterization. Each trace represents a different PSD from Field2007.

Appendix E. Parametrized fits

Wavelength, m	K_{ext}	K_{sca}	g
2.0×10^{-07} – 3.2×10^{-07}	$92.4557 \times q_i^{1.25807}$	$92.4557 \times q_i^{1.25807}$	$0.809881 \times q_i^{5.22739 \times 10^{-03}}$
3.2×10^{-07} – 5.05×10^{-07}	$92.7110 \times q_i^{1.25847}$	$92.7111 \times q_i^{1.25847}$	$0.841690 \times q_i^{6.38061 \times 10^{-03}}$
5.05×10^{-07} – 6.90×10^{-07}	$92.3745 \times q_i^{1.25793}$	$92.3761 \times q_i^{1.25794}$	$0.844428 \times q_i^{6.14116 \times 10^{-03}}$
6.9×10^{-07} – 1.19×10^{-06}	$92.5359 \times q_i^{1.25816}$	$92.6756 \times q_i^{1.25852}$	$0.855544 \times q_i^{7.21452 \times 10^{-03}}$
1.19×10^{-06} – 2.38×10^{-06}	$92.0046 \times q_i^{1.25726}$	$104.484 \times q_i^{1.29188}$	$0.927497 \times q_i^{1.03785 \times 10^{-02}}$
2.38×10^{-06} – 1.00×10^{-05}	$92.2832 \times q_i^{1.25774}$	$64.4584 \times q_i^{1.27846}$	$0.967942 \times q_i^{6.66089 \times 10^{-03}}$

Table E.4: Parametrized fits of K_{ext} , K_{sca} and g for 6 short-wave bands for the hex_cav1 parameterization. Where q_i is the ice mass mixing ratio in Kg per Kg.

Wavelength, m	K_{ext}	K_{sca}	g
2.0×10^{-07} – 3.2×10^{-07}	$92.4557 \times q_i^{1.25807}$	$92.4557 \times q_i^{1.25807}$	$0.792337 \times q_i^{5.40227 \times 10^{-03}}$
3.2×10^{-07} – 5.05×10^{-07}	$92.7110 \times q_i^{1.25847}$	$92.7111 \times q_i^{1.25847}$	$0.815496 \times q_i^{5.57400 \times 10^{-03}}$
5.05×10^{-07} – 6.90×10^{-07}	$92.3745 \times q_i^{1.25793}$	$92.3761 \times q_i^{1.25794}$	$0.819914 \times q_i^{5.62200 \times 10^{-03}}$
6.9×10^{-07} – 1.19×10^{-06}	$92.5359 \times q_i^{1.25816}$	$92.6756 \times q_i^{1.25852}$	$0.824879 \times q_i^{5.99128 \times 10^{-03}}$
1.19×10^{-06} – 2.38×10^{-06}	$92.0046 \times q_i^{1.25726}$	$104.484 \times q_i^{1.29188}$	$0.901148 \times q_i^{9.62755 \times 10^{-03}}$
2.38×10^{-06} – 1.00×10^{-05}	$92.2832 \times q_i^{1.25774}$	$64.4584 \times q_i^{1.27846}$	$0.958268 \times q_i^{5.73484 \times 10^{-03}}$

Table E.5: Parametrized fits of K_{ext} , K_{sca} and g for 6 short-wave bands for the hex_cav2 parameterization. Where q_i is the ice mass mixing ratio in Kg per Kg.

Acknowledgments

This work was funded by a Doctoral Training Grant from the Natural Environment Research Council (NERC) in conjunction with a CASE studentship from Met Office.

References

- [1] Intergovernmental Panel on Climate Change, The Physical Science Basis: Contribution of Working Group 1 to the Fifth Assessment Report of the IPCC, Cambridge University Press, Cambridge, 2013.
- [2] Sassen, K., Wang, Z., Liu, D., Global distribution of cirrus clouds from CloudSat Cloud-Aerosol Lidar and Infrared Pathfinder Satellite Observations (CALIPSO) measurements., Journal of Geophysical Research 113.
- [3] Macke, A., Francis, P. N., Mcfarquhar, G. M., Kinne, S., The Role of Ice Particle Shapes and Size Distributions in the Single Scattering Properties of Cirrus Clouds, Journal of the Atmospheric Sciences 55 (1998) 2874–2883.

- [4] Bacon, N. J., Swanson, B. D., Laboratory measurements of light scattering by single levitated ice crystals, *Journal of the Atmospheric Sciences* 57 (2000) 2094–2104.
- [5] Baran, A. J., From the single-scattering properties of ice crystals to climate prediction: A way forward, *Atmospheric Research* 112 (2012) 45–69. doi:10.1016/j.atmosres.2012.04.010.
- [6] Baum, B. A., Yang, P., Heymsfield, A. J., Bansemer, A., Cole, B. H., Merrelli, A., Schmitt, C., Wang, C., Ice cloud single-scattering property models with the full phase matrix at wave-lengths from 0.2 to 100microns., *Journal of Quantitative Spectroscopy and Radiative Transfer* 146 (2014) 123–139.
- [7] Macke, A., Mishchenko, M. I., Applicability of regular particle shapes in light scattering calculations for atmospheric ice particles, *Applied Optics* 35 (1996) 4291–4296.
- [8] Um, J., McFarquhar, G. M., Single-Scattering Properties of Aggregates of Bullet Rosettes in Cirrus, *Journal of Applied Meteorology and Climatology* 46 (June) (2007) 757–775. doi:10.1175/JAM2501.1.
- [9] Xie, Y., Yang, P., Kattawar, G. W., Baum, B. A., Hu, Y., Simulation of the optical properties of plate aggregates for application to the remote sensing of cirrus clouds., *Applied Optics* 50 (8) (2011) 1065–81.
- [10] Baran, A., Labonnote, L. C., A self-consistent scattering model for cirrus. I: The solar region, *Quarterly Journal of the Royal Meteorological Society* 1912 (2007) 1899–1912. doi:10.1002/qj.
- [11] Baran, A. J., Hill, P., Furtado, K., Field, P., Manners, J., A Coupled Cloud Physics-Radiation Parameterization of the Bulk Optical Properties of Cirrus and its Impact on the Met Office Unified Model Global Atmosphere 5.0 Configuration, *Journal of Climate* 27 (2014) 7725–7752.
- [12] Schmitt, C. G., Heymsfield, A. J., On the Occurrence of Hollow Bullet Rosette and Column Shaped Ice Crystals in Midlatitude Cirrus, *Journal of the Atmospheric Sciences* 64 (12) (2007) 4514–4519. doi:10.1175/2007JAS2317.1.

- [13] Yang, P., Zhang, Z., Kattawar, G. W., Warren, S. G., Baum, B., Huang, H-L., Hu, Y. X., Winker, D., Iaquina, J., Effect of Cavities on the Optical Properties of Bullet Rosettes: Implications for Active and Passive Remote Sensing of Ice Cloud Properties, *Journal of Applied Meteorology and Climatology* 47 (9) (2008) 2311–2330.
- [14] Schnaiter, M., Kaye, P. H., Hirst, E., Ulanowski, Z., Wagner, R., Exploring the surface roughness of small ice crystals by measuring high resolution angular scattering patterns., *AAPP* 89 (1) (2011) 5–8. doi:10.1478/C1V89S1P084.
- [15] Ulanowski, Z., Hesse, E., Kaye, P. H., Baran, A. J., Light scattering by complex ice-analogue crystals, *Journal of Quantitative Spectroscopy and Radiative Transfer* 100 (1-3) (2006) 382–392. doi:10.1016/j.jqsrt.2005.11.052.
- [16] Gerber, H., Takano, Y., Garrett, T. J., Hobbs, P. V., Nephelometer measurements of the asymmetry parameter, volume extinction coefficient, and backscatter ratio in Arctic clouds, *Journal of the Atmospheric Sciences* (1999) (2000) 3021–3034.
- [17] Gayet, J.-F., Mioche, G., Shcherbakov, V., Gourbeyre, C., Busen, R., Minikin, A., Optical properties of pristine ice crystals in mid-latitude cirrus clouds: a case study during CIRCLE-2 experiment, *Atmospheric Chemistry and Physics* 11 (6) (2011) 2537–2544.
- [18] Korolev, A. V., Emery, E. F., Strapp, J. W., Cober, S. G., Isaac, G. A., Wasey, M., Marcotte, D., Small ice particles in tropospheric clouds: Fact or artifact? Airborne Icing Instrumentation Evaluation experiment., *Bulletin of the American Meteorological Society* 92 (2011) 967–973. doi:10.1175/2010BAMS3141.1.
- [19] Macke, A., Mueller, J., Raschke, E., Single scattering properties of atmospheric ice crystals, *Journal of the Atmospheric Sciences* 53 (1996) 2813–2825.
- [20] Macke, A., Mishchenko, M. I., Cairns, B., The influence of inclusions on light scattering by large ice particles, *Journal of Geophysical Research* 101 (1996) 23,311–23,316.

- [21] Yang, P., Liou, K. N., Single-scattering properties of complex ice crystals in terrestrial atmosphere., *Contr. Atmos. Phys.* 71 (1998) 223–248.
- [22] Labonnote, L. C., Brogniez, G., Buriez, J.-., Doutriaux-Boucher, M., Gayet, J.-F., Macke, A., Polarized light scattering by inhomogeneous hexagonal monocrystals: Validation with ADEOS-POLDER measurements, *Journal of Geophysical Research: Atmospheres* 106 (D11) (2001) 12139–12153. doi:10.1029/2000JD900642.
- [23] Baum, B. A., Heymsfield, A. J., Yang, P., Bedka, S. T., Bulk scattering properties for the remote sensing of ice clouds. Part I: Microphysical data and models., *Journal of Applied Meteorology* 44 (2005) 1885–1895.
- [24] Bozzo, A., Maestri, T., Rizzi, R., Tosi, E., Parameterization of single scattering properties of mid-latitude cirrus clouds for fast radiative transfer models using particle mixtures., *Geophysical Research Letters* 35 (2008) L16809.
- [25] Van Diedenhoven, B., Ackerman, A. S., Cairns, B., Fridlind, A. M., A Flexible Parameterization for Shortwave Optical Properties of Ice Crystals., *Journal of the Atmospheric Sciences* 71 (5) (2014) 1763–1782. doi:10.1175/JAS-D-13-0205.1.
- [26] Fu, Q., Sun, W. B., Yang, P., Modeling of scattering and absorption by nonspherical cirrus ice particles at thermal infrared wavelengths., *Journal of the Atmospheric Sciences* 56 (1999) 2937–2947.
- [27] McFarquhar, G. M., Heymsfield, A.J., The definition and significance of an effective radius for ice clouds., *Journal of the Atmospheric Sciences*.
- [28] Mitchell, D. L., Lawson, R. P., Baker, B., Understanding effective diameter and its application to terrestrial radiation in ice clouds, *Atmospheric Chemistry and Physics* 11 (2011) 3417–3429.
- [29] Baran, A. J., The dependence of cirrus infrared radiative properties on ice crystal geometry and shape of the size distribution function., *Quarterly Journal of the Royal Meteorological Society* 131 (2005) 1129–1142. doi:10.1256/qj.04.91.

- [30] Mitchell, D. L., Effective diameter in radiative transfer: General definition, applications and limitations, *Journal of the Atmospheric Sciences* 59 2330–2346.
- [31] Smith, H. R., Connolly, P. J., Baran, A. J., Hesse, E., Smedley, A. R. D., Webb, A. R., Cloud chamber laboratory investigations into the scattering properties of hollow ice particles, *Journal of Quantitative Spectroscopy and Radiative Transfer* 157 (2015) 106–118.
- [32] Edwards, J. M., Havemann, S., Thelen, J.-C., Baran, A. J., A new parameterization for the radiative properties of ice crystals: Comparison with existing schemes and impact in a GCM., *Atmospheric Research* 83 (2007) 19–35.
- [33] Stephens, G. L., et. al, An update on Earth’s energy balance in light of the latest global observations., *Nature Geoscience*.doi:10.1038/NNGEO1580.
- [34] Loeb, N. G., Wielicki, B. A., Doelling, D. R., Smith, G. L., Keyes, D. F., Kato, S., Manalo-Smith, N., Wong, T., Toward optimal closure of the earth’s top-of-atmosphere radiation budget, *Journal of Climate* 22 (2009) 748–766. doi:10.1175/2008JCLI2637.1.
- [35] Dee, D. P., et. al., The era-interim reanalysis: Configuration and performance of the data assimilation system., *Quarterly Journal of the Royal Meteorological Society* 137 (2011) 53–597. doi:10.1002/qj.828.
- [36] Walden, V. P., Warren, S. G., Tuttle, E., Atmospheric ice crystals over the Antarctic Plateau in winter, *Journal of Applied Meteorology* 42 (2003) 1391–1405.
- [37] Heymsfield, A. J., Bansemer, A., Field, P. R., Durden, S. L., Stith, J. L., Dye, J. E., Hall, W., Grainger, C. A., Observations and Parameterizations of Particle Size Distributions in Deep Tropical Cirrus and Stratiform Precipitating Clouds : Results from In Situ Observations in TRMM Field Campaigns, *Journal of the Atmospheric Sciences* 59 (2002) 3457–3491.
- [38] Bailey, M. P., Hallett, J., A Comprehensive Habit Diagram for Atmospheric Ice Crystals: Confirmation from the Laboratory, AIRS II, and

- Other Field Studies, *Journal of the Atmospheric Sciences* 66 (9) (2009) 2888–2899.
- [39] Schmitt, C. G., Iaquinta, J., Heymsfield, A. J., Iaquinta, J., The Asymmetry Parameter of Cirrus Clouds Composed of Hollow Bullet Rosette Shaped Ice Crystals from Ray-Tracing Calculations, *Journal of Applied Meteorology and Climatology* 45 (2006) 973–981.
- [40] Weickmann, H., Die Eisphase in der Atmosphäre, *Berichte des Deutschen Wetterdienstes in der US-Zone, Dt. Wetterdienst in der US-Zone*, 1949.
- [41] Hesse, E., McCall, D., Ulanowski, Z., Stopford, C., Kaye, P. H., Application of rtdf to particles with curved surfaces, *Journal of Quantitative Spectroscopy and Radiative Transfer* 110 (2009) 1599–1603.
- [42] Heymsfield, A. J., Miloshevich, L. M., Parameterizations for the Cross-Sectional Area and Extinction of Cirrus and Stratiform Ice Cloud Particles, *Journal of the Atmospheric Sciences* 60 (2003) 936–956.
- [43] McFarquhar, G. M., Um, J., Jackson, R., Small Cloud Particle Shapes in Mixed-Phase Clouds, *Journal of Applied Meteorology and Climatology* 52 (5) (2013) 1277–1293.
- [44] Field, P. R., Heymsfield, A. J., Bansemer, A., Twohy, C. H., Determination of the combined ventilation factor and capacitance for ice crystal aggregates from airborne observations in a tropical anvil cloud., *Journal of the Atmospheric Sciences* 65 (2008) 376–391. doi:10.1175.2007JAS2391.1.
- [45] Cotton, R. J., Field, P. R., Ulanowski, Z., Kaye, P. H., Hirst, E., Greenaway, R. S., Crawford, I., Crosier, J., Dorsey, J., The effective density of small ice particles obtained from in situ aircraft observations of mid-latitude cirrus, *Quarterly Journal of the Royal Meteorological Society* 139 (676) (2013) 1923–1934.
- [46] Havemann, S., Baran, A. J., Calculation of the phase matrix elements of elongated hexagonal ice columns using the T-matrix method, *Journal of Quantitative Spectroscopy and Radiative Transfer* 89 (2004) 87–96. doi:10.1016/j.jqsrt.2004.05.014.

- [47] Warren, S. G., Brandt, R. E., Optical constants of ice from the ultra-violet to the microwave: A revised compilation, *Journal of Geophysical Research* 113 (D14) (2008) 1–10.
- [48] Field, P. R., Heymsfield, A. J., Bansemer, A., Snow size distribution parameterization for midlatitude and tropical ice cloud., *Journal of the Atmospheric Sciences* 64 (2007) 4346–4365.
- [49] Field, P. R., Heymsfield, A. J., Bansemer, A., Shattering and particle interarrival times measured by optical array probes in ice clouds., *Journal of Atmospheric and Oceanic Technology* 23 (2006) 1357–1371.
- [50] Walters, The Met Office Unified Model Global Atmosphere 6.0/6.1 and JULES Global Land 6.0/6.1 configurations, in preparation.
- [51] Furtado, K., Field, P. R., Cotton, R., Baran, A. J., The sensitivity of simulated high clouds to ice crystal fall speed, shape and size distribution., *Quarterly Journal of the Royal Meteorological Society*-doi:10.1002/qj.2457.
- [52] Manners, J., A correlated-k radiative transfer scheme for the Met Office Global Atmosphere 7.0 model configuration, in preparation.
- [53] Yang, P., Hu, Y. X., Winker, D. M., Zhao, J., Hostetler, C. A., Poole, L., Baum, B. A., Mishchenko, M. I., Reichardt, J., Enhanced lidar backscattering by quasi-horizontally oriented ice crystal plates in cirrus clouds, *Journal of Quantitative Spectroscopy and Radiative Transfer* 79-80 (2003) 1139–1157. doi:10.1016/S0022-4073(02)00346-1.
- [54] Hashino, T., Chiruta, M., Polzin, D., Kubicek, A., Wang, P. K., Numerical simulation of the flow fields around falling ice crystals with inclined orientation and the hydrodynamic torque, *Atmospheric Research* 150 (2014) 79–96. doi:10.1016/j.atmosres.2014.07.003.
- [55] Foster, T. C., Hallett, J., Enhanced alignment of plate ice crystals in a non-uniform electric field, *Atmospheric Research* 90 (1) (2008) 41–53. doi:10.1016/j.atmosres.2008.02.017.
- [56] McFarquhar, G. M., Yang, P., Macke, A., Baran, A. J., A new parameterization of single scattering solar radiative properties for tropical anvils

- using observed ice crystal size and shape distributions., *Journal of the Atmospheric Sciences* 59 (2002) 2458–2478.
- [57] Mishchenko, M. I., Cairns, B., Kopp, G., Schueler, C. F., Fafaul, B. A., Hansen, J. E., Hooker, R. J., Itchkawich, T., Maring, H. B., Travis, L. D., Accurate monitoring of terrestrial aerosols and total solar irradiance introducing the glory mission., *Bulletin of the American Meteorological Society* 88 (2007) 677–691.
- [58] Baran, A. J., Labonnote, L.-C., On the reflection and polarisation properties of ice cloud., *Journal of Quantitative Spectroscopy and Radiative Transfer* 100 (2006) 41–54.
- [59] Stephens, G. L., Vane, D. G., Boain, R. J., Mace, G. G., Sassen, K., Wang, Z., Illingworth, A. J., O'Connor, E. J., Rossow, W. B., Durden, S. L., Miller, S. D., Austin, R. T., Benedetti, A., Mitrescu, C., The CloudSat Science Team, The Cloudsat Mission and the A-Train, *Bulletin of the American Meteorological Society* 83 (12) (2002) 1771–1790. doi:10.1175/BAMS-83-12-1771.
- [60] Schnaiter, M., Schon, R., Mohler, O., Saathoff, H., Wagner, R., Backscattering linear depolarization ratio of laboratory generated ice clouds composed of pristine and complex-shaped ice crystals., in: 10th International Conference on Light Scattering by Non-spherical Particles, 2007, pp. 193–196.
- [61] Platt, C. M. R., Lidar backscatter from horizontal ice crystal patterns, *Journal of Applied Meteorology* 17 (1978) 482–8.
- [62] Chepfer, H., Brogniez, G., Goloub, P., Breon, F. M., Flamant, P. H., Observations of horizontally oriented ice crystals in cirrus clouds with POLDER-1 ADEOS-1, *Journal of Quantitative Spectroscopy and Radiative Transfer* 63 (1999) 21–43.
- [63] Westbrook, C. D., Origin of the parry arc, *Quarterly Journal of the Royal Meteorological Society* 137 (655) (2011) 538–543. doi:10.1002/qj.761.

This thesis has examined the single scattering properties of ice crystals using a combination of laboratory based experiments and modelling. Chapters 4 and 5 focused on laboratory experimentation, measuring the phase function and linear depolarisation ratio, respectively. For both experiments, observations were used to create particle models for use in scattering simulations, and measured and modelled results were compared. Chapter 6 used observations from laboratory experiments to develop and test a single habit parametrization for cirrus.

7.1 Principal Conclusions

One of the scattering properties of importance to climate modelling, is the asymmetry parameter, g , and by extension, the phase function, P_{11} (which is used to compute the asymmetry parameter, see section 2.3.2). As discussed in chapters 3 and 4, in-situ and laboratory studies have previously found that measurements yield lower asymmetry parameters, and smoother phase functions, than those predicted by scattering models [1]. The first paper (chapter 4) reported the first single-scattering measurements in the Manchester Ice Cloud Chamber (MICC). The phase function, P_{11} , and asymmetry parameter, g , were measured for five ice clouds, each consisting of a predominant habit with a narrow size distribution, and therefore measurements of P_{11} and g could be attributed to specific particle habits. One of the main findings of this paper was the difference in internal structure between the hollow columns grown at -7°C and those grown below -20°C . The hollow columns grown at warmer temperatures exhibited a pyramidal shaped cavity, similar to those modelled by previous studies [2, 3]. However, below -20°C , hollow cavities appeared as a series of stepped hexagonal prisms (see figure 6, chapter 4). Microscope measurements were made of the formvar replicas and used to construct a new particle ge-

ometry to represent this stepped hollow column (see figure 7, chapter 4). For each of the five clouds, formvar replicas were used to take measurements of particle size and habit. These were used to create a series of particle models which were used in Ray Tracing and Ray Tracing with Diffraction on Facets (RTDF) [4, 5]. The models used included the solid hexagonal column, solid hexagonal plate, hexagonal hollow column with pyramidal cavities (named ‘hollow 1’), and a hollow column with stepped cavities (named ‘hollow 2’). Ray Tracing and RTDF results for the hollow 1 geometry showed a general *increase* in asymmetry parameter when compared with a solid column of the same size and aspect ratio, similar to results found previously [3]. For the stepped hollow column model, both Ray Tracing and RTDF showed a net *decrease* in asymmetry parameter. For a particle of aspect ratio 1, Ray tracing results predicted a reduction in asymmetry of 0.23%, whereas RTDF predicted a reduction in asymmetry parameter of 1.94%. Furthermore, the use of RTDF produced smoother phase functions, with less prominent peak features when compared to Ray Tracing results. Comparing measured and modelled results, we see in all cases, modelled results over-predicted the asymmetry parameter with deviations between 3% and 12%. In general, RTDF predictions of g and P_{11} were closer to measured results than those predicted by Ray Tracing. Observations from this experiment show that clouds grown below -20°C are composed almost exclusively of hollow particles with stepped internal cavities. In conjunction with early in situ observations [6], this would suggest that this crystal geometry is a common occurrence in the atmosphere. In addition to columns, plates grown within the dendrite region (-10°C – -20°C) show similar internal structures before developing into sectorised plates or dendrites, and therefore the stepped hollow column geometry may be applicable to this temperature range too. These findings highlight the sensitivity of single scattering properties to the accurate representation of the crystal geometry and offer a new particle model which can be used to represent real ice crystals, or as a novel way to reduce the asymmetry parameter.

The second paper (Chapter 5) also investigated single scattering properties of solid and hollow ice crystals. For the first time, measurements of the linear depolarisation ratio were taken in the Manchester Ice Cloud Chamber. The optical arrangement from the first paper was altered to take polarised measurements of scattering at exact and near backscattering angles. The co- and cross-polarised components of scattered light were taken to find the Linear Depolarisation Ratio, δ at 178° , 179° and 180° . The experimental set-up varied slightly from that of paper 1 such that the supersaturation in the cloud chamber was allowed to vary in time, so that in each experiment the crystal habit also varied in time. Three experiments were conducted at temperatures of -7°C , -15°C and -30°C . For experiments at -7°C , habits ranged from hollow columns with pyramidal cavities to solid columns, at -15°C habits ranged from dendrites to complex plates to pristine plates. At -30°C , only columns with stepped internal cavities were observed, although they transitioned from column-like to plate-like throughout the experiment. Similarly to Paper 1, geometric particle models were constructed to represent the observed habits, and these

were used in a Ray Tracing code to predict δ [4]. A comparison of measured and modelled results showed that Ray Tracing results largely over-predicted δ for solid columns and hollow columns with pyramidal cavities, with average differences of $\approx 120\%$. Whilst Ray Tracing results from the stepped hollow column model also over-predicted δ , differences between measured and modelled results were reduced to an average of just 30%. Although the ability of Ray Tracing to accurately treat polarisation has been questioned, these results show that improvements in the particle modelling can produce significantly more realistic results. Although improvements to scattering models are still necessary, improvements to particle models cannot be overlooked. This paper supported the findings from paper 1 regarding the need for accurate representation of crystal geometry, and showed that this is not only crucial for predicting radiances, but also polarisation dependent properties.

The third paper uses a stepped hollow column particle model (developed in paper 1 and further tested in paper 2) to develop a new radiative parametrization for cirrus, the parametrization was then tested in the Met Office Unified Model. The stepped hollow column was commonly observed at temperatures $< -20^\circ\text{C}$ and these observations were used to create a physically representative particle model. The modelled results using this new model have returned more realistic values not only for P_{11} and g , but also for δ . As discussed in section 3.2.1, the use of ‘distortion’ is widely used in optical parametrizations as a way of achieving lower asymmetry parameters, more in line with measured values. An alternative technique which is also used in optical parametrizations is the use of internal scatterers embedded into the main particle [7]. Recent literature has argued that by adhering to the same microphysical relationships regarding mass, m , area ratio, A_r and maximum dimension, D , as the microphysical scheme, that the exact shape of the particle need not be accurately represented [8]. The $A_r(D)$ relationship should, in theory, ensure that correct scattering cross-sections are assumed, and the additional $m(D)$ relationship ought to ensure that absorption cross sections and single scattering albedos are correct. This covers three of the four parameters used to describe the bulk optical properties of cirrus in a Global Circulation Model (GCM). The fourth parameter, g , can then be achieved with the use of the distortion parameter or particle inclusions. To test this theory, the parametrization presented in Paper 3 uses a single particle habit (the stepped hollow column model) fitted to observed $A_r(D)$ and $M(D)$ relationships. In order to fit the stepped hollow column model to these relationships, preferentially oriented particles had to be assumed. By doing so, large aspect ratios up to $\alpha = 20$ were required, and the high densities observed for particles $\leq 70 \mu\text{m}$ could not be achieved. As a result, the predictions of mass extinction were significantly lower than other parametrizations [9, 10]. The effect of this was to under-predict the reflected short-wave radiation at the Top Of Atmosphere (TOA). As a whole, the new parametrization (from this point forward referred to as `hex_cav`) differed from observations more so than the comparison parametrizations, however regional improvements were observed. For TOA fluxes, improvements were

seen mainly over ocean areas, including the North Atlantic, Indian and Pacific Oceans. Furthermore, existing biases in the zonal mean temperature and specific humidity in polar regions were reduced. These regional improvements may correspond to areas consisting of smaller ice particles, and therefore the large, elongated particles have little influence on the region. Alternatively, the improvements may be associated with more randomized crystal orientations. By achieving random orientation, A_r is reduced when compared with a preferentially oriented particle. Therefore, mass extinction was under-predicted for areas with preferentially oriented particles more so than those with randomly oriented particles. These results suggest that a single particle model, even when physically consistent with the microphysical scheme, cannot accurately represent the optical properties of the full diversity of cirrus ice particles. However, the particle model has been observed both in laboratory and field experiments and could be used in any model of habit distributions at the small end of particle size distribution.

7.2 Further Work

7.2.1 Particle modelling

This work has highlighted the sensitivity of model predictions to the accurate representation of fine details in the crystal geometry. This applies not only for radiances, but also for polarised scattering. Although the stepped hollow column has yielded more realistic results for P_{11} , g and δ , the full extent of ice crystal geometries remains largely unrepresented. Throughout the experiments, several other deviations were noted. In particular, the presence of scalene or trigonal particles were a regular occurrence as observed in various field and laboratory studies [6, 11]. A theoretical study investigated the extinction and absorption efficiencies of trigonal particles using Anomalous Diffraction Approximation (ADA), with results showing a reduction in absorption efficiency for scalene and trigonal particles when compared to hexagonal particles [11]. An extension to this study may include Ray Tracing, RTDF or IGO simulations of the single scattering properties of scalene/trigonal particles in order to investigate the effect on other fundamental parameters such as P_{11} , P_{12} , g and δ . Furthermore, results could be tested in a radiative transfer model to assess the impact of trigonal particles on atmospheric fluxes. In addition to the occurrence of trigonal particles, hollow particles grown below -10°C tended to show indentations not only on their basal facets, but their prism facets too. Unfortunately due to imaging techniques, the exact structures of these indentations were difficult to determine. Improvements in replication or imaging techniques may be useful in determining these cavity shapes, allowing them to be implemented into future particle models.

7.2.2 Instrumentation

The second paper presented measured and modelled results of the linear depolarisation ratio of various ice crystal habits. The linear depolarisation ratio is commonly used in remote sensing instrumentation that take polarised reflectances at near back-scattering angles to determine thermodynamic phase, and to an extent, particle habit and orientation. Certain in-situ instruments also utilize polarised scattering measurements for the purpose of distinguishing particle sphericity (such as the APSD) and discriminating between droplets and small ice (such as the CPSD and CAS-DPOL). The exact and near backscattering measurements presented here show that the near backscattering angles 178° and 179° are sensitive to particle hollowness. This sensitivity could, in theory, be used for near backscattering measurements in remote or in-situ instrumentation for determining particle hollowness. Linear depolarisation ratio was modelled using Ray Tracing for a variety of habits between angles 0.25° and 179.75° [4]. In addition to the backscattering region, different particle habits exhibit different values of δ at smaller scattering angles. In particular, the forward scattering region (0° – 20°) showed a reduction in δ for the pyramidal hexagonal cavity, but not for the stepped hexagonal cavity. Although these measurements cannot be taken with remote sensing instruments, in-situ instrumentation has the capability to take single-scattering measurements at a variety of different scattering angles. Further experimental and modelling studies could highlight additional angular sensitivities of δ on particle habit. Targeted angular measurements could then be made in-situ to determine microphysical properties not discernible from optical imaging probes.

7.3 Final remarks

Overall, this work supports existing evidence that fine features of ice crystals can have significant affects on their scattering behaviour. Overlooking these intricacies can lead to errors in single scattering properties (both natural and polarised) which can then permeate into bulk optical properties, causing errors in climate models. Improvements in the accuracy of ice crystal modelling can help to reduce these errors, although there are still many common crystal geometries left unrepresented. Other than net fluxes and radiances, polarised scattering properties are also highly dependent upon these deviations in particle habit. While polarisation is as yet overlooked in climate modelling, improved knowledge in this area can be applied to remote sensing and in-situ instrumentation allowing for more accurate retrievals of cloud microphysical properties, which can then feed into improvements in climate models in terms of flux and radiance simulations. Continued investigation into the scattering properties of single ice crystals can offer a way to improve upon these techniques, opening avenues in microphysical instrumentation, remote sensing and climate modelling.

References

- [1] Gerber, H., Takano, Y., Garrett, T. J., and Hobbs, P. V. “Nephelometer measurements of the asymmetry parameter, volume extinction coefficient, and backscatter ratio in Arctic clouds”. In: *Journal of Atmospheric Science* 1999 (2000), pp. 3021–3034.
- [2] Schmitt, C. G., Iaquinta, J., Heymsfield, A. J., and Iaquinta, J. “The Asymmetry Parameter of Cirrus Clouds Composed of Hollow Bullet Rosette - Shaped Ice Crystals from Ray-Tracing Calculations”. In: *Journal of Applied Meteorology and Climatology* 45.July (2006), pp. 973–981.
- [3] Yang, P., Zhang, Z., Kattawar, G. W., Warren, S. G., Baum, B., Huang, H-L., Hu, Y. X., Winker, D., and Iaquinta, J. “Effect of Cavities on the Optical Properties of Bullet Rosettes: Implications for Active and Passive Remote Sensing of Ice Cloud Properties”. In: *Journal of Applied Meteorology and Climatology* 47.9 (2008), pp. 2311–2330.
- [4] Macke, A., Mueller, J., and Raschke, E. “Single scattering properties of atmospheric ice crystals”. In: *Journal of Atmospheric Science* 53 (1996), pp. 2813–2825.
- [5] Hesse, E., Macke, A., Havemann, S., Baran, A. J., Ulanowski, Z., and Kaye, P. H. “Modelling diffraction by faceted particles”. In: *Journal of Quantitative Spectroscopy and Radiative Transfer*. 113.5 (2012), pp. 342–347.
- [6] Weickmann, H. *Die Eisphase in der Atmosphäre*. Berichte des Deutschen Wetterdienstes in der US-Zone. Dt. Wetterdienst in der US-Zone, 1949.
- [7] Baran, A. J. and Labonnote, L. C. “On the reflection and polarization properties of ice cloud”. In: *Journal of Quantitative Spectroscopy and Radiative Transfer* 100 (2006), pp. 41–54.
- [8] van Diedenhoven, B., Ackerman, A. S., Cairns, B., and Fridlind, A. M. “A Flexible Parameterization for Shortwave Optical Properties of Ice Crystals.” In: *Journal of the Atmospheric Sciences* 71.5 (2014), pp. 1763–1782. DOI: 10.1175/JAS-D-13-0205.1.
- [9] Baran, A. J., Hill, P., Furtado, K., Field, P., and Manners, J. “A Coupled Cloud Physics-Radiation Parameterization of the Bulk Optical Properties of Cirrus and its Impact on the Met Office Unified Model Global Atmosphere 5.0 Configuration”. In: *Journal of Climate* November (June 2014), p. 140625124737000. DOI: 10.1175/JCLI-D-13-00700.1.
- [10] Edwards, J. M., Havemann, S., Thelen, J.-C., and Baran, A. J. “A new parameterization for the radiative properties of ice crystals: Comparison with existing schemes and impact in a GCM.” In: *Atmospheric Research* 83 (2007), pp. 19–35.

- [11] Murray, B. J., Salzmann, C. G., Heymsfield, A. J., Dobbie, S., Neely, R. R., and Cox, C. J. “Trigonal ice crystals in Earth’s atmosphere”. In: *Bulletin of the American Meteorological Society* (2014). DOI: 10.1175/BAMS-D-14-00017.1.

List of Figures

1.1	Left: Cirrus clouds over The University of Manchester, August 2013. Right: Ice halo and sun dogs over North Dakota, photograph courtesy of Ron Stenz, University of North Dakota.	8
1.2	Radiative fluxes in the atmosphere. Figure courtesy of the IPCC [IPCC1].	9
1.3	Radiative forcing contributions and uncertainties, figure reproduced courtesy of the IPCC (figure SPM.5, page 14 WG1AR5) [IPCC2013].	10
1.4	Global distributions of cirrus cloud from CloudSat Cloud-Aerosol Lidar and Infrared Path-finder Satellite Observations (CALIPSO) measurements. Image reproduced from Sassen et. al. 2008 [Sassen2008]	11
2.1	A plane electromagnetic wave propagating in the z direction. The electric, (E), and magnetic, (B) field components are depicted in red and blue respectively.	15
2.2	Three different polarisations as seen from the trace of one full cycle. From left to right: a linearly polarised beam, polarised in the y plane, a right-hand elliptically polarised beam, polarised in the y plane, and a right hand circular polarised beam.	16
2.3	An xy view of a right hand elliptically polarised beam propagating in the z direction. The polarisation is defined by the electric field component and therefore the magnetic field component is not shown. ψ describes the orientation of the polarisation in the xy plane, and χ describes the width of the ellipse.	17
2.4	An incident beam propagating in the x direction is scattered by a non-spherical particle at the origin. The scattering angle, θ is defined as the angle between the direction of the incident and scattered beams in the scattering plane, where the scattering plane in this example is the xz plane.	19

2.5	. An incident beam is scattered by a particle at the origin. The light is scattered in direction \mathbf{a} , into a solid angle element $d\Omega$. Vector \mathbf{a} makes an angle θ with the x -axis in the scattering plane (shaded), and an angle ϕ with the x axis in the xy plane. $d\Omega$ is equal to $d\theta d\phi$	20
2.6	Definition of the c axis and a axes of an ice crystal: the c axis is parallel to the prism facet (shaded blue), whereas the a axes are parallel to the basal facet (shaded grey). For an E-field polarised parallel to the c axis (an ‘extraordinary wave’), the real refractive index, n , is a maximum. For an E-field polarised perpendicular to c , the real refractive index is a minimum. Example refractive indices given in the diagram are for a wavelength of 546 nm. For a wave propagating in the c direction, refractive index is not polarisation dependent.	22
2.7	A ray travels from medium 1 to medium 2, according to Snell’s law of refraction. The left hand ray path shows an incident ray, where the angle of incidence (θ_1) is less then the critical angle (θ_{crit}), the ray is therefore refracted. The ray path shown on the right hand side show the case where the angle of incidence is greater than the critical angle, at which point the ray is reflected.	27
3.1	Illustrations of observed snow crystal habits by Robert Hooke, published in ‘Micrographia’ [Micrographia].	32
3.2	Photographs of ground based ice crystal samples. Photography by Aaron Kennedy, University of North Dakota.	32
3.3	Formar images collection in-situ. Left to right: a short column, a hollow column, a budding 4 branched rosette, a plate and a trigonal ice crystal. Figure adapted from Heymsfield et al. 1986 [Heymsfield1986].	33
3.4	Optical imaging arrangement of the SPEC CPI. Figure reproduced courtesy of the Stratton Park Engineering Company [SPEC].	34
3.5	Ice crystal images taken using the CPI-v1.0 in the Manchester Ice Cloud Chamber. As a coherent light source is used, diffraction fringes are evident on the particle images, this can complicate habit recognition.	34
3.6	Left: original tip design: Particle shatter on the probe inlet and shattered fragments are redirected into the sample volume. Right: anti-shatter tips direct particles incident on the tips away from the sample volume. Figure courtesy of Droplet Measurement Technologies [DMT].	35

3.7	Left: A polar plot showing the scattered intensity with respect to scattering angle, the ‘forward scattering lobe’ can be seen in the 0° – 5° region. Right: a cartesian plot of the normalised scattered intensity with respect to scattering angle (phase function). Calculations are done for a $10\ \mu\text{m}$ homogeneous sphere with real refractive index 1.33, in a medium of real refractive index 1. Results are obtained using Jan Schaefer’s ‘MatScat’ code [MatScat].	36
3.8	Diffraction patterns taken from the SID-3. From left to right: pristine hexagonal column, roughened hexagonal column, bullet rosette & dust grain. Images adapted from Ulanowski et al. 2014 [Ulanowski2014].	36
3.9	CPI images of mid-latitude cirrus particles at a) cloud top and, b) cloud bottom. Figure from Baran 2009 [Baran2009].	38
3.10	CPI images of tropical cirrus particles in a a) fresh anvil and, b) aged anvil. Figure from Baran 2009 [Baran2009].	39
3.11	Ice crystal habit with respect to temperature and supersaturation. Figure from Bailey & Hallet 2009 [Bailey2009].	41
3.12	Left: a rough ice surface imaged in a VP-SEM sample stage. Right: A heavily rimed ice crystal observed during in situ studies by Ono 1969 [Ono1969].	43
3.13	Models of plate aggregates with varying aggregation index, AI . a) $AI = 1$, b) $AI = 0.81$, c) $AI = 0.6$ and d) $AI=0.4$. Figure from Um & McFarquhar 2009 [Um2009].	45
3.14	Representation of nonspherical particles. a) chebyshev particle, b) gaussian random sphere, c) droxtal, d) budding bucky ball, e) koch fractal crystal. Figures adapted from Um & McFarquhar 2011 [Um2011], and Macke et al. 1996 [4].	46
3.15	The Inhomogeneous Hexagonal Monocrystal: a hexagonal prism is embedded with internal scatterers to alter the single scattering properties of the prism. Figure from Labonnote et al. 2001 [7].	47
3.16	Optical set-up of a polar nephelometer. Particles enter the probe in an air flow where they pass through a 800nm laser beam. Light scattered in the plane of the paraboloidal mirror is reflected onto an array of photodiodes where the intensity is measured. The measured intensities at different scattering angles is used to produce a phase function. Figure adapted from Gayet et al. 1997 [Gayet1997].	49

3.17	Optical arrangement of the Cloud Integrating Nephelometer (Gerber Scientific Inc., Reston, Virginia). Particles in an air flow are passed through a sample volume where they are illuminated by a laser. Four photomultipliers (S1-4) are used to measure the intensity of scattered light. S1 and S3 measure forward scattered light, whereas S2 and S4 measure backward scattered light. Cosine masks are used to weight the measurements of S3 and S4 with respect to scattering angle. Figure adapted from Gerber et al. 2000 [1].	50
3.18	Application of scanning detector optics to measure the phase function from an ensemble of particles in a laboratory cloud chamber. A laser beam is directed through a cloud of particles, which scatter the beam in all directions. 10% Beam splitters are used to measure the intensity of the incident and attenuated beam (and therefore extinction), and a rotating detector measures scattered intensity at different scattering angles. Figure from Saunders et al. 1998 [Saunders1998].	52
3.19	Current particle models used for MODIS satellite retrievals from Baum et al. 2005 [Baum2005].	55
3.20	Elements of the ensemble model. a) the hexagonal column, b) the bullet rosette, c) the three branched hexagonal aggregate, d) the compact five branched hexagonal aggregate, e) the eight element chain like hexagonal aggregate and f) the ten element chain like hexagonal aggregate. Figure from [Baran2007].	56